
**Isospin symmetry in the sd shell:
Coulomb excitation of ^{33}Ar at relativistic energies
and the new 'Lund-York-Cologne-Calorimeter'**

Inaugural-Dissertation
zur
Erlangung des Doktorgrades
der Mathematisch-Naturwissenschaftlichen Fakultät
der Universität zu Köln

vorgelegt von
Andreas Wendt
aus Göttingen

Köln 2013

Berichtersteller: Prof. Dr. Peter Reiter
Prof. Dr. Jan Jolie

Tag der mündlichen Prüfung: 15.11.2012

Sometimes, you have to roll a hard six.

William Adama

Contents

1	Introduction	5
2	Physics of mirror nuclei	7
2.1	Isospin formalism	7
2.2	Isospin symmetry	8
2.3	Energy differences in mirror nuclei	9
2.3.1	Coulomb displacement energies (CDE)	9
2.3.2	Energy differences between excited isobaric analog states	11
2.3.3	Application on $f_{7/2}$ - shell nuclei	14
2.3.4	Application on sd - shell nuclei	16
2.4	The mirror pair ^{33}Ar - ^{33}P	23
3	The PreSpec campaign	25
3.1	PreSpec experiments	25
3.1.1	Commissioning	25
3.1.2	Coulomb excitation of ^{88}Kr	26
3.1.3	Coulomb excitation of ^{104}Sn	26
3.1.4	Coulomb excitation of ^{33}Ar : Transition strengths of mirror nuclei	26
3.2	Production of radioactive ion beams	27
3.3	The GSI-FRS setup	28
3.3.1	Accelerators	28
3.3.2	The fragment separator (FRS)	29
3.4	Beam preparation for the ^{33}Ar experiment	33
3.4.1	FRS setups	34
3.4.2	Comparison of simulation and FRS identification	38
3.5	The PreSpec setup	40
3.6	Data acquisition (DAQ) and trigger logic	42

4 The LYCCA detector array	45
4.1 Setup and detection principle	45
4.2 Detectors and hardware	46
4.2.1 Double-sided silicon strip detector (DSSD)	46
4.2.2 Caesium iodide scintillators (CsI)	48
4.2.3 $\Delta E - E$ module	50
4.2.4 Plastic scintillators	52
4.2.5 Chamber and holding structure	53
4.2.6 Preamplifiers and electronics	57
4.3 Test results	58
4.3.1 Detector tests with α -sources	58
4.3.2 In-beam test at the Cologne tandem accelerator	60
4.3.3 Commissioning and experiments at the GSI/FRS facility	62
4.3.4 In-beam tracking and particle identification	66
4.4 Conclusions	71
5 Data analysis of experiment S377	73
5.1 Detector observables	74
5.1.1 Particle information provided by FRS detectors	74
5.1.2 Particle information provided by LYCCA detectors	74
5.1.3 γ -ray detectors	75
5.2 Setting particle gates	76
5.2.1 Secondary beam mass cut	76
5.2.2 Z identification after the secondary target	77
5.2.3 $\Delta E_{target} - \Delta E_{wall}$ - gate	77
5.2.4 $\beta_{FRS} - \beta_{LYCCA}$ - gate	78
5.2.5 $\beta_{LYCCA} - CsI$ - gate	79
5.2.6 Target DSSD energy-time-correlation	79
5.3 Multi-hit events in the target DSSD	80
5.4 Doppler correction and germanium time-gates	86
5.5 Optimization of γ -ray spectroscopy	89
5.5.1 Target DSSD multiplicity	89
5.5.2 γ -rays emitted from sources in rest	90
5.5.3 Optimizing the particle-gates	93

CONTENTS

5.5.4	Optimizing the time gate	95
5.5.5	Add-back	99
5.5.6	Scattering angle	99
5.5.7	Background subtraction	103
5.5.8	Disparities in the γ -ray spectra of the different germanium detector rings	108
5.6	Summary of data analysis	110
6	Experimental results	113
6.1	γ -ray detection efficiency	114
6.2	Corrections for the γ -ray detection efficiency	116
6.2.1	Energy dependence of the efficiency of germanium detectors	116
6.2.2	Correction for different ion velocities	119
6.3	Reduced transition strengths in ^{33}Ar	122
6.3.1	Effects of the branching ratio	123
6.3.2	Calculation of the $B(E2)$ value of the first excited state (1359 keV)	125
6.3.3	Calculation of the $B(E2)$ value of the second excited state (1798 keV)	125
6.3.4	Experimental data for the $B(E2; 2_1^+ \rightarrow g.s.)$ value of ^{36}Ar	127
6.4	Summary	128
7	Comparison with shell model calculations	131
7.1	Effective interactions for shell model calculations	131
7.2	The $T_z = \pm \frac{3}{2}$ mirror pair ^{33}Ar - ^{33}P	135
7.3	Systematics of transition strengths in sd shell mirror nuclei	140
8	Outlook	149
A	The nuclear shell model	153
B	Transition probabilities	155
C	Graphs and pictures	157
D	Technical drawings	165

Abstract

The 'Lund-York-Cologne-Calorimeter' (LYCCA) is the first operational NUSTAR (Nuclear structure astrophysics and reactions) device for the HiSpec (High resolution in flight spectroscopy, starting in 2017) experiment at FAIR (Facility for anti proton and ion research). LYCCA is a high efficient detector array for identification and tracking of exotic nuclei and the design, testing and commissioning of LYCCA was the main part of this work. The first part of this thesis discusses tests performed with α -sources, a proton beam at the Cologne FN-Tandem accelerator and heavy ion beams at the GSI facility. The successful operation of LYCCA achieved resolutions of $\frac{\Delta Z}{Z} = 0.6(1)$ (for $Z = 36$) and $\frac{\Delta A}{A} = 1.1(1)$ (for $A = 104$) FWHM for in-beam measurements with relativistic heavy ions.

A relativistic beam Coulomb excitation experiment using a radioactive beam was recently performed at GSI employing LYCCA, with the aim of measuring the reduced transition strengths ($B(E2)$ values) of the first two excited states in ^{33}Ar . The radioactive ion beam was produced by impinging a primary ^{36}Ar beam on a primary ^9Be target. At the central position of the γ -array (consisting of 15 EUROBALL Cluster high-purity germanium detectors and eight HECTOR BaF_2 scintillators) the secondary ^{33}Ar beam hit a ^{197}Au target with an energy of approximately 145 MeV/u. LYCCA was used to track the outgoing ions and to reject all nuclear reaction channels.

For the two lowest energetic excited states of ^{33}Ar (excitation energies: $(\frac{3}{2})_1^+$: 1359 keV and $(\frac{5}{2})_1^+$: 1798 keV) the reduced transition strengths have been determined:

$$B\left(E2; \left(\frac{3}{2}\right)_1^+ \rightarrow \left(\frac{1}{2}\right)_{g.s.}^+\right) = 6.39(1.49) \text{ W.U.}$$

$$B\left(E2; \left(\frac{5}{2}\right)_1^+ \rightarrow \left(\frac{1}{2}\right)_{g.s.}^+\right) = 5.80(1.62) \text{ W.U.}$$

These are the first transition strength values for proton-rich $T_z = -\frac{3}{2}$ sd shell nuclei. The new experimental data is used to test effective interactions for shell model calculations, describing excitation energies of sd shell mirror pairs. Shell model calculations based on a modified USD interaction employing full sd model space, yields the transition strengths 4.790 W.U. ($(\frac{3}{2})_1^+ \rightarrow (\frac{1}{2})_{g.s.}^+$) and 6.225 W.U. ($(\frac{5}{2})_1^+ \rightarrow (\frac{1}{2})_{g.s.}^+$) for the two new experimental results in ^{33}Ar .

Kurzzusammenfassung

Das 'Lund-York-Cologne-Calorimeter' (LYCCA) ist der erste einsatzbereite NUSTAR (Nuclear structure astrophysics and reactions) Detektor für die 'High resolution in flight spectroscopy' Kampagne (HiSpec, ab 2017) an FAIR (Facility for anti proton and ion research). LYCCA ist ein hoch effizienter Detektor für die Identifikation und das Tracking (Rekonstruktion der Trajektorie) von exotischen Ionen. Design, Tests und Inbetriebnahme von LYCCA waren ein wesentlicher Teil dieser Arbeit. Dazu gehören Messungen, die mit α -Quellen, Protonen des Kölner FN-Tandem Beschleunigers und Schwerionenstrahlen der GSI Beschleuniger, durchgeführt wurden. LYCCA erreichte Auflösungsweite von $\frac{\Delta Z}{Z} = 0.6(1)$ (für $Z = 36$) und $\frac{\Delta A}{A} = 1.1(1)$ (für $A = 104$) FWHM bei in-beam Messungen mit relativistischen Ionen.

Es wurde ein relativistisches Coulombanregungs-Experiment mittels eines radioaktiven Ionenstrahls mit Hilfe von LYCCA an der GSI durchgeführt. Das Ziel war die Messung der Reduzierten Übergangsstärken ($B(E2)$ Werte) der ersten angeregten Zustände in ^{33}Ar . Der radioaktive Ionenstrahl wurde durch Fragmentation eines stabilen ^{36}Ar Strahls in einem ^9Be Target produziert. In der zentralen Position des γ -Arrays (bestehend aus 15 hoch-reinen EUROBALL Cluster Germanium Detektoren und acht HECTOR BaF_2 Szintillatoren), traf der sekundäre ^{33}Ar Strahl auf ein ^{197}Au Target mit einer Energie von ca. 145 MeV/u. LYCCA wurde benutzt um die Trajektorie der Ionen zu bestimmen und um alle nuklearen Reaktionskanäle zu unterdrücken.

Für die ersten zwei angeregten Zustände von ^{33}Ar (Anregungsenergien: $(\frac{3}{2})_1^+$: 1359 keV und $(\frac{5}{2})_1^+$: 1798 keV) wurden die reduzierten Übergangsstärken bestimmt:

$$B\left(E2; (\frac{3}{2})_1^+ \rightarrow (\frac{1}{2})_{g.s.}^+\right) = 6.39(1.49) \text{ W.U.}$$

$$B\left(E2; (\frac{5}{2})_1^+ \rightarrow (\frac{1}{2})_{g.s.}^+\right) = 5.80(1.62) \text{ W.U.}$$

Dies sind die ersten bekannten Übergangsstärken für protonenreiche $T_z = -\frac{3}{2}$ Atomkerne der sd -Schale. Diese neuen experimentellen Daten wurden benutzt um effektive Wechselwirkungen für Schalenmodellrechnungen zu testen, die erfolgreich Energiedifferenzen angeregter Zustände in Spiegelkernpaaren beschreiben. Neue Schalenmodellrechnungen, basierend auf einer modifizierten USD Wechselwirkung im vollen sd Valenzraum, ergeben Übergangsstärken von 4.790 W.U. ($(\frac{3}{2})_1^+ \rightarrow (\frac{1}{2})_{g.s.}^+$) und 6.225 W.U. ($(\frac{5}{2})_1^+ \rightarrow (\frac{1}{2})_{g.s.}^+$) für die zwei neu gemessenen Übergänge in ^{33}Ar .

Chapter 1

Introduction

The 'Lund-York-Cologne-Calorimeter' (LYCCA) is a dedicated device for the HiSpec-DeSpec (High resolution in flight Spectroscopy, Decay Spectroscopy) program, which is part of the NUSTAR (Nuclear Structure Astrophysics and Reactions) collaboration within FAIR (Facility for Anti proton and Ion research). LYCCA is a flexible array of 26 detector modules with each module containing a set of cesium iodide (CsI) detectors for the energy measurement of the reaction products, and a double-sided silicon strip detector (DSSD) for energy loss and position information. The measurement of the time-of-flight (ToF) between the target position and LYCCA is performed using large-area ultra-fast plastic scintillators. The main objective of LYCCA is to uniquely characterize exotic nuclei at relativistic energies by their mass, A , and charge, Z . This is needed for identification of secondary reaction products following Coulomb excitation, direct reactions, or fragmentation reactions of relativistic radioactive ion beams. Future beams will be provided by the new Superconducting Fragment Separator (Super-FRS) and will have energies of 100 to 200 MeV/u when hitting the secondary target. LYCCA-0 (a forerunner of the full array comprising 12 to 16 detector modules) was used for the PreSpec physics campaign from 2010 to 2012.

The $1s0d$ shell between ^{16}O and ^{40}Ca is one of the most thoroughly studied region of the Segré chart, both experimentally and theoretically. The proton and neutron drip lines are experimentally accessible, and the proton-rich side is of utmost interest for the astrophysical rp-process path. Therefore, the region is an excellent study ground for drip line effects, isospin symmetry distortion and monopole driven shell evolution. A PreSpec experiment was proposed and performed in order to investigate the large distortions of the isospin symmetry in the sd shell that were recently found in the mirror pair ^{36}Ca - ^{36}S . The exceptionally large mirror energy differences (MED) for 2^+ states have been explained by a reduction of the $N = 14$ shell gap in proton-rich nuclei close to $Z = 20$ and the proton drip line. Shell model calculations that assume a similar reduction for the $Z = 14$ gap (close to $N = 8$) are in full agreement with the observed $T = 2, J = 2^+$ MED. Recent investigations of $T = \frac{3}{2}$ mirror pairs confirmed these shell structure modifications. A Coulomb excitation experiment in ^{33}Ar was performed in order to test the modified, effective interaction and its predictive power. For the first time, transition strengths of an $T_z = -\frac{3}{2}$ isotope have been measured. LYCCA was used to exclude all nuclear reaction channels, which turned out to be of major importance.

Chapter 2

Physics of mirror nuclei

The following chapter provides a brief overview of the isospin formalism and the results of experimental and theoretical isospin symmetry research is given.

2.1 Isospin formalism

Ernest Rutherford's assumption of the existence of neutral particles within a nucleus was verified when James Chadwick discovered the neutron in 1932 [2]. It turned out that this so-called 'neutron' has a mass close to the mass of the proton and that it is affected by the nuclear interaction in a very similar way as the proton. These findings motivated Werner Heisenberg to characterize proton and neutron as two quantum states of the so-called 'nucleon'. A nucleon has an internal degree of freedom; the 'isobaric spin' or 'isospin' $t = \frac{1}{2}$. The projection on a quantization axis z , in the abstract isospin space, is defined as:

$$\begin{aligned} t_z &= +\frac{1}{2} && \text{for the neutron and} \\ t_z &= -\frac{1}{2} && \text{for the proton.} \end{aligned}$$

A nucleus consisting of N neutrons and P protons comprises a total isospin projection:

$$T_z = \sum_{N+P} t_z = \frac{(N-Z)}{2}.$$

The isospin, T , itself is defined by the vector sum of the individual isospins:

$$T = t_1 \oplus t_2 \oplus \dots \oplus t_n.$$

Therefore, the involved nucleons couple to a total isospin, which is limited by N and Z in the following way:

$$\frac{|N-Z|}{2} \leq T \leq \frac{N+Z}{2}.$$

Fig. 2.1 shows the coupling of two nucleons to four possible (T, T_z) -states.

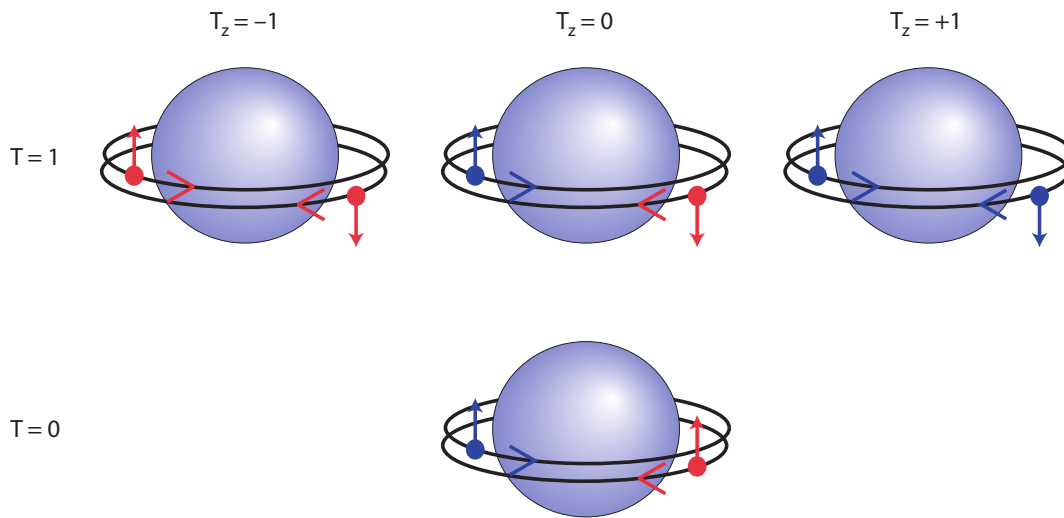


Figure 2.1: Possible couplings of a pair of $l = 0$ nucleons (protons red, neutrons blue). Arrows indicate the spin of the nucleons (picture taken from ref. [1]).

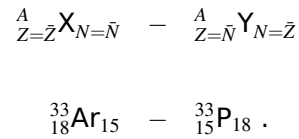
It is obvious, that both $T_z = 0$ states consist of two completely different configurations. The $(T = 0, T_z = 0)$ -state requires parallel spins and due to the Pauli principle, can only be formed by diverse nucleons. The $(T = 1)$ -state comprises an anti-parallel spin configuration and is possible for any combination of nucleons.

This terminology is driven by the assumption that the nuclear interaction is independent (or at least very slightly dependent) on the isospin. In the following, nuclei with the same mass number, A , are denoted as 'isobaric nuclei'.

2.2 Isospin symmetry

Isospin symmetry is related to identical behavior of protons and neutrons in the nuclear field. This implies that the nuclear interaction remains unchanged if the protons and the neutrons are interchanged. Thus, 'isospin symmetry breaking' and 'charge symmetry breaking' can be used synonymously. The nuclear interaction is described in terms of two-body potentials: V_{pp} (proton-proton), V_{nn} (neutron-neutron) and $V_{pn} = V_{np}$ (proton-neutron) [1]. An undisturbed isospin symmetry requires charge symmetry where $V_{pp} = V_{nn}$ and (the even stronger assumption of) charge independence where $V_{pn} = \frac{V_{pp} + V_{nn}}{2}$. Charge symmetry and charge independence of the nuclear interaction are fundamental principles of nuclear physics. The isospin formalism directly couples the constraints of the Pauli principle in the concept of a charge symmetric / independent nuclear interaction and is very helpful in describing the details of the nuclear interaction.

As the fundamental assumption leads to an exchange symmetry between protons and neutrons, two partners with exchanged proton / neutron numbers are called 'mirror nuclei'.



Studying such pairs of mirror nuclei, especially differences between their properties gives direct insight into isospin symmetry breaking effects. The most important charge symmetry breaking effect is caused by the electric charge of the proton and the Coulomb interaction. This well understood interaction causes unexpected effects which are described in the following sections.

2.3 Energy differences in mirror nuclei

2.3.1 Coulomb displacement energies (CDE)

Charge independence requires that an excited state that exists in one nucleus, must also exist in the other members of the isospin multiplet. It has to be mentioned that T is not an observable quantity, but can often be 'assigned' by logical arguments. For the $N \sim Z$ nuclei, the ground state usually has the lowest possible value of T . States that have the same quantum numbers (T , J^π , etc.) that only differ in T_z are called isobaric analog states (IAS). The total energy of these states is affected by the Coulomb field of the protons, and as a result, the energy differs for each nucleus in the isobaric multiplet.

The following figure shows the ground states and the set of IASs that includes the $T_z = \pm \frac{3}{2}$ ground states of a $T = \frac{3}{2}$ quadruplet. The energy difference between isobaric analog states, caused by the different total charges of isobaric nuclei, is called 'Coulomb displacement energy (CDE)'.

The binding energies of the ground states are given by the Weizsäcker mass equation [6]. For isobaric nuclei, A is constant, and therefore the binding energy is a (nearly quadratic) function of Z . The binding energy of isobaric analog states are described by Wigner's 'Isobaric Multiplet Mass Equation (IMME)' (cf. eq. 2.1, [10]). In the derivation of this formula, it was assumed that the charge symmetry breaking force is a two body interaction.

$$BE(A, T, T_z, \chi) = a + b \cdot T_z + c \cdot T_z^2 \quad (2.1)$$

Here, χ denotes all other quantum numbers, that describe the set of IASs (e.g. spin, parity, etc.). The parameters a , b , and c only depend on A , T and χ , but not explicitly on T_z . Thus the three parameters describe:

1. a charge independent 'isoscalar' part,
2. a part that is linear in T_z and is denoted the 'isovector' contribution (caused by $V_{pp} \neq V_{nn}$)
3. a fraction that has quadratic dependence of T_z and is denoted the 'isotensor' part (caused by $V_{pn} \neq \frac{V_{pp} + V_{nn}}{2}$).

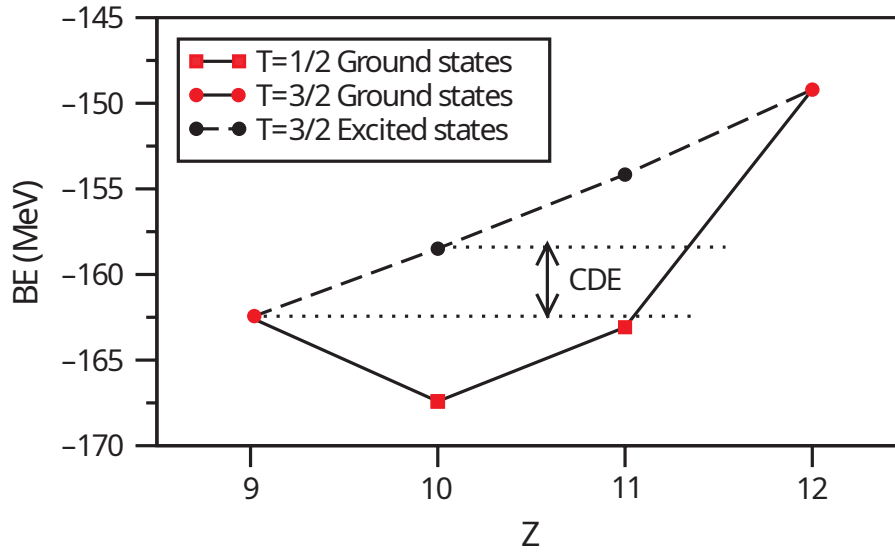


Figure 2.2: Ground states and IASs of the $A = 21$, $T = \frac{3}{2}$ quadruplet ($^{21}\text{Mg,Na,Ne,F}$) showing the binding energy vs. proton number. The circles mark a set of IASs (modified picture from ref. [1]).

The contribution of the isovector to the binding energy is 1% the level of the isoscalar part and the contribution of the isotensor is 2% the level the isoscalar part [11].

The Coulomb displacement energy, for a replacement of n protons by neutrons, is given by the change in mass of a nucleus. This can be expressed as a function of T and T_z :

$$CDE(T, T_z) = M_{T, T_z} - M_{T, (T_z+n)} + n \cdot \Delta_{nH},$$

where M is the mass of the nucleus with given T and T_z . Here, T_z is the isospin projection of the larger Z isobar and Δ_{nH} is the mass difference between a neutron and a hydrogen atom. This can be directly linked to the coefficients of the IMME [7]:

$$CDE(T, T_z) = -p(b + (c - 2T_z + n) - \Delta_{nH}).$$

The CDEs have been calculated for wide ranges of IAS and the understanding of CDEs has been a major topic of nuclear structure theory for a long time. A first explanation was given by Nolen and Schiffer [12]. CDEs are caused entirely by the effects of the Coulomb interaction. For this, they introduced two correction terms: an electro-magnetic spin-orbit term (EMSO) and an exchange term to take into account the Pauli principle. The resulting CDEs were underestimated by the theoretical approach by approximately 7 %, which equates to several hundreds of keV. This is the so called 'Nolen-Schiffer' anomaly [12]. This anomaly is still not completely understood and many interpretations such as neutron skin effects and a charge asymmetric contribution to the nucleon-nucleon interaction were suggested [13, 14]. However, the complete origin of the Coulomb displacement energies still remains still an open question.

2.3.2 Energy differences between excited isobaric analog states

The energy differences of the different excited levels of mirror nuclei are relatively small and are typically of the order of tens of keV. Assuming charge independence of the nuclear interaction, they should be caused entirely by the Coulomb interaction.

The excitation energy of a nucleus is one of the most fundamental observable spectroscopic properties. By measuring the excitation energy, i.e. detection of the de-exciting γ -rays, the energy is always 'normalized' to the binding energy of the ground state. As a result, the main effect of CDE cancels out. The energy difference between excited states is named 'Coulomb energy difference (CED)'. The CED of a J^π -state in a T -multiplet is defined as:

$$CED_{J^\pi, T} = E_{J^\pi, T, T_z}^* - E_{J^\pi, T, (T_z+n)}^*,$$

for replacement of n protons by neutrons [1]. Here, J is the spin and π is the parity of the isobaric analog states. It turns out that the CDE are strongly affected by the spin of the states. The range of the CED is typically 100 keV or less. Within the last two decades, due to the progress in experimental development, it was possible to enlarge the range of investigated CEDs from $T = \frac{1}{2}$ doublets and $T = 1$ triplets up to high angular momenta. Also, the lower energetic excited states of some $T = \frac{3}{2}$ and $T = 2$ multiplets are currently known (e.g. [15, 21, 16]). However, due to limitation only at low angular momenta, the J -dependency cannot be studied in such detail as for the $T = \frac{1}{2}, 1$ multiplets.

As experimental variables, the so called 'mirror energy differences (MED)' (for a $T = \frac{1}{2}$ doublet) and 'triplet energy differences (TED)' (for a $T = 1$ triplet) are defined (according to [7] and references therein) as follows:

$$\begin{aligned} MED_J &= E_{J^\pi, (T_z=-\frac{1}{2})}^* - E_{J^\pi, (T_z=+\frac{1}{2})}^* = -\Delta b_J \\ TED_J &= E_{J^\pi, (T_z=-1)}^* + E_{J^\pi, (T_z=+1)}^* - 2E_{J^\pi, (T_z=0)}^* = 2 \cdot \Delta c_J. \end{aligned}$$

Here, Δb_J and Δc_J are the change of the IMME coefficients which is dependent on the spin J relative to the ground state. The MEDs are sensitive to the isovector component (cf. sub sec. 2.3.1), whereas the TEDs are sensitive to the isotensor component. Hence, MEDs describe the deviation of the nuclear interaction from a charge symmetry interaction and the TEDs from a charge independent one.

If the assumption of a charge symmetric and independent nuclear interaction is fully valid, all differences between excited states in isobaric nuclei would be of electro-magnetic origin and could be described as effects of the Coulomb interaction.

Multipole Coulomb contribution

The nucleon alignment is explained in the following subsection as an example of a second order effect that acts on the level energy differences in isobaric nuclei.

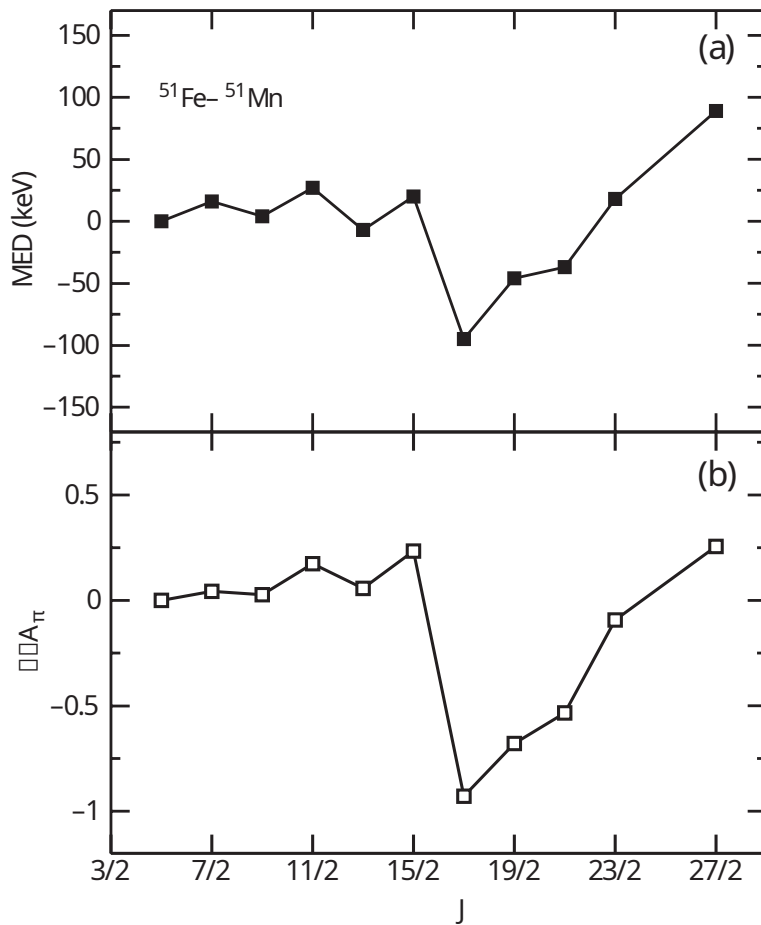
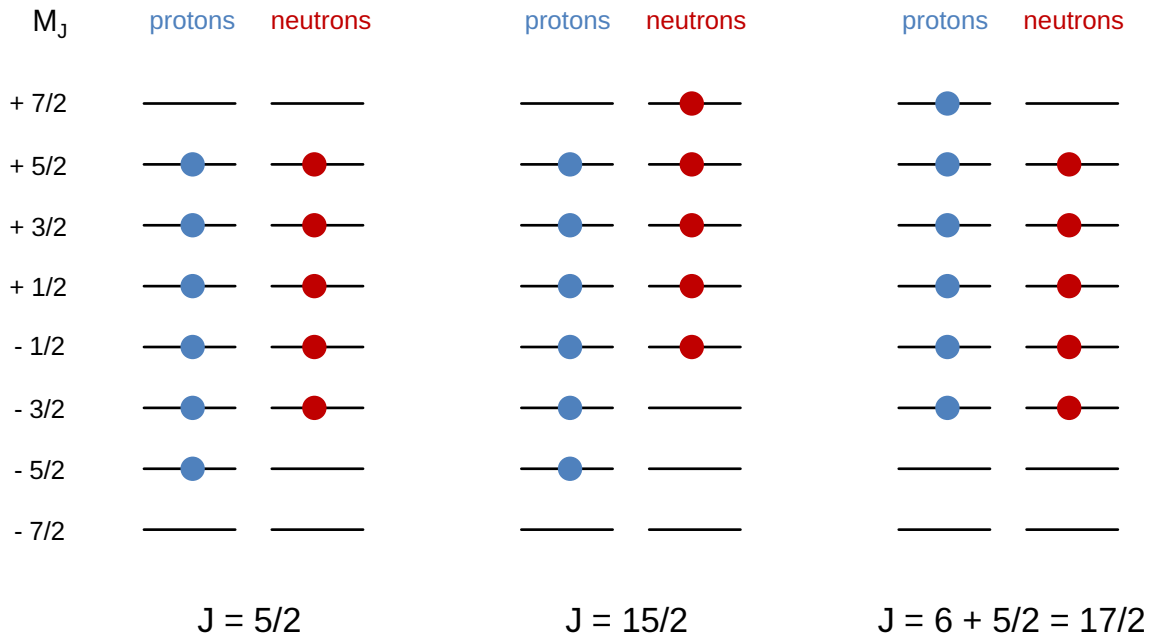


Figure 2.3: (a) MEDs of the $A = 51, T_z = \pm \frac{1}{2}$ doublet as function of the angular momentum J , (b) Calculated 'nucleon alignment' in the shell model (modified picture from ref. [7]).

Fig. 2.3a shows the the mirror energy differences of the $A = 51$ doublet ${}^{51}_{26}\text{Fe}_{25} - {}^{51}_{25}\text{Mn}_{26}$. The configuration can be described as a doubly-magic ${}^{40}_{20}\text{Ca}_{20}$ - core with 11 valence nucleons (6 protons and 5 neutrons (${}^{51}\text{Fe}$) and vice versa in the case of ${}^{51}\text{Mn}$). All these valence nucleons are located in the $1f_{7/2}$ shell that can house 8 nucleons of each type. The shell is clearly separated from the neighbouring $1d_{3/2}$ - and $2p_{3/2}$ - shells (cf. fig. A.1). Thus, it can be assumed, that the configurations of the excited states do not include shells other than the $1f_{7/2}$ shell.

The clear drop in the MED at $J = \frac{17}{2}$ can be explained by nucleon alignment. Fig. 2.4 shows the configuration of the $J = \frac{5}{2}, \frac{15}{2}, \frac{17}{2}$ states.

Figure 2.4: Illustration of level configurations for ^{51}Fe .

The spin increases with higher excitation up to $J = \frac{15}{2}$ and can be reached with pure neutron excitation in the case of ^{51}Fe (pure proton excitation for ^{51}Mn). To generate even higher spins, e.g. for the $J = \frac{17}{2}$ configuration, a pair of protons has to be broken. This excitation of the proton to the $+\frac{7}{2}$ level leads to a larger spatial separation and thus to a reduction of the repulsive Coulomb interaction. This so called alignment effect reduces the energy of the $J = \frac{17}{2}$ level of ^{51}Fe , while it does not affect the analog state in ^{51}Mn (a pair of neutrons is broken, so there is no energy gain from reduced Coulomb interaction). Hence, the MED drops dramatically.

This alignment effect is described by the so called Coulomb Multipole potential (V_{CM}) and can be reproduced in shell-model calculations very precisely (cf. fig. 2.3).

Monopole Coulomb effects

Monopole Coulomb effects, as Lenzi et. al. point out in ref. [9], state that the monopole part of the Coulomb field (V_{Cm}) has a crucial impact on the MED. The monopole part can be separated into three parts:

$$V_{Cm} = V_{Cr} + V_{CII} + V_{CIs}. \quad (2.2)$$

V_{Cr} is the radial effect of the potential. In addition to the Coulomb multipole interaction between the valence protons, there is an effect that is caused by a change in the nuclear radii. If a nucleus becomes excited, valence particles can populate other orbits and this changes the radius of the nucleus. In the case the radius decreases, the valence protons are closer to the bulk of protons and thus have more Coulomb energy. This effect is the main contribution to the CDE, however it has a small effect onto the MED [14].

V_{CII} and V_{CIs} are single particle corrections that take care of shell effects. The first one is caused by a shift of orbits, with respect to their main quantum number and the angular momentum [7]. Another correction is the electromagnetic spin-orbit effect (EMSO), as investigated by Nolen and Schiffer [12]. This contribution can be understood as a Lamor precession of the nucleons in the electric field of the nucleus. This effect is discussed in detail by Ekman et al. in [38].

Summing up all the described Coulomb effects (V_{CM} , V_{Cr} , V_{CII} and V_{CIs}) highlights that another contribution of the same order of magnitude is still missing. This is called the 'Isospin Symmetry Breaking (ISB)' term (V_B). The different impact of these effects becomes visible in shell model calculations, as shown in the next subsection. Typically, the parameters for the calculation of V_B are deduced from isobaric triplets, e.g. $A = 42$, $T_z = -1, 0, 1$ [22].

2.3.3 Application on $f_{7/2}$ - shell nuclei

For nuclei in the $f_{7/2}$ - shell, three effects dominate the MEDs:

- Nucleon alignment (coupling of angular momenta) as described in subsection 2.3.2 and illustrated by fig. 2.3 and 2.4
- Change of the nuclear radius
- 'Isospin symmetry breaking' effects (ISB).

It turns out that the unexpected ISB effects have the same order of magnitude as the Coulomb effects (cf. fig. 2.5 and 2.6, [22]). The single particle effects V_{II} and V_{Is} are of less importance, but will have a large influence on the MEDs of sd - shell nuclei (cf. sub sec. 2.3.4). For the shell model calculations that are presented in the following paragraphs, the KB3G interaction [41] was used.

The radial contribution

To have a closer view on the radial contribution, the MEDs of the $A = 48$, $T_z = \pm 1$ pair are shown in fig. 2.5. In this specific case the usually dominant Coulomb multipole contribution is reduced significantly. Assuming a pure $f_{7/2}$ - configuration, ^{48}Mn has 3 valence proton holes and 3 valence neutrons, whereas ^{48}V has 3 valence protons and 3 valence neutron holes. In both nuclei the re-coupling effect has to be the same. Even though this pure configuration is not realistic, fig. 2.5 shows that Coulomb multipole effects are not dominant anymore, however, the radial effect, C_r , is (caused by the Coulomb radial potential V_{Cr} , cf. eq. 2.2).

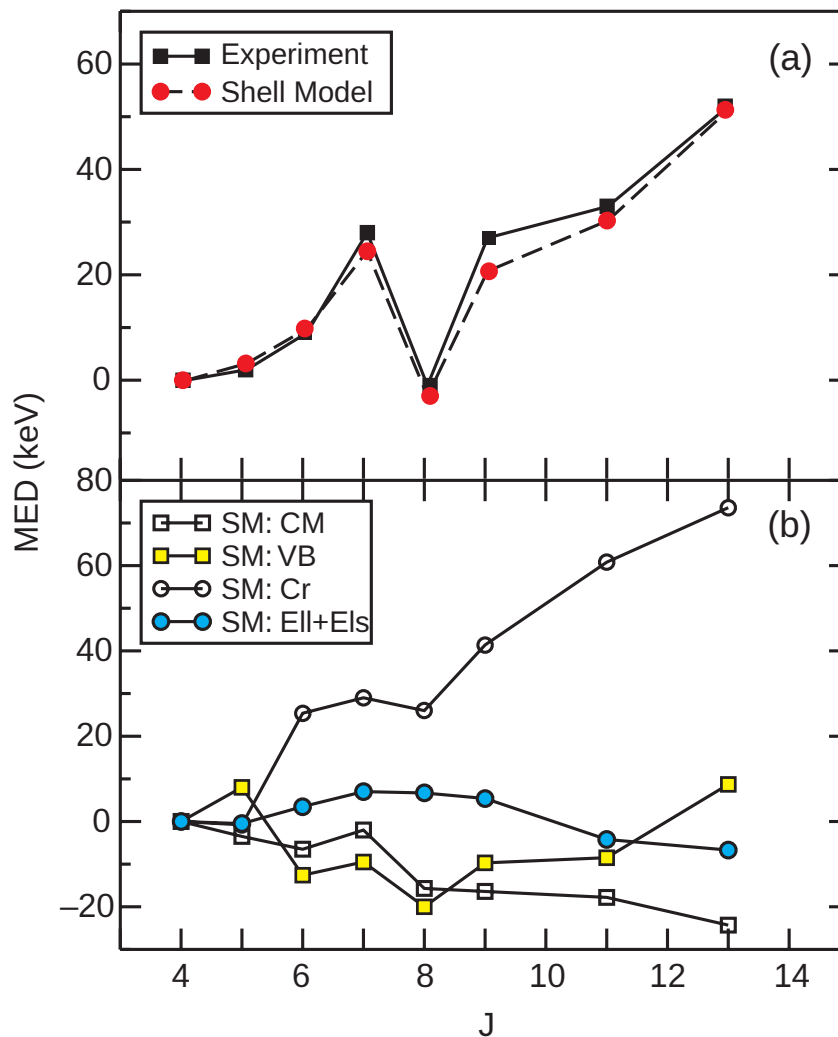


Figure 2.5: (a) MEDs of the $T_z = \pm 1$ pair $^{48}\text{Mn} - ^{48}\text{V}$ from experiment and theory vs. the angular momentum of the state [8]. (b) The four contributions to the MEDs plotted in (a). CM is the Coulomb multipole, VB the isospin symmetry breaking, Cr the radial effect and EII and EIs the single particle contributions. See sub sec. 2.3.2 for details (Fig. modified from ref. [7]).

The Cr part increases steadily with spin and depends on changes of the occupancy of the $p_{3/2}$ orbit. Near the ground state, significant admixtures from the $p_{3/2}$ are expected. For higher spins these admixtures decrease due to alignments. Thus, the effective nuclear radius decreases for higher spins. The reduction of the radius increases the Coulomb energy for both mirror nuclei, but more for the $T_z = +1$ (proton rich) nucleus.

Isospin symmetry breaking (nuclear) effects ('ISB')

In the previous examples, the mirror energy differences of isobaric analog states can all be explained as effects of the Coulomb interaction. This description leads to a good reproduction of the experimental data by the shell model calculations. A last effect that is discussed with data from $f_{7/2}$ nuclei is the so-called 'isospin symmetry breaking' contribution. Fig. 2.6 shows experimental data and calculations for the mirror pair $^{54}\text{Ni} - ^{54}\text{Fe}$. This pair can be interpreted as a doubly-magic ^{56}Ni core with two proton (neutron) holes.

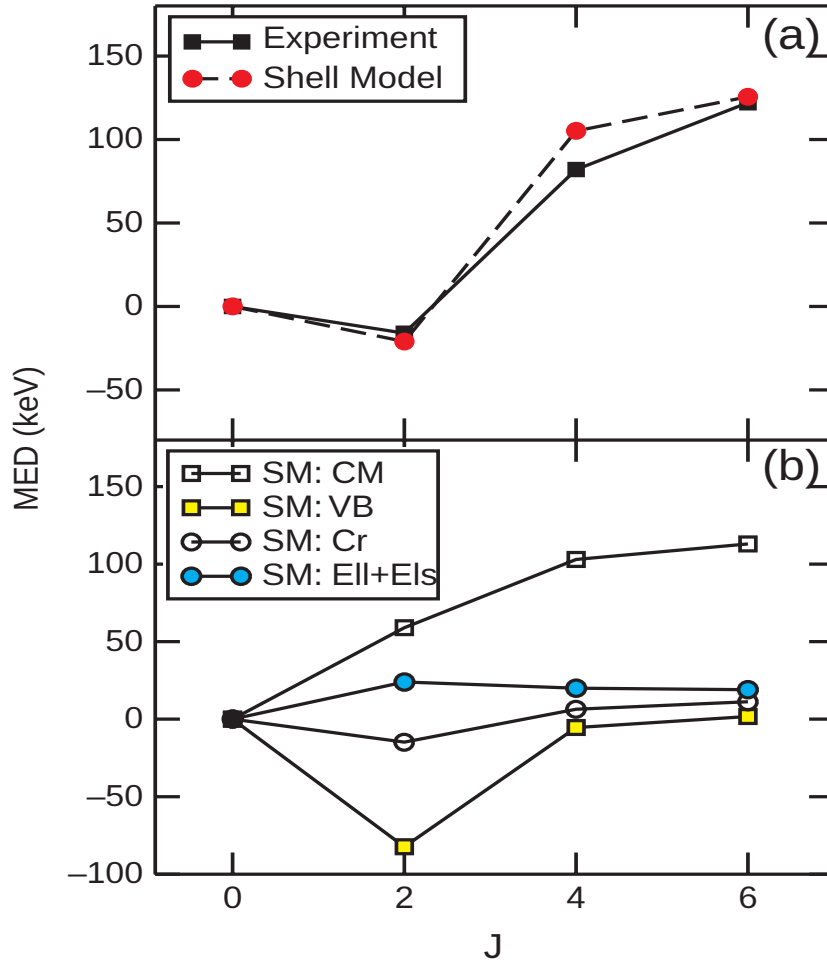


Figure 2.6: (a) MEDs of the $T_z = \pm 1$ pair $^{54}\text{Ni} - ^{54}\text{Fe}$ from experiment and theory vs. the angular momentum of the state. (b) The four contributions to the MEDs plotted in (a). Labelling as in fig. 2.5. See sub sec. 2.3.2 for details (Fig. modified from ref. [7]).

In both nuclei the holes can couple to $J = 0, 2, 4, 6$. Assuming this structure, a smooth rise in MEDs up to $J = 6$ is expected. Surprisingly, fig. 2.6 shows a dip for $J = 2$. This is called ' $J = 2$ - anomaly', which also exists in the cross-conjugate $^{42}\text{Ca} - ^{42}\text{Ti}$ pair. However, the ISB effects are present in the whole shell and a complete description has so far not been determined. Technically, this effect is treated as a positive $J = 2$ component of isovectorial type.

In summary, it can be stated that the understanding of non-Coulomb isospin breaking effects in mirror nuclei is still a fundamental open question in nuclear structure physics.

2.3.4 Application on sd - shell nuclei

The knowledge from studies in the $f_{7/2}$ - shell can be expanded to the neighbouring mass regions, e.g. the sd - shell. In this region, the limit of validity of isospin symmetry can be investigated and new Coulomb effects or other isospin symmetry breaking effects can be studied. Shell model calculations that are shown in the following section were created by usage of the sd pf-interaction [42], unless otherwise stated.

While the $f_{7/2}$ - shell from ^{40}Ca to ^{56}Ni has been intensely studied and a lot of data is available, the information for the sd - shell (^{16}O to ^{40}Ca) is limited. The $f_{7/2}$ - shell is described by shell model calculations with good precision, even when the model space (valence space) is limited to the $f_{7/2}$ - shell itself. This is due to its large energetic separation to the lower $1d_{3/2}$ - shell and the higher $2p_{3/2}$ - shell. In the case of sd - shell nuclei, several orbits can be involved and therefore truncations in the valence space (excitement between orbits) have to be considered.

Within the last few years, the energies of highly excited states for several $T_z = \pm \frac{1}{2}$ pairs have been published ($A = 31$: [39], $A = 35$: [38], $A = 39$: [23]). For larger proton excess and higher isospin values the data is limited to low-spin states (e.g. ^{36}Ca [16]). To describe these nuclei, the two main shells (sd and pf) become relevant. For excitations from one shell to another, the electromagnetic spin-orbit coupling (EMSO), which is caused by Lamor precession of the nucleons in the nuclear electric field, has to be taken into account. This is described by the V_{Cl_s} term of the Coulomb Monopole part (cf. par. 2.3.2).

The V_{Cl_s} term has a large influence on mirror pairs where a pure single particle excitation from $j = l - s$ to $j = l + s$ takes place. The energy gap between a state with anti-parallel $l - s$ alignment and a neighbouring one with parallel alignment is reduced for protons and increased for neutrons (cf. fig. 2.7). This changes the single-particle-energies dramatically (in the order of hundreds of keV). The exact changes of level energies have been calculated by F. D. Vedova [40]. For example, if a $d_{3/2}$ proton is excited to the $f_{7/2}$ orbit, the energy gain with respect to a neutron amounts to approximately 230 keV (cf. fig. 2.7).

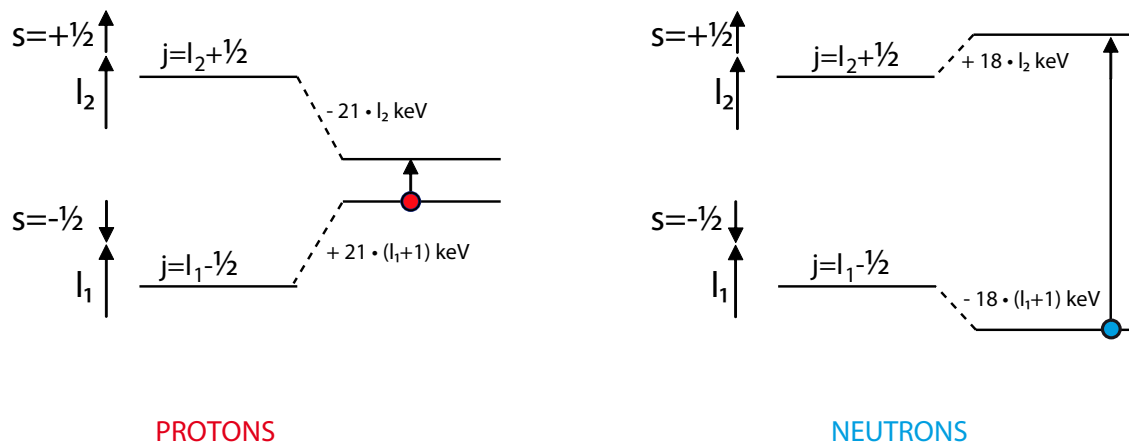


Figure 2.7: Increase and decrease of neighbouring orbits, caused by different $l - s$ alignment due to V_{Cl_s} (Fig. modified from ref. [40])

A very prominent result was achieved by Ekman et al., where large MEDs were reported for the $\frac{13}{2}^{(-)}$ state of the $^{35}\text{Ar} - ^{35}\text{Cl}$ pair (cf. fig. 2.9, [38]). This is explained as an excitation from the $d_{3/2}$ to the $f_{7/2}$ orbit. Furthermore, completely different decay patterns occur for the $\frac{7}{2}^{(-)}$ state (cf. fig. 2.8), which is discussed in sec. 7.3.

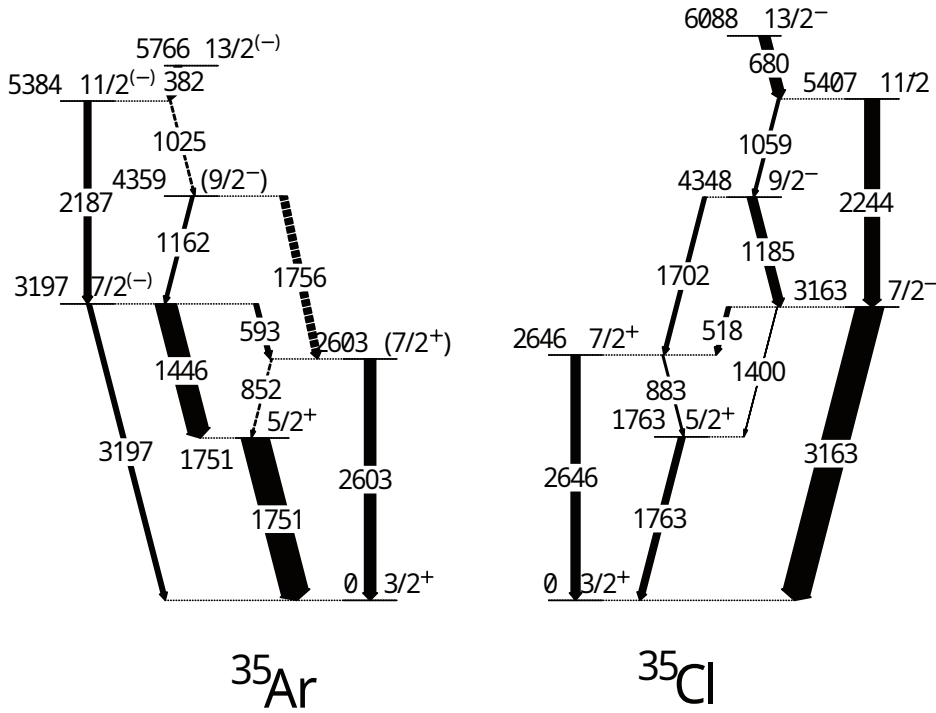


Figure 2.8: Level schemes of the $A = 35$, $T = \pm \frac{1}{2}$ mirror pair, energies given in keV and the widths of the arrows correspond to the relative γ -ray intensity (Fig. modified from ref. [38]).

Fig. 2.9 illustrates the importance of the electro-magnetic spin-orbit coupling, E_{ls} , where its strength is comparable to the Coulomb multipole effect. The MEDs of the $A = 35$ pair are reproduced by the multipole Coulomb term with good agreement, although the single particle contributions overestimate the MEDs. In the case of the $A = 39$ pair, the E_{ls} term is crucial for the reproduction of the experimental MEDs by the shell model calculations.

2.3.4.1 Application for even-mass sd - shell mirror pairs

Over the last years the energies of the first excited states (2_1^+) of even-mass, proton-rich, sd shell nuclei have become available (^{20}Mg [18], ^{24}Si [20], ^{28}S , ^{32}Ar [97], ^{36}Ca [16]). The MED of the 2_1^+ states of the $A = 36$ pair turned out to be significantly larger (-276(16) keV) than the MEDs of the lower-mass mirror pairs. Fig. 2.10 shows shell model calculations with four different interactions. A starting point for these interactions is the USD interaction [87, 86]. This interaction was created without any experimental data and contains full isospin symmetry.

An interaction for the sd -model-space is described by the following parameters:

- Single-particle energies (SPE): $0d_{\frac{5}{2}}, 1s_{\frac{1}{2}}, 0d_{\frac{3}{2}}$
- Two-body matrix elements (TBME): $\langle j_1, j_2 | V | j_3, j_4 \rangle^{J,T}$, where j_i can be any sd -orbit and J, T any available value of spin / isospin.

This set of parameters forms a Hamiltonian H_{SM} . The energy eigenvalues $E_{J_1^{\pi}}$ depend on the parameters:

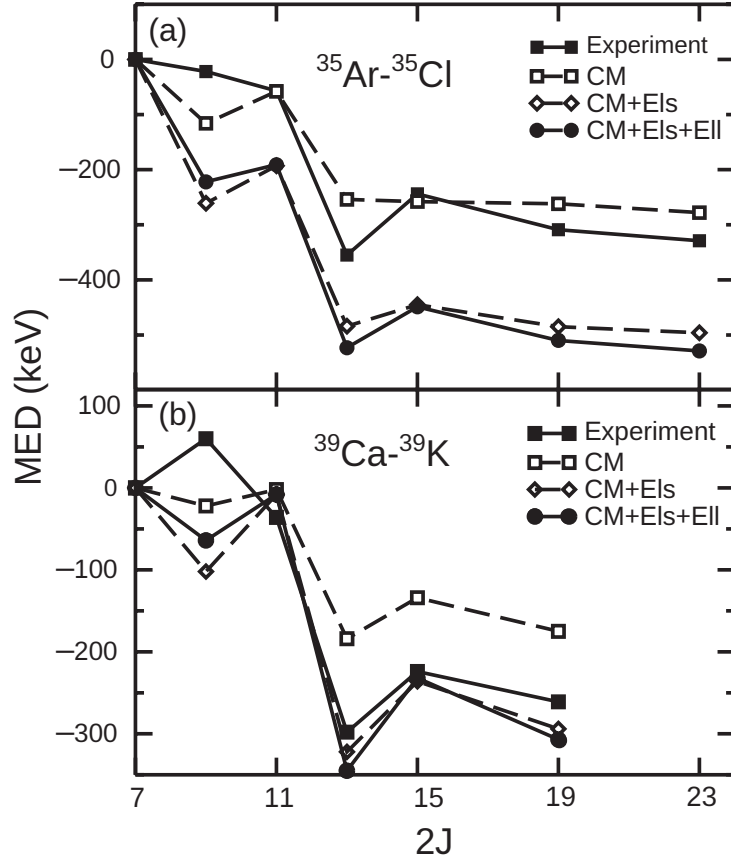


Figure 2.9: Experimental MEDs for the negative-parity yrast states of the $A = 35, 39$, $T = \pm\frac{1}{2}$ mirror pairs, relative to the $J^\pi = \frac{7}{2}^-$ MED. Shell model calculation contributions labeled according to fig. 2.6 (Fig. modified from ref. [38]) .

$$H_{SM}(SPE, TBME)\Psi_{J_i^\pi}(n) = E_{J_i^\pi}\Psi_{J_i^\pi}(n),$$

where n is the number of valence nucleons or holes (the deviation from the magic numbers 8 and 20).

The interactions, that are used in fig. 2.10 are based on the USD [86] interaction. Here, the isospin symmetric SPEs are replaced by experimental values of the $A = 17$, $T_z = \frac{1}{2}$ pair $^{17}\text{O} - ^{17}\text{F}$.

The USD_1^m provides modified monopole parts of the TBME. According to ref. [88, 17], the relative modifications with respect to the USD interaction are:

$$\begin{aligned}\delta V_{d_{\frac{5}{2}}, d_{\frac{3}{2}}}^{T=1,0} &= +0.2, -0.6 \text{ MeV} \\ \delta V_{d_{\frac{5}{2}}, s_{\frac{1}{2}}}^{T=1,0} &= -0.1, +0.1 \text{ MeV}.\end{aligned}$$

For an additional improvement of the description of the data, two other interactions are used one for lower and one for the higher mass triangle in the sd shell:

- USD_2^m for $A \leq 28$: $\pi 0d_{5/2}$ SPE is increased by 200 keV and $\pi(0d_{5/2}, 0d_{5/2})$ TBME is quenched by 5%.
- USD_3^m for $A > 28$: $\pi 0d_{5/2}$ SPE is reduced by 300 keV and $\nu 0d_{5/2}$ SPE is increased by 900 keV.

The final values of the different SPEs of the three interactions are summarized in tab. 2.1.

	Orbit	USD_1^m	USD_2^m	USD_3^m
protons	$\pi 0d_{5/2}$	- 600	- 400	- 900
	$\pi 0s_{1/2}$	- 105	- 105	- 105
	$\pi 0d_{3/2}$	+ 4400	+ 4400	+ 4400
neutrons	$\nu 0d_{5/2}$	- 4143	- 4143	- 3243
	$\nu 0s_{1/2}$	- 3272	- 3272	- 3272
	$\nu 0d_{3/2}$	+ 942	+ 942	+ 942

Table 2.1: Single particle energies used in the $USD_{1,2,3}^m$ interactions, given in keV. See text for details. (Values taken from [17]).

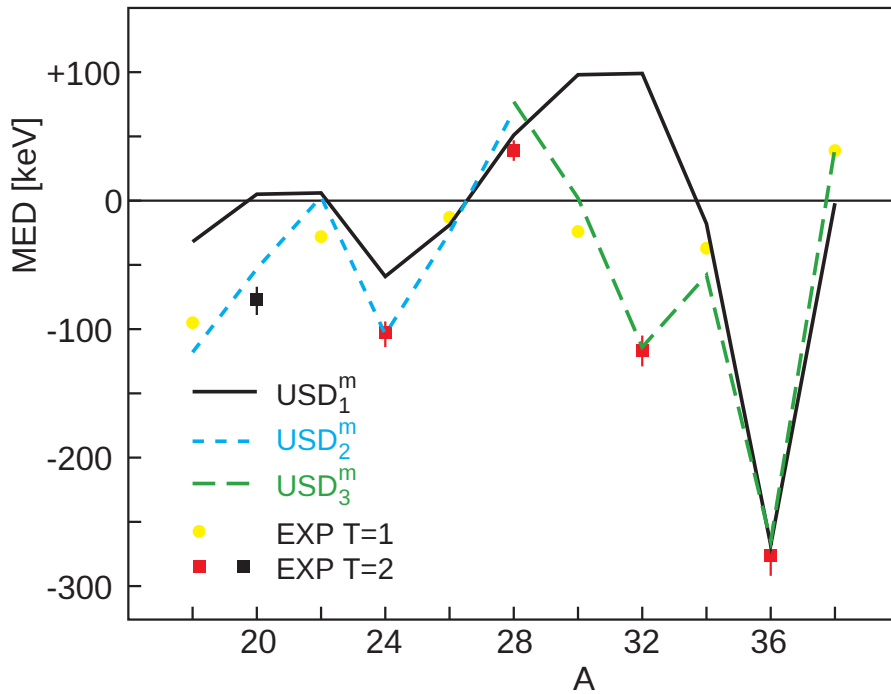


Figure 2.10: Experimental MEDs of the 2_1^+ states of the $T = 1, 2$ sd shell mirror pairs and shell model calculations of different interactions. For details see text. (Fig. modified from ref. [17]). Data marked with red squares have been taken from refs. [20], [97], [16]. The black square indicates a data point that was measured after the publication of these interactions, published by A. Gade et al. [18].

Fig. 2.10 shows, that the modified interactions $USD_{2,3}^m$ are in excellent agreement with the available data. This proves that the MEDs are sensitive to the unknown $P = 14$ proton gap Δ_p in ^{22}Si and the $N = 14$ neutron gap Δ_n in ^{34}Ca . Thus, the mirror energy difference is a probe for shell structure in these experimentally (so far) inaccessible regions. The strong reduction of the neutron gap in ^{34}Ca is confirmed by the evidence in ^{32}Ar of a reduced neutron $0d_{5/2}$ occupation seen in recent experiment [19]. An explanation for the reduction could be that the approach of the drip line leads to gradual coupling to the continuum. So, the assumption of a constant modification of the SPE in both mass regions of the sd shell is a crude approach. The quenching of the $\pi 0d_{5/2}, 0d_{5/2}$ TBME interaction in the lower sd shell, can be taken as first evidence for the reduced overlap of the involved protons, caused by coupling to the continuum. The following subsection shows the application of these interactions onto the $T = \frac{1}{2}, \frac{3}{2}$ sd shell mirror pairs.

2.3.4.2 Application for odd-mass sd - shell mirror pairs

Fig. 2.12 shows experimental MEDs of the first excited states of $T = \frac{3}{2}$ mirror pairs. The data points are well reproduced by the $USD_{2,3}^m$ interactions. When Reynolds et al. published the excitation energies of ^{25}Si and ^{29}S [15] (after the the publication of these interactions), measured by a one-neutron knockout experiment, they found out that the production cross section that populate excited states was significantly lower than expected with respect to the production cross section of the ground states. That was explained by the understanding of the knock-out reaction as coupling a $0d_{5/2}$ neutron hole to the parent nuclei (^{30}S and ^{26}Si). This mechanism has no high yield to populate strongly collective states. Thus, it was assumed that the first two excited states in both nuclei are rotational excitations of the ground states. From shell model calculations, strong $E2$ transitions are expected (9 – 15 W.U. in ^{25}Si and 6 – 16 W.U. in ^{29}S).

The expectation of strong collective behavior of proton-rich sd shell nuclei can be tested by measuring reduced transition strengths as done in this experiment. Furthermore, the aim of the newly proposed experiment was to demonstrate that the shown effective shell model interactions can predict the excitation energies and the transition strengths simultaneously. Predictions for $B(E2)$ values based on these interactions are shown in chap. 7.

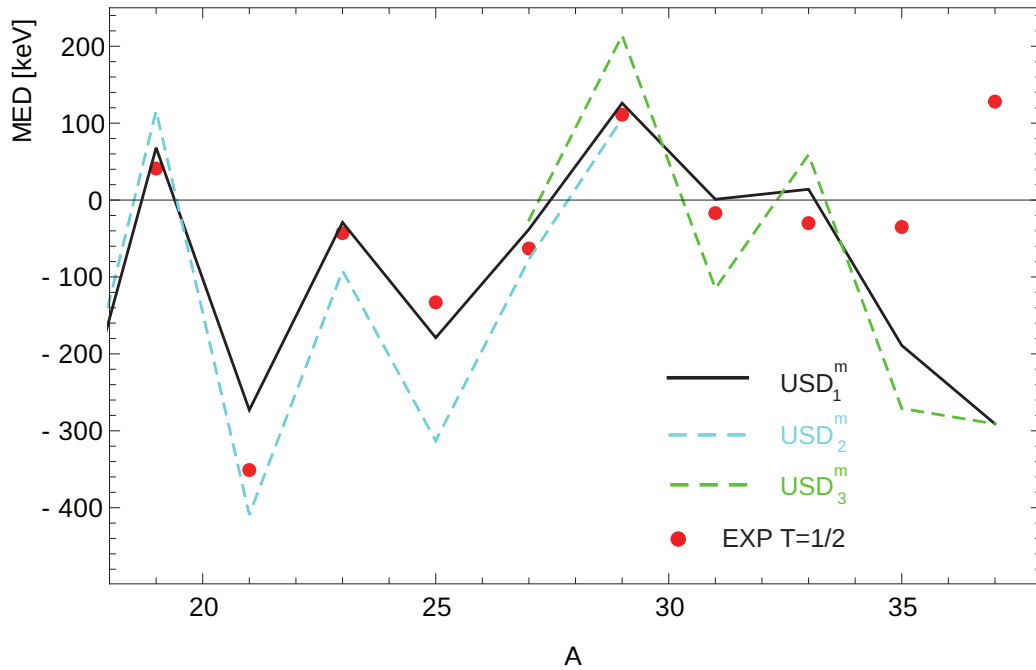


Figure 2.11: Experimental MEDs of the first excited states of the $T = \frac{1}{2}$ sd shell mirror pairs and shell model calculations with the same interactions as shown in fig. 2.10. Shell model calculations from [52] and the experimental data taken from [57].

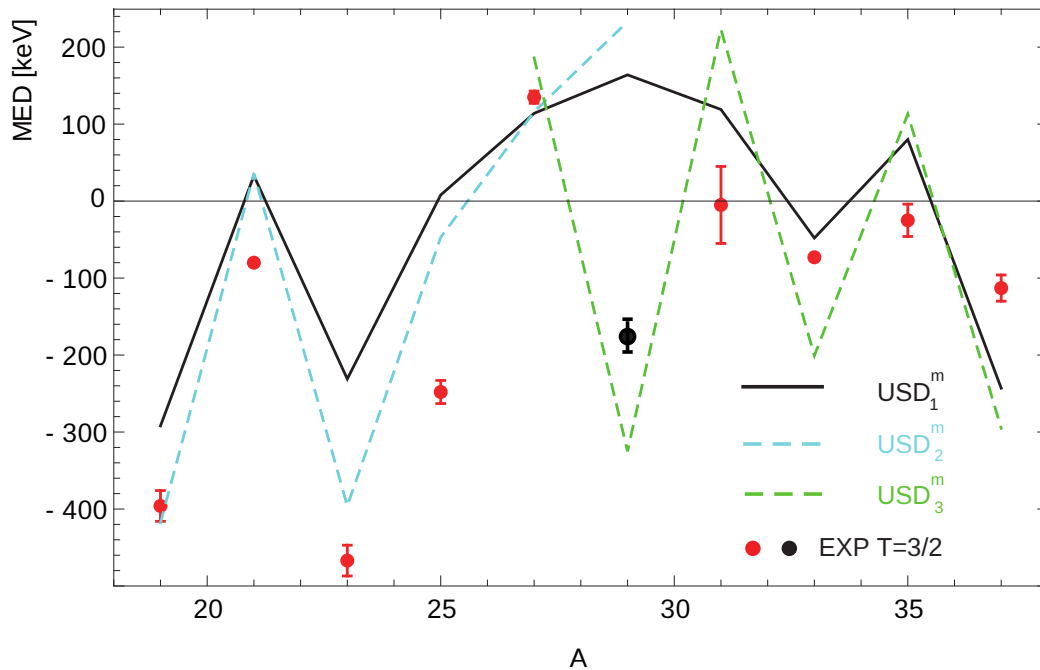


Figure 2.12: Experimental MEDs of the first excited states of the $T = \frac{3}{2}$ sd shell mirror pairs and shell model calculations with same interactions as shown in fig. 2.10. The black circle indicates a data point that was measured after the publication of these interactions, published by R. R. Reynolds [15]. Shell model calculations from [52] and the other experimental data taken from [57].

2.4 The mirror pair ^{33}Ar - ^{33}P

The close to stable ^{33}P (β -decaying to ^{33}S , $T_{1/2} = 25.4(1)\text{d}$) has been studied intensively [24, 25, 26, 27, 28, 29, 30, 31, 32, 33, 34] and a good knowledge of the level energies (up to 10 MeV excitation energy) and the spins and lifetimes has been achieved. The lifetimes of the first two excited states (0.43(7) ps and 0.77(11) ps) are known with a precision of $\frac{\Delta\tau}{\tau} \approx 14 - 16\%$ [83, 84].

For the proton-rich ^{33}Ar , experimental data is very limited. Only two publications [35, 36] report on excited states, whereas no lifetimes / transition strengths are known.

Fig. 7.3 shows the complete known ^{33}Ar level scheme and a fraction of the ^{33}P level scheme.

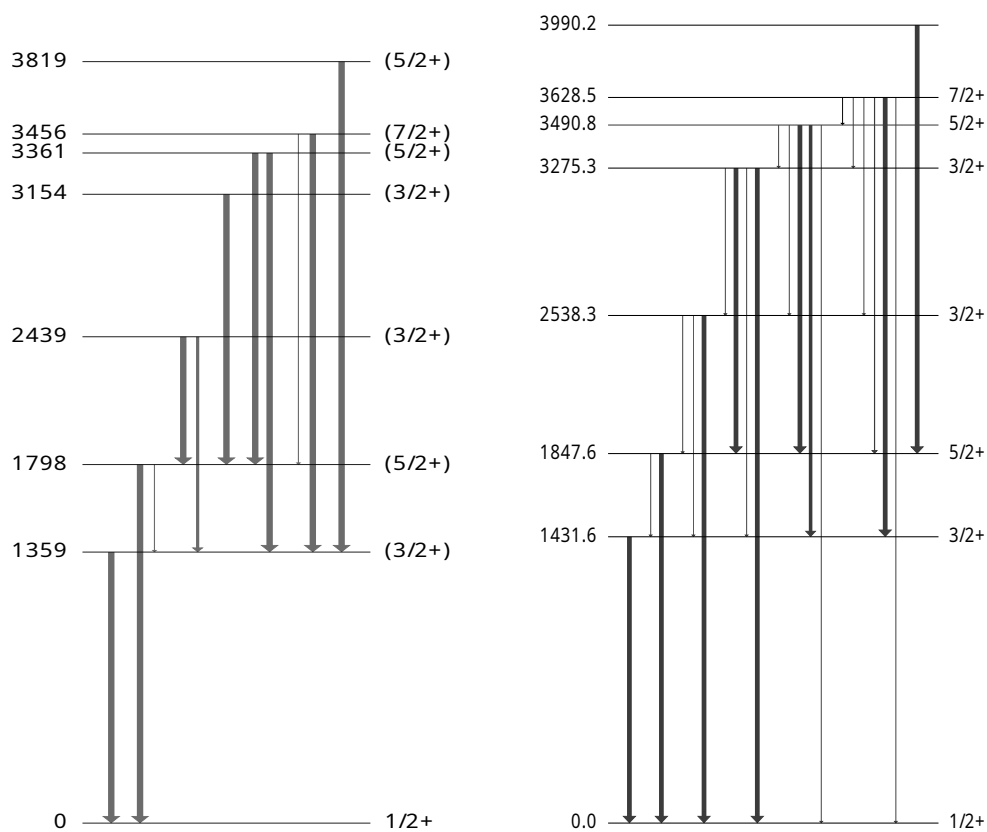


Figure 2.13: Level schemes of ^{33}Ar (full) and ^{33}P (fraction), data taken from [57].

Chapter 3

The PreSpec campaign

PreSpec is a γ -spectroscopy campaign at the GSI facility [76] and is the successor of the RISING fast beam campaign [78, 72] with an upgraded setup. Over the forthcoming years, this setup will be augmented and ultimately form the HiSpec/DeSpec setup [73]. PreSpec is a campaign of the NUSTAR collaboration [74] within the FAIR project [75].

Two intentions are pursued by the PreSpec campaign. Firstly, the state of the art γ -spectrometer together with the experimental setup at the FRS (described below), in combination with the GSI accelerator facility, will be employed for nuclear structure physics investigations. The experimental results of the present experiment clearly follow this intention. The second goal will be to test and commission new detectors and equipment for the future HiSpec/DeSpec experiments under realistic conditions. LYCCA will be a crucial part of the HiSpec setup and was launched into operation during the PreSpec campaign. The design, the prototype and the commissioning of the LYCCA detector is described in chap. 4. LYCCA-0 is the precursor to the full detector array.

3.1 PreSpec experiments

In September / October 2010, the PreSpec setup started operation and was used for a first physics campaign of three experiments in October / November 2010 and May 2011. In the following subsections, a short overview of the experiments is given. The second PreSpec physics campaign will start in October 2012 with the 'Advanced γ -ray tracking array'.

3.1.1 Commissioning

The commissioning experiments of LYCCA-0 and the PreSpec setup took place in September and October 2010. Stable heavy ion beams of ^{64}Ni and ^{86}Kr were used to test the operativeness of the setup and especially the cooperation of the individual LYCCA detectors. Results of these commissioning experiments are shown in subsection. 4.3.3.

3.1.2 Coulomb excitation of ^{88}Kr

The first PreSpec experiment was the relativistic Coulomb excitation of ^{88}Kr . The main goal was to study the strength and effects of the proton-neutron interaction, which are manifested in particular in the existence and the properties of the so-called 'mixed symmetry' (MS) states [91]. The $N = 52$ isotones close to the $Z = 38, 40$ sub shell closures correspond to sufficiently small valence spaces for a practical description in terms of the nuclear shell model. This fact offers the unique possibility to compare the interacting boson model (IBM-2) calculations with shell-model calculations and to achieve a microscopic understanding of the building blocks of nuclear collectivity. Moreover, the evolution of MS states in $N = 52$ isotones can be tracked over different proton shells. This allows the investigation of the variation of the proton-neutron interaction as a function of the nuclear valence space. The ^{88}Kr isotopes were produced by fission of a ^{238}U primary beam at 650 MeV/u on a 0.66 g/cm^2 ^9Be target.

This summary is modified from K. Moschner et al. [90].

3.1.3 Coulomb excitation of ^{104}Sn

The Sn isotopes represent the longest chain of semi-magic nuclei in nature which makes them attractive for systematic investigations. How the shell structure evolves as a function of the number of protons and neutrons can be related to collective as well as single-particle effects. Unique correlation effects may be manifested at a self-conjugate shell-closure as the same spin-orbit partners for neutrons and protons reside just above and below the shell gap. A sensitive probe for correlations of this kind is to measure transition probabilities for certain selected states. With this approach the results of large-scale shell-model calculations based on microscopically derived interactions can be tested through direct comparison with experiment. The study of simple nuclear systems, with only a few nucleons outside a closed core, can thus provide insight into the underlying nucleon-nucleon interaction as applied to finite nuclei.

The focus of the current experiment is to measure the reduced transition probability for the first 2^+ state in ^{104}Sn , but several other isotopes of interest will additionally be produced. These include, for example, ^{100}Cd . Coulomb excitation of such a fragment beam at GSI is currently the most competitive technique available for studying the lightest isotopes in the Sn chain. A primary beam of ^{124}Xe , impinging on a ^9Be target of thickness 4 g/cm^2 was used to create the isotopes of interest.

This summary is modified from J. Cederkall et al. [92].

3.1.4 Coulomb excitation of ^{33}Ar : Transition strengths of mirror nuclei

Very neutron deficient *sd* shell nuclei may exhibit large distortions of the isospin symmetry. Differences in transition matrix elements between mirror nuclei provide access to changing collective behaviour which is expected according to recent theoretical calculations. The matrix elements between the ground state and low lying excited states of the $T = -\frac{3}{2}$ isotope ^{33}Ar are subject of the relativistic Coulomb excitation experiment. The ^{33}Ar isotopes were produced by fragmentation of a ^{36}Ar primary beam at 450 MeV/u on a 4 g/cm^2 ^9Be target.

This summary was published by the author et al. in ref. [89]. Further information about this experiment, which is a major part of this work, can be found in chapters 2 and 5.

3.2 Production of radioactive ion beams

The favoured techniques to produce radioactive ion beams (RIB) are 'isotope separation on-line' (ISOL, [80]) and fragmentation / fission. The GSI research center is specialized in the fragmentation / fission technique. A stable heavy ion beam is shot onto a production target where a nuclear reaction produces the nuclei of interest. The produced radioactive ions are selected by a magnetic separator ('fragment separator', FRS). Furthermore, the FRS is able to identify and track the produced ions.

This chapter gives an overview of the physics of projectile fragmentation and the use of fragmentation beams at the GSI research center. Heavy ion fragmentation reactions start at projectile energies of 20 MeV/u. At a lower energy regime Coulomb excitation, transfer reactions and fusion-evaporation reactions dominate. A fragmentation reaction consists of two major steps called abrasion and ablation [61, 62].

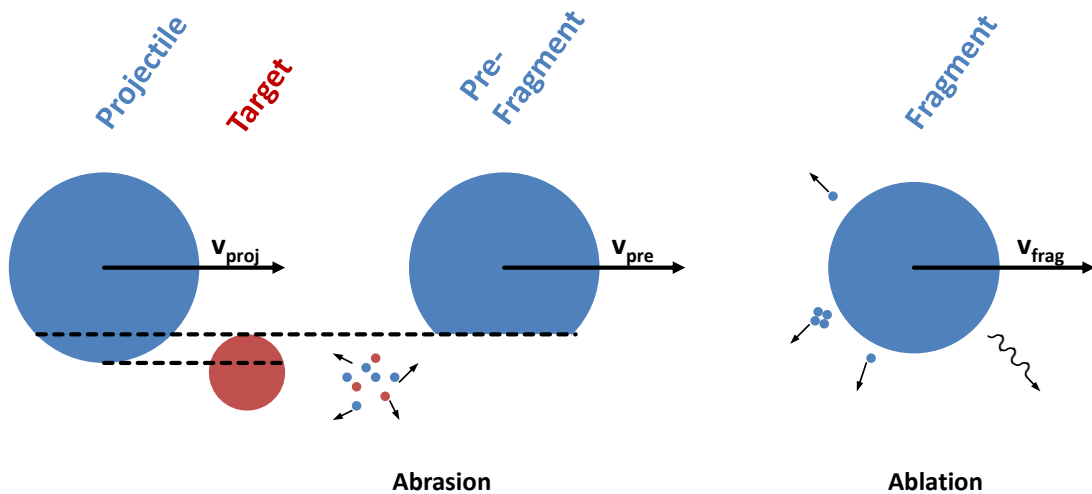


Figure 3.1: Illustration of the fragmentation mechanism.

Abrasion is a rather direct process that runs on a time scale of 10^{-23} to 10^{-22} s. The region of geometric overlap is called the 'interaction zone'. Nucleons that are inside this zone are called 'participants' and the others are 'spectators'. Due to the direct impact of the participants on the target nucleons, they are sheared off the projectile nucleus, whereas the spectator nucleons continue (highly excited) on their flight path. The excitation is caused by the drastic change of shape and therefore the change of surface energy.

The second step, ablation, is a slower process. Depending on the excitation energy, a prefragment de-excites by the emission of particles, fission or γ -rays at time scales of 10^{-20} to 10^{-16} s. Both steps lead to a wide range of reaction products.

3.3 The GSI-FRS setup

3.3.1 Accelerators

At the 'Gesellschaft für Schwerionenforschung' (GSI) radioactive ion beams are produced by using an accelerated primary heavy ion beam. It is provided by the 'UNILAC' [63] heavy ion linear accelerator and is able to accelerate all stable ions up to energies of 11.4 MeV/u. The beam is then injected into the heavy ion synchrotron 'SIS' [64] for further acceleration. During a typical ramping time from 1 to 4 seconds, the energy of the ions is increased up to 1 GeV/u for heavy ions or 4.5 GeV for protons. The beam is guided to the production target where the primary (fragmentation) reaction takes place and creates the radioactive nuclei of interest. The production target is located at the entrance window of the 'fragment separator' (FRS). Fig. 3.2 illustrates the layout of the GSI accelerator complex.

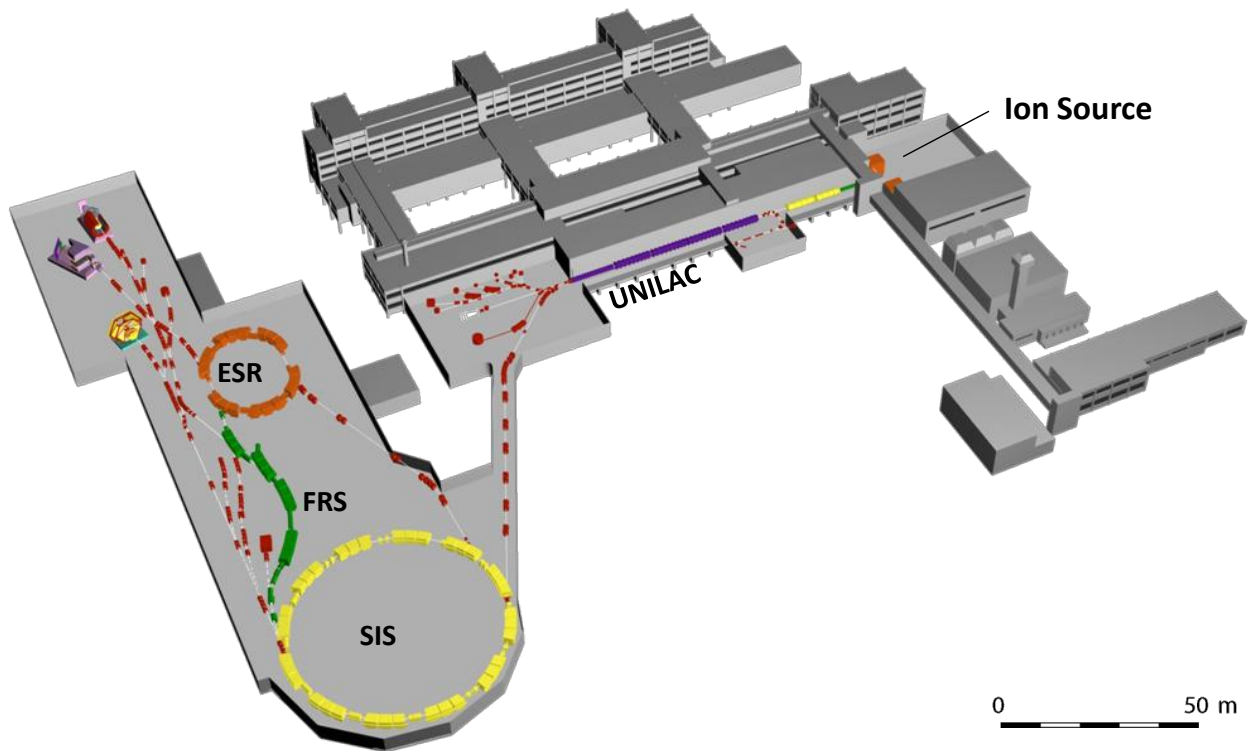


Figure 3.2: Schematic drawing of the GSI accelerator complex, the UNILAC/SIS/FRS as explained in the text and the Experimental storage ring (ESR), (modified from [66]).

3.3.2 The fragment separator (FRS)

The number of different nuclei from fragmentation reactions is large. In some cases, the nuclei of interest might only make a small percentage of the secondary beam and a device is needed to select only the ions of interest after the production target. At GSI the 'fragment separator' (FRS) is used to separate the fragmentation products [67, 68, 69]. The FRS is a magnetic 0° spectrometer with a total length of 74 m. Its main constituent parts are four 30° dipole magnets and a wedge-shaped degrader at the central focal plane. Every dipole magnet is surrounded by two sets of quadrupole magnets for beam focusing. The maximum magnetic rigidity ($B\rho^{\max}$) of the FRS is 18 Tm and is matched to the maximum $B\rho$ of the SIS.

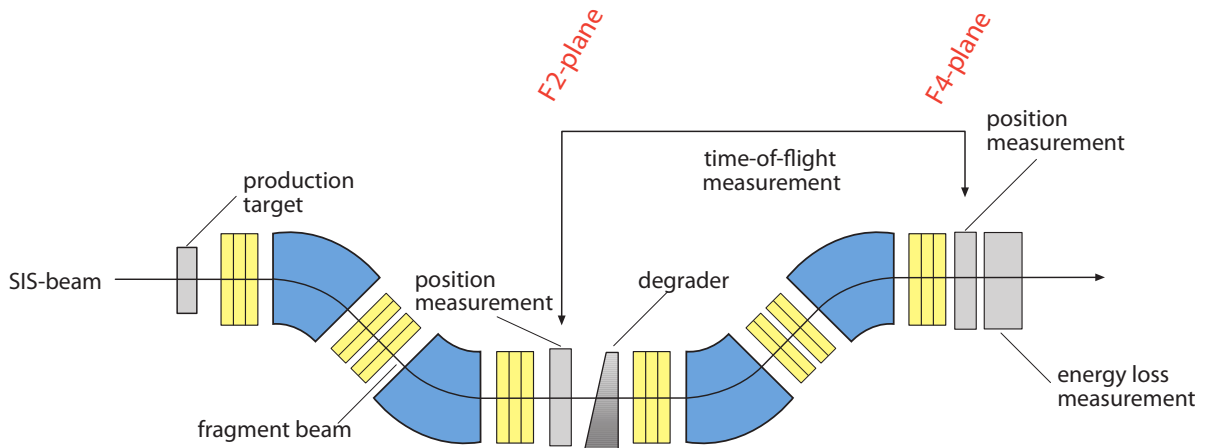


Figure 3.3: Schematic drawing of the FRS (modified from [70]).

The selection of a $B\rho$ value yields a selectivity in the A/Q acceptance ($B\rho \propto A/Q$, cf. subsection 3.3.2.2 for details). From the production to the middle focal plane (F2-plane, cf. fig. 3.3) the particle rate drops drastically (primary beam: 10^{10} pps, F2 plane $< 10^5$ pps). Particle detectors can be used for tracking and timing in the second half of the separator. Each ion that passes through the FRS can be identified uniquely by its mass and charge by combining this information with the energy loss measurement at the final focal plane (F4).

At the F2 plane a wedge shape degrader is inserted. The reason is twofold. Firstly, due to the energy loss (proportional to Z^2) inside the degrader, a large spread in the energy of the ions (depending on the charge of the ions) for different ion species occurs. This helps to filter out the nuclei of interest during the second dipole stage. The simulations in fig. 3.7a and 3.7b show the effect on the purity of the ion beam. The second effect of the degrader is that it can correct the energy spread of the ions. The middle plane is dispersive, meaning that ions with different velocities pass at different x-positions. The deviation from the central trajectory Δx is given by:

$$\Delta x = D \cdot \frac{\Delta\beta\Delta\gamma}{\beta\gamma}.$$

Here D is the dispersion of the setup, which is (from production target to middle plane) $D_{\text{target-F2}} = -6.474 \text{ cm}/\%$. The wedge shaped degrader is applied to cause a higher energy loss at larger

radii and a smaller one at smaller radii. This leads to a smaller distribution in momentum space.

For some experiments, especially if the secondary beam is close to stable nuclei ($A/Q \sim 2$) another degrader can be used between the first two dipole magnets. This helps to reduce the particle rate at the F2-plane. In experiment S377, two degraders of $2 \frac{mg}{cm^2}$ ^{27}Al were used at the F1-plane (between first and second dipole) and at the F2-plane.

For the complete identification of an ion, the proton number, Z , and the mass number, A , is needed. At relativistic energies of around 100 MeV/u, as used at GSI experiments, the ions are completely stripped (Charge $Q = Z$) and it is sufficient to measure the charge of the ions. The following subsections explain how the identification is obtained.

3.3.2.1 FRS detectors for particle identification and tracking

Time-of-flight detectors: Plastic scintillators and Finger detector

The basic FRS time-of-flight (ToF) measurement system relies on two plastic scintillators called SC21 (at the middle focal plane) and SC41 (at the final focal plane). They are used to determine the velocity of the ions and the interaction points at these two scintillators. The detector material is BC-4200 (Bicron corp.), which provides a high light output and a fast rise time (~ 500 ps). Each scintillator is read out by two photomultiplier tube (PMTs), one on each side. The PMTs are coupled directly to constant fraction discriminators (CFDs). Thus, by the time difference of the signals, the x-position of the interaction can be deduced. The average of the time difference of the signals from both sides give the ToF-signal

$$T = \frac{1}{2} (SC21_{left} - SC41_{left}) + (SC21_{right} - SC41_{right}).$$

This way of calculation accounts for deviations from the central trajectory. The intrinsic ToF resolution with this system is in the range of 250 ps.

For a higher rate capability a new ToF-start detector is additionally used at the central F2 plane: the Finger detector. It is a segmented plastic scintillator, read out by 16 PMTs. As fig. 3.4 shows, each strip is connected to two PMTs. Thus, the horizontal position can be determined from the strip with the highest energy deposition and the vertical position from the time difference of the two PMTs.

Energy loss detectors: MUSIC

For complete identification, the nuclear charge, Z , of the ions has to be determined due to several different ion species providing very similar A/Q ratios. This is done by the MUSIC ionization chamber [71] which is a fast multiple sampling detector, with eight independent anode strips, a Frisch grid and a cathode as shown in fig. 3.5. The chamber covers a surface area of 8×20 cm² and a total length of 40 cm. CF₄ is used as counting gas. At typical ion energies of ~ 100 MeV/u, it works as an 'energy loss' detector, so only a fraction of the energy of the ions is deposited in the ionization chamber. A heavy ion that passes through this detector ionizes the gas and produces a cloud of electrons that drift to the anode strips. The detected charge is proportional to the energy loss of the ions at each strip. The geometrical average of all anode strips forms the total energy loss $\Delta E_{MUSIC} = \left(\prod_{i=1}^8 \Delta E_i \right)^{1/8}$.

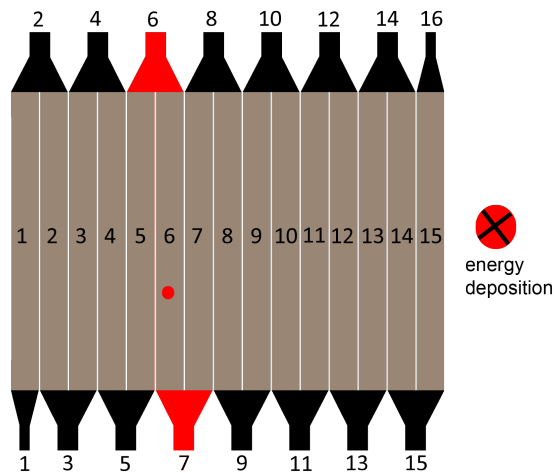


Figure 3.4: Illustration of the Finger detector (modified from [101]).

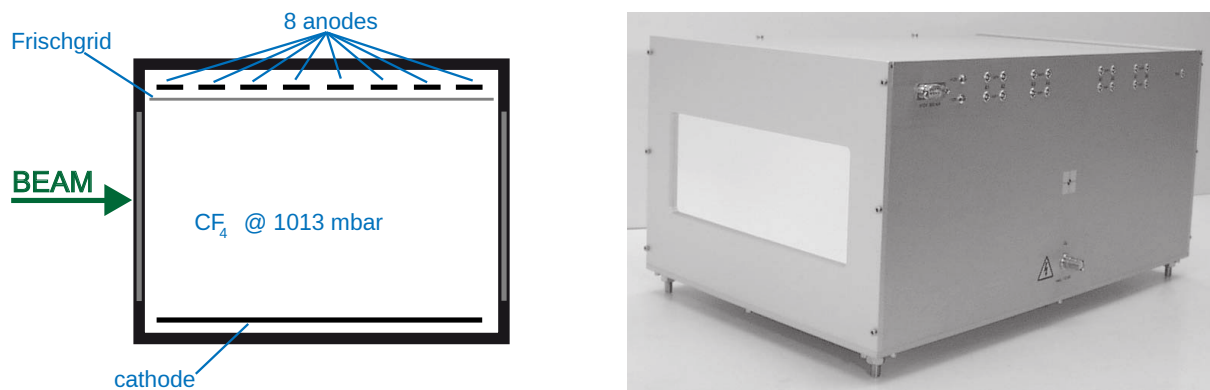


Figure 3.5: Pictures of a MUSIC detector (taken from [71]).

Position sensitive detectors: TPCs

A time projection chamber (TPC) is a drift chamber with a highly uniform electric field. The detector consists of a cathode, where the high voltage is applied, five anodes and a delay line. The y-position is deduced from the drift time of the electrons. For determination of the x-position, the signals of the anodes are split and the time difference between left and right side's signal is compared. Fig. 3.6 shows a schematic drawing and a photograph of a TPC as it was used in the PreSpec experiments.

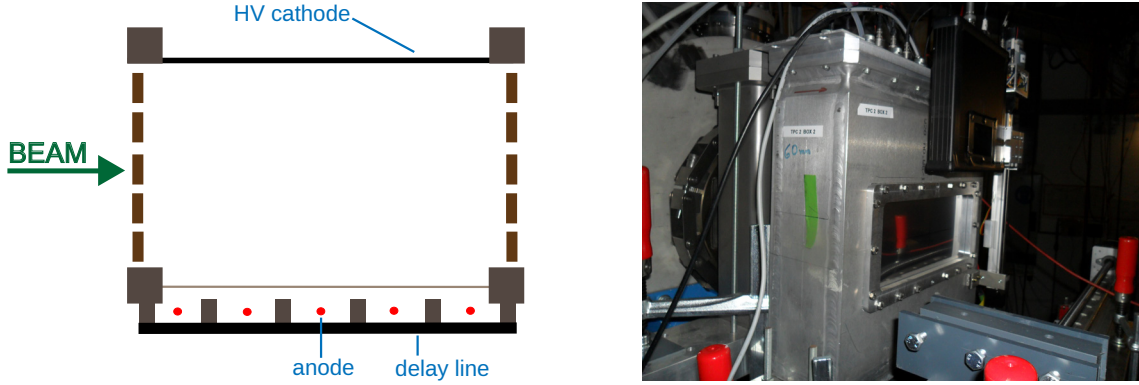


Figure 3.6: Pictures of a TPC; schematic drawing (left) and photograph of a mounted TPC (right). Fig. taken from [77].

3.3.2.2 Determination of the mass-to-charge-ratio A/Q

Ions that move along the optical axis in the second half of the FRS have the same magnetic rigidity as the dipole magnets. However, most trajectories deviate from the optical axis. So the magnetic rigidity of the trajectory is corrected with the help of the measured positions at the central (x_2) and final focal plane (x_4). Thus, the corrected magnetic rigidity $B\rho_{co}$ is given by:

$$B\rho_{co} = B\rho_{oa} \left(1 - \frac{x_2 - M_{F2-F4} \cdot x_4}{D_{F2-F4}} \right).$$

In this expression $B\rho_{oa}$ is the magnetic rigidity of central trajectory along the optical axis, x_2 and x_4 the position deviation from the optical axis, $M_{F2-F4} = 1.12$ the magnification between the middle and final focus and $D_{F2-F4} = 7.239 \text{ cm}/\%$ the dispersion between F2 and F4. Together with the velocity (β) measurement of the time-of-flight detectors the mass-to-charge-ratio can be deduced:

$$\frac{A}{Q} = \frac{e}{cu} \cdot \frac{B\rho_{co}}{\beta\gamma},$$

where e is the elementary charge, c is the speed of light, u is the atomic mass unit, β is the velocity of the ion in units of c and ($\gamma = \frac{1}{\sqrt{1-\beta^2}}$) is the relativistic Lorentz factor.

3.3.2.3 Determination of the nuclear charge Z

The energy loss of an ion in matter depends strongly on Z . The energy loss of a charged ion, moving at relativistic speed, in matter is given by the Bethe-Bloch-Equation [47, p. 121]:

$$-\frac{dE}{dx} = \frac{4\pi}{m_e c^2} \cdot \frac{\bar{Z} Z^2 N_a \rho}{A \beta^2} \cdot \left(\frac{e^2}{4\pi\epsilon_0} \right)^2 \cdot \left[\ln \left(\frac{2m_e c^2 \beta^2}{I \cdot (1-\beta^2)} \right) - \beta^2 \right], \quad (3.1)$$

where E is the energy of the ion, x is the distance traveled by the ion, Z is the charge of the ion, in full stripped case the proton number, m_e is the rest mass of an electron, β is the velocity of the ion in units of the speed of light, \bar{Z}, A, ρ, I are the proton number, the mass number, the

density and the mean excitation potential of the absorber material and N_a is the Avogadro number.

For an ion that is passing the absorber this can be expressed as

$$-\frac{dE}{dx} = Z^2 \cdot f(\beta).$$

Here $f(\beta)$ depends only on the velocity of the ion. Thus it can be deduced from measurements with a primary beam (known Z) at different velocities and scaled to energy losses of fragments $\left(-\frac{dE}{dx}\right)_{frag}$ afterwards.

$$\left(-\frac{dE}{dx}\right)_{frag}(\beta) = -\frac{Z_{frag}^2}{Z_{prime}^2} \left(-\frac{dE}{dx}\right)_{prime}(\beta)$$

Thus, by providing the energy loss and the velocity of the ion from the FRS time-of-flight measurement, the proton number of the ion, Z , can be determined unambiguously. Experimental results from FRS identification (including MUSIC data) are shown in the next section.

3.4 Beam preparation for the ^{33}Ar experiment

For the preparation of the Coulomb excitation experiment of ^{33}Ar several simulations were performed in order to optimize the FRS setup. The FRS detectors have been calibrated within the foregoing commissioning experiment.

Efficient settings in order to perform a radioactive beam Coulomb experiment at the SIS-FRS-setup have to fulfill the following conditions:

1. Secondary beam rate onto secondary target is maximal.
2. The energy of the ions at the secondary target is in the range of 100 – 150 MeV/u.
3. Primary beam energy and production target thickness matched for highest production rate.
4. Enough degrader material to reduce beam contaminations at F2 and F4 plane.
5. Total instantaneous F2 rate \lesssim 200 kHz.
6. Total instantaneous F4 rate \lesssim 20 kHz, thus the highest ratio between nuclei of interest and total secondary beam rate is needed.
7. Some settings allow calibration of FRS and LYCCA detectors.
8. In all settings that are used, the energy deposition stays in the dynamic range of all detectors.

The energy range of 100 – 150 MeV/u is chosen, because it is a compromise of energy dependence of the Coulomb excitation cross section, the forward boost of the emitted γ -rays and the transmission through the FRS. Limitations at F2 prevent damaging of the SC21 scintillator and

F4 the reduce pileup in the MUSIC detectors is reduced. Thus, the degrader material is chosen in a way, that the secondary beam, that reaches the S4 area is as clean as possible and the setting provides also the highest possible transmission.

3.4.1 FRS setups

The tables 3.1 and 3.2 give details on the settings that were used in commissioning and experiment.

In the first column the setting's name and use is given. For example, for the FRS 'TOF1' and 'dE1' mean that this setting was used as first calibration point for FRS-ToF and for the MUSIC detectors. For LYCCA 'LdE1' means first ΔE calibration point, 'LE1' the first CsI calibration point. The second column gives amount of material that was used as production target (^9Be) and as degraders (^{27}Al). Not mentioned is the secondary target, which always stayed in (^{197}Au , 386 mg/cm^2). In the third column the theoretical values of the dipole magnets' magnetic rigidity is given and in the the second table also the expected transmission of the nuclei of interest is shown. Fourth and fifth column give the energy loss at the FRS detectors and the time-of-flight between the S2 and S4 scintillators. In the sixth and seventh columns the energy losses at the different LYCCA detectors are shown. The eighth column gives the particle rates of ions at different stages. The numbers are given in thousand particles per 4 second spill (1 s ramping up - 2 s extraction - 1 s ramping down). The SC21 rate and the MU1 rate (rate at the first MUSIC detector) are given, because they are limited by the detectors. The S2 rate should not exceed 200 kHz, the MUSIC rate not 20 kHz. In the third row, the rate of nuclei of interest per spill is shown, in the fourth row the rate between the nuclei of interest to the total secondary beam rate is given. The ninth column gives the energy of the nuclei of interest before and after the secondary target, the total Coulomb excitation cross section at shown mid target energy, the ratio between the differential cross section ($\vartheta \leq 2.1^\circ$, cf. subsection. 6.1) and the number of estimated detected γ -rays at given efficiency.

The settings shown in table 3.1 were used to calibrate LYCCA within the commissioning experiment. It turned out that approximately 30 minutes of beam time are required to take enough data for a calibration point.

Table 3.2 show the settings that were used in the S377 experiment. LYCCA had to be recalibrated, because other experiments in between required other detector ranges. Calibration of LYCCA was done with the settings 'Prime', 'Ar-ht' and 'Ar-cal'. During the main experiment 'Prime' was used to calibrate the efficiency of the PreSpec setup and 'Ar-ht' for the Coulomb excitation of ^{33}Ar . The latter was an optimization of the original 'Ar-1' setup to compensate the reduced primary beam rate. 'S-1' was planned to be used for Coulomb excitation of ^{29}S .

Mocadi [102] was used to calculate beam contaminations in addition to Lise++. The latter uses a Gaussian approximation of the beam profile and cuts the spacial beam distribution at the per mill level. Mocadi is a true Monte Carlo simulation that calculates transmission rates without analytical beam profile approximations. This is needed, because even very small transmission rates can cause large contaminations if the production rate is high enough. Table 3.3 shows results from the Mocadi simulation.

Name	Material	Magnets	FRS-TOF	S4 detectors	LYCCA TOF	LYCCA $\Delta E - E$	Rates (4s/spill)	Coulex
Setting	Prod. tar.	$B\rho$ D1	S2-S4 ToF	ΔE @ MU1	ΔE @ Start	ΔE @DSSD _{tar}	R_{total} @ SC21	E bef./aft. tar.
Use FRS	S1 degr.	$B\rho$ D2	ΔE @ SC21	ΔE @ MU2	ΔE @ Stop	ΔE @DSSD _{wall}	R_{total} @ MU1	$\sigma_{tot,coulex}$ @ E
Use LYCCA	S2 degr.	$B\rho$ D3/4	ΔE @ SC41	ΔE @ TPC41		E @ Csl	R_{Not} @ wall	$\sigma_{diff}/\sigma_{tot}$
	[g/cm ²]	[Tm]	[ns-MeV]	[MeV]	[MeV]	[MeV]	[kp/spill]	Exp. $\gamma_s/h - \epsilon$
P1	0	6.8106	183.7	99	420	120	9.3	[MeV - mbarn]
TOF1, dE1	0	6.8106	598	100	438	122	8.9	294 / 286
LdE1	0	6.5179	647	27		14690	7.5	
P2	3.992	5.4102	215.9	131	636	195	5.8	143 / 131
TOF2, dE2	0	5.4102	753	136	756	218	5.4	
L-dE2, L-E1	0	4.9785	928	36		5819	4.6	
P3	0	6.8106	221.4	137	691	219	300	125 / 111
TOF3, dE3	2.5	6.0215	672	143	869	257	232	170 @ 117
L-dE3, L-E2	2	4.7968	990	38		4576	200	0.97
								1072 (3%)
P4	0	6.8106	230.3	147	804	279	300	96 / 80
TOF4, dE4	3	5.8444	693	155	1210	400	200	220 @ 87
L-E3	2	4.5302	1107	41		2324	192	0.75
								1076 (3 %)

Table 3.1: FRS settings for commissioning experiment, primary beam ^{54}Cr (10^5 pps, 370 MeV/u). Calculations with Lise++ [65].

Name	Material	Magnets	FRS-TOF	S4 detectors	LYCCA TOF	LYCCA $\Delta E - E$	Rates (4s/spill)	Coulex
Setting 2nd beam	Prod. tar. S1 degr. S2 degr. Transmis.	Bp D1 Bp D2 Bp D3/4	S2-S4 ToF ΔE @ SC21 ΔE @ SC41	ΔE @ MU1 ΔE @ MU2 ΔE @ TPC41	ΔE @ Start ΔE @ Stop	ΔE @DSSD _{tar} ΔE @DSSD _{wall} E @ Csi	R_{total} @ SC21 R_{total} @ MU1 R_{wall} @ wall Purity	E bef./aft. tar. $\sigma_{tot,coulex}$ @ E $\sigma_{diff}/\sigma_{tot}$ Exp. $ys/h - \epsilon$
Min. Matter ³⁶ Ar	0 0 0	6.7977 6.7977 6.6119	171.96 304 317	49.4 49.7 13.5	203 207	57 58 13588	100 %	393 387
Prime ³⁶ Ar	3.992 3 2	5.9712 5.2470 4.3241	219.8 384 530	75.4 77.8 20	361 417	109 119 4093	306 226 200 100 %	143 / 133 58.1 @ 137 0.967 120 (1%)
Ar-1 ³³ Ar	3.992 2.5 2	5.4276 4.8206 3.8846	222.8 384 557	77.5 80.4 21	386 472	120 138 3024	600 36 32 99.6 %	127 / 115 51.6 @ 120 0.796 29 (2%)
Ar-ht ³³ Ar	3.992 2 2	5.4276 4.9510 4.0685	215.6 373 511	73.0 75.3 20	347 400	105 115 3949	560 42 37 97.5 %	151 / 140 44.5 @ 145 0.95 34 (2%)
Ar-cal ³³ Ar	3.992 3 2	5.4276 4.6846 3.6832	230.8 395 611	82.7 86.5 22	436 600	146 190 1924	230 25 22 99.9 %	
S-1 ²⁹ S	3.992 3 2	5.3944 4.7490 3.9293	219.5 304 416	59.4 61.2 16	282 324	85 92 3390	450 16 8.8 98.2 %	145 / 135 22.3 @ 140 0.922 3.9 (2%)

Table 3.2: FRS settings for ³³Ar experiment, primary beam ³⁶Ar (5.10⁹ pps, 450 MeV/u). Calculations with Lise++ [65].

<i>Prime</i>	^{36}Ar	^{35}Ar					
Transmission [%]	0.227	4.2E-2					
Prod. Rate [pps]	2.8E5	4					
S4 Rate [pps]	63560	0.2					
<i>Ar-1</i>	^{33}Ar	^{32}Ar	^{34}Ar	^{31}Cl	^{32}Cl		
Transmission [%]	0.163	6.8E-3	5E-3	1.7E-2	9.4E-4		
Prod. Rate [pps]	2E5	8E3	5E6	1E5	3E6		
S4 Rate [pps]	32600	54	25000	1700	2820		
<i>S-1</i>	^{29}S	^{28}S	^{30}S	^{31}Cl	^{27}P	^{28}P	^{26}Si
Transmission [%]	0.1	6.2E-3	7.4E-3	1.7E-2	1.1E-2	3.7E-3	2.8E-5
Prod. Rate [pps]	1E5	5E3	2E6	1E5	1E5	2E6	1.7E6
S4 Rate [pps]	10000	31	14800	1700	1100	7400	48

Table 3.3: Mocadi [102] calculation of beam contaminations for the settings 'Prime', 'Ar-1' and 'S-1'.

For the ^{33}Ar setting a contamination of ^{34}Ar is expected that was not predicted by the Lise++ calculation. Furthermore the admixture of ^{32}Cl is calculated to be 8.5 %, whereas Lise++ predicts only 2 %. The contamination of ^{32}Cl detected during the experiment (cf. tab. 3.5) is in good agreement with the Mocadi simulation, the predicted ^{34}Ar was not detected.

Table 3.4 shows the original plan and the realized measurements during the S377 experiment. Due to the loss of one day of beam time at the beginning of the experiment (accelerator malfunction) and problems to reach the expected primary beam rate (below $1\text{E}10$ p/spill within the first 2 days) the available beam time was concentrate on the ^{33}Ar part of the experiment.

	Expected	Realized	FRS-Setting
Primary beam rate	$2\text{E}10$ p/spill	$4\text{E}9 - 2.5\text{E}10$ p/spill	
Accelerator / FRS setup	8 h	32 h	Misc.
Primary beam Coulex	8 h	18 h	Prime
^{33}Ar Coulex	16 h	66 h	Ar-1 / Ar-ht
^{29}S Coulex	88 h	—	S-1

Table 3.4: Plan and realization of the S377 experiment.

3.4.2 Comparison of simulation and FRS identification

Fig. 3.7a shows a Monte Carlo simulation of 10 million ions that reach the central focal plane of the FRS. In this case, the $B\rho$ value is set for $A/Q = \frac{33}{18}$, which is ^{33}Ar . However, several species are in the beam cocktail.

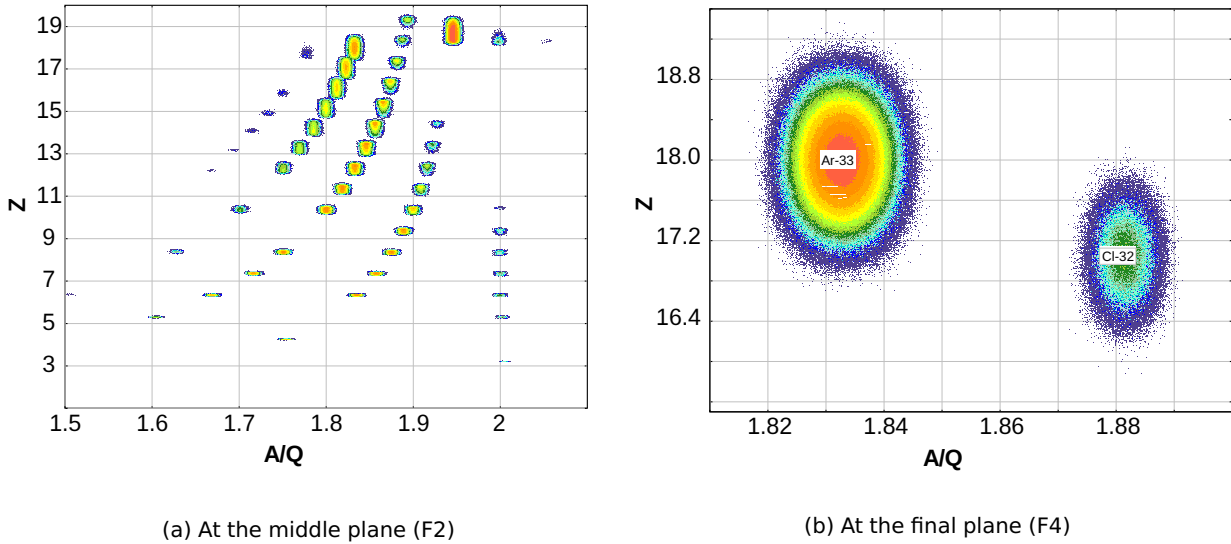


Figure 3.7: Monte Carlo simulation of fragmentation reaction with 'Ar-1'-setting.

At the final focal plane, the simulation comprises only two different ion species: ^{33}Ar and ^{32}Cl (cf. fig. 3.7b). From this simulation, the relative amount of ^{32}Cl is expected to be 2.5 %. This setting is optimized for high transmission of ^{33}Ar ($\sim 22\%$). A cleaner setting could be achieved by using thicker degraders (e.g. 4.5 g/cm^2 instead of 4 g/cm^2) but this would reduce also the transmission of ^{33}Ar to $\sim 18\%$. Therefore this small contamination is accepted. The simulation results can be compared to the FRS identification plot shown in fig. 3.8.

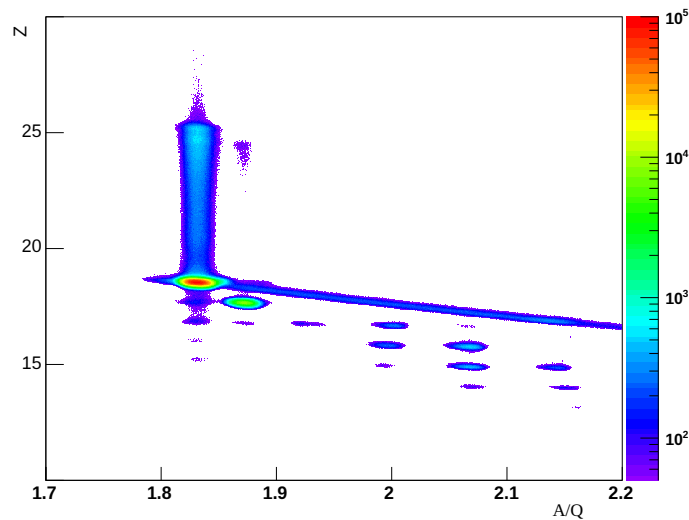


Figure 3.8: FRS identification plot for the ^{33}Ar setting.

The plot of the experimental data is in good agreement with the Lise++ simulation. The secondary beam is completely dominated by ^{33}Ar and the admixture of ^{32}Cl is at the percent level. The band from the main accumulation to higher Z is caused by pileup in the MUSIC detector (more than one ion is depositing energy in the counting gas within the same event) and the band to higher A/Q is caused by an incorrect measurement of the velocity of the ion. The other contaminants are summarized in tab. 3.5.

Species	Amount [M]	Relative fraction [%]
^{33}Ar	29.4	90
^{32}Cl	2.3	7
^{31}Cl	0.13	0.4
^{32}S	0.12	0.4
^{31}S	0.10	0.3
^{30}S	0.06	0.2
^{29}S	0.07	0.2
^{31}P	0.24	0.7
^{30}P	0.10	0.3
^{30}Si	0.12	0.4
^{29}Si	0.15	0.5
^{28}Si	0.03	0.1
^{28}Al	0.04	0.1
^{27}Al	0.03	0.1

Table 3.5: Composition of the secondary fragmentation beam identified by FRS detectors for the ^{33}Ar setting. Data analyzed from the S377 experiment.

This FRS setting provides a beam of 90 % ^{33}Ar , 7 % ^{32}Cl and small amounts of other species. This setup was chosen to have the highest transmission for ^{33}Ar . Furthermore, the resulting secondary beam is clean enough not to put too high an extra load on the data acquisition system.

3.5 The PreSpec setup

Besides the ancillary detectors (LYCCA), PreSpec comprises of several different γ -ray detectors. In the three 2010/11 experiments (^{88}Kr , ^{104}Sn , ^{33}Ar , cf. sec. 3.1), 15 former EUROBALL Cluster germanium detectors [58] and 8 HECTOR BaF_2 scintillators [59] were used for γ -ray detection. Fig. 3.9 illustrates the arrangement of detectors; the photo in fig. 3.10 shows the setup from a bird's eye view and fig. 3.11 shows both types of γ -ray detectors.

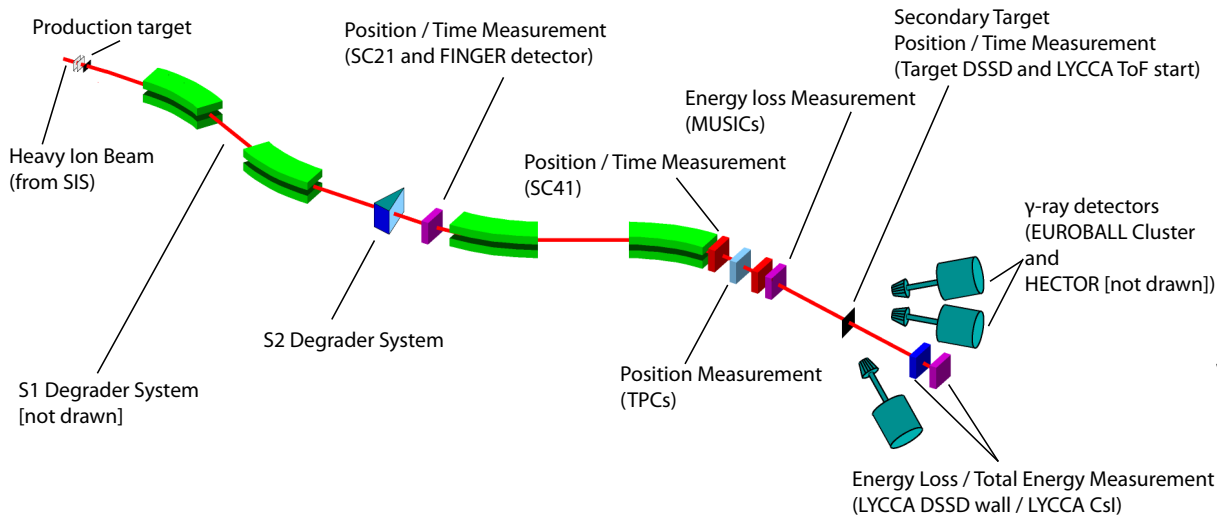


Figure 3.9: Schematic layout of the FRS/PreSpec setup.

Each EUROBALL Cluster detector comprises seven high-purity encapsulated germanium crystals housed in a common cryostat. The Cluster detectors are mounted in two rings at forward angles around the beam line; an inner ring at an average angle $\vartheta = 15.9^\circ$ and an outer ring at an average angle $\vartheta = 34.5^\circ$. The signals are coupled to different electronic stages, firstly to digital electronics; the 'digital gamma finders' (DGF). They record the energy signal and also a low resolution time signal (25 ns step size) of all channels. Secondly, commercial, analog electronics consisting of: timing filter amplifiers (TFA), constant fraction discriminators (CFD) and time to digital converters (TDC) are used to create a high resolution timing signal (short range timing, 'SR').

The HECTOR BaF_2 scintillators are highly efficient detectors and are optimized for high energetic γ -rays. They are located at a angle of $\vartheta = 85^\circ$ (slightly in the forward direction). The typical energy resolution is 12-14 % FWHM (at 1.3 MeV), The time resolution (~ 1 ns) is excellent.

In the future, following the first part of the PreSpec campaign, the Cluster detectors are to be replaced by several AGATA ('Advanced γ -ray tracking array', [60]) detectors. AGATA is a next generation array that provides superior resolution and efficiency by using the novel γ -ray tracking method.

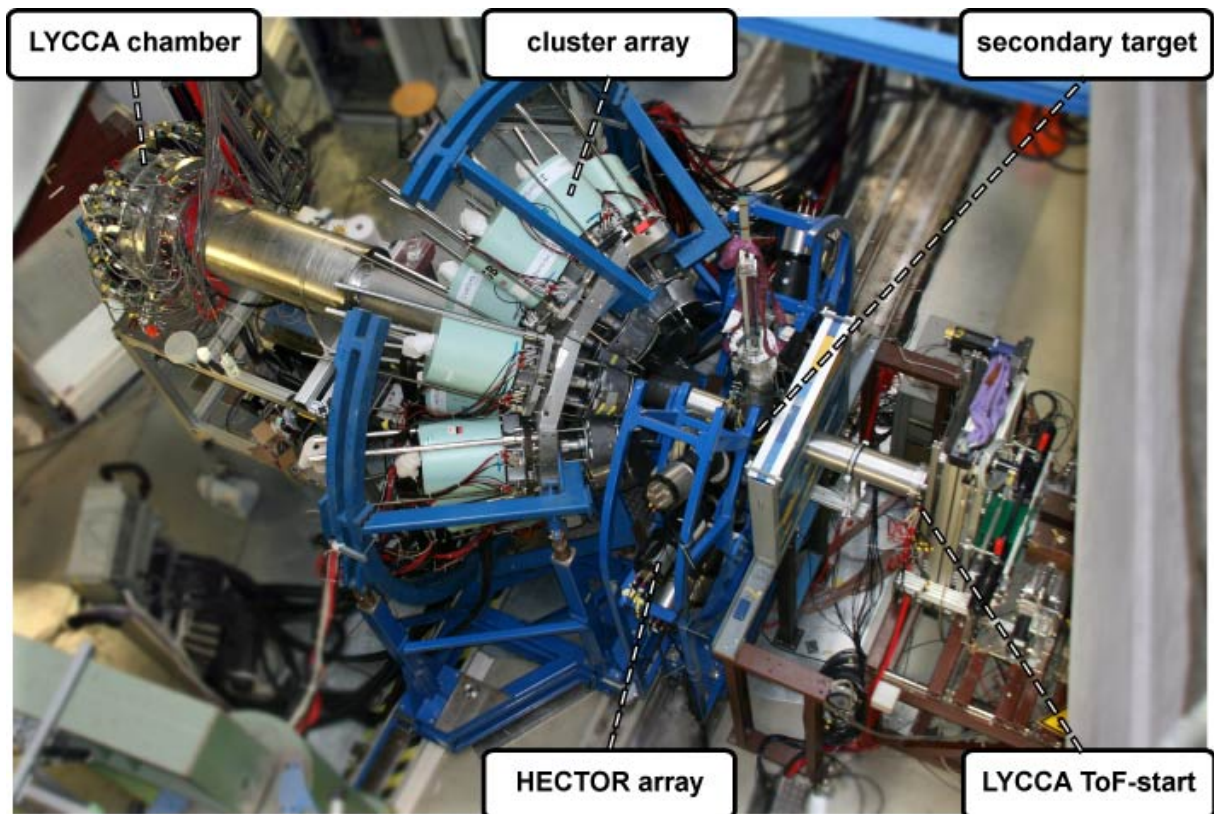


Figure 3.10: Photograph of the PreSpec setup (Picture from J. Grebosz, Univ. of Cracow).

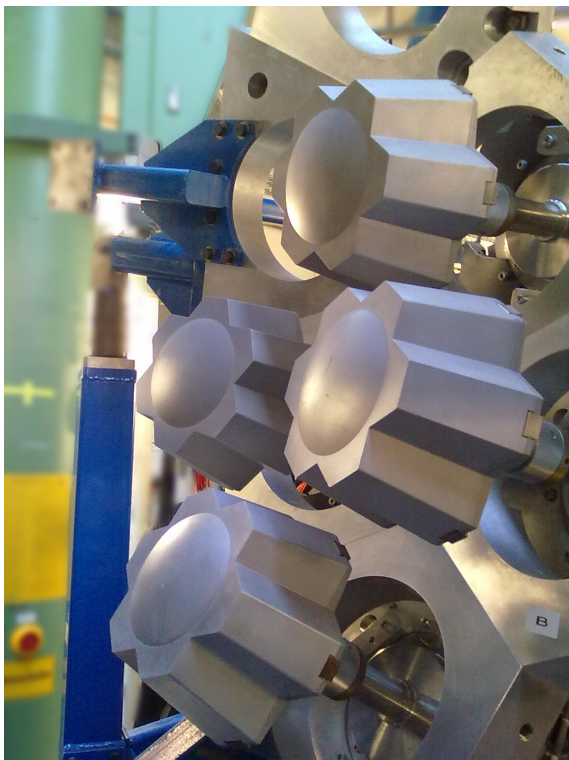


Figure 3.11: Photograph of EUROBALL Cluster detectors (left) and HECTOR (right), taken during the described S377 experiment.

3.6 Data acquisition (DAQ) and trigger logic

For acquisition of the analog detector signals, electronic devices are needed that convert the signals to digital ones. The mostly used devices are amplitude to digital converters (ADCs). They measure the maximal amplitude of the incoming signal. There are also charge to digital converters (QCD) that integrate the analog signal. For timing measurements, time to digital converters (TDCs) are used. Time measurement is done between a logic start and stop signal, deduced from a detector signals with the help of discriminators (most common: constant fraction discriminators, CFDs).

For the EUROBALL Cluster detectors, specific sampling ADCs (digital gamma finder, DGF) are used. They measure the amplitude, the shape and a time difference to a reference channel of the germanium detectors' preamplifiers. In addition the output signal of the germanium detectors is also coupled to analog electronics (fast timing filter amplifier, CFD, TDC), because this provides best timing resolution.

The DAQ modules (ADCs, TDCs, QCDs and DGFs) are mounted in VME crates and communicate via the VME bus with the processor in each crate. The processor collects the data and sends it via ethernet to the event builder (EB). The event builder reconstructs the event from all data sent by the VME crates (cf. fig. 3.12).

The Multi Branch System (MBS, [94]) is composed of eleven crates, which contains a RIO processor, a TRIVA trigger module [95] and the DAQ modules (see above). The TRIVA modules assures synchronized read-out of all crates and handles dead time locking. One crate is called Master Crate, here the Master trigger is generated. This master trigger is sent to all crates. When all data is sent to the EB and the event is reconstructed it is stored on disk. If the system is not too busy some events are sent to the online analysis. More details on this system is given in ref. [93].

Most detectors that see a signal create a trigger request. The signal can be caused either by noise or by an expected event. In order to reduce the noise (and thus the data rate) all signals are sent to the control room for forming of coincidences. If the coincidence requirements are fulfilled, a so called 'Free Trigger' (FT) is generated. If this takes place when the DAQ is in readiness (not in dead time period) the FT become an 'Accepted Trigger' (AT). All ATs generate a gate for each DAQ module to start the read-out / data sending process.

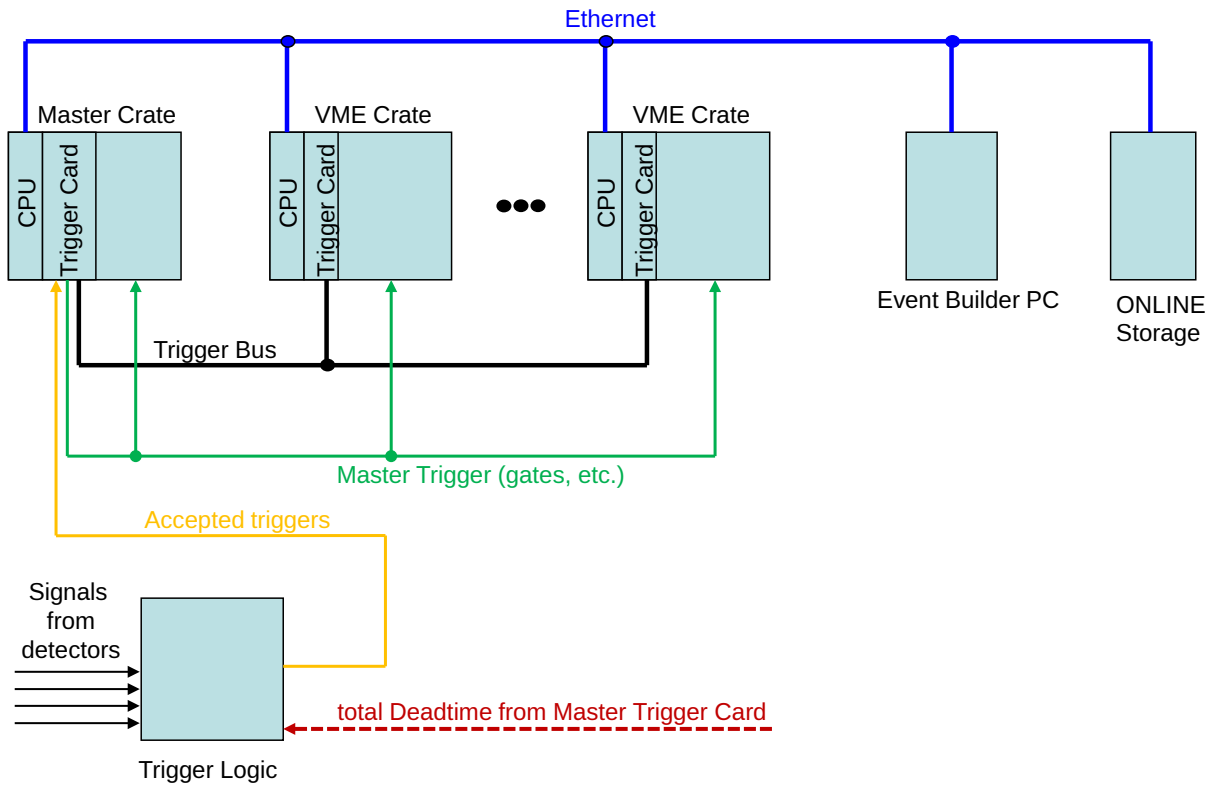


Figure 3.12: Structure of the Multi Branch System (MBS) for the PreSpec experiments. Fig. modified from [96].

	Coincidence	Read out crates	Usage	RF
Trigger 1	Any FRS detector (most common SC21)	FRS, TPC, USER, MUSIC	Calibration of FRS detectors	-
Trigger 2	HECTOR & SC41	All	Hector particle- γ -trigger	4
Trigger 3	EUROBALL & SC41	All	Main experimental particle- γ -trigger	1
Trigger 4	SC41	All	Pure particle-trigger	1024
Trigger 7	Any PreSpec detector	USER, LYCCA, DGF, Ge-time, Hector	Calib. of PreSpec detectors (LYCCA, Cluster, etc.)	-

Table 3.6: Used triggers in the described S377 experiment.

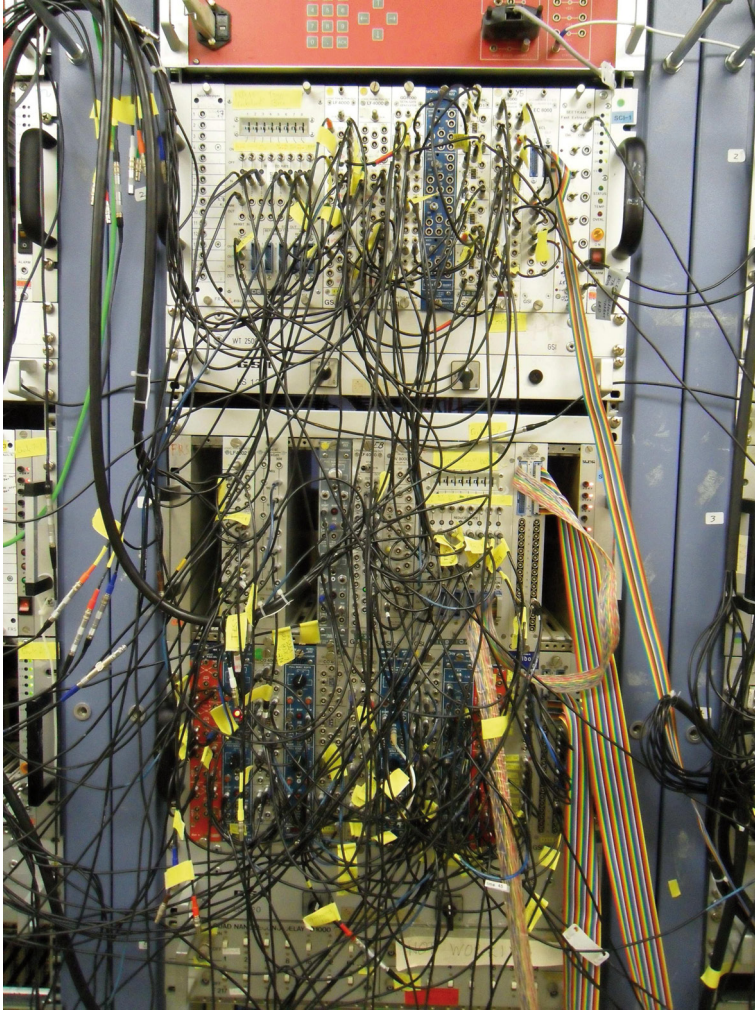


Figure 3.13: Photo of the trigger logic modules during this experiment. Taken from [93].

To cope with the various requirements of such a complicated system as the FRS-PreSpec setup, several triggers are needed for testing, calibration and experimental usage of detectors. In total twelve different triggers are used (cf. ref. [93]). They differ in the coincidence requirements and the crates that are read out. For this experiment only five triggers are needed. Each trigger that is activated during the experiment (2,3,4) is scaled down by an individual reduction factor RF (depending on its importance). Five different triggers are used. They are summarized in table 3.6.

Chapter 4

The LYCCA detector array

The 'Lund-York-Cologne-Calorimeter' (LYCCA) is a ΔE - E , time-of-flight detector array. Its main objective is the identification and tracking of radioactive heavy ions after reactions at the secondary target. The design and testing of LYCCA was a main part of this work. This chapter describes the development from the testing of a first detector module with sources and beams from the Cologne tandem accelerator to the first experiments with radioactive ion beams at the GSI.

In the first section, the setup and the detection principle, including the calculation of proton and mass number is described. The second section gives information about the detectors used and their specifications. This is followed by experimental results on identification and tracking from the ^{88}Kr Coulomb excitation experiment [90]. Details on all the corrections used for the calculation of mass and charge are given in [50].

4.1 Setup and detection principle

To identify ions after the secondary target, the proton number, Z , and the mass number, A , need to be determined. Analogue to the identification with the FRS (cf. sec. 3.3.2), it is sufficient to measure the charge of the ions to determine Z with LYCCA. In addition, for γ -ray spectroscopy the tracking of the emitting ion is needed for the best possible Doppler correction.

For these tasks, LYCCA comprises different types of detectors:

- Double-sided silicon strip detectors (DSSD) for energy loss (ΔE) and position measurement of the ions
- Caesium iodide scintillators (CsI) for the measurement of the total kinetic energy (E) of the ions
- Plastic scintillators as timing detectors for the time-of-flight measurement of the ions, or as an option at a later stage, polycrystalline diamond detectors (PCD) as time-of-flight start detector

The schematic layout of the LYCCA array is illustrated in fig. 4.1.

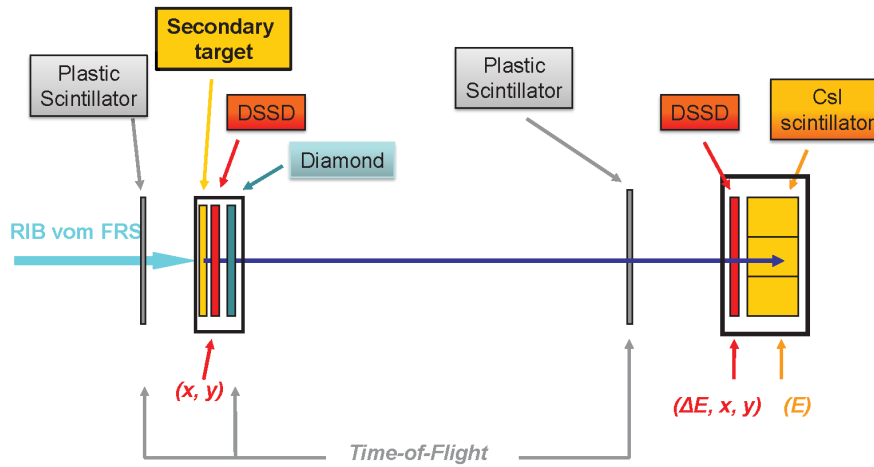


Figure 4.1: Schematic view of the LYCCA array where the radioactive ion beam is entering from the left.

The detectors' output is combined to deduce information about the ion:

1. Twofold position measurement to determine the trajectory of the ions.
2. ΔE and E to assign the charge of the ions.
3. E and time-of-flight to deduce the mass of the ions.

Results of identification and tracking are shown in section 4.3.

4.2 Detectors and hardware

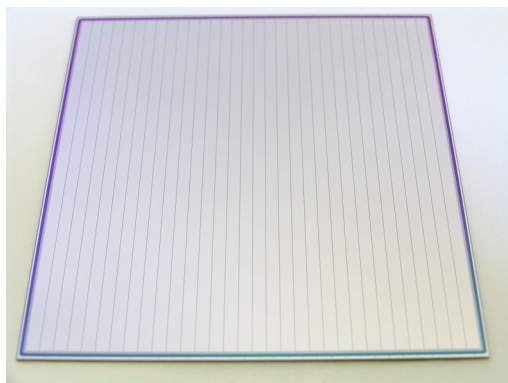
4.2.1 Double-sided silicon strip detector (DSSD)

DSSDs are used at two positions; one directly behind the secondary target and twelve other DSSDs mounted in the $\Delta E - E$ (energy-loss and total energy are detected, cf. sub sec. 4.2.3) modules inside the LYCCA chamber.

The target DSSD is used to detect the interaction point close to the target. It is located 1.5 cm downstream with respect to the secondary target. Moreover, it also provides an energy loss signal (ΔE) and a time signal (typical resolution is 0.5 ns FWHM, cf. sec. 5.2). This detector has an active area of $58 \times 58 \text{ mm}^2$ and is segmented in 32 strips on the front (p-side) and back (n-side). These individual, perpendicular strips allow the assignment of any energy deposition within the detector to one of the corresponding 1024 pixels (defined by the hit p- and n-strip). The typical energy resolution is 1-2% at energies of around 5 MeV (tested with an α -source). The various tests that were performed with the silicon detectors are described in sec. 4.3. A photograph and a technical drawing of a DSSD in its frame to be mounted in a $\Delta E - E$ module are shown in figures 4.2 and 4.3.

Chip dimension	60.0(2) x 60.0(2) mm ²
Active area	58.0 x 58.0 mm ²
Number of strips	32 x 32
Inter-strip distance	75 μm
Thickness	303(3) μm
Dead layer junction side	0.48 μm
Dead layer ohmic side	0.55(3) μm
Full depletion voltage	typical 40 V
Operation voltage	50 V
Total capacity	1060 pF
Resistivity	6.3 k Ωcm
Leakage current	typical 10-15 nA per strip

Table 4.1: Overview of DSSD characteristics.

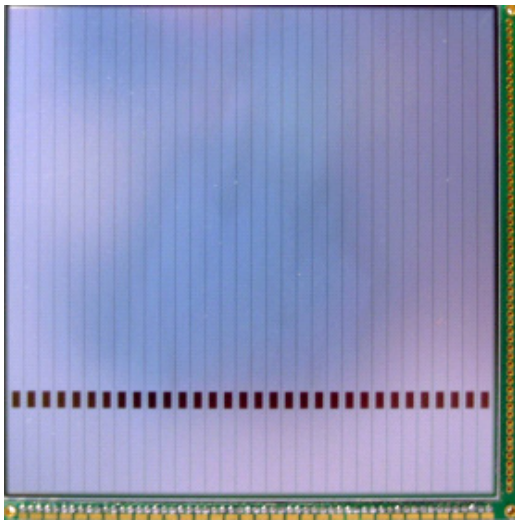


(a) N-side.

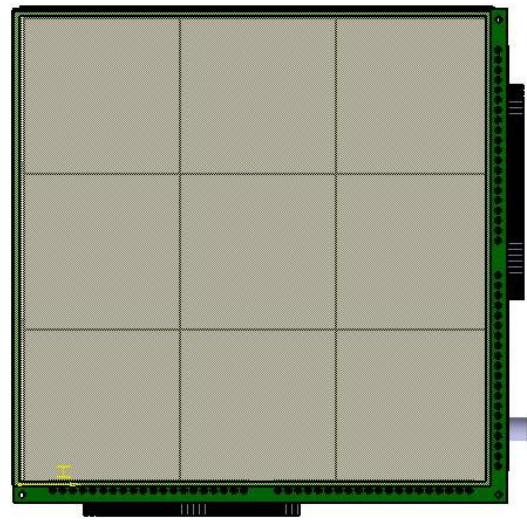


(b) Detailed view on n-side.

Figure 4.2: Photographs of a DSSD wafer without frame.



(a) Photograph of DSSD front side in the frame for a $\Delta E - E$ module.



(b) Technical drawing of a DSSD in its frame.

Figure 4.3: Images of a DSSD mounted on the frame for $\Delta E - E$ module.

4.2.2 Caesium iodide scintillators (CsI)

CsI scintillators are used to measure the total kinetic energy of the implanted ions. The CsI(Tl) crystals originate from Kharkov, Ukraine. The scintillators front face is $19.0(5) \times 19.0(5) \text{ mm}^2$ and nine pieces cover the surface of one DSSD. There are two varieties of the CsI scintillators: a long version (33 mm long, cf. fig. 4.5b) which was used for all PreSpec experiments up to now and a short version (13 mm, cf. fig. 4.5a) which is built for future experiments. In the course of a pyramid of additional 7 mm depth, the face is reduced to $10.0 \times 10.0 \text{ mm}^2$ (cf. Fig. 4.4). The crystals are wrapped in three layers of VM2000 foil, summing up to about 0.25 mm. Thus one CsI detector is effectively $19.5(5) \times 19.5(5) \text{ mm}^2$ in size. The energy resolution of CsI detectors is directly coupled to the efficiency of light collection and the uniformity of light collection over the active volume of the detector. The photons that are produced in the scintillators are converted to a charge pulse by photo diodes which have a size of $10.5 \times 11.5 \text{ mm}^2$ (produced by RADCON). They are glued onto the crystal with optical epoxy (cf. fig. 4.6). The output of the photo diodes is connected to charge sensitive preamplifiers (cf. subsection. 4.16).

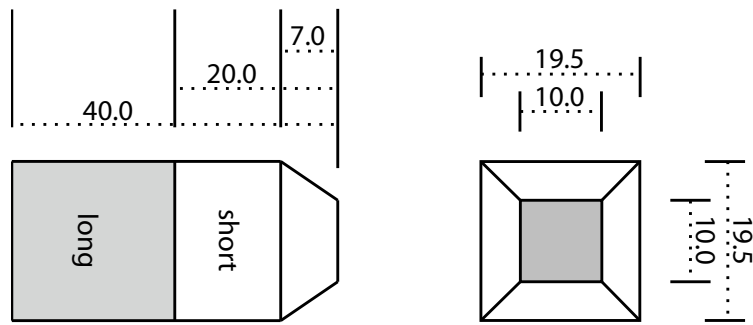
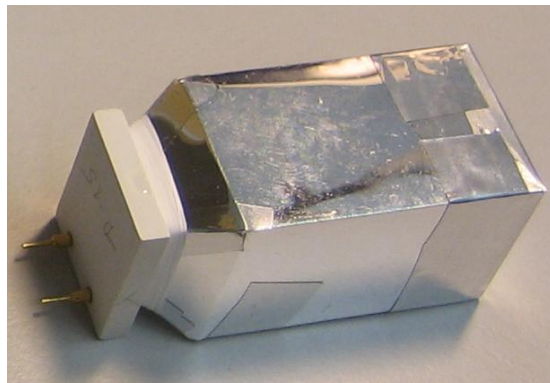


Figure 4.4: Illustration of the different types of CsI scintillators.



(a) Short CsI crystal.



(b) Long CsI crystal.

Figure 4.5: Photograph of CsI crystals.

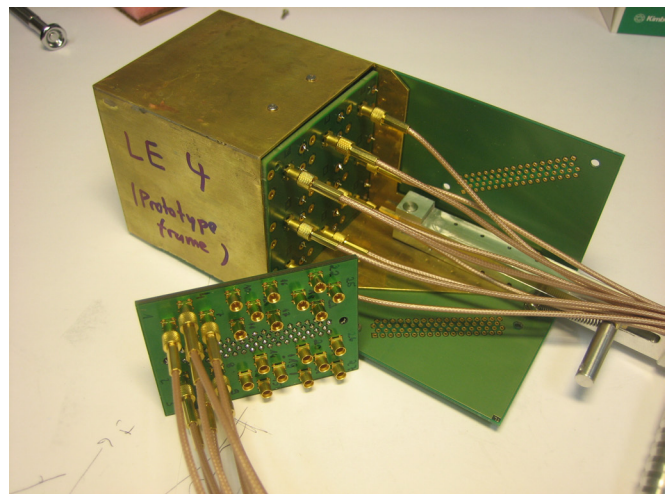
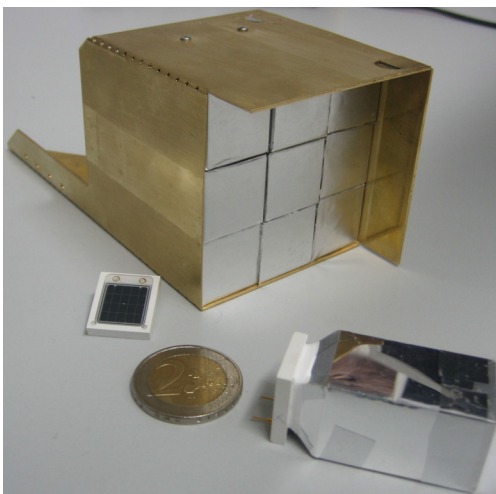


Figure 4.6: Left: A CsI scintillator of the long type showing a photo diode mounted on its ceramic frame and nine pieces mounted on their common brass frame. Right: Nine CsI crystals, connected with cables and adapter boards.

4.2.3 $\Delta E - E$ module

Each $\Delta E - E$ module consists of a DSSD and a block of nine CsI scintillators. The DSSD is mounted on a perpendicular frame to provide the possibility to place modules close to each other with the least dead space in between. The CsI-scintillators are packed in sets of nine pieces. The ions are stopped inside the CsI crystals to determine the total kinetic energy of the ions.

The main design principle was to obtain the highest solid angle coverage under extreme forward angles in order to have the highest feasible efficiency. This was achieved by arranging the detectors in the form a 'tiled wall'. Another design consideration was to keep maximal flexibility with the option to arrange the modules in different geometries and to be able to replace individual detectors. Fig. 4.7 shows technical drawings of the first design study to the final $\Delta E - E$ module version. More detailed technical drawings are shown in the appendix (cf. fig. D.3).

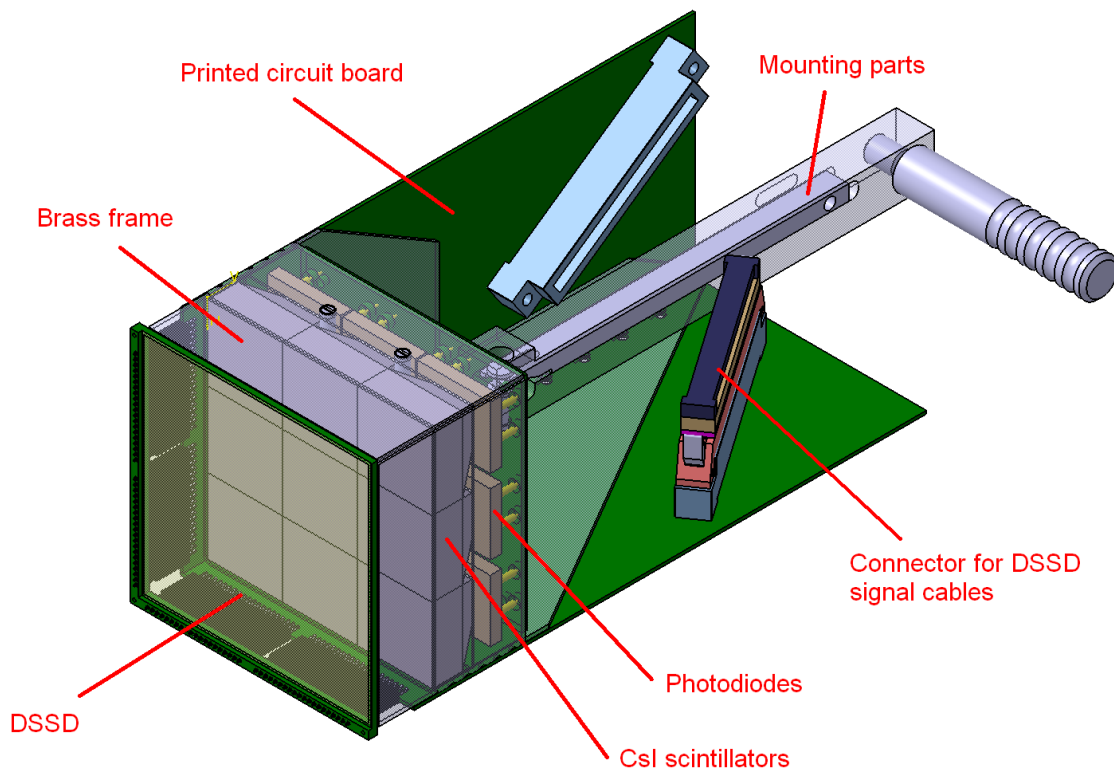
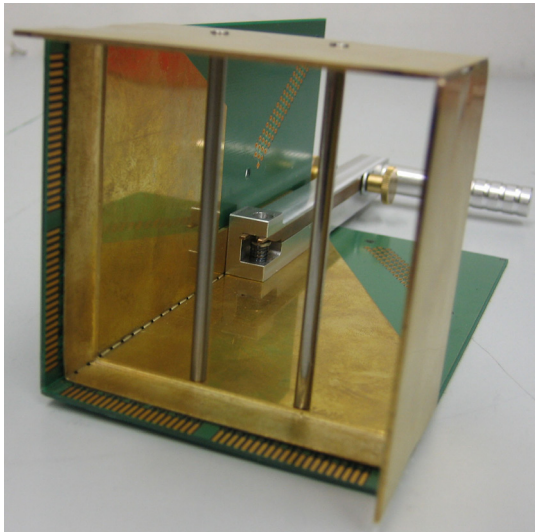
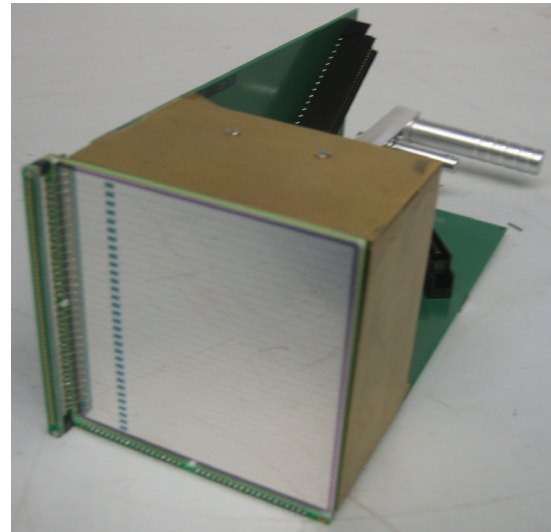


Figure 4.7: Technical drawing of the $\Delta E - E$ modules.



(a) Without detectors.



(b) Equipped with DSSD and CsI scintillators, as it is used in the PreSpec experiments.

Figure 4.8: Final version of the $\Delta E - E$ module's frame.

The grazing angles of different reactions at typical energies and the covered scattering angles by LYCCA-0 (12 detector modules in 4 x 3 arrangement) as well as the covered scattering angles by LYCCA (26 detector modules) are shown in table 4.2. The covered scattering angles are estimated by transforming the area covered by LYCCA in a circular surface.

Detector arrangement	Covered scattering angle [LAB]
LYCCA-0	2.2°
LYCCA	2.8°

Projectile @ Energy	Grazing angle [LAB]
³⁶ Ar @ 137 MeV/u	1.95°
³³ Ar @ 145 MeV/u	2.04°
¹² C @ 100 MeV/u	2.88°
¹² C @ 150 MeV/u	1.96°
³⁶ Ar @ 100 MeV/u	2.63°
³⁶ Ar @ 150 MeV/u	1.79°
⁶⁴ Ni @ 100 MeV/u	2.18°
⁶⁴ Ni @ 150 MeV/u	1.48°
¹²⁴ Xe @ 100 MeV/u	2.01°
¹²⁴ Xe @ 150 MeV/u	1.37°
²³⁸ U @ 100 MeV/u	1.64°
²³⁸ U @ 150 MeV/u	1.12°

Table 4.2: Covered scattering angles by the LYCCA array and grazing angles of Coulomb excitation reactions at typical GSI energies.

LYCCA-0 covers the grazing angles for heavy nuclei ($A \gtrsim 100$) even at lower energies, for lighter nuclei higher energies are needed. With the full LYCCA array, the angular coverage is improved, that also light nuclei can be studied at lower energies, which would increase Coulomb excitation cross sections.

4.2.4 Plastic scintillators

Plastic scintillators are used as start and stop detectors for the time-of-flight measurement. They consist of a 2 mm thick plastic membrane (type BC-420) in a plastic frame, which contains 32 photo multiplier tubes (PMTs). This large number of independent time measurements can be used to improve the time resolution if the location of the ion impact on the membrane is precisely known. By tracking the ions with the LYCCA DSSDs, the position at the membranes can be determined within an error of $\Delta x = \Delta y = \pm 1$ mm. An uncertainty in the time resolution (from spacial uncertainty) of $\Delta t(x,y) \approx \frac{1}{c} \sqrt{(\Delta x)^2 + (\Delta y)^2} \approx 5$ ps has been estimated. Both detectors provide the identical PMT configuration and differ only in the holding structure.

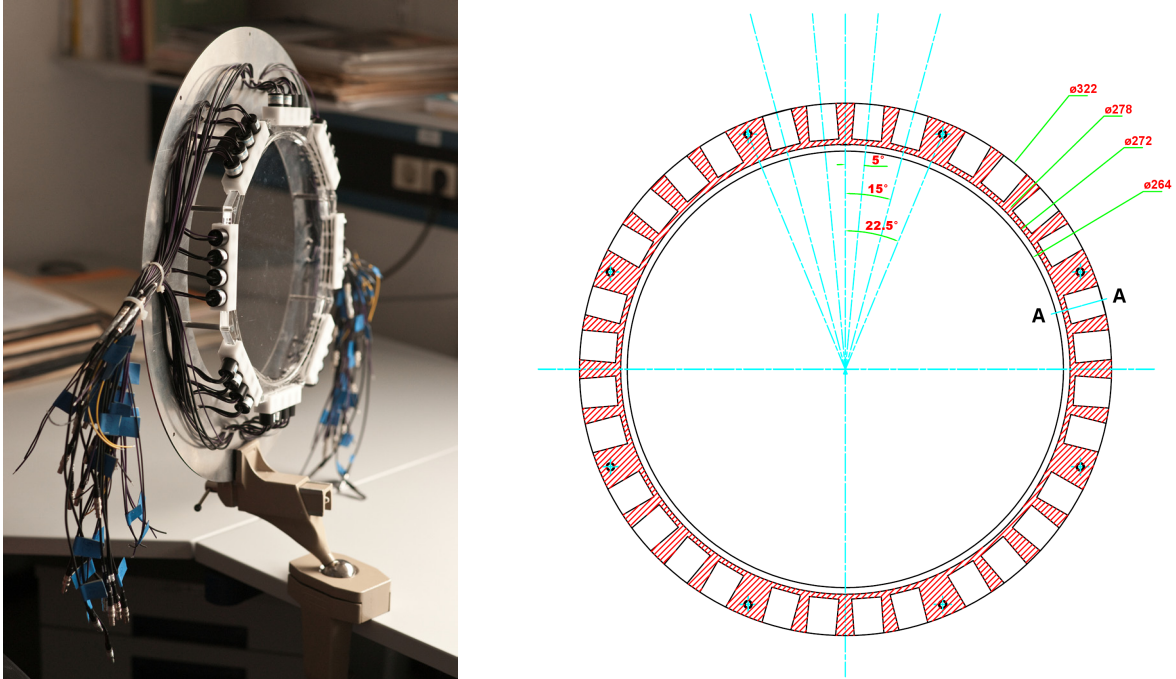


Figure 4.9: Images of a plastic scintillator with 32 photo multiplier tubes and HV / signal cables (taken from R. Hoischen et al. [48]).

With this setup, time-of-flight resolutions below $\sigma = 20$ ps are achieved under realistic experimental conditions with ^{64}Ni and ^{124}Xe beams [48]. Details on the used algorithms and corrections are described in [49].

4.2.5 Chamber and holding structure

The LYCCA chamber was developed and manufactured at the Cologne mechanical workshop. It is designed to house up to 26 $\Delta E - E$ modules and a plastic stop-detector. Up to 72 feedthroughs for DSSDs signal cables and CsI signal cables can be installed (32 channels each). These feedthroughs are modular and can be exchanged for other devices, for example, a grounding connection to the chamber or a temperature measurement device. The chamber also provides 64 feedthroughs for the high voltage and the signals of the stop detector photomultiplier tubes.

The chamber and the beam line up to the secondary target contain a large volume and is pumped by one turbo molecular pump. The number of feedthroughs worsen the leak tightness. The vacuum inside the chamber is constantly measured to be better than 10^{-5} mbar.

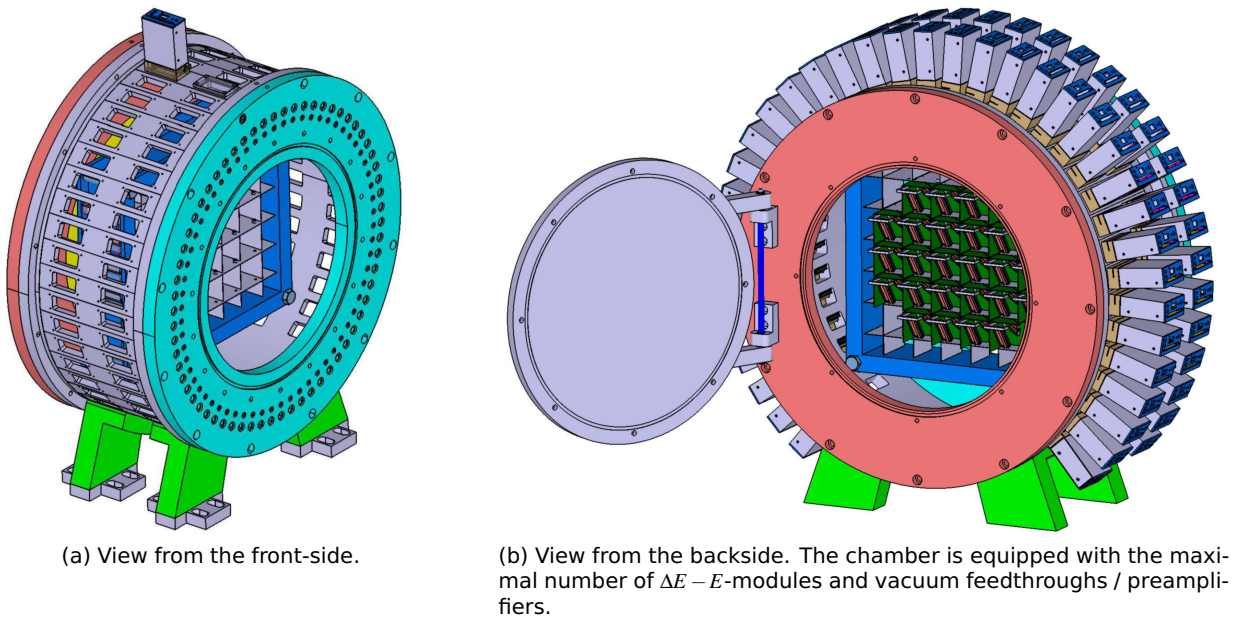


Figure 4.10: Technical drawing of the LYCCA chamber.

The holding structure inside the chamber (cf. fig. 4.11 and 4.13) that houses the $\Delta E - E$ -modules, allows the removal and replacement of single modules and gives the opportunity to place detector modules in different arrangements. The temperature of the holding structure and the plastic frame of the stop scintillator are monitored by a PT-100. Fig. 4.12 shows a technical drawing of the chamber (two more in fig. D.1 and D.2) and fig. 4.15 show photographs of the chamber.

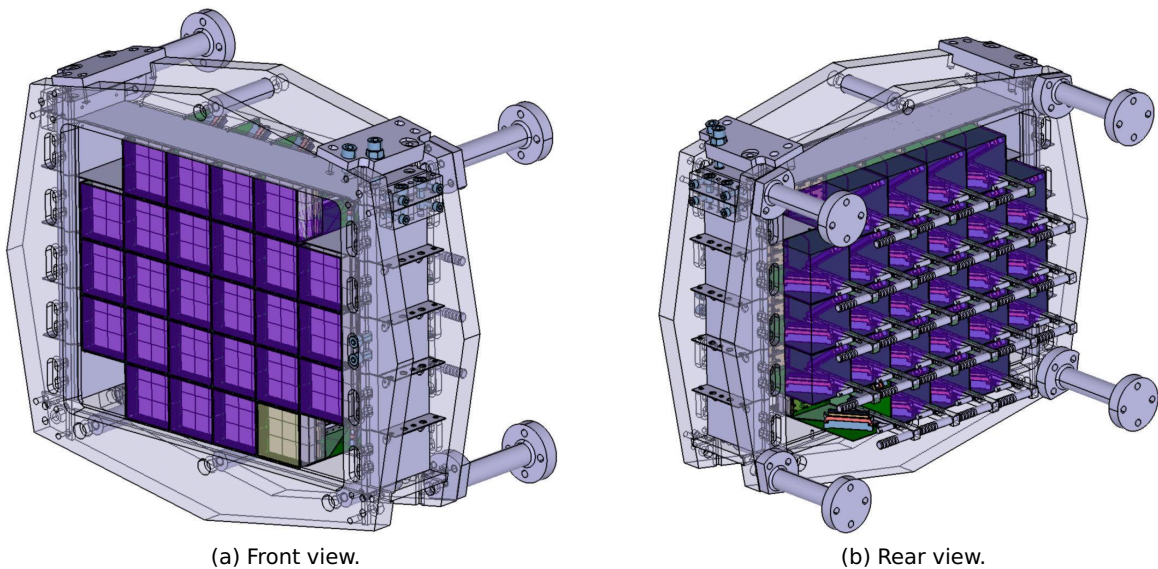


Figure 4.11: Technical drawing of the holding structure equipped with detector modules.

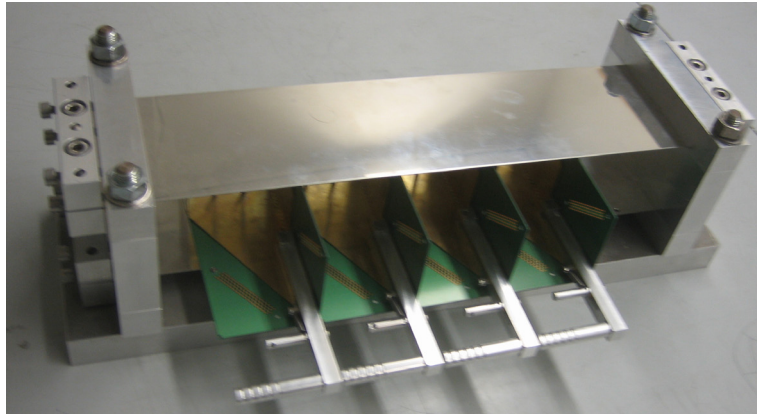


Figure 4.13: Photograph of a single bank of the holding structure, equipped with four detector modules.

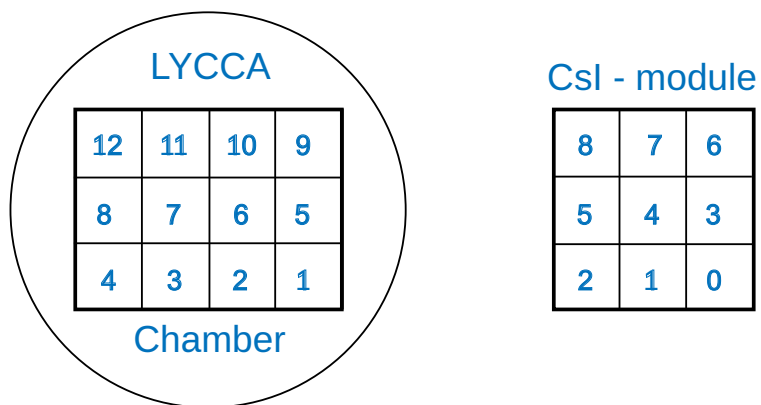
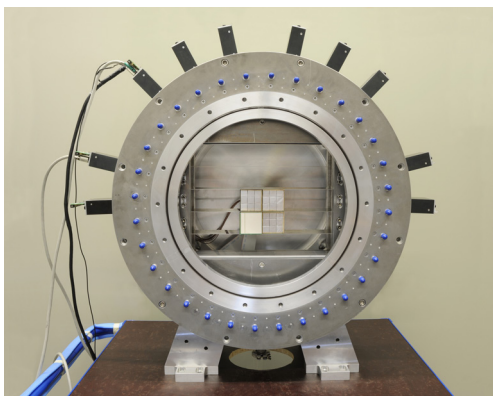
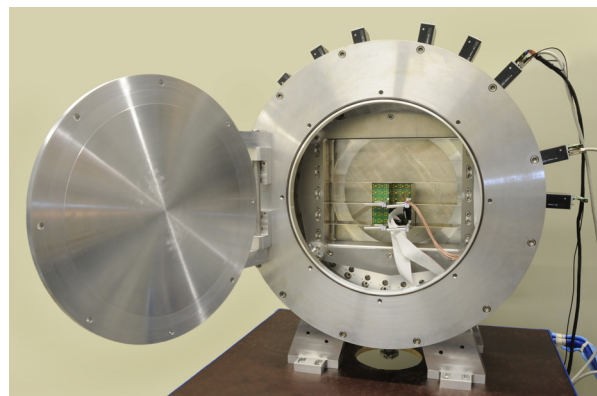


Figure 4.14: Alignment of LYCCA detector modules.



(a) View from the front-side.



(b) View from the backside.

Figure 4.15: LYCCA chamber with four installed detector modules for the first commissioning experiments in Sept. 2010 (Photo: G. Otto, GSI).

4.2.6 Preamplifiers and electronics

The output of all LYCCA detectors that provide an energy signal is a charge pulse. This is processed by a charge sensitive preamplifier that converts the charge pulse to a voltage signal. These preamplifiers are designed and manufactured by the Cologne electronics workshop especially for the LYCCA project [51]. They each process 32 channels. Two types are available with an active range of either 200 MeV or 4 GeV (energy equivalent for a DSSD). Each type can be applied to the DSSDs and CsI detectors. Fig. 4.16 and 4.17 show a charge sensitive preamplifier of the 4 GeV type, as was used in experiment. Table 4.3 summarizes the specifications of the LYCCA preamplifiers.

Type	CSP_2007_MeV or CSP_2007_GeV
Channels	32
Input	Positive and negative charge pulses
Connectors	IDC 68 (Half Pitch 68) Male for 0.25mm Ribbon Cable
Dynamic range	200 MeV or 5 GeV (depending on type)
Gain	x1 or x3
Rise time (gain x1)	18 ns (with detector capacity 10 pF)
Rise time (gain x3)	29 ns (with detector capacity 10 pF)
P/Z cancellation	Factory adjustable
Noise	5 keV + 0.05 eV/pF
Pulser Input	Any polarity
Output	Differential output signal
Output amplitude	± 1 V

Table 4.3: Specifications of LYCCA preamplifiers.

The output signal of the preamplifiers is coupled to analog shapers/amplifiers. The types used are Mesytec MSCF-16 and STM16+ [81]. The energy and time signals are then digitized by analog-to-digital-converters) and time-to-digital-converters (Caen Type 785 and Type 767 [82], cf. sec. 3.6).

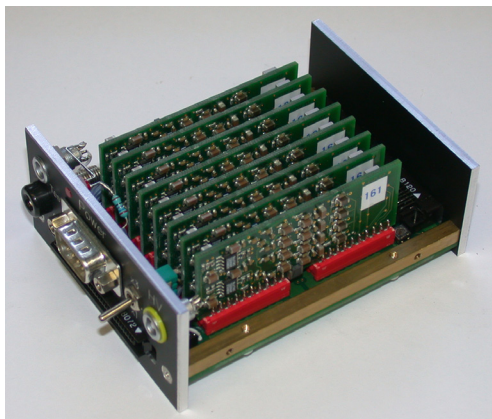


Figure 4.16: Charge sensitive preamplifier prototype.

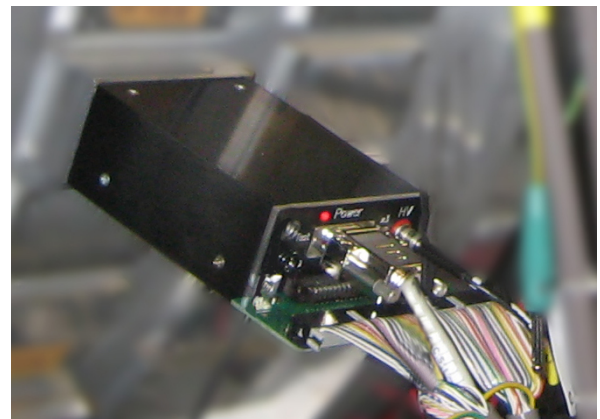


Figure 4.17: Final version of the charge sensitive preamplifier (4 GeV type) mounted on the LYCCA chamber.

4.3 Test results

4.3.1 Detector tests with α -sources

First basic tests of the DSSDs were done with α -sources to determine the energy resolution and to check the routing of the signals through the different stages of amplification and digitizing. For these tests the high-gain preamplifier (200 MeV active range) had to be used. With the available preamplifiers the CsI scintillators could not be properly checked, because the converted energy was too low. Fig. 4.18 to 4.22 shows various plots and pictures from the off-beam tests.

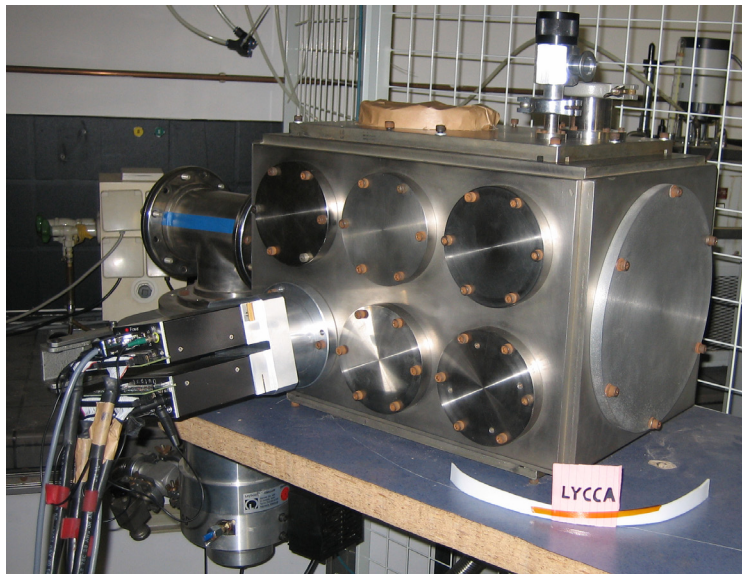


Figure 4.18: LYCCA test chamber for off-beam-tests.

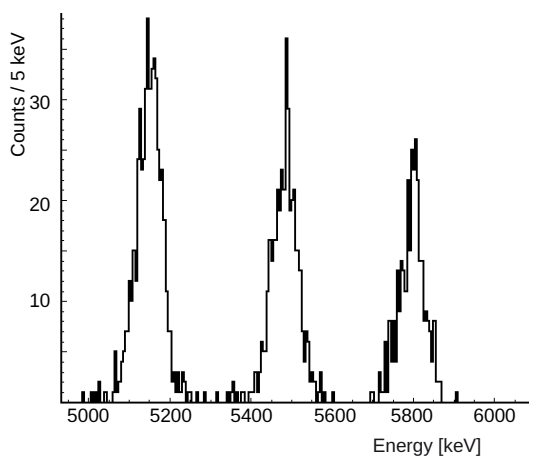


Figure 4.19: Energy spectrum of a DSSD strip with a triple- α -source ($\frac{\Delta E}{E} \sim 1.0\%$).

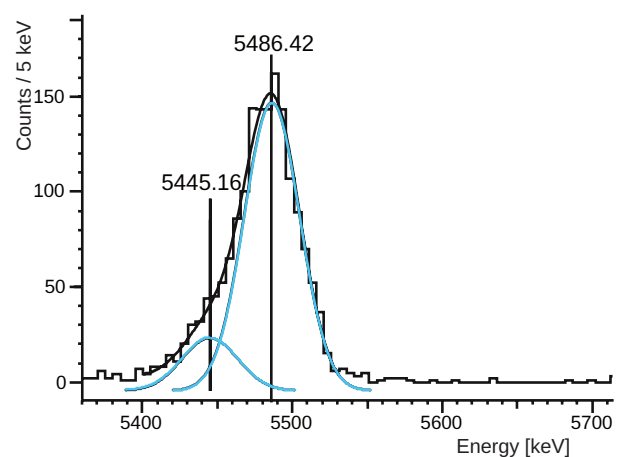


Figure 4.20: Decomposition of an α -transition. An energy resolution $\lesssim 45$ keV FWHM $\sim 0.8\%$ was achieved.

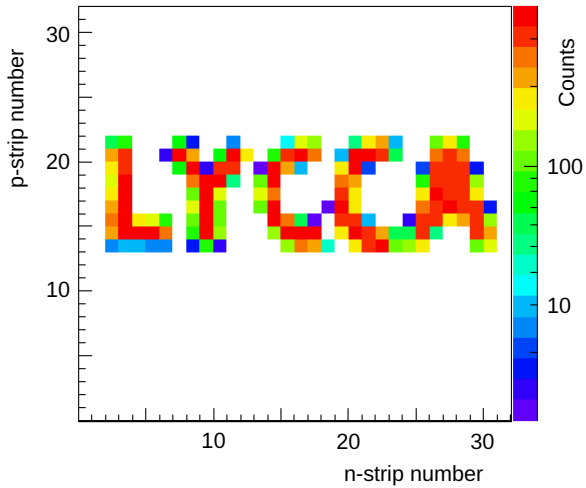


Figure 4.21: Position plot, measured with an α -source in front of a mask (cf. fig. 4.22).

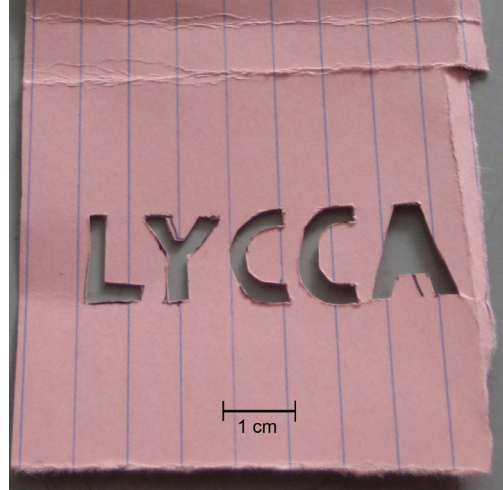


Figure 4.22: Mask for signal allocation check.

The results from a source test of a DSSD are summarized in table 4.4. The α -source was located on both sides to determine the individual resolutions. If the source was not located in front of the tested side, the resolution was approximately 0.1 % worse. This is caused by the stopping of the α -particles close to the surface and thus the long drift distance of the electrons / holes if the source was on the opposite side.

Strip	P-side $\frac{\Delta E}{E}$ [%]	N-side $\frac{\Delta E}{E}$ [%]	Strip	P-side $\frac{\Delta E}{E}$ [%]	N-side $\frac{\Delta E}{E}$ [%]
0	0.94	1.02	16	1.00	0.96
1	1.00	0.98	17	0.99	0.93
2	0.98	0.98	18	0.98	0.99
3	1.03	1.01	19	1.01	0.90
4	1.00	1.04	20	0.96	0.97
5	0.98	0.99	21	0.99	1.01
6	0.96	0.99	22	1.00	1.10
7	0.98	0.96	23	1.02	1.11
8	0.98	0.95	24	0.97	1.04
9	1.00	1.01	25	1.01	0.93
10	1.02	0.99	26	0.99	1.08
11	0.98	1.01	27	1.02	0.97
12	1.00	0.97	28	1.00	1.15
13	0.98	0.93	29	1.02	0.90
14	1.01	0.98	30	0.94	1.02
15	1.00	0.98	31	0.91	1.10

Table 4.4: Resolutions of the first LYCCA DSSD obtained with α -source. The source was in front of each tested side.

The energy resolution was determined on the following conditions:

- All tested DSSD strips provide an energy resolution is in the range of 0.9 – 1.02% for the p-side and 0.9 – 1.15% for the n-side.
- All other tested DSSDs show a similar performance.
- If the α -transition is decomposed in the transition to the daughter nucleus' ground state and the first excited state and fit simultaneously, the resolution improves to $\sim 0.8\%$ for both sides (cf. fig. 4.20).

The final conclusion of the off-beam tests (which were done for each individual DSSD) were that all tested DSSDs worked properly and could be used in experiments. The CsI scintillators could no be tested with sources, because the converted energy was too low to be read out with LYCCA electronics.

4.3.2 In-beam test at the Cologne tandem accelerator

To test the correlation between the DSSD and the CsI scintillators, particles that can penetrate the DSSD are needed. This was achieved by using 10 MeV protons which were provided by the Cologne FN Tandem accelerator. A $\Delta E - E$ module was placed in a scattering chamber to cover the scattering angle from approximately 37° to 52° with respect to the un-scattered beam (cf. fig. 4.23). The protons were scattered at a $0.2 \frac{mg}{cm^2} {}^{197}\text{Au}$ target.

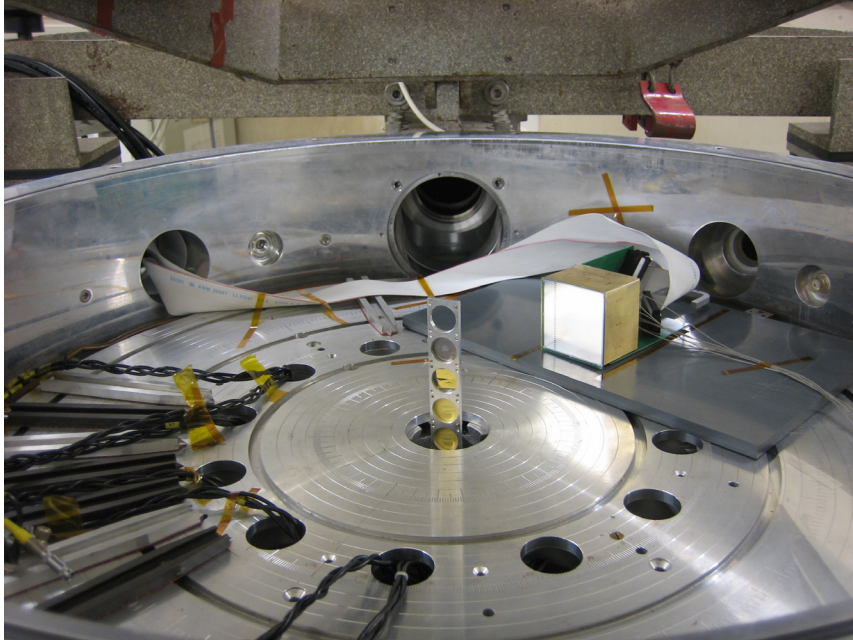


Figure 4.23: $\Delta E - E$ module during the first in-beam test at the Cologne Tandem accelerator. The beam enters from below.

With this setup, two features were identified. Firstly, the energy loss signal (detected by the DSSD) and the proton's rest energy (detected by the CsI scintillator) is detected simultaneously. Secondly, the angular dependence of the Rutherford scattering cross section can be reproduced.

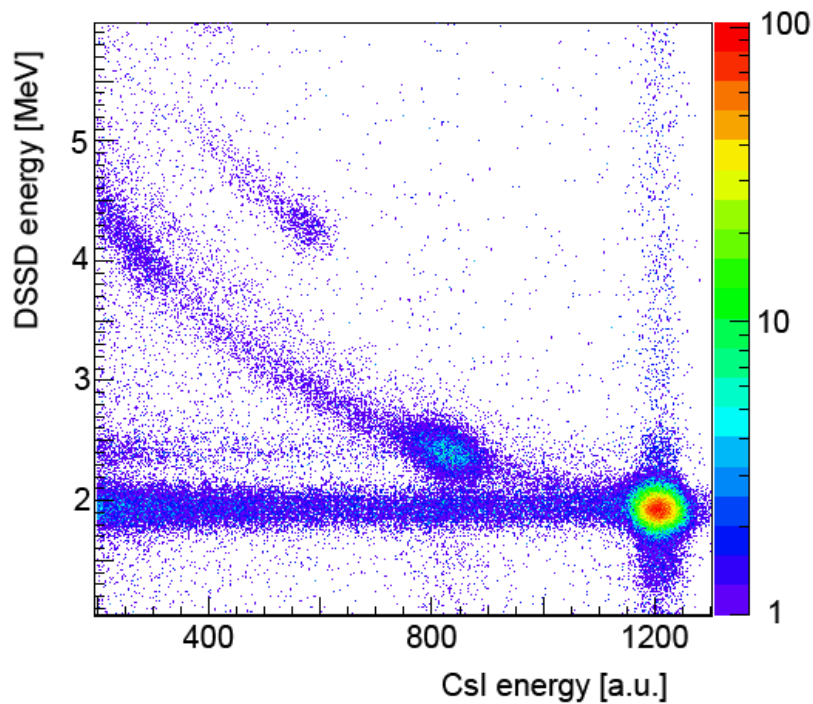


Figure 4.24: LYCCA's first $\Delta E - E$ plot, details see text.

The first correlated DSSD and Csl data was also achieved with the proton beam. Fig. 4.24 shows the sum spectrum of all DSSD strips and Csl scintillators. The condition to record an event was an energy deposition of at least 500 keV in a DSSD strip. The spectrum shows a major accumulation that is caused by properly detected protons (1200 units \sim 8 MeV, 2 MeV). The band to the left is caused by noise in the Csl scintillators (no threshold for readout could be applied due to the low signal strength). The smaller accumulation (800 units, 2.5 MeV) is caused by energy loss of the protons in an additional layer of matter.

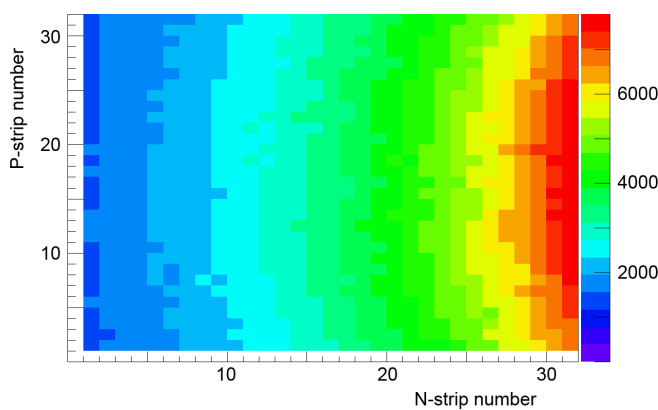


Figure 4.25: 2d distribution of hit DSSD pixels where $\vartheta \approx 37^\circ + (n\text{-strip number}) \cdot 0.5^\circ$.

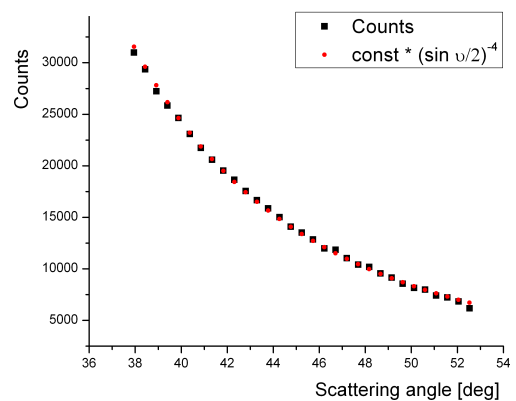


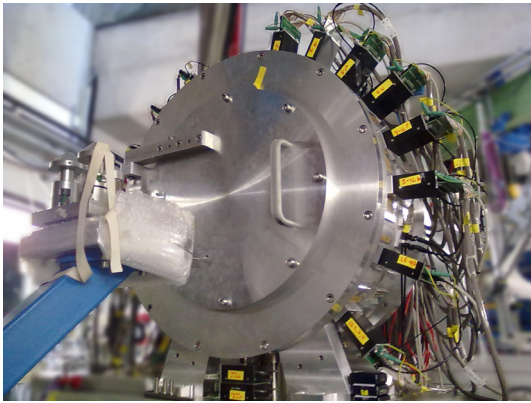
Figure 4.26: Partial projection on the x-axis. See text for details.

Fig. 4.25 shows the position plot of the scattered protons. Fig 4.26 illustrates the projection of the four central, horizontal strips onto the x-axis and the strip number has been converted into the scattering angle, ϑ . The number of counts per $\Delta\vartheta$ is proportional to the probability for

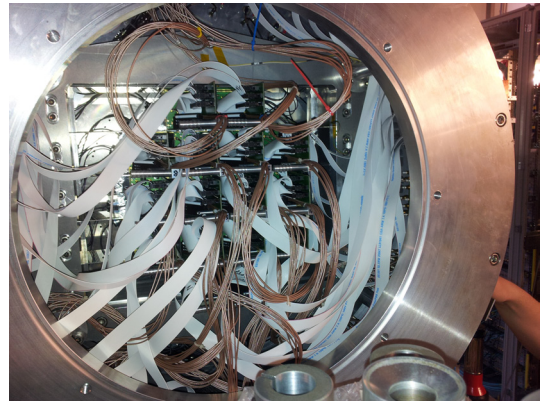
elastic scattering and thus to the differential Rutherford cross section. The data points show very good agreement with the well known $\sin\left(\frac{\vartheta}{2}\right)^{-4}$ dependency of Rutherford scattering.

4.3.3 Commissioning and experiments at the GSI/FRS facility

Illustrated in fig 4.27a is the LYCCA chamber with installed preamplifiers as was used for the first experimental campaign in 2010/11, whereas fig. 4.27b illustrates the future LYCCA upgrade for the 2012 PreSpec-AGATA campaign where 16 detector modules are installed.



(a) Closed chamber with installed Preamplifiers.



(b) Rear view of the opened chamber with installed detector modules.

Figure 4.27: LYCCA chamber with installed detector modules as used for the first experimental campaign.

In 2010/11 LYCCA was tested for the first time with ions at the typical energies used at GSI for radioactive ion beam experiments (~ 100 MeV/u). Fig. 4.28 shows energy spectra of a DSSD strip and a CsI scintillator.

The energy resolutions of detector module 6 are shown in fig. 4.29. The energy resolution is defined as:

$$R = \frac{\Delta(\Delta E)}{\Delta E} \text{ (for DSSDs) and } R = \frac{\Delta E}{E} \text{ (for CsI).}$$

Here $\Delta(x)$ represents the FWHM width of the energy loss signal (ΔE) or of the rest energy signal (E). To separate the effects of the beam's energy spread and the intrinsic detector resolution, a cut on the beam velocity ($0.502 < \beta < 0.503 \rightarrow \Delta E = 0.7$ MeV) is applied using quantities measured with the LYCCA time-of-flight detectors (cf. sec. 4.1).

The average values of energy resolution for the DSSDs and CsI scintillators used are summarized in tables 4.5 and 4.6. The resolution of the DSSDs is determined using only the six central detectors due to limited statistics in the outer detector modules (see layout in fig. 4.14).

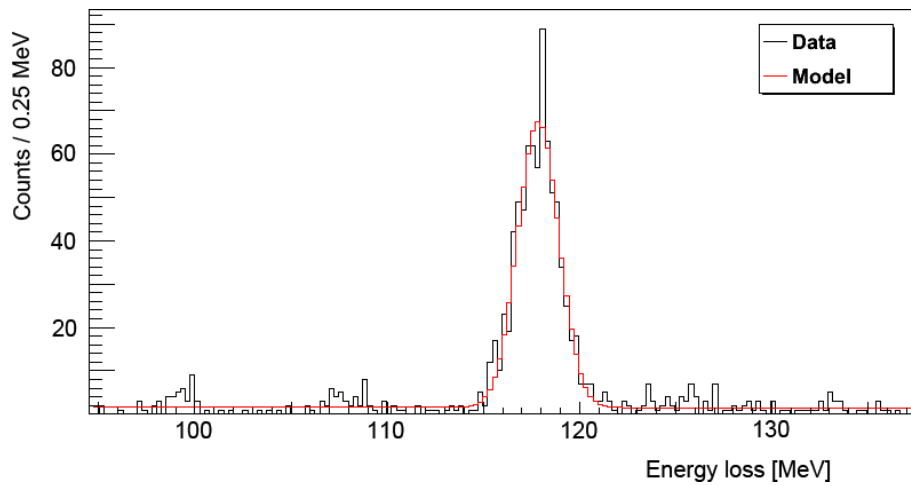
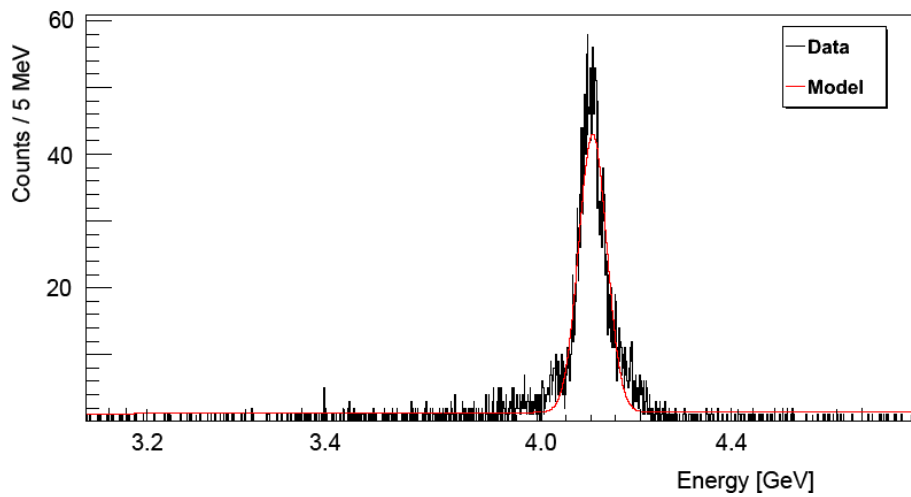
(a) P-strip number 13. $R = 2.2(1)$.(b) CsI crystal number 5. $R = 1.5(1)$.

Figure 4.28: Energy spectra of detector module 6. Fit with Gaussian function.

DSSD number	P-side resolution [%]	N-side resolution [%]
2	2.48 (24)	2.39 (13)
3	2.76 (21)	2.64 (36)
6	2.25 (18)	2.21 (14)
7	2.57 (16)	2.48 (17)
10	2.56 (34)	2.70 (16)
11	3.76 (52)	3.62 (40)
Average	2.73 (28)	2.51 (23)

Table 4.5: Average energy resolutions of the central DSSDs. The average value from the 32 strips is given.

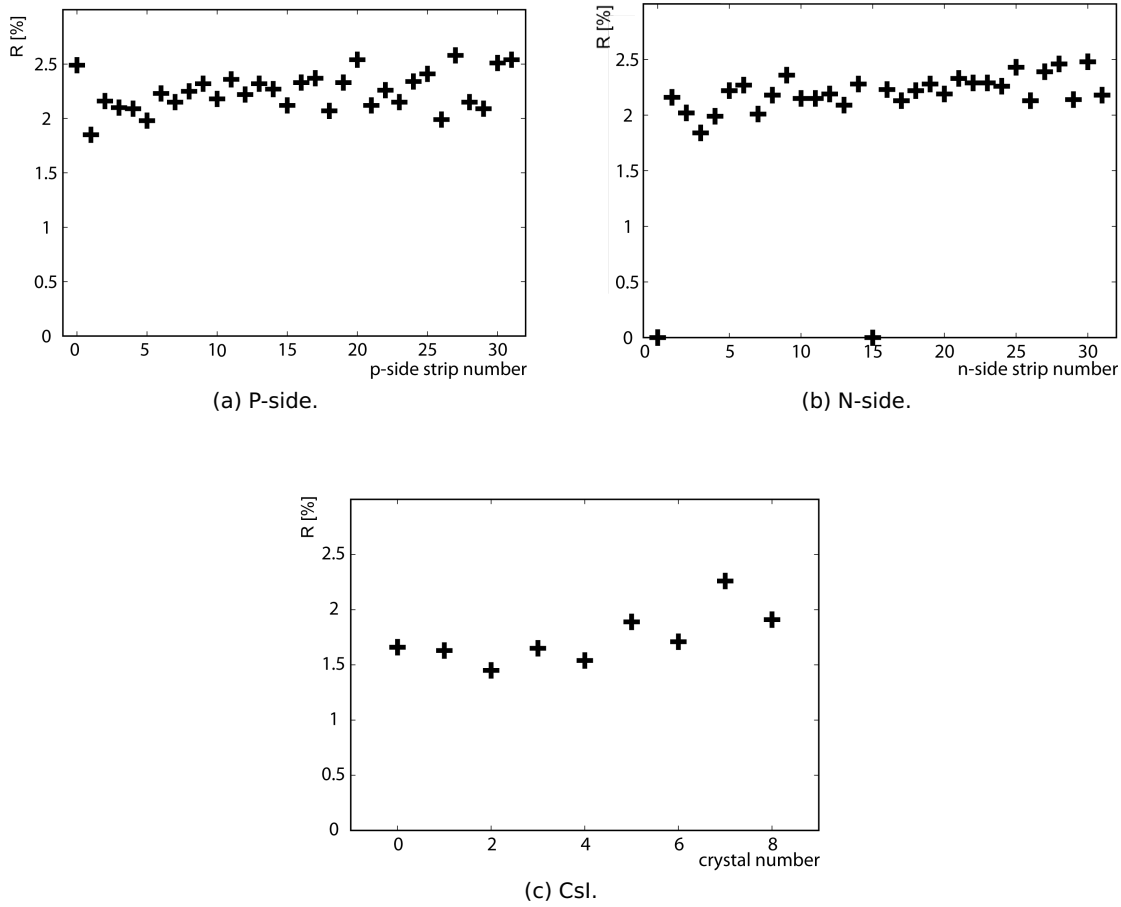


Figure 4.29: Energy resolutions of LYCCA module 6 determined for experiment S377. Incoming: ^{36}Ar ($0.502 < \beta < 0.503$) ~ 120 MeV/u. The measured energy loss in the DSSD is approximately 118 MeV, the energy deposition in the CsI scintillators is approximately 4.1 GeV.

CsI number	Resolution [%]	CsI number	Resolution [%]
1	3,00 0,65	7	2.00 (21)
2	1,68 0,31	8	1.84 (37)
3	1,72 (20)	9	1.96 (09)
4	1.87 (43)	10	2.41 (29)
5	2.06 (36)	11	2.09 (25)
6	1.75 (24)	12	2.15 (29)

Table 4.6: Average energy resolutions of the CsI scintillators. The average value from the nine individual crystals is given.

LYCCA has been commissioned in-beam and the resolutions of the detectors have been determined. These values can not be directly compared to the specifications stated in the technical design report [53] due to energy spread of the beam. During this experimental campaign, 380 out of the 384 DSSD strips and 106 out of the 108 CsI scintillators were functional. With an operational detector readiness of more than 98 %, LYCCA can be addressed as fully operational.

LYCCA in beam calibration

LYCCA is calibrated with the primary heavy ion beam. The energy deposition at the different detectors is varied by different amounts of degrader material in the FRS. Three different FRS settings have been used (cf. tab. 3.2 and 4.7) to generate three calibration points for each DSSD strip and CsI scintillator. The peak in each energy spectrum was fitted (as shown in fig. 4.28). Fig. 4.30 shows the energy plot of all DSSD strips and the plot of the fitted functions for one DSSD calibration point.

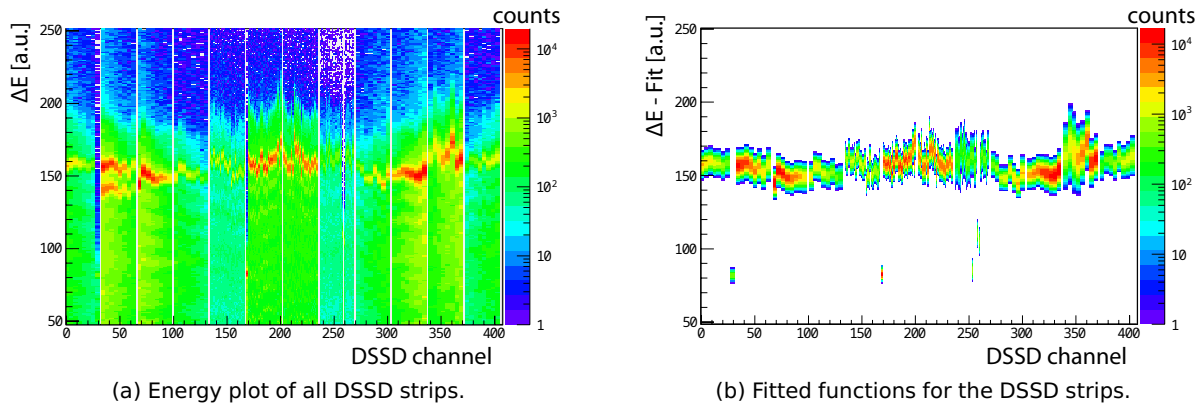


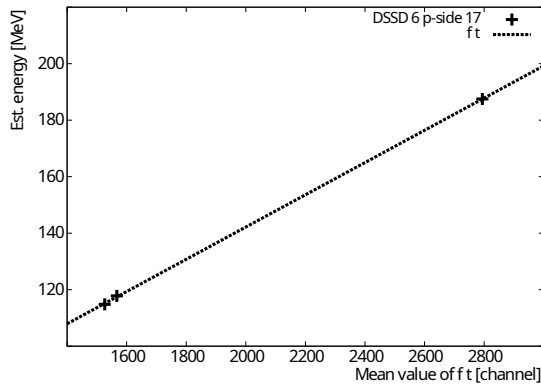
Figure 4.30: Plots for LYCCA DSSD calibration.

The estimated energy depositions of the ions in DSSDs and CsI scintillators for the settings that were used to calibrate LYCCA are shown in table 4.7.

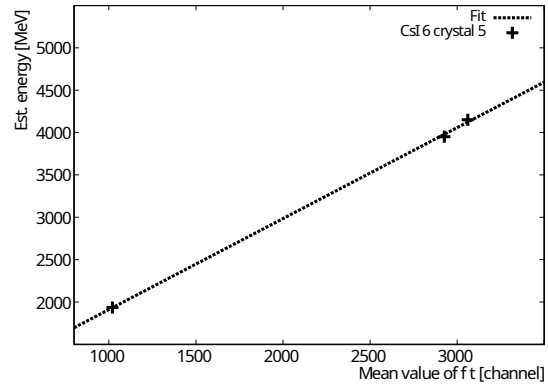
Setting	ΔE @ DSSD wall	E @ CsI
"Prime"	119 MeV	4.093 GeV
"Ar-ht"	115 MeV	3.949 GeV
"Ar-cal"	190 MeV	1.924 GeV

Table 4.7: Energy deposition at LYCCA detectors used for calibration. Calculated with Lise++.

After the measurement of calibration points, the calibration function for each detector channel can be generated by fitting a linear function to the calibration data. Fig. 4.31 shows this exemplary for a DSSD strip and a CsI crystal.



(a) Calibration function for strip no. 17 (p-side) of DSSD 6.



(b) Calibration function for the fifth CsI crystal of detector module 6.

Figure 4.31: Calibration functions for a DSSD strip and a CsI scintillator.

4.3.4 In-beam tracking and particle identification

4.3.4.1 Determination of the proton number Z

LYCCA's combined ΔE and E measurement allows the determination of the charge of the incoming ions. Usually the identification of an ion can be performed using only the ΔE and E signal. The energy loss in a thin detector and the total energy of the ion in a thick detector provides the necessary information. The energy loss of a charged ion, moving at relativistic speed in matter is given by the Bethe-Bloch-Equation (similar as the FRS Z determination, [47, p. 121]):

$$-\frac{dE}{dx} = \frac{4\pi}{m_e c^2} \cdot \frac{\bar{Z} Z^2 N_a \rho}{A \beta^2} \cdot \left(\frac{e^2}{4\pi\epsilon_0} \right)^2 \cdot \left[\ln \left(\frac{2m_e c^2 \beta^2}{I \cdot (1 - \beta^2)} \right) - \beta^2 \right], \quad (4.1)$$

where E is the energy of the ion, x is the distance traveled by the ion, Z is the charge of the ion, in full stripped case the proton number, m_e is the rest mass of an electron, β is the velocity of the ion in units of the speed of light, \bar{Z} , A , ρ , I are the proton number, the mass number, the density and the mean excitation potential of the absorber material and N_a is the Avogadro number.

The representation of energy loss in matter, $\Delta E = \int -\frac{dE}{dx} dx$, along a path, Δx , can be described as follows:

$$Z = \sqrt{\Delta E} \cdot f(\beta) = \sqrt{\Delta E} \cdot \tilde{f}(\gamma).$$

As the relativistic kinetic energy is a function of the relativistic Lorentz factor γ

$$E_{kin} = m_0 c^2 \cdot (\gamma - 1) = \tilde{f}(\gamma)$$

(m_0 : rest mass of the ion), the Z of the ion can be also expressed as a function of energy loss and total energy:

$$Z = \sqrt{\Delta E} \cdot \check{f}(E_{kin}).$$

Thus, plotting ΔE vs. E allows the identification of the charge of the ions. A typical energy resolution of 1-2 % for both the energy loss and total kinetic energy measurement allows for a relative Z resolution of $\frac{\Delta Z}{Z} = 0.15 \dots 0.6$ which is sufficient to discriminate between neighbouring proton numbers. Fig. 4.32 shows the FRS identification of the incoming ^{84}Kr beam and LYCCA's Z -identification plot ($\sqrt{\Delta E}$ vs E). In both plots, the main contribution is the primary Kr beam.

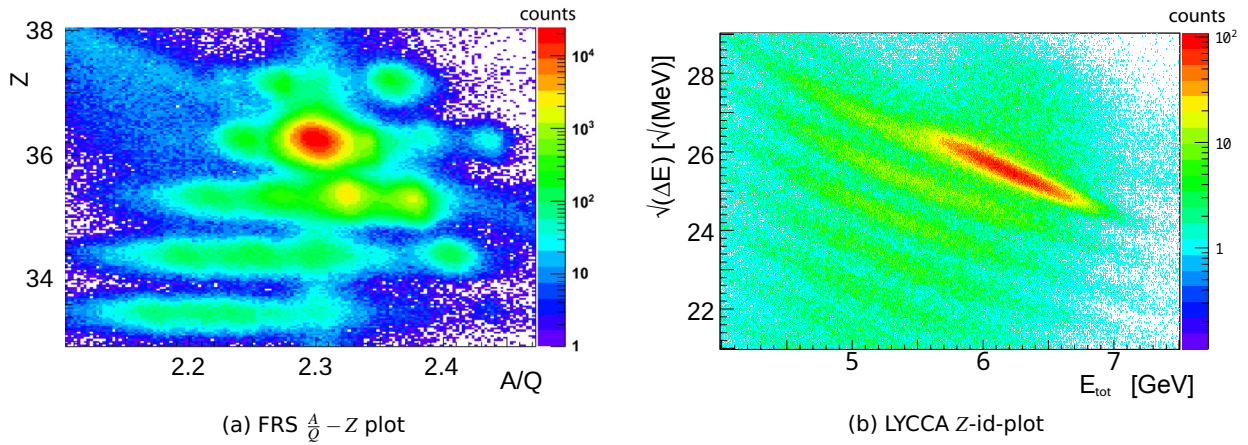


Figure 4.32: Identification plots from S369 the experiment (^{84}Kr fission beam)

Z -identification can be achieved with the $\sqrt{\Delta E} - E$ correlation without further corrections. To determine the Z resolving power, a velocity (β) correction was applied (details in ref. [50]). Fig. 4.33 shows the β -corrected Z -identification plot and the fit to determine the Z resolution of LYCCA.

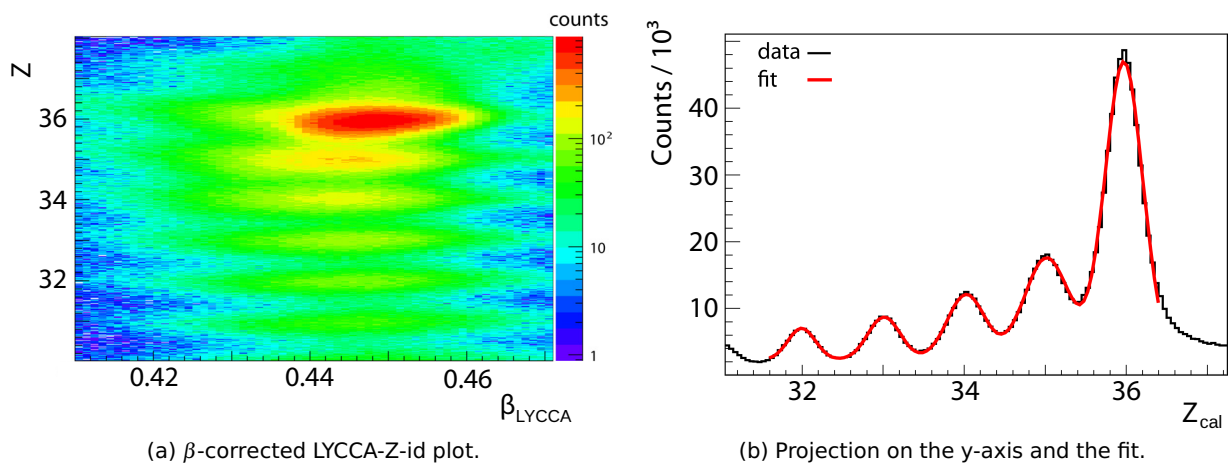


Figure 4.33: β -corrected Z -identification plots

The Z resolution (determined from the fit in fig. 4.33) is $\frac{\Delta Z}{Z} = 0.6(1)$ FWHM for Kr isotopes ($Z = 36$). Even in the one dimensional picture, neighbouring elements can be separated. However, separation in a 2d plot remains superior (cf. fig. 4.32).

4.3.4.2 Determination of the nuclear mass A

Mass identification with LYCCA is achieved by combining the total kinetic energy, $E_{kin,tot}$, and the velocity, β , of the ion. The nuclear mass number, A , is proportional to the mass, m , of the ion. As the ion travels at relativistic speeds (typically $\beta \sim 0.5$), the relativistic energy-momentum correlation must be applied ([46, p. 73]):

$$E_{kin,tot} = m\gamma c^2 - mc^2.$$

Here, $E_{kin,tot}$ is the total kinetic energy carried by an ion directly after the secondary target. The total kinetic energy is the sum of the energy depositions at both DSSD stages (ΔE_{target} and ΔE_{wall}), the plastic scintillator, other insensitive material and the CsI scintillators (E_{kin}). The typical energy depositions of an ion are 100 MeV in each DSSD, 40 MeV in the plastic detector and 4 GeV in the CsI scintillators. For identification, the last stage of ΔE detectors are used where $E_{kin,tot}$ is given by

$$E_{kin,tot} = \Delta E_{wall} + E_{kin},$$

which is approximately 97 % of the original total kinetic energy after the secondary target. The relativistic Lorentz factor, $\gamma = (1 - \beta^2)^{-\frac{1}{2}}$, must also be determined. By measuring the time-of-flight of the ions over the fixed distance of 3.4 meter the β value can be deduced. Ions of different masses are separated by plotting $E_{kin,tot}$ vs. γ . A typical beam composition is shown in fig. 4.32a.

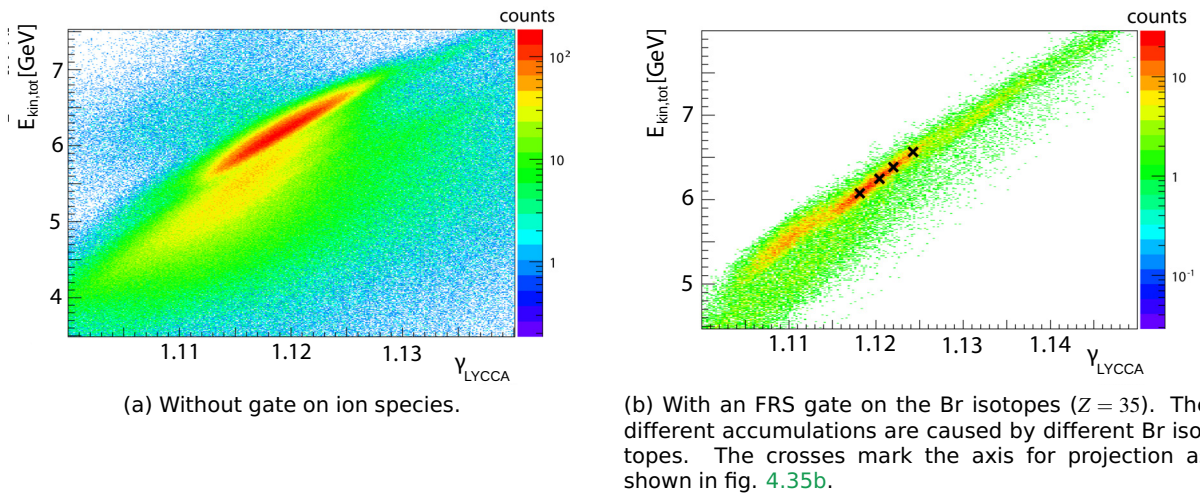
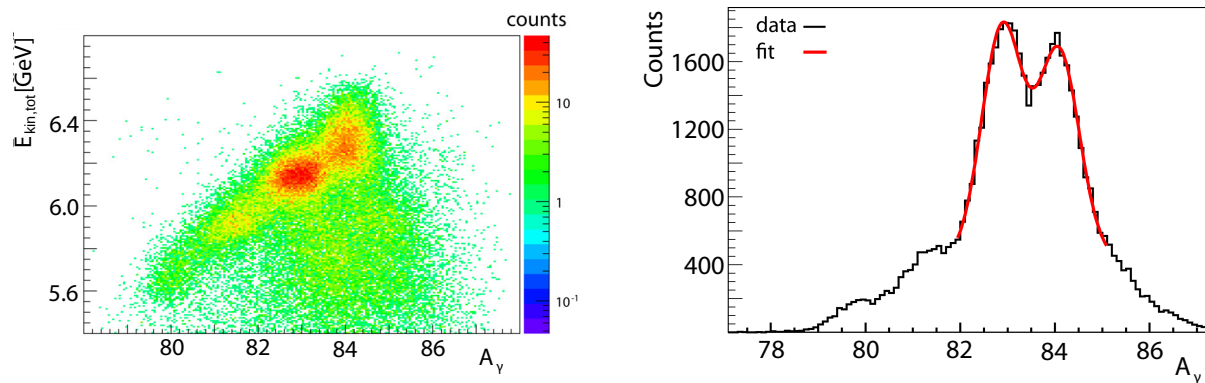


Figure 4.34: Mass identification plots showing the total kinetic energy $E_{kin,tot}$ vs. relativistic factor γ .

Prior to mass identification, an ion specie is chosen. In this data-set, different isotopes of bromine (according to the beam composition shown in fig. 4.32) are identified by the FRS. The main components are $^{83,84}\text{Br}$. These can also be seen in the mass identification plot shown in fig. 4.34b; one in the region of the marks and one shifted to lower energies and lower values of γ .



(a) Masses (calculated from LYCCA measurement) vs corrected $E_{kin,tot}$.

(b) Projection on the mass-axis and the fit.

Figure 4.35: Mass identification plots.

After the velocity corrections (described in detail in [50]) the corrected total kinetic energy of the ions is plotted vs. the calculated mass and a 2d mass gate can be applied (cf. fig. 4.35a). By projecting on the mass axis and fitting, the mass resolution can be determined (cf. fig. 4.35b). The resolution in the mass region $A \approx 80$ is calculated as $\frac{\Delta A}{A} = 1,0(1)$ FWHM (^{84}Br). In another experiment in the $A \approx 100$ region, LYCCA shows a quite similar performance with a mass resolution of $\frac{\Delta A}{A} = 1,1(1)$ FWHM (^{104}Sn).

4.3.4.3 Ion tracking

LYCCA uses the crossed DSSD strip pattern at the target and at the wall locations for two position measurements to track ions that exit the secondary target and to calculate the orientation of the momentum vector of the ions. This information is needed for several reasons:

- Exact position information is needed for optimal time-of-flight measurement (cf. subsection 4.2.4).
- The angle between a detected γ -ray and the trajectory of an ion is crucial for the Doppler correction.
- The scattering angle at the secondary target is determined. Additionally tracking information from the FRS relating to the incoming ion before the target is used (cf. sec. 3.3.2).

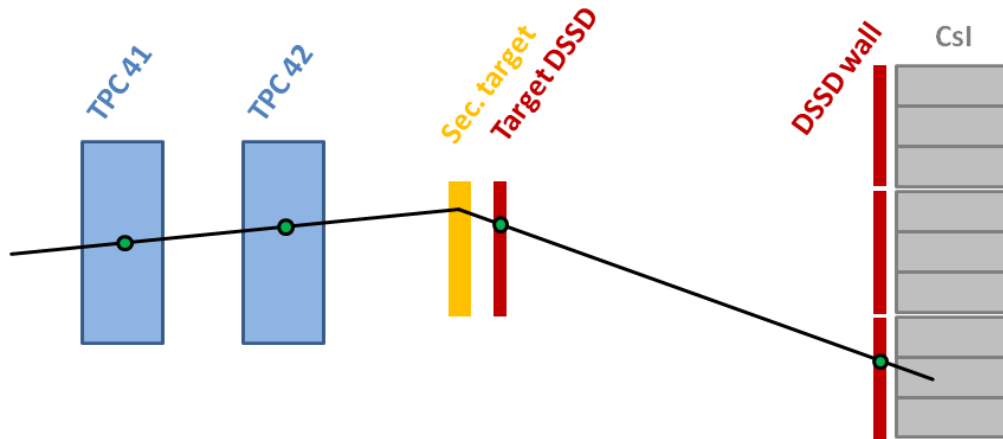
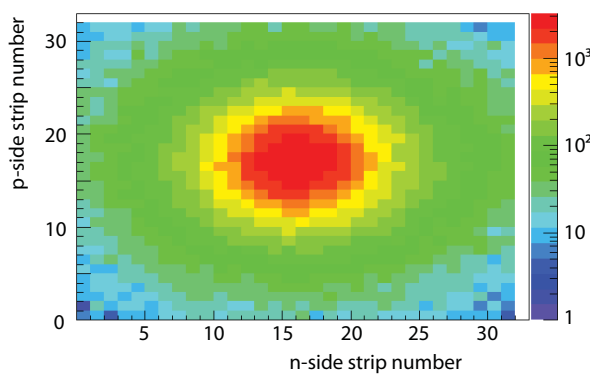
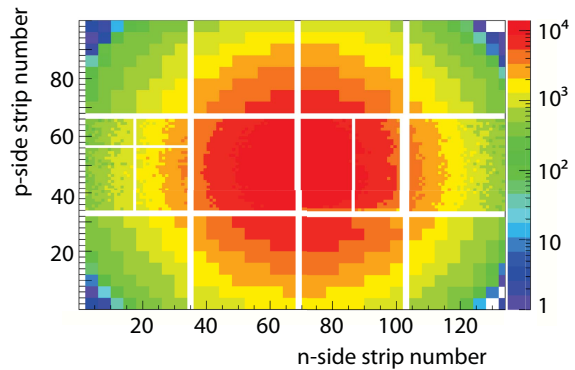


Figure 4.36: Tracking along the path of an ion is performed with four position sensitive detectors. Dots indicate the interaction points at the detectors.

Fig. 4.36 shows the setup of the tracking detectors and the flight path of an ion. Fig. 4.37 shows the hit pattern of the target and wall DSSDs from the ^{88}Kr experiment.



(a) Hit pattern of the target DSSD.



(b) Hit pattern of the wall DSSDs (lines mark borders between detectors).

Figure 4.37: Hit pattern of the LYCCA DSSDs taken from experimental data of the fragmentation beam.

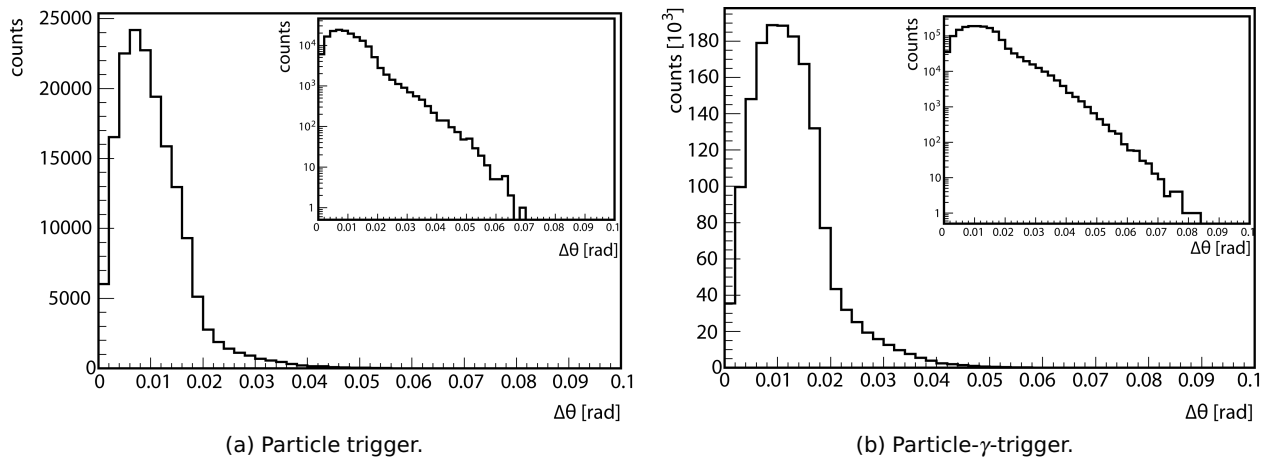


Figure 4.38: Distribution of the change in scattering angle dependent on trigger type which is determined from FRS- and LYCCA-tracking. Taken from [50]

Fig. 4.38 shows distributions of scattering angles for two different reaction types. If a particle- γ -coincidence was detected (fig. 4.38b), a reaction took place and the change in scattering angle, $\Delta\vartheta$, is larger than the case where no reaction was requested (fig. 4.38a). Thus, a correlation between the reaction type and $\Delta\vartheta$ determined by the FRS and LYCCA tracking was observed.

4.4 Conclusions

Within the PreSpec campaign, all LYCCA-components were put into operation for the first time. The development and testing of LYCCA is a major part of the work discussed in this thesis. The detector evolved from the design study, to the prototype and testing phase, to detector manufacturing and final use in experiments at GSI. All specifications defined in the technical design report [53] have been achieved. In chapter 5, the importance of the measured LYCCA quantities on the capability of handling the beam correlated background in a fast-beam experiment is shown.

Chapter 5

Data analysis of experiment S377

The aim of experiment S377 is to determine the reduced transition strengths of the first two excited states of ^{33}Ar . For this a radioactive beam of ^{33}Ar is produced by fragmentation of a ^{36}Ar beam. The stable beam with an energy of 450 MeV/u is shot on a production target of 4 g/cm² ^9Be . From the various fragmentation products ^{33}Ar is selected, tracked, identified and guided to the secondary target by the FRS. The secondary target, where the Coulomb excitation takes place, consists of 0.386 g/cm² ^{197}Au and is located in the center of the γ -ray detector array. The ions are tracked and identified by LYCCA after the secondary target. To determine the total efficiency of the system the known transition strength of ^{36}Ar was used as a reference.

The analysis of experiment S377 is based on an event-by-event ion identification where tracking is performed before and after the secondary target with the FRS and the LYCCA detector array. The experiment is performed at relativistic energies and requires unambiguous reaction channel identification after the secondary target performed with LYCCA. The relativistic projectile energy is much higher than the Coulomb barrier and unwanted nuclear reactions can occur that need to be rejected for the final result. The following chapter describes the data analysis which is based on a sequence of analysis conditions or 'gates' deduced from a combination of various measured detector signals. The impact of different gates on the particle and time spectra (named in the following as 'particle gates' and 'time gates') and on the resulting γ -spectra has been studied carefully. The analysis efficiency is a major concern in experiments of this type. Typically, the gates are applied subsequently to an already previously gated data set and the number of remaining events (reflected by the integral of the spectrum) is reduced with each additional gate. After introducing the various types of analysis conditions, called gates or cuts, the sub-chapter 5.5.3 shows a comparison of different combinations of gates (for each type of cut, three or four gates were compared). All spectra shown in the following chapter are taken from the measurement with ^{36}Ar ions unless otherwise stated.

5.1 Detector observables

The following section summarizes the observables and the deduced quantities provided by the different FRS detectors and LYCCA (details given in subsection. 3.3.2.1 and 4.3.4). The listing is limited to quantities used in the following data analysis.

5.1.1 Particle information provided by FRS detectors

The FRS utilities various detectors to track and identify the ions that pass through. The used detectors are described in further detail in subsection. 3.3.2.1.

- Average velocity of the ions at second FRS stage β_{FRS} : deduced by time-of-flight measurement with Finger/SC21 and SC41.
- Trajectory of the ions through second FRS stage $\vec{x}(z)$: deduced by TPCs at S2 and S4.
- Mass to charge ratio $\frac{A}{Q}$: deduced by β_{FRS} , $\vec{x}(z)$ and magnetic rigidity $B\rho$ of dipole magnets.
- Atomic number Z : deduced from energy loss (ΔE) in MUSIC detectors and β_{FRS}

By the threefold position measurement with the different TPCs, the angles of the ions, relative to the central beam axis (ϑ_{FRS} , ϕ_{FRS}) are calculated. From the position at the last TPC and the angles, the flight path of the ions can be extrapolated onto the secondary target ($x_{tar,ex}$, $y_{tar,ex}$). With the full tracking information, flight-path corrections are applied for the β_{FRS} determination.

5.1.2 Particle information provided by LYCCA detectors

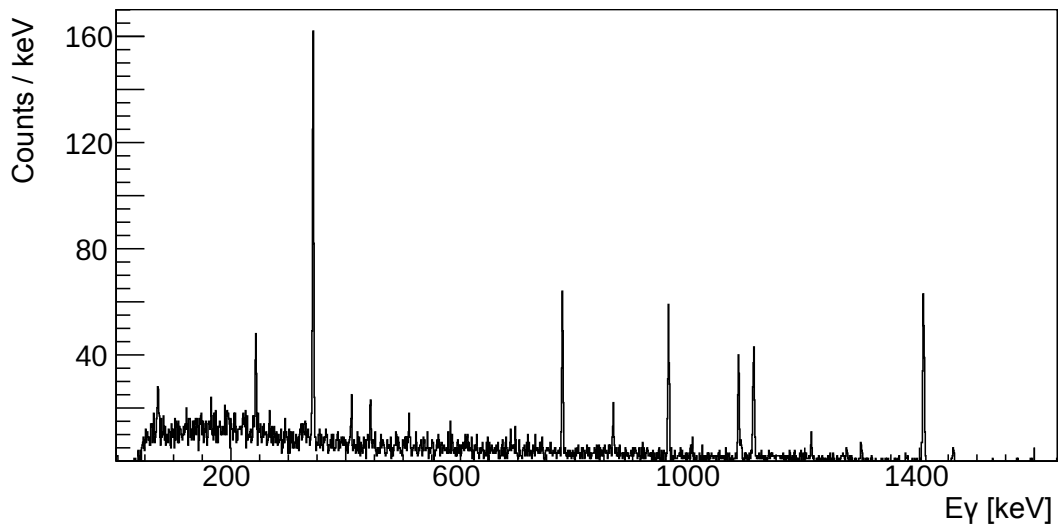
- Average velocity of the ions on LYCCA flight-path β_{LYCCA} : deduced by time-of-flight measurement with ToF-start and ToF-stop detector.
- Trajectory after the secondary target (ϑ_{LYCCA} , ϕ_{LYCCA}): calculated with the position information provided by the position measurement with target DSSD and the $\Delta E - E$ modules.
- Energy loss in target DSSD ΔE_{tar} (uncalibrated).
- Multiplicity of target DSSD signal M_{tar}
- Energy loss in DSSD wall ΔE_{wall} .
- Rest energy in CsI scintillators E .

The multiplicity of the target DSSD signal M_{tar} is determined from the number of the individual strips of the target DSSD that are hit. Here an energy condition is imposed. M_{tar} is the quantity of strips, that provide an energy signal that is larger than $\sim 3\%$ of the full range.

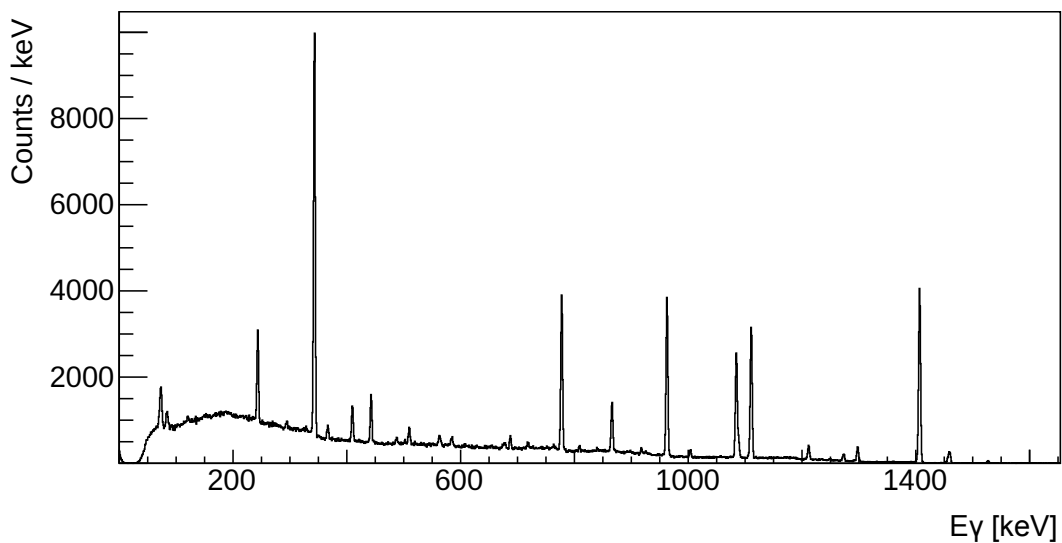
Two quantities are deduced from combination of LYCCA and FRS detectors. The target DSSD provides a timing signal T_{tar} . This is measured in reference to the timing signal of SC41. The angular change between the trajectories before and after the secondary target is called scattering angle θ .

5.1.3 γ -ray detectors

The main γ -ray detectors used in the discussed experiment are the Cluster detectors. Each Cluster detector contains seven independent large volume high-purity germanium crystals and 14 Clusters were operational during the experiment. Due to the coupling of digital and analog electronics, every crystal provides a digital energy signal (E_γ) and two types of time signals: high-precision analog time (T_{SR}) and a time signal based on the digital electronics (T_{DGF}). Both time signals are measured with respect to the time signal of the SC41 scintillator. For the Doppler correction, the angle between the germanium crystal and the flight path of the ion (ϑ_γ) is calculated from the position of the hit crystal. The Cluster detectors are calibrated with an ^{152}Eu source. Fig. 5.1 shows a spectrum of a single crystal as it is used for detector calibration and the summed spectrum of all EUROBALL detectors. The typical energy resolution of a Cluster detector is in the range of 2.5 to 3 keV FWHM for γ -rays of 1481 keV.



(a) Spectrum of a single EUROBALL crystal.



(b) Summed spectrum of all EUROBALL detectors.

Figure 5.1: γ -ray spectra of a ^{152}Eu source.

HECTOR (eight BaF₂ scintillators) provides a slow (E_{slow}) and a fast (E_{fast}) energy signal. The first signal is taken from the photomultiplier tube's anode and the second one from the first dynode. Furthermore, the time difference between the BaF signal and the SC41 (T_{HEC}) is measured.

5.2 Setting particle gates

Even though the $B\rho-\Delta E-B\rho$ -method applied to the selected secondary beam passing through the FRS is utilized, the beam may contain contaminants. Due to the 'unsafe' relativistic energies (larger than the Coulomb barrier), other reaction channels such as knockout or fragmentation may occur in addition to Coulomb excitation. By setting energy and time gates based on the measured signals in the detectors (see subsections 3.3.2.2 & 3.3.2.3), unwanted reaction channels can be identified and removed from the Coulomb excitation analysis. The following subsections describe the different analysis conditions applied to the various measured detector quantities in the order they appear along the flight path of an ion.

5.2.1 Secondary beam mass cut

The main FRS identification of the individual incoming ions is based on the knowledge of the magnetic rigidity, a time-of-flight measurement and the energy-loss signal of the ion in a gas-filled detector (cf. chapter 3.3.2). From this information, the proton number, Z , and the mass number, A , can be calculated. After calibration and correction for different trajectories, the mass-to-charge ratio $\frac{A}{Q}$ is plotted versus the charge Q . At these high energies (> 100 MeV/u), the ions are completely stripped and the plot is simply an $\frac{A}{Q} - Z$ plot.

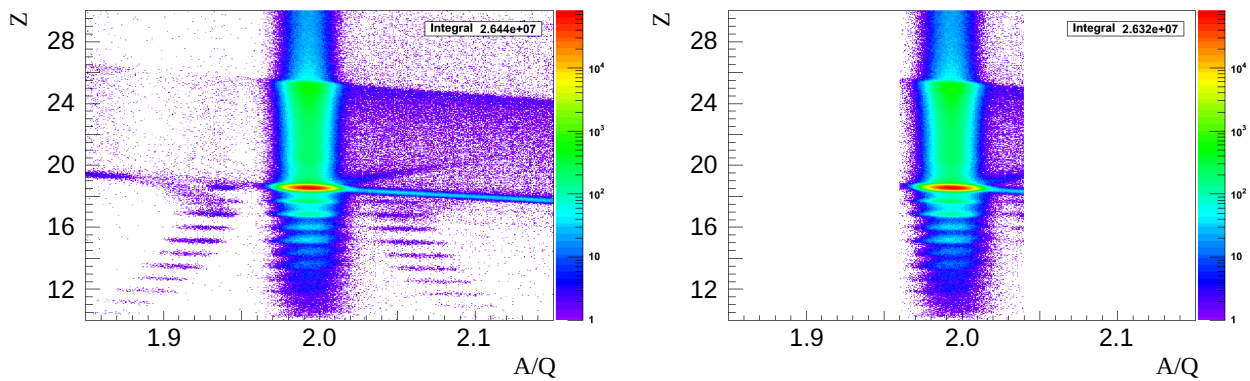


Figure 5.2: $\frac{A}{Q} - Z$ plots without a cut (left) and with a cut on $\frac{A}{Q}$ of ^{36}Ar ($1.96 < \frac{A}{Q} < 2.04$).

Fig. 5.2 shows the $\frac{A}{Q} - Z$ plot of the primary beam run. In the second plot, the chosen $\frac{A}{Q}$ gate is shown. No cut in Z has been applied due to malfunction / saturation of the MUSIC detector (cf. subsection 3.3.2.3) where a large number of events were identified with a Z abundantly higher than the primary beam. The incorrect identification is caused by pile-up effects. Based on the MUSIC detector alone, not all of the ions could be unambiguously identified. Nonetheless, due to the Z identification capabilities of LYCCA (cf. subsection 4.3.4.1), the ions can be identified and the events used in the analysis. As the Z determination fully relies on LYCCA, a cut on the

MUSIC-generated Z -distribution would not be helpful and is replaced by the LYCCA $\Delta E - E$ cut (shown in the subsequent subsection).

5.2.2 Z identification after the secondary target

Not all of the ions that pass the secondary target and are detected following the target have the same proton number. The two reasons for this is:

1. As described in subsection 3.4.2, the beam contains contaminants with a Z value different from the Z of the primary beam. These contaminants were not discarded by the FRS identification (cf. subsection 5.2.1).
2. Nuclear reactions (except Coulomb excitation) may take place within the secondary target. This changes the proton number in most cases.

For this reason, the LYCCA detector is used to gate on $Z = 18$ (argon). The LYCCA Z identification can be seen in the 2d-plot of the total kinetic energy (E deposited in the CsI and the wall DSSD) vs. the energy loss of an ion in the hit wall DSSD (ΔE).

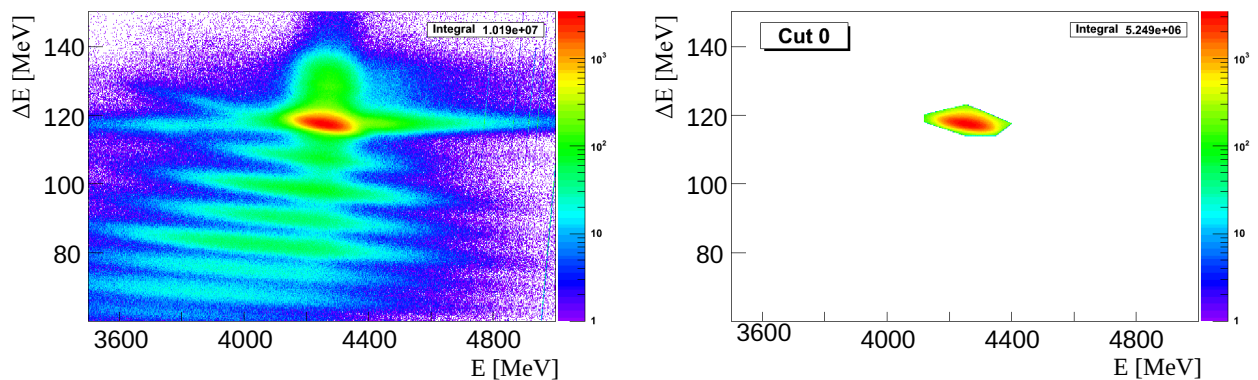


Figure 5.3: LYCCA $\Delta E - E$ plot without (left) and with the applied argon cut (right).

The major part of the 2d-spot in the full spectra is caused by the primary argon beam. This beam is an isotopically clean (>99%) ^{36}Ar beam. The FRS setting selects this isotope and has to be the main component. The so-called tertiary beam (the beam after passing the secondary target) consists of additional $Z < 18$ elements and the one-proton-pickup product potassium ($Z = 19$). From this group of chemical elements, argon is selected by a polygonal gate (see 5.3, right).

The selection using these analysis conditions is further improved by using correlations of all the particle detectors. The following subsections show the possibilities offered by the the FRS and LYCCA detectors to reduce the background in the γ -spectra. In section 5.5.3 these particle gates are varied to obtain the optimal γ -spectra.

5.2.3 $\Delta E_{\text{target}} - \Delta E_{\text{wall}}$ - gate

LYCCA provides two energy-loss measurements, the target DSSD and the wall DSSD (cf. fig. 5.4). These signals are strongly correlated providing that both detectors work properly and the

passing ion does not react in matter after the secondary target. Fig. 5.4 shows the correlation.

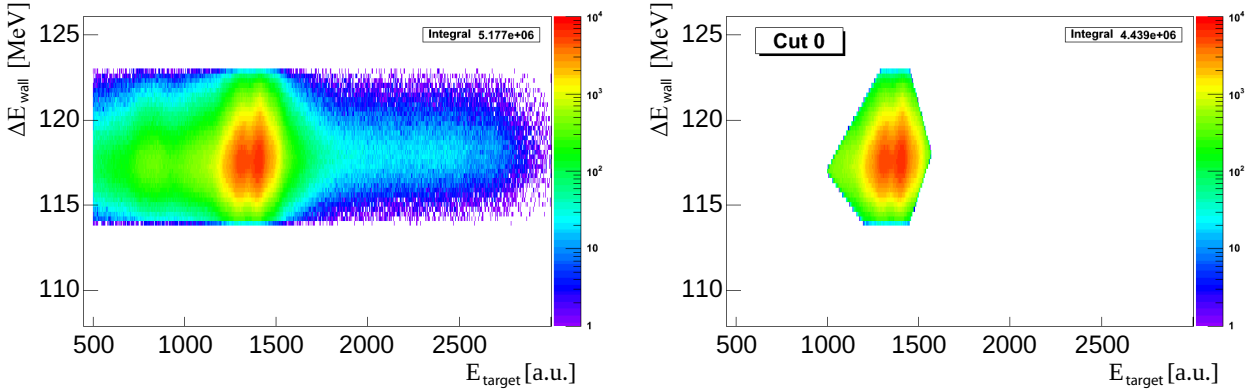


Figure 5.4: LYCCA $\Delta E - \Delta E$ plot without (left) and with the applied cut (right).

The double structure in the x-direction is caused by two slightly different amplifications for the 32 energy signals of the target DSSD. The sharp cut in the y-direction is caused by the $\Delta E - E$ argon cut (cf. fig. 5.3).

Fig. 5.4 shows that 85% of the events are inside of the central (strongly correlated) spot. The events outside the selected range belong to other reaction channels or where no proper energy loss was measured at the target DSSD position. For these reasons they are neglected. A complete detection at both DSSD positions is crucial for complete ion tracking after the secondary target.

5.2.4 $\beta_{FRS} - \beta_{LYCCA}$ - gate

Indispensable for γ -spectroscopy at relativistic energies ($\beta \sim 0.5$) is a precise Doppler correction which requires knowledge of the velocity vector of the emitting ion. The technique of choice for high precision velocity determination is a time-of-flight (ToF) measurement of the ions over a flight path with an accurately known length. The velocity of the ion is measured twice: firstly in the second half of the FRS (finger detector to S4 scintillator, cf. 3.3.2.2) and secondly with LYCCA's time-of-flight detectors (cf. 4.2.4). These two independently measured velocities are correlated if both measurements were successful (cf. fig. 5.5).

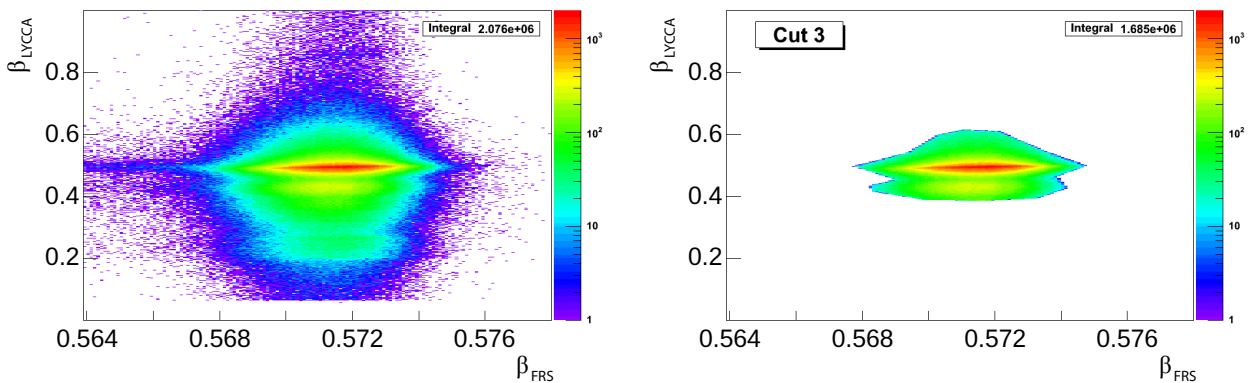


Figure 5.5: Velocity correlation plot without (left) and with the applied cut (right).

The reason for the double structure in the LYCCA time-of-flight measurement (y-axis) is likely to be the result of ions passing through additional matter such as the frame of the secondary target. In section 5.5.3, the possibility of using events from the lower spot is shown which are used to obtain the best γ -spectra.

5.2.5 $\beta_{LYCCA} - CsI$ - gate

Even though there is matter present in the time-of-flight path of LYCCA which includes the secondary target and the target DSSD, a clear correlation between the total kinetic energy and the velocity of the ions is expected. Events where either the TOF or energy measurement was corrupt, or where a reaction took place between the secondary target and the CsI detectors are rejected (cf. fig. 5.6).

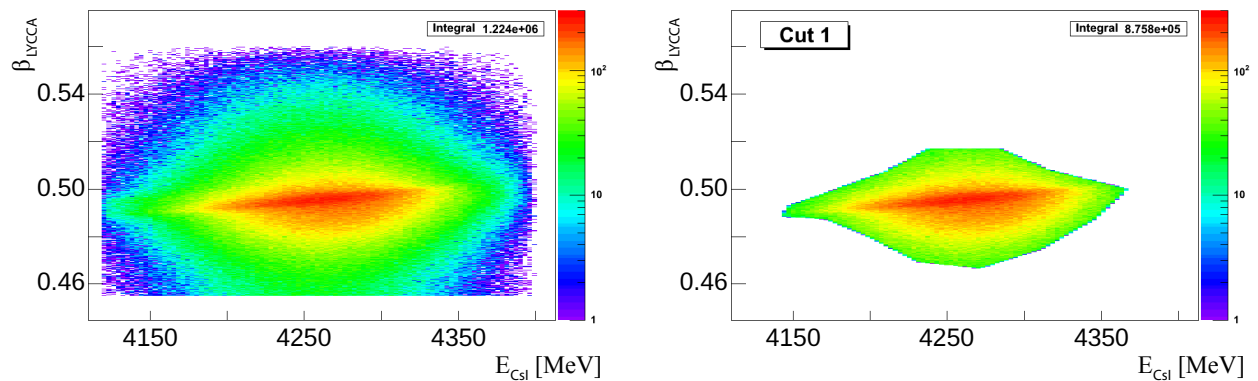


Figure 5.6: LYCCA $\beta - CsI$ plot without (left) and with the applied cut (right).

5.2.6 Target DSSD energy-time-correlation

The LYCCA TOF system works independently from the master timing reference supplied by the S4 scintillator (cf. Chapter 4.2.4) and therefore does not provide any information regarding the time with reference to the S4 scintillator signal. The time correlation (SC41 passing - target passing) is created with the time signal of the target DSSD (cf. subsection 4.2.1). Fig. 5.7 shows the time difference between passing SC41 and the target DSSD vs. the energy loss of an ion at the target DSSD.

The full plot (left) shows the beam pulse structure (830 ch \simeq 250 ns) of the primary beam which is caused by a 4 MHz high frequency oscillator used to flatten the beam intensity of the spill structure. Events belonging to a later (time is progressing backwards with respect to the channel number) beam pulse are neglected. In addition, the applied cut discards particles that do not have an energy loss at the target DSSD within a certain range. The rectangular analysis cut is shown on the right hand side of fig. 5.7.

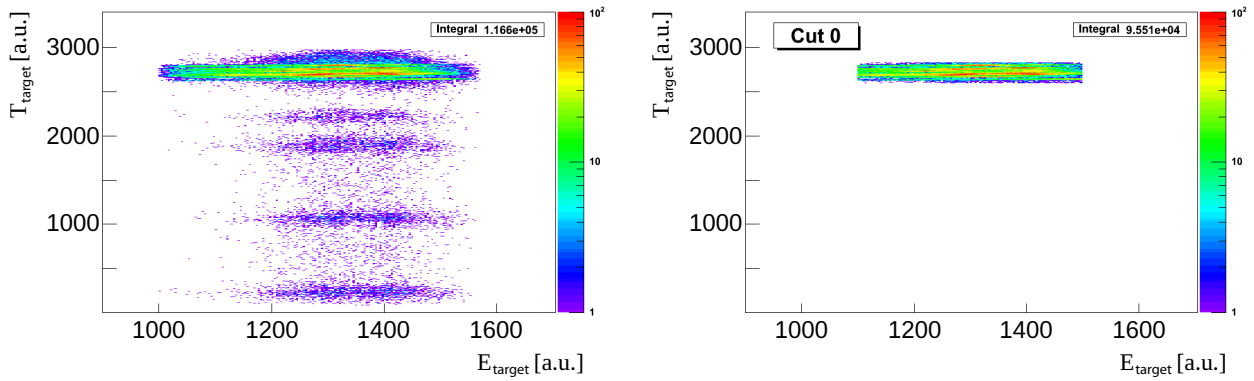


Figure 5.7: LYCCA target DSSD $T - \Delta E$ plot without (left) and with the applied cut (right).

5.3 Multi-hit events in the target DSSD

In fig. 5.8, the multiplicity distribution is shown for the particle- γ -trigger and for the particle-trigger separately, following the application of all particle gates described in sec. 5.5.3.

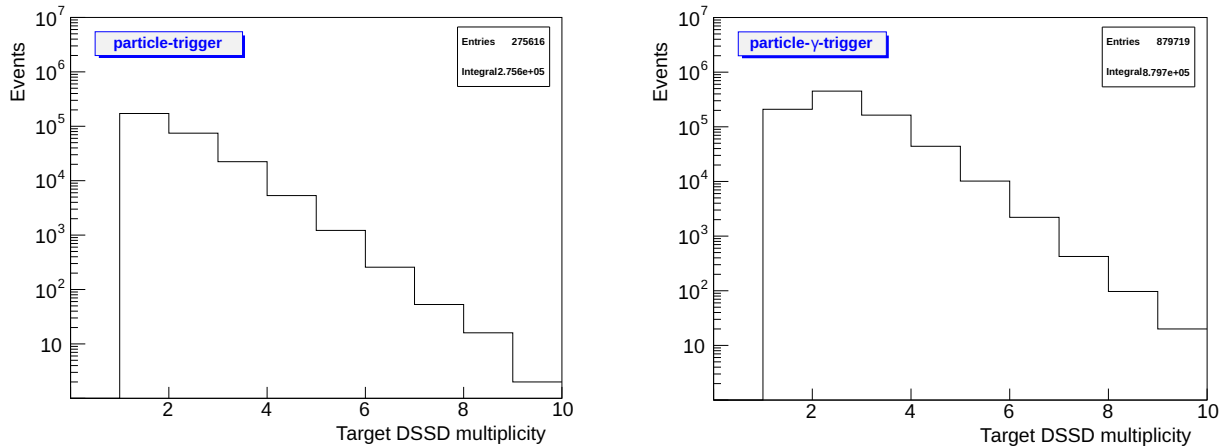
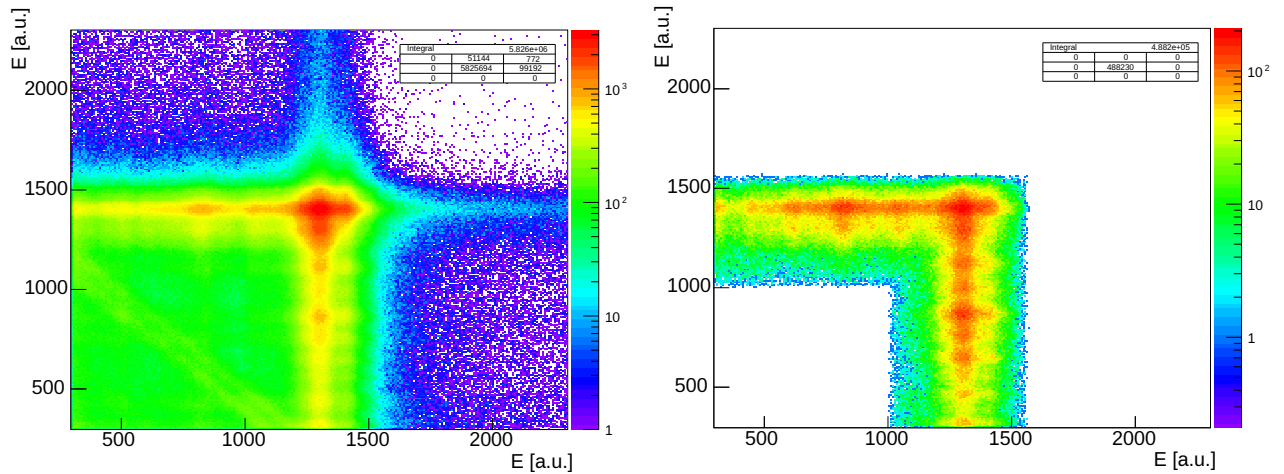


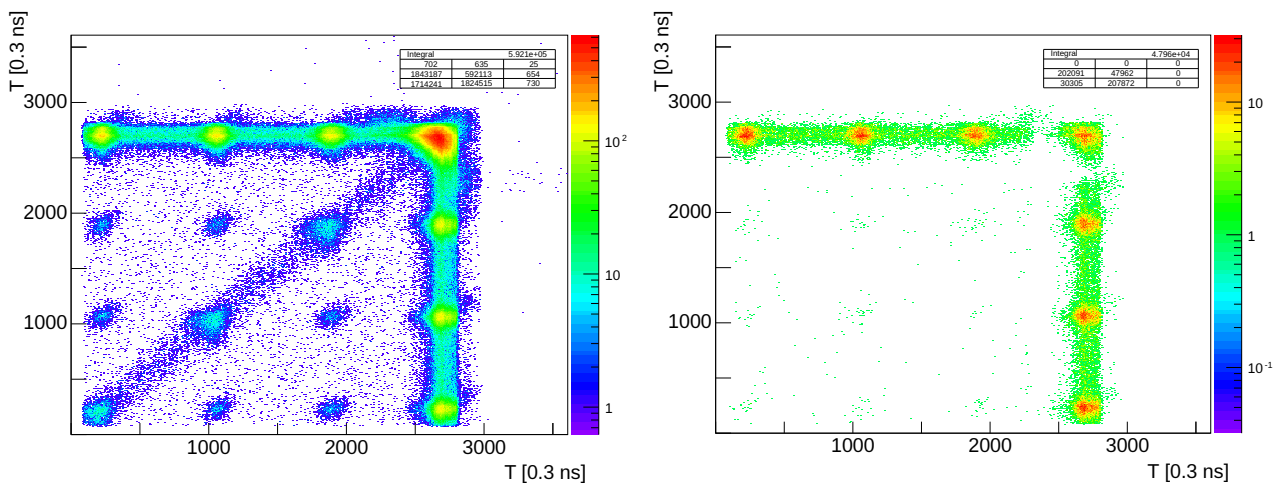
Figure 5.8: Multiplicity of the target DSSD (M_{tar}) for particle trigger (left) and particle- γ -trigger (right).

The multiplicity distribution $M_{\text{tar}} = 1$ of the particle-trigger has the highest number of events, but this changes when looking at the particle- γ -trigger distribution. In both cases, a large fraction of $M_{\text{tar}} > 1$ events (40 % with particle-trigger and 75 % with particle- γ -trigger) are unexpected. A secondary beam rate of less than 50k pps leads to an average time interval of at least $20 \mu\text{s}$ between subsequent ions. The time window of the ADC is approximately $8 \mu\text{s}$ and that of the TDC is approximately $1.2 \mu\text{s}$.

Events with $M_{\text{tar}} = 0$ do not appear in this histogram as the requested particle gates require LYCCA tracking and therefore a target DSSD hit is required. To understand which effects cause the large number of multi-hit events, fig. 5.9 shows energy-energy ($E - E$) and time-time ($T - T$) correlations for $M_{\text{tar}} = 2$ events. In all spectra E is the energy signal from the DSSD's p-side and T the time difference between the time signal of a p-side DSSD strip and SC41 (cf. par. 3.3.2.1).



(a) $E - E$ correlation of both hits without any gates (left) and with particle gates (right).



(b) $T - T$ correlation of both hits without any gates (left) and with particle gates (right).

Figure 5.9: Energy and time correlations of $M_{tar} = 2$ events .

The correlation of the energies of both hits (fig. 5.9a) comprises four types of events:

- Both particles deposit the full typical energy, which in this case is the large accumulation around $(x = y = 1300)$
- One particle deposits the full typical energy, the other carries part of that energy. This causes the horizontal and vertical bands
- Two particles deposit a fraction of the full typical energy which causes the green area in the histogram
- one particle deposits its energy in two neighbouring strips which are located on the couterbrace ('split energy events')

The periodic (250 ns) structure in the time correlation (cf. fig. 5.9b) is caused by the 4 MHz frequency of the beam time structure. This high frequency was applied on the SIS extraction system to flatten the micro structure of the beam.

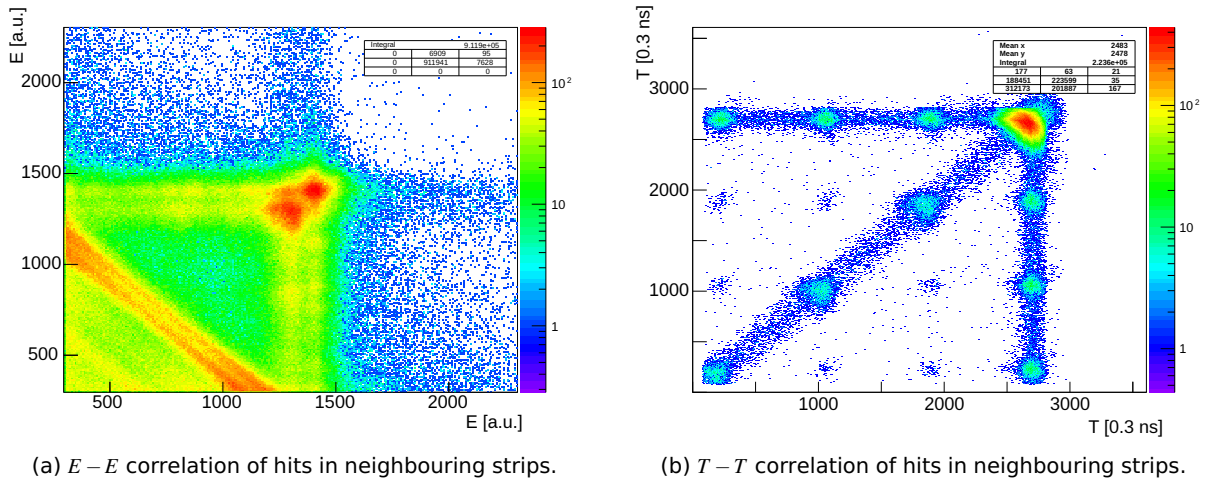


Figure 5.10: Correlations of hits in neighbouring strips without any particle gates .

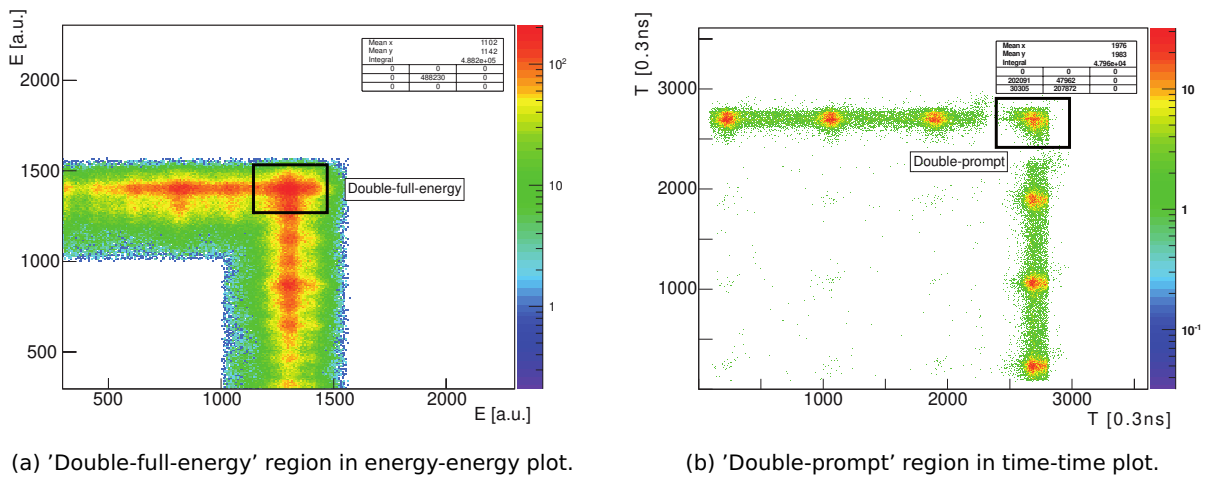
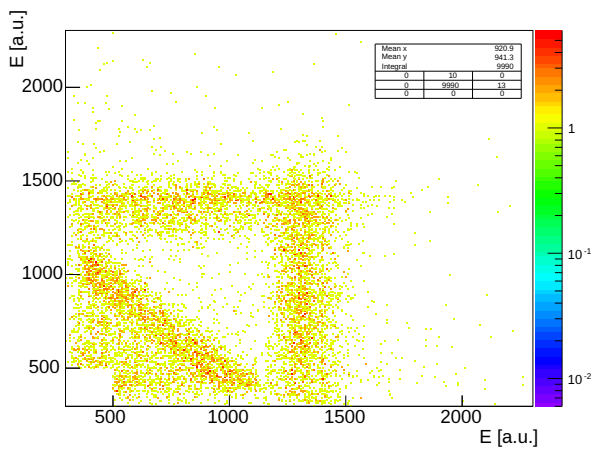


Figure 5.11: Definition of energy and time regions.

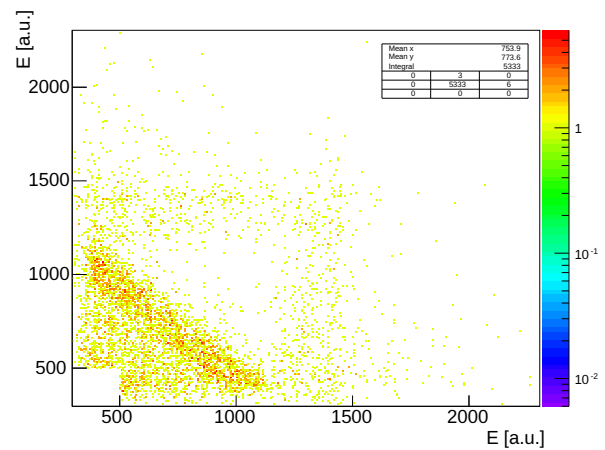
These correlations look different, if it is demanded, that both strips which are hit are adjacent (cf. fig. 5.10). In the energy-energy correlation the number of “split energy events” is enriched, whereas the time-time correlation looks quite the same as before.

Both correlations ($E - E$ and $T - T$) can be combined to get a better understanding of these events. Thus, in the energy-energy correlation a “double-full-energy” (dfE) region is defined, whereas the rest of the spectrum is treated as a “not double-full-energy” ($ndfE$) region (cf. fig. 5.11a). Accordingly, in the time-time correlation a “double-prompt” (dp) region is defined (cf. fig. 5.11b). Everything outside of this area is called “not double-prompt” (ndp).

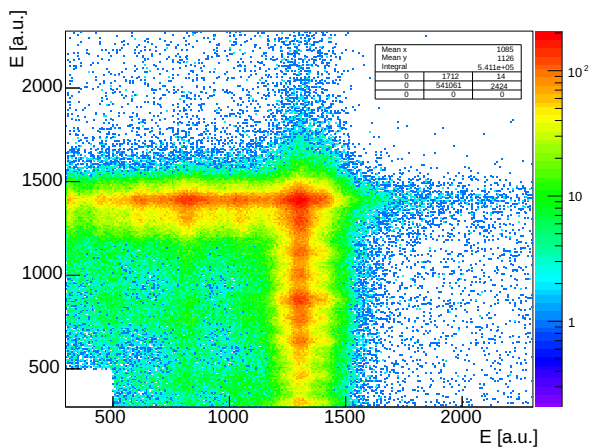
The following figures (5.12 and 5.13) show the correlations shown in fig. 5.9 with additional conditions on dfE , $ndfE$, dp and ndp receptively. Fig. 5.12 shows the $E - E$ correlation of hits for both time regions and fig. 5.13 shows the $T - T$ correlation for the energy regions.



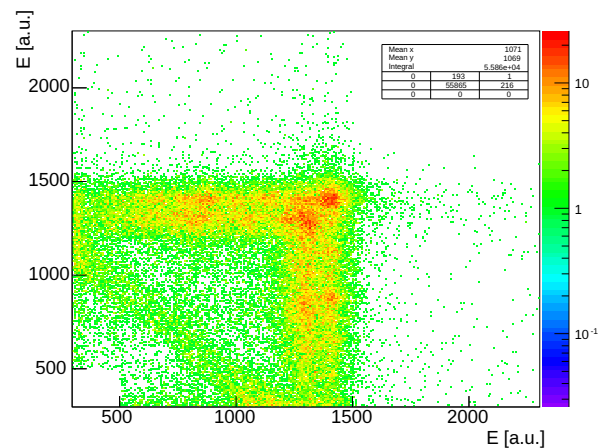
(a) Correlation of energies that are double-prompt.



(b) Correlation of energies on neighbouring strips that are double-prompt.



(c) Correlation of energies that are not double-prompt.

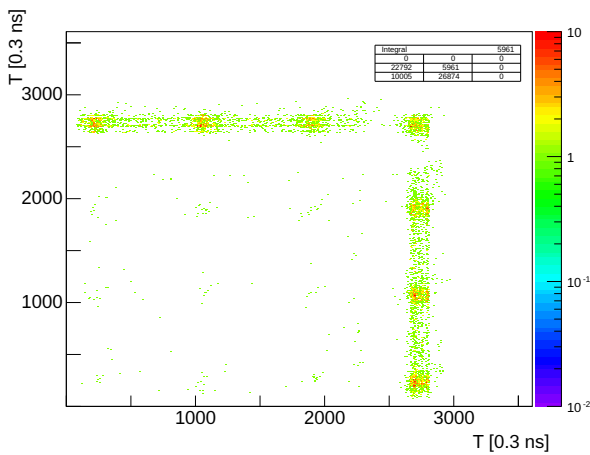


(d) Correlation of energies on neighbouring strips that are not double-prompt.

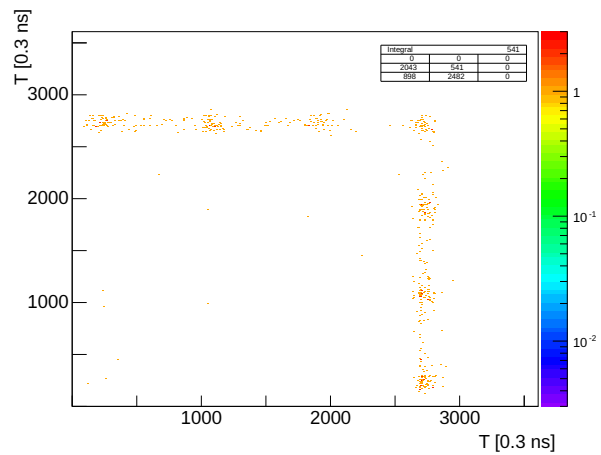
Abbildung 5.12: $E - E$ correlation for different time and space conditions with all particle gates apart from the $\Delta E - \Delta E$ gate.

In summary:

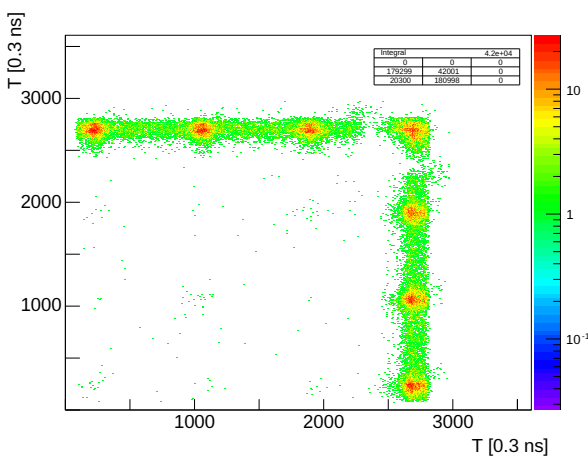
- Only a small fraction ($< 5k$ of $5.8M$) of $M_{tar} = 2$ events are caused by energy splitting between adjacent DSSD strips (cf. fig. 5.12b)
- Even if both strips were hit at nearly the same time, for at least 50 % of the events the full typical energy is deposited in both strips (cf. fig. 5.12a)
- In the case where two hits occur separated by a longer time difference, the $E - E$ plot mainly comprises of coincidences of one particle depositing the full energy of the ion and a second particle with random energy deposition up to the full energy (cf. fig. 5.12c)
- The time-time correlations show a periodic 250 ns peak structure caused by a HF signal applied to the spill structure of the FRS beam (cf. fig. 5.13)



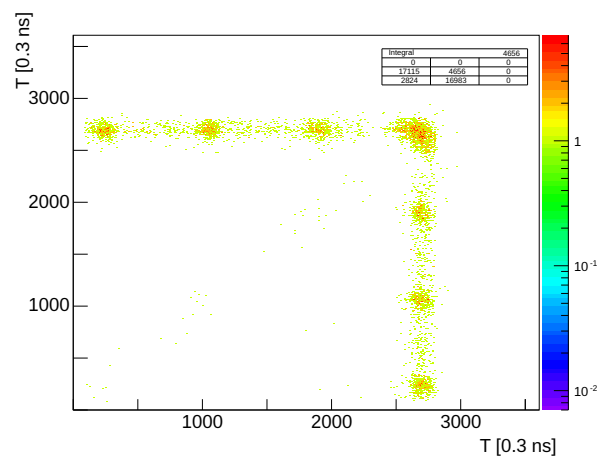
(a) Correlation of times for double-full-energy events.



(b) Correlation of times on neighbouring strips for double-full-energy events.



(c) Correlation of times that are not double-full-energy events.



(d) Correlation of times on neighbouring strips that are not double-full-energy events.

Figure 5.13: $T - T$ correlation for different energy and space conditions.

To conclude, the $M_{tar} = 2$ events consist of a small fraction ($\sim 1\%$) of events where the ion hits the space between two adjacent strips of the target DSSD and a much larger fraction (99 %) of beam particles within a small time window. To verify this conclusion, fig. C.1 shows the FRS A/Q vs. Z plot for different target DSSD multiplicities. Increasing pileup in the MUSIC detectors with increasing M_{tar} (cf. subsection 3.3.2.3) is expected, which would cause larger mean values in the Z identification ($Z \propto \Delta E_{MUSIC}$). The plots in fig. C.1 show that the mean Z -values are increasing for higher M_{tar} . The accumulation at $Z \approx 25 - 26$ is caused by non-linearity of the MUSIC calibration. These events can be identified with two detected argon ions. Tab. 5.1 summarizes the mean Z -values for the different target DSSD multiplicities.

M_{tar}	mean Z-value
0	18.59
1	18.81
2	19.30
3	19.95
4	20.59
5	21.04
6	21.29
> 1	19.72

Table 5.1: Mean Z values from FRS identification of different Target DSSD multiplicities (shown in fig. C.1).

The FRS identification plots support the interpretation that the $M_{tar} > 1$ events are produced by beam correlated particles (of a different type than the heavy ions) and are not a product of a malfunction of the target DSSD. Finally, it is not fully understood which particles create these $M_{tar} > 1$ events, but as an analysis condition it is sufficient to neglect all these events. In principle, it is possible to recover the 'split energy' events, but due to their low impact ($< 1\%$) they are also neglected.

5.4 Doppler correction and germanium time-gates

After applying all particle gates that are described in section 5.2, the next step is to evaluate the timing and energy signals of the Germanium detectors. The best timing information is given by the SR timing branch (cf. chapter 3). Fig. 5.14 shows the time distribution of the γ -rays. The time signal corresponds to the time difference between the SC41 signal that detects a passing ion and the SR time signal of a Cluster detector with an arbitrary offset. A preliminary time gate (50 channels $\simeq 15$ ns) was set on the rising flank of the maximum of the time distribution. The rising flank was chosen because the photons emitted from the secondary target are expected to be the first particles that interact with the Cluster detectors (as they travel at the speed of light). All other particles, e.g. neutrons from the FRS or the secondary target, are slower and thus do not appear on the right-hand side of the time distribution. In chapter 5.5.3, the preliminary time gate is replaced by an optimized gate, although the preliminary time gate is useful when trying to identify a first peak in the γ -spectrum. The different contributions to the time spectrum are discussed in section 5.5.7 in detail.

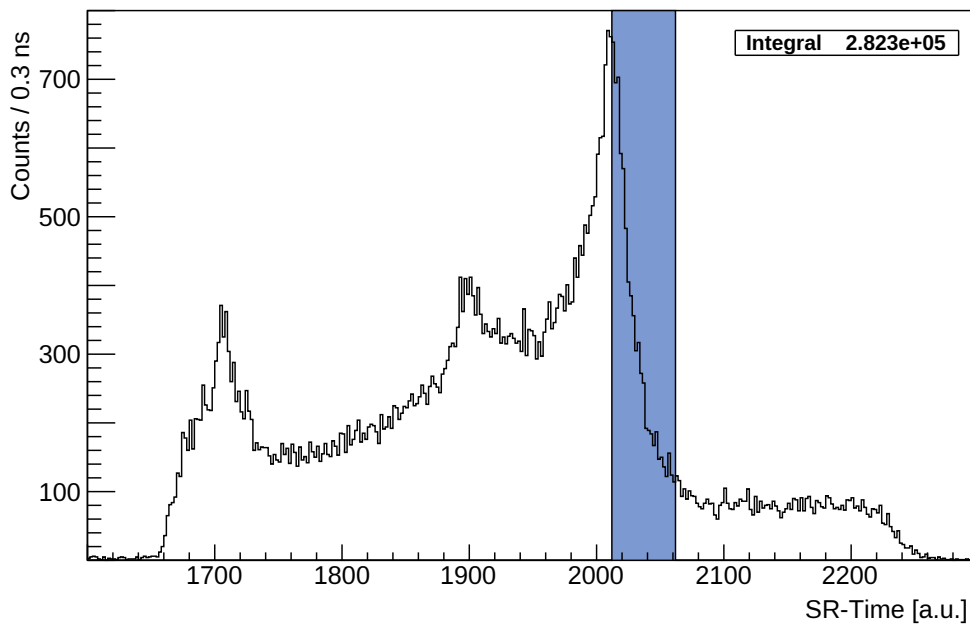


Figure 5.14: *SR* spectrum from the Cluster detectors which has an arbitrary offset where one channel is the equivalent to 0.3 ns. The marked region is the preliminary time-gate.

The Doppler correction is a crucial part in the analysis of the data of the germanium detectors. The angle of emission is deduced by combining the angle of the detecting germanium detector segment and the trajectory of the emitting ion, which is determined by LYCCA (cf. sec. 4.3.4). Furthermore, the velocity of the source is needed for a proper Doppler correction. This information is provided by the LYCCA time-of-flight system (cf. section 4.2.4). Thus, the energy detected by the germanium detectors can be transformed in the center of mass system of the ions employing the relativistic Doppler-shift formula [85]:

$$E_{lab}(E_{com}, \beta, \alpha) = E_{com} \cdot \frac{\gamma}{1 - \beta \cdot \cos \alpha},$$

where E_{com} is the energy of the γ -ray in the com system of the ion, E_{lab} is the energy detected by the Ge detectors, β is the velocity of the ion in units of the speed of light, γ is the relativistic Lorentz factor and α is the angle between the detected γ -ray and the trajectory of the ion. Fig. 5.17 shows Cluster energy spectra with and without Doppler correction for events with a germanium crystal multiplicity of 1 (only one crystal detects with an energy above the threshold of approximately 150 keV).

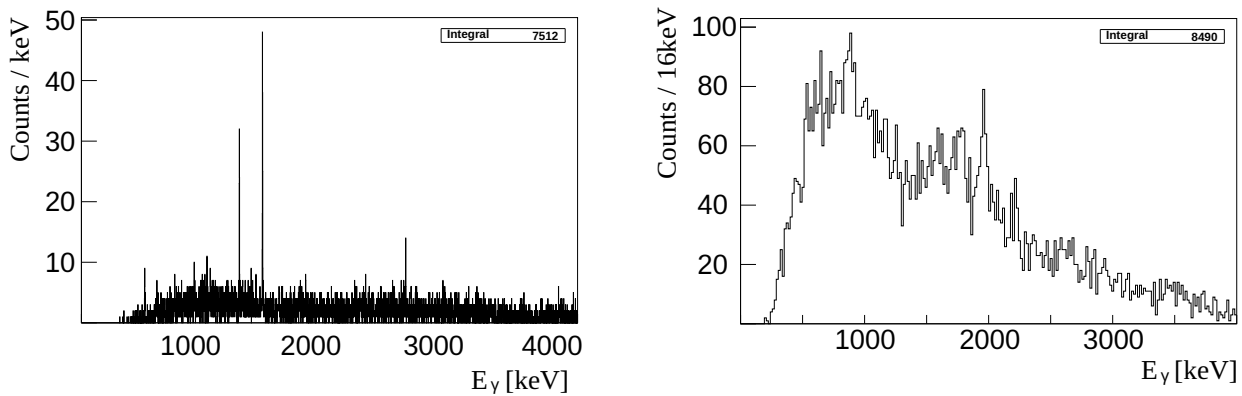


Figure 5.15: Energy spectra of the Cluster detectors with $M_{cry} = 1$ without (left) and with Doppler correction (right).

Fig. 5.16 shows the correlation of all calibrated energy signals of the Cluster detectors and their SR-time. The energy in the plot has been Doppler corrected as described above.

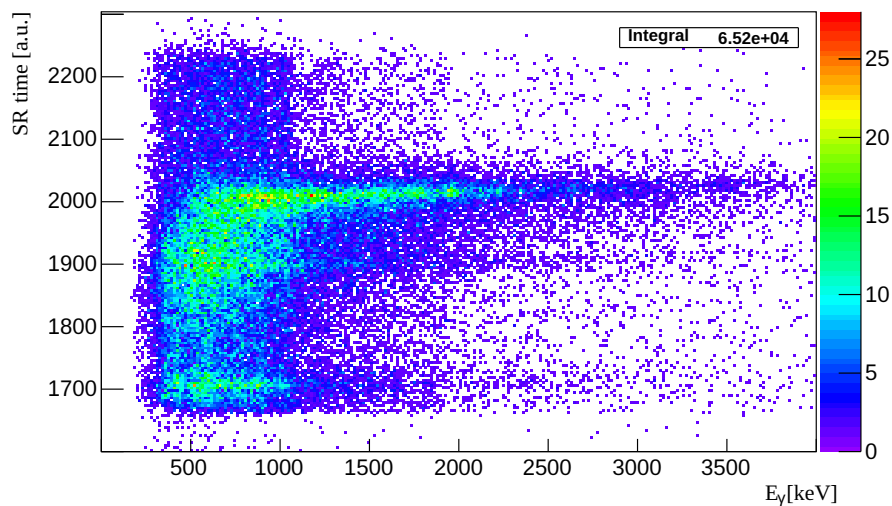


Figure 5.16: Doppler corrected $SR - E$ plot from the Cluster detectors.

The functions used for the fit in fig. 5.17 and for upcoming fits is the sum of a Gauss-function (for the signal) and a 3rd order polynomial (for the background). The variables fitted for the Gaussian are the volume (Vol), the mean value (μ) and the standard deviation (σ).

The precise measurement of the volume parameter of the peak and the improvement of the following ratio is desired:

$$Res_{vol} = \frac{\Delta Vol}{Vol} \quad (5.1)$$

is the aim of further analysis (where ΔVol is the uncertainty of Vol). Here, Res_{vol}^{poly} and Res_{vol}^{lin} indicate whether a polynomial or a linear background function is used. The numerical value of Res_{vol} is the average of both approaches:

$$Res_{vol} = \frac{1}{2} \cdot (Res_{vol}^{poly} + Res_{vol}^{lin}). \quad (5.2)$$

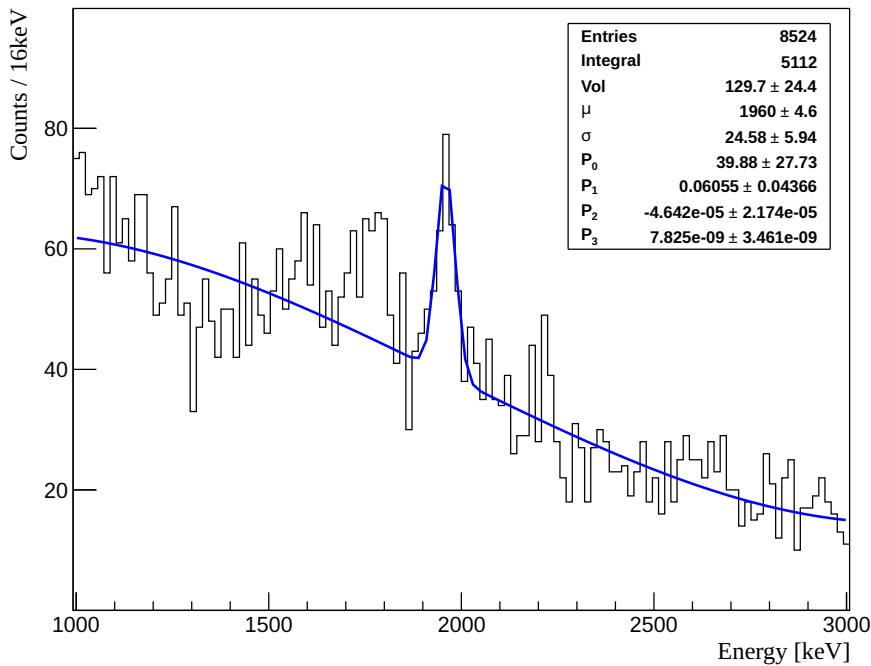


Figure 5.17: Fit of the peak where $Res_{vol} = 18.8\%$, (cf. 5.1).

Important attributes of each event are the germanium crystal multiplicity (M_{cry}) and Cluster multiplicity ($M_{cluster}$). They are integer values that are incremented for each Cluster/crystal that detects an energy that is larger than approximately 150 keV. The distribution of M_{cry} is shown in fig. 5.18. There are no $M_{cry} = 0$ events as a particle- γ -coincidence is requested. The condition $M_{cry} = 2$ can be caused by noise or by an energy splitting of a single γ -ray in more than one crystal (unlikely for $M_{cry} > 2$). At this point, events with $M_{cry} > 1$ are neglected. The technique to restore events with energy splitting over two crystals is called 'add-back' and is described in section 5.5.5.

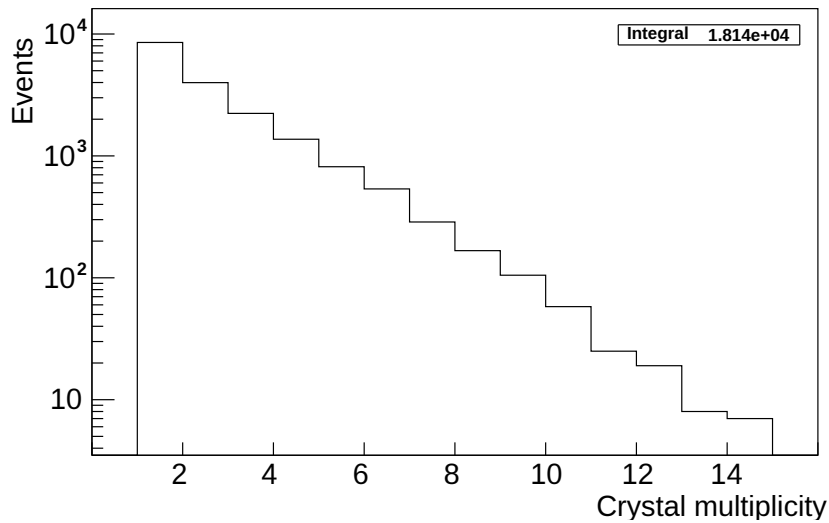


Figure 5.18: Crystal multiplicity (M_{cry}) which is incremented for each germanium crystal when an energy larger than 150 keV is detected.

In the following, further conditions are required to increase the signal-to-noise ratio (to minimize Res_{vol}).

5.5 Optimization of γ -ray spectroscopy

5.5.1 Target DSSD multiplicity

As shown in section 5.3, the target DSSD shows a multiplicity distribution (M_{tar}) with a long tail from hits with more than one incoming ion. This is caused by the structure of the SIS beam which was tuned for high intensity bunches. Other charged reaction particles hit the target detector (the threshold for incrementing M_{tar} is approximately 6 MeV). Fig. 5.19 shows the distribution of different target multiplicities and fig. 5.20 shows the germanium spectra for $M_{tar} = 1$ and $M_{tar} = 2$. The determination of M_{tar} depends only on the target DSSD's energy signals of a single event. No further timing condition is applied.

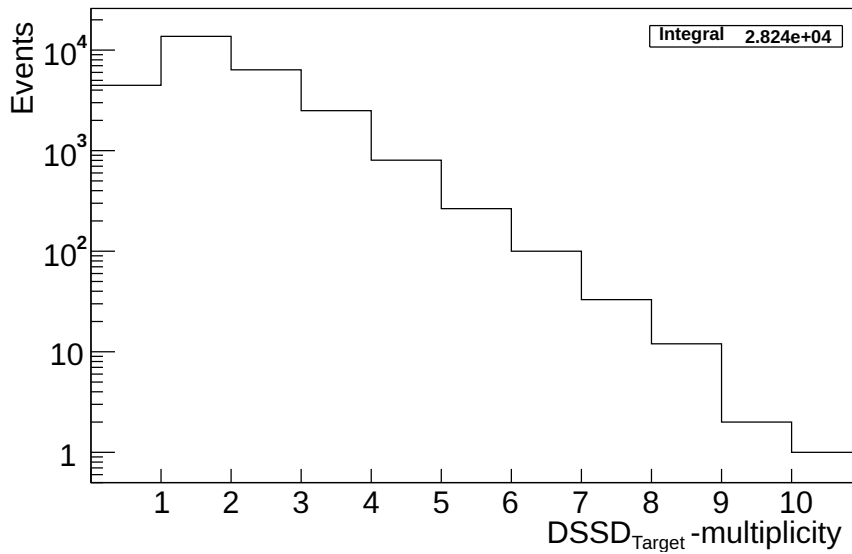


Figure 5.19: Multiplicity of the target DSSD (M_{tar}). Each p-side strip with an energy deposition $\gtrsim 6$ MeV causes an incrementation of the multiplicity.

As expected, events with $M_{tar} = 1$ are more common than all other multiplicities ($\frac{M_{tar}=1}{M_{tar} \geq 0} = 39.2\%$), although $M_{tar} \geq 2$ events have quite a large effect on the germanium spectra (cf. fig. 5.20).

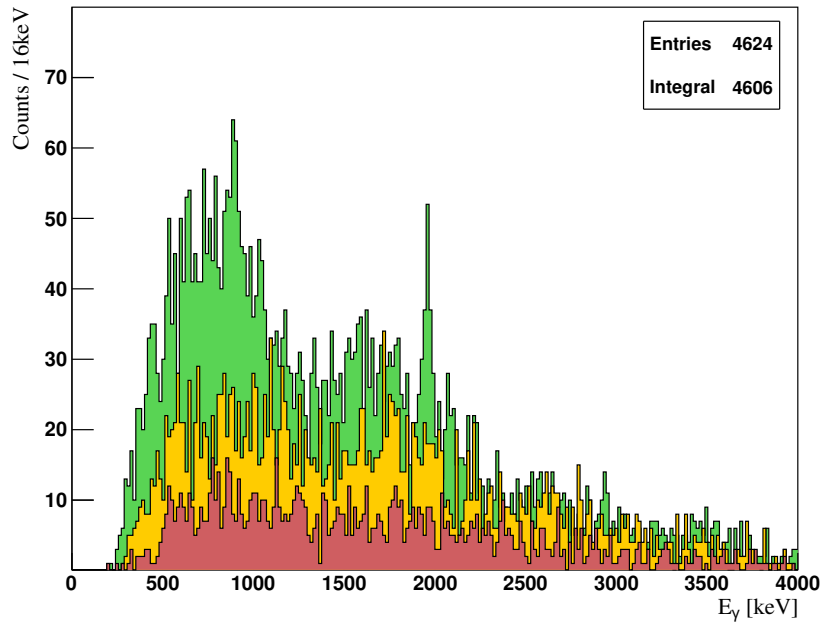
The γ -spectra for three different M_{tar} values are given in Fig. 5.20a. The γ -peak from the $2^+ \rightarrow 0^+$ transition in ^{36}Ar is clearly visible and dominant in the spectrum for the $M_{tar} = 1$ events (cf. fig. 5.20a (green) and 5.20b). The γ -spectra with higher multiplicities, $M_{tar} \geq 2$ (cf. fig. 5.20a orange and red), do not contribute to the ^{36}Ar peak seen in the $M_{tar} = 1$ spectrum. Therefore, in the forthcoming analysis, only $M_{tar} = 1$ events are considered.

5.5.2 γ -rays emitted from sources in rest

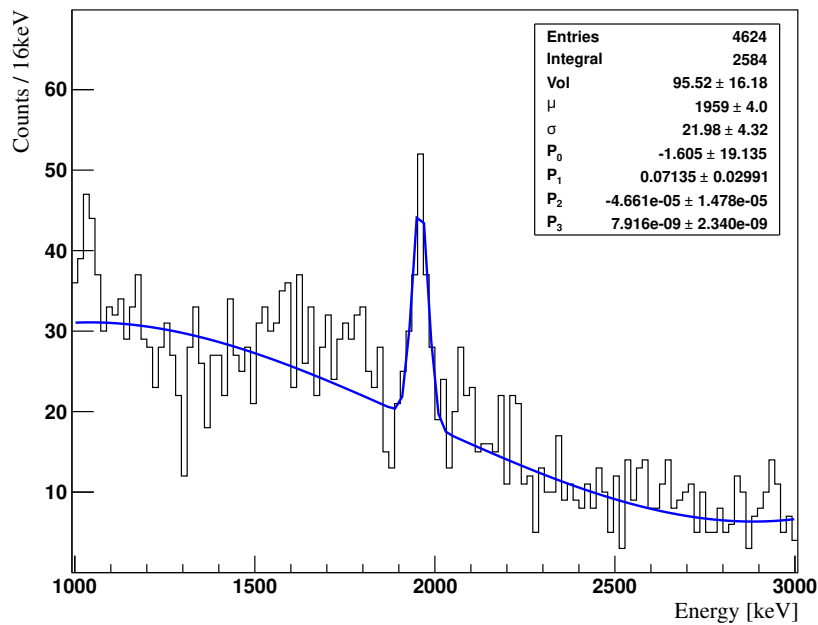
Narrow γ -peaks with a width of $\lesssim 5$ keV FWHM) are present in the uncorrected γ -spectrum. These peaks originate from γ -rays that are emitted from a source at rest. If the source is moving at a relativistic speed (e.g. $v = 0.5 \cdot c$), Doppler broadening causes peak widths of $\gtrsim 50$ keV FWHM. Fig. 5.21a shows the uncorrected γ -spectrum following the application of the particle and time gates described above. Three intense, sharp lines are visible in the spectrum and can be attributed to the following background reactions and decays:

- $^{197}\text{Au} (n, \gamma) ^{198}\text{Au}$, $E_\gamma = 1272$ keV
- $^{40}\text{K} \rightarrow ^{40}\text{Ar}^* + e^+ + \nu_e \rightarrow ^{40}\text{Ar} + \gamma$, $E_\gamma = 1461$ keV
- $^{207}\text{Pb} (n, \gamma) ^{208}\text{Pb}$, $E_\gamma = 2615$ keV

The emission of these γ -rays is caused by uncorrelated background events. However this time-independence cannot be seen in the data, because the trigger (particle- γ) is correlated to the passing ions.



(a) γ -spectra of different M_{tar} where green: $M_{tar} = 1$, orange: $M_{tar} = 2$ and red: $M_{tar} \geq 3$.



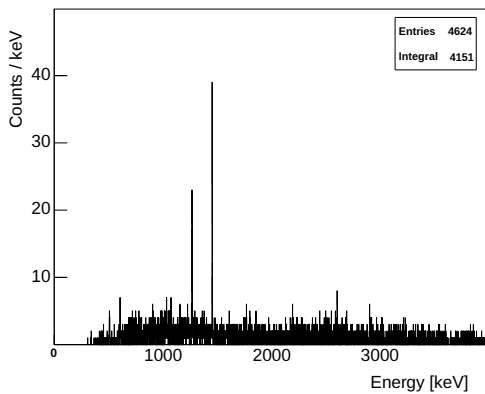
(b) Fit of the $M_{tar} = 1$ spectrum where $Res_{vol} = 16.9\%$.

Figure 5.20: Doppler corrected energy spectra of the Cluster detectors with $M_{cry} = 1$.

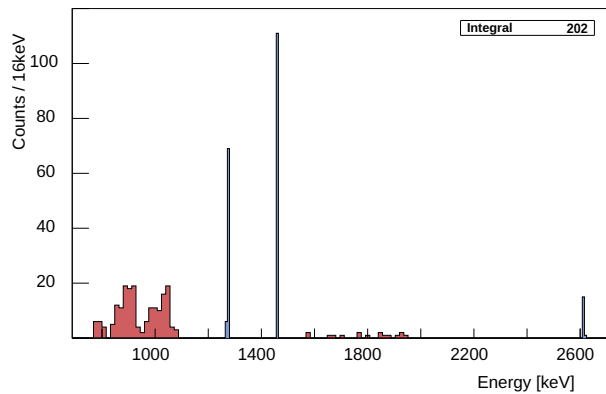
This is demonstrated by the comparison of two ratios: the ratio of counts within the prompt time gate and a much longer time gate.

$$\frac{\text{Counts (in time gate)}}{\text{Counts (in full time range)}} = \frac{355}{3223} = 11\% \neq \frac{\text{Length of time gate}}{\text{Length of full time range}} = \frac{50 \text{ ch}}{4096 \text{ ch}} = 1.2\%.$$

In order to remove this well understood background from the natural radiation in the experimental area and the neutron capture reaction of target and absorber nuclei in the spectrum, the discrete lines are removed by cutting out the lines from the uncorrected spectrum. Fig. 5.21b shows an uncorrected spectrum with the three discrete lines cut out and the same lines superimposed with Doppler correction which are broadened.



(a) Uncorrected γ -spectrum following application of particle and time gates.



(b) Spectrum with three neglected discrete lines. Blue: uncorrected energies. Red: the same entries following Doppler correction.

Figure 5.21: Cluster detector γ -ray energy spectra with applied particle and time gates.

After the cut-out had been applied, new Doppler corrected spectra were created. Fig. 5.22 shows the Doppler corrected γ -spectra with and without the described treatment of stopped lines. As the cut-out has no negative influence on the peak region, it is applied in the upcoming analysis.

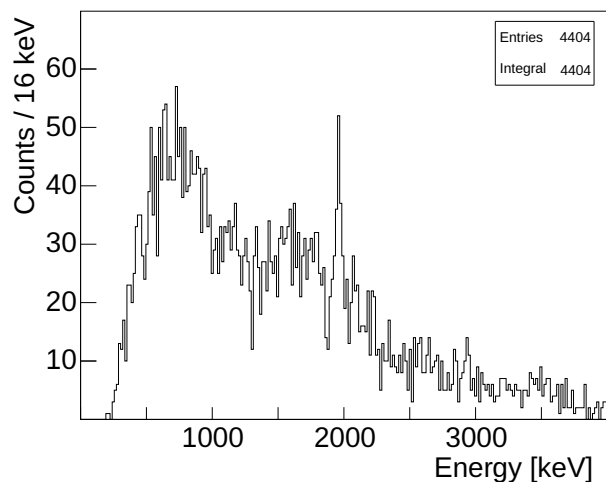
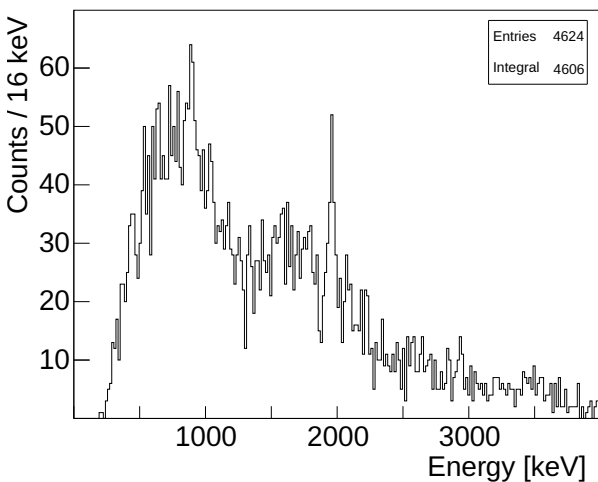


Figure 5.22: Doppler corrected γ -spectra without (left) and with (right) the cut-out of the remaining stopped lines.

5.5.3 Optimizing the particle-gates

The next step to improve the analysis is to find the optimal combination of gates for the particle spectra. As an example, fig. 5.23 show three different $\Delta E - E$ gates. Hence, for all particle gates (as described in section 5.2), alternative cuts were created and compared, which are shown in the figures of chap. C.

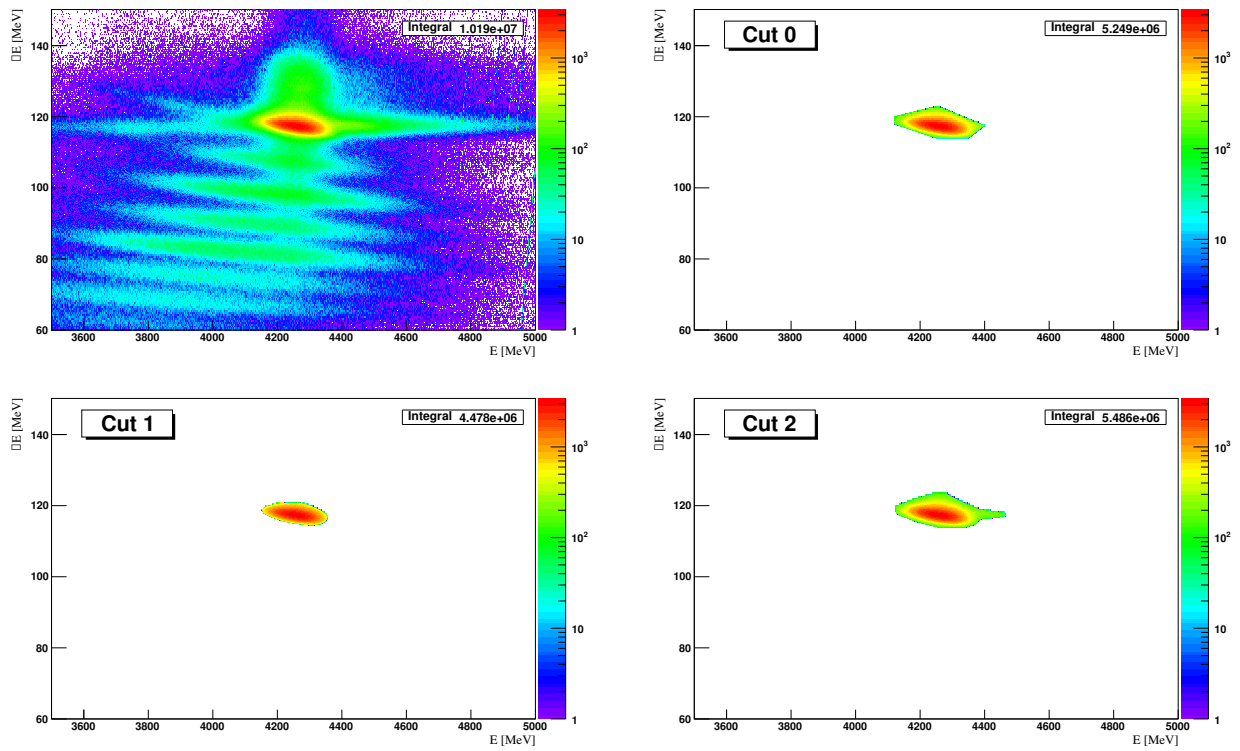


Figure 5.23: Different $\Delta E - E$ gates.

A particle gate analysis configuration is given by the chosen gates, for example:

$$\left[\begin{array}{ll} \Delta E - E & \text{Cut-1} \\ \Delta E - \Delta E & \text{Cut-2} \\ \beta_{FRS} - \beta_{LYCCA} & \text{Cut-3} \\ \beta_{LYC} - CsI & \text{Cut-0} \\ \text{Target DSSD } E - T & \text{Cut-0} \end{array} \right].$$

In total, 16 different gates were used:

- three $\Delta E - E$ gates
- three $\Delta E - \Delta E$ gates
- four $\beta_{FRS} - \beta_{LYCCA}$ gates
- three $\beta_{LYC} - CsI$ gates
- three Target DSSD $E - T$ gates.

In the figures, 'Cut-0' is the original gate (used before in sec. 5.2). Each gate configuration creates a unique γ -ray spectrum. The ideal gate configuration of the gates optimizes the peak-to-background ratio of the final peaks from transitions in ^{36}Ar and ^{33}Ar or minimizes Res_{vol} (cf. eq. 5.1).

For a quantitative comparison of all possible ($3^4 \cdot 4 = 324$) gate configurations, the relative error of the peak volume Res_{vol} (as defined in eq. 5.1 and 5.2) is calculated for each resulting γ -spectrum. Fig. 5.24 shows $(Res_{vol})^{-1}$ of all gate configurations. Each data point represents one gate configuration.

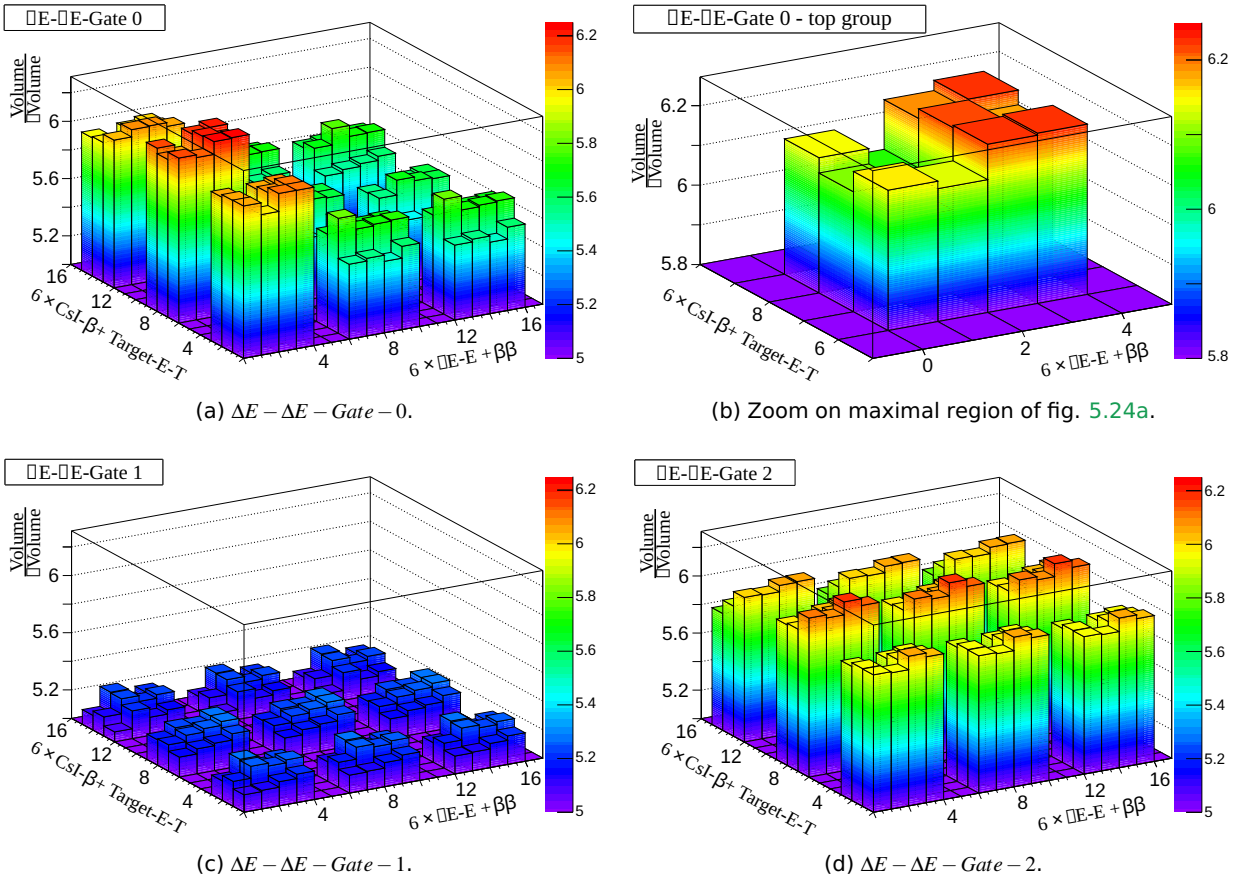


Figure 5.24: Plot of $(Res_{vol})^{-1}$ for different combinations of gates where x-axis: $6 \cdot N(\Delta E - E) + N(\beta_{FRS} - \beta_{LYCCA})$ and y-axis: $6 \cdot N(\beta_{LYC} - CsI) + N(\text{TargetDSSD } E - T)$.

Fig. 5.24a,c,d show the results of all gate configurations for a fixed $\Delta E - \Delta E$ gate. $N(\text{gate})$ is the number of the gate (e.g. $N(\Delta E - E - \text{Cut}-0) = 0$). The x-axis represents the choice of $\Delta E - E$ (three groups) and $\beta_{FRS} - \beta_{LYCCA} - \text{Gate}$ (four distinctive blocks in each group). The y-axis represents the selection of $\beta - CsI$ (three groups) and Target DSSD $E - T - \text{Gate}$ (three distinctive blocks in each group).

Thus, the maximum in this plot determines the optimal combination of gates. Out of all $\Delta E - \Delta E$ -gates, the $\Delta E - \Delta E - \text{Gate} - 0$ (cf. fig. 5.24a) provides the best results. The region of combinations that contains the highest values ($0 \leq x \leq 4$ and $6 \leq y \leq 9$) is defined by $\Delta E - \Delta E - \text{Gate} - 0$, $\Delta E - E - \text{Gate} - 0$ and $\beta_{LYC} - CsI - \text{Gate} - 1$. This region is shown in fig. 5.24b. The maximum $(Res_{vol})^{-1} = 6.21$ is located at $x = 3$, $y = 6$. This corresponds to the following gate combination:

$$\begin{bmatrix} \Delta E - E & \text{Cut-0} \\ \Delta E - \Delta E & \text{Cut-0} \\ \beta_{FRS} - \beta_{LYCCA} & \text{Cut-3} \\ \beta_{LYC} - CsI & \text{Cut-1} \\ \text{Target DSSD } E - T & \text{Cut-0} \end{bmatrix}.$$

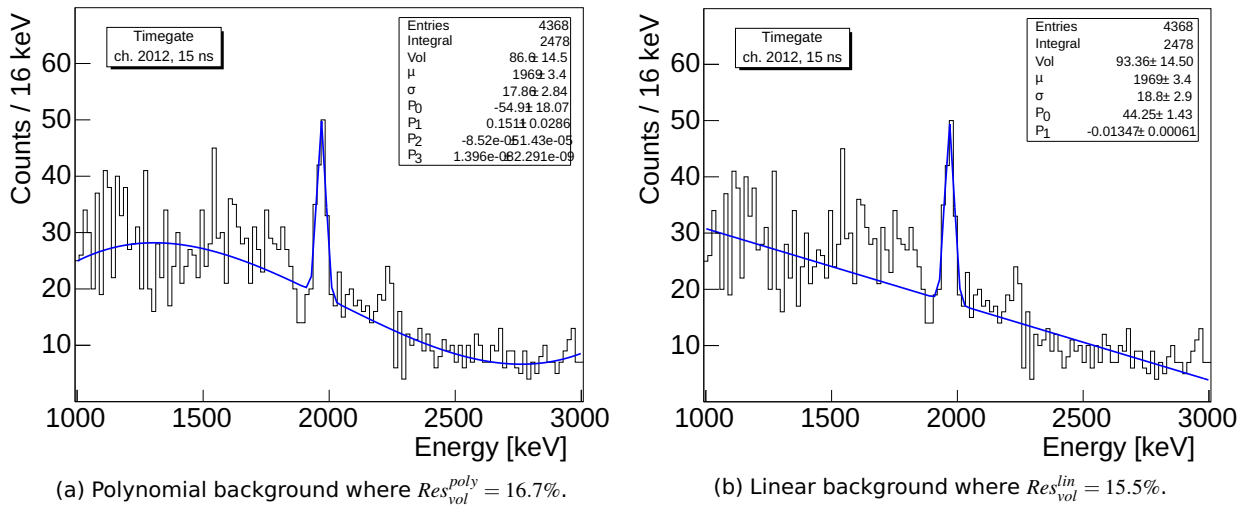


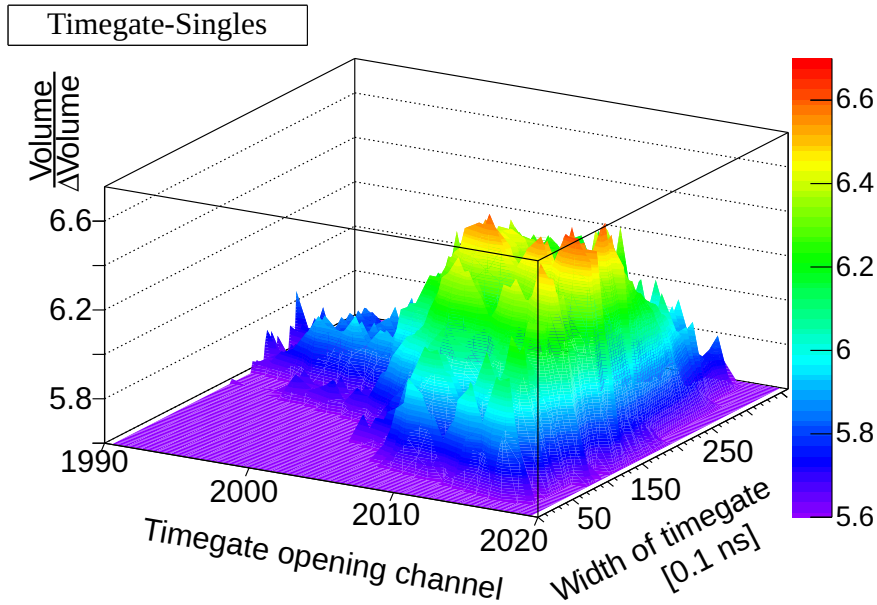
Figure 5.25: γ -spectra for the optimal particle gate combination where $Res_{vol} = 16.1\%$.

The new gate combination yields an improvement of 0.8% in Res_{vol} and is therefore used in the forthcoming analysis.

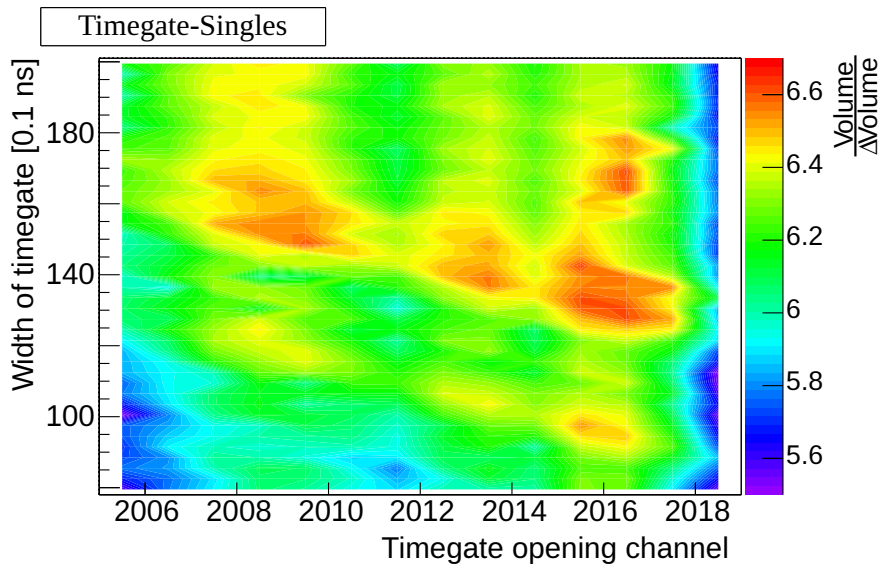
5.5.4 Optimizing the time gate

The time gate set in sec. 5.4 is good enough to see a peak in the γ -spectra (cf. e.g. fig. 5.25). However, background contributions cannot be separated via the timing condition due to the limited time resolution of the HPGe cluster detectors. Therefore, a systematic inspection was used in order to improve Res_{vol} of the gamma-spectrum. The following two variables were used to vary the time gate: the 'opening channel' that defines one boundary of the time gate and the 'width' of the time gate. Here, the 'opening channel' is the channel number of the lower limit of the interval that defines the gate. As time runs backwards with respect to the increasing time channels, the 'opening channel' defines the closing of the time gate or the

separation of a prompt from a delayed signal. The result of this analysis is shown in fig. 5.26 where values of $(Res_{vol})^{-1}$ are shown depending on the opening channel and the width of the gate. This was calculated for opening channels between ch. 1950 and ch. 2050 and widths between 10 and 150 channels (14k combinations). The events shown are characterized by $M_{cry} = 1$ and are labeled as 'Singles'.



(a) Large range.



(b) Zoom on the region with the highest values.

Figure 5.26: Plot of $(Res_{vol}^{poly})^{-1}$ in dependency of different time gates .

The maximum value ($(Res_{vol}^{poly})^{-1} = 6.61 \rightarrow Res_{vol} = 16.1\%$) is obtained for opening channel 2009 and a width of 15 ns which is in good agreement with the time resolution expected for the Ge-detectors. The new time gate is given by the interval [2009;2048], the former was [1212;2061]. For the ^{33}Ar run, the same analysis was performed. Here, a time gate of 16.5 ns ([2009;2070]) yields the best results causing only a small degradation in the ^{36}Ar -spectra (cf. figs. 5.27, 5.28).

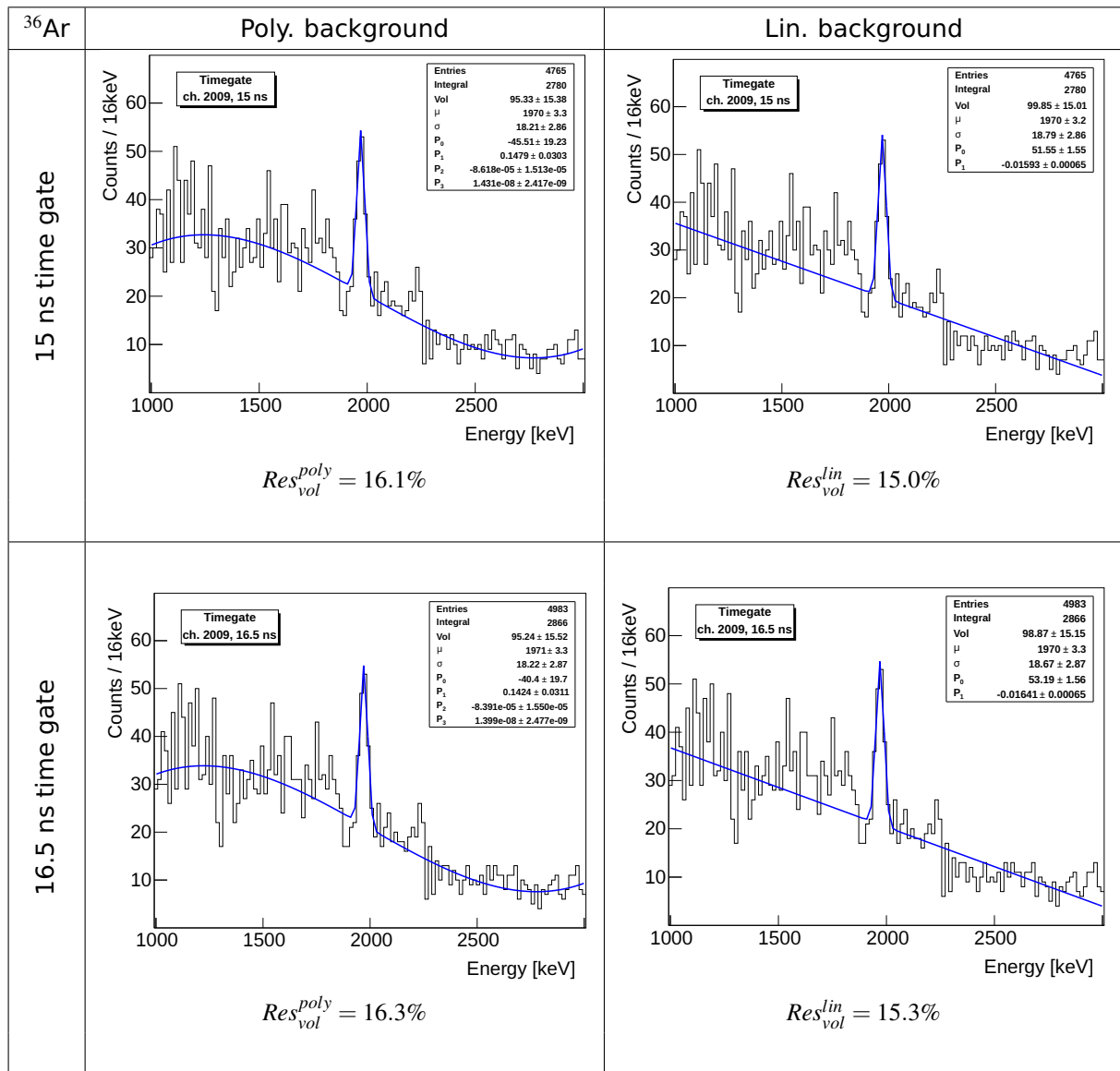


Figure 5.27: ^{36}Ar γ -spectra for both new time gates. Polynomial fitted background is shown on the left and linear fitted background on the right.

With a time gate of width 16.5 ns, Res_{vol} is reduced by 0.6% down to 15.6%. The polynomial function describes the background better although causes larger uncertainties. Fig. 5.28 shows the same spectra for the ^{33}Ar experiment.

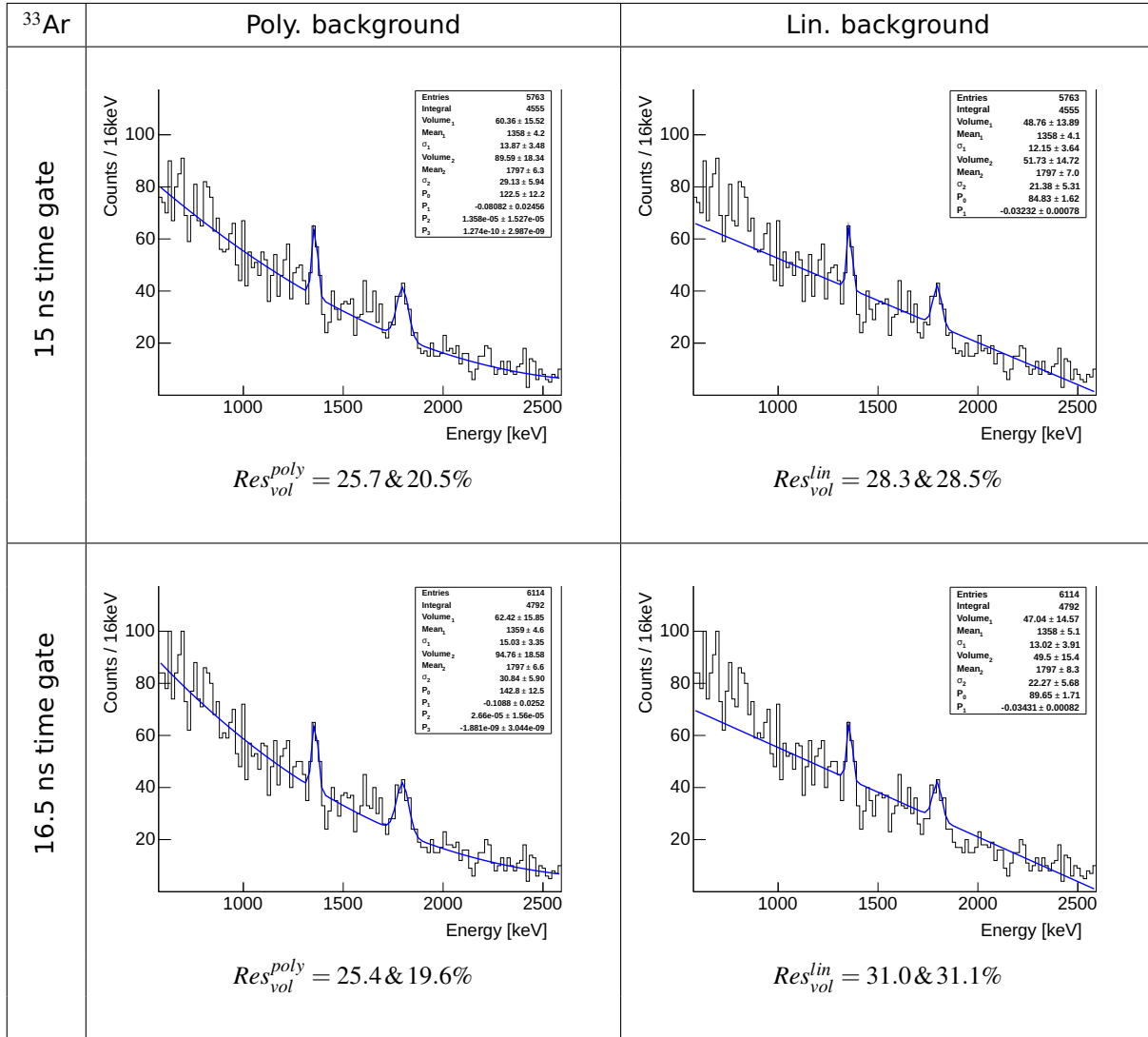


Figure 5.28: ³³Ar γ -spectra for both new time gates. Polynomial fitted background is shown on the left and linear fitted background on the right. Res_{vol} is given for the 1359 keV and 1798 keV peak .

The 16.5 ns time gate improves all γ -spectra, beside the ³³Ar spectra with a linear background fit. The large uncertainty in peak volume determination is caused by poor matching of the linear background. However, this new 16.5 ns time gate is used in the following analysis, because it improved all other resolutions.

5.5.5 Add-back

The next stage of the analysis utilizes an add back algorithm which makes use of events with ($M_{cry} > 1, M_{cluster} = 1$) where several individual HPGe detectors per cluster fired simultaneously. This type of event occurs when the energy of a γ -ray is deposited in more than one crystal of a Cluster after Compton scattering. It can also take place when background radiation is accidentally detected in coincidence with a γ -ray. This is most probable for events with ($M_{cry} = 2, M_{cluster} = 1$). After Compton scattering in a certain crystal, typically a γ -quant has lost a large portion of its energy and does not travel long distances through the germanium crystals. If Compton scattering happens close to the border between two germanium crystals inside the common Cluster, the quant is likely to deposit its energy in two neighbouring crystals.

Fig. 5.29 shows the add-back γ -spectrum for ($M_{cry} = 2, M_{cluster} = 1$). This is created with the same particle gates as for singles, but with an offset in the time gate (16 ch. \sim 5 ns later). This is chosen because the timing of the germanium detectors is affected by an energy dependent walk effect. Fig. 5.30 and 5.31 show the γ -spectra with single and add back events for ^{36}Ar and ^{33}Ar . The values of Res_{vol} in fig. 5.31 are the average values of both peaks in each fit.

Step of analysis	^{36}Ar			^{33}Ar
	poly. bg.	lin. bg.	average	poly. bg.
Singles	16.3	15.3	15.8	22.5
Singles + add back	12.0	12.4	12.2	19.8

Table 5.2: Values of Res_{vol} (in %) after each step of the analysis, steps are applied cumulatively, replacing gates of the same type.

The consideration of add-back events lead to an improvement of Res_{vol} in the range of 3 – 4%. Thus, the add back data is used in the further analysis.

5.5.6 Scattering angle

The scattering angle θ is the angle between trajectories of an ion before and after a reaction. θ is related to the reaction mechanism, especially large scattering angles are correlated to close approaches of nuclei and thus to nuclear reactions. The largest scattering angle that can be caused without a contact of the involved nuclei is the so called grazing angle. The information about a reaction's scattering angle can be used to select or exclude certain reactions mechanisms. It is shown in this section that a condition on θ does not help to reduce background caused by other reactions than Coulomb excitation. The grazing angles are for 34.1 mrad for ^{36}Ar at 137 MeV/u and 35.5 mrad for ^{33}Ar at 145 MeV/u.

As explained in subsection 4.3.4.3, the trajectory of the incoming ions before the secondary target and after the target is determined via position sensitive detectors. The two LYCCA DSSDs

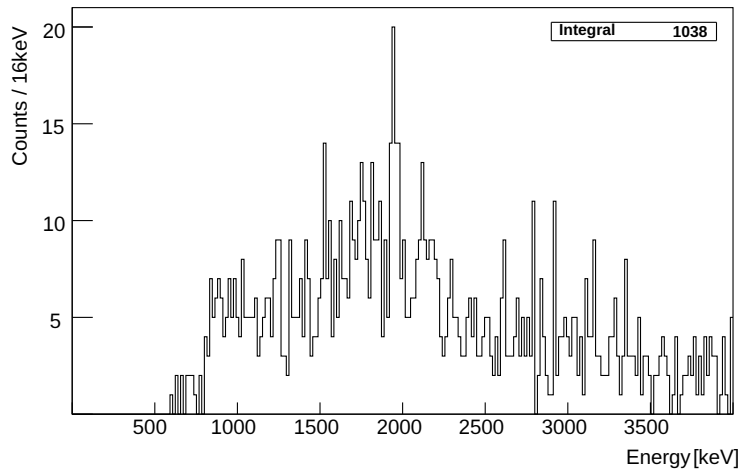
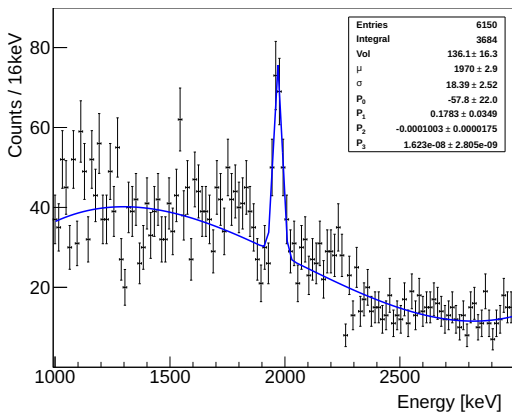
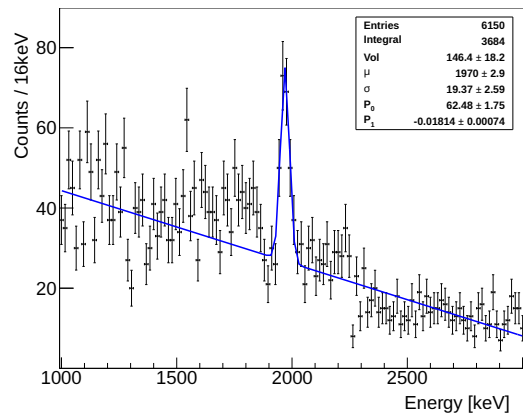


Figure 5.29: Add back γ -spectrum for ($M_{cry} = 2, M_{cluster} = 1$).

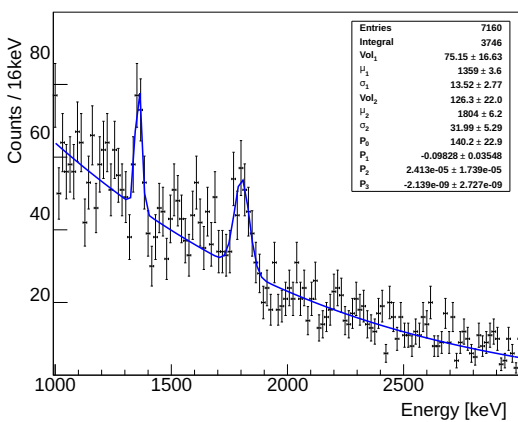


(a) Polynomial background where $Res_{vol}^{poly} = 12.0\%$.

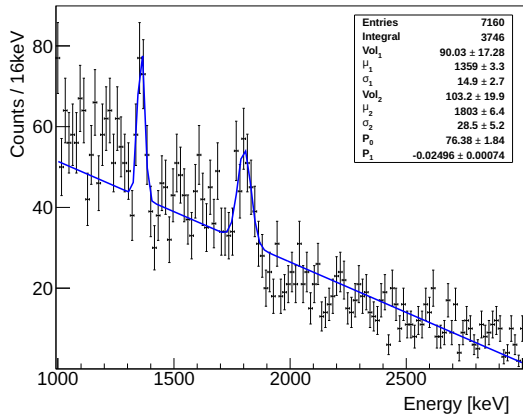


(b) Linear background where $Res_{vol}^{lin} = 12.4\%$.

Figure 5.30: ^{36}Ar γ -spectra with optimal gates containing singles and add-back events. $Res_{vol} = 12.2\%$.



(a) Polynomial background where $Res_{vol}^{poly} = \frac{22.1\% + 17.4\%}{2} = 19.8\%$.



(b) Linear background where $Res_{vol}^{lin} = \frac{19.2\% + 19.3\%}{2} = 19.3\%$.

Figure 5.31: ^{33}Ar γ -spectra with optimal gates containing singles and add-back events. $Res_{vol} = 19.6\%$.

are used to measure the change of angle after a reaction within the secondary target. Together with the FRS tracking information, the scattering angle is deduced for each single ion. The precise determination of the angle can be very important for the selection of Coulomb excitation events and for the rejection of other reaction mechanisms. The scattering angle, θ , is deduced from the angular deviation of the trajectory of the ion behind the secondary target with respect to the momentum vector before the target. Fig. 5.32 shows a sketch of the trajectories and the available position sensitive detectors.

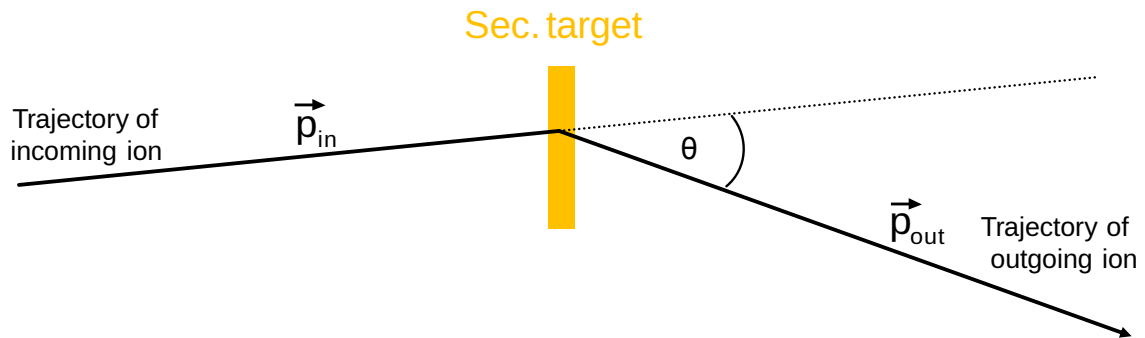


Figure 5.32: Illustration of determination of the scattering angle θ from ion tracking before and after the secondary target.

The distribution of counts per scattering angle interval ($\frac{\text{Counts}}{\delta\theta}$) is studied for the full energy range of the coincident γ -spectrum and separately for the discrete peaks relating ^{33}Ar and ^{36}Ar . Fig. 5.33 shows the counts per $\delta\theta = 2$ mrad for both regions in the ^{36}Ar γ -spectrum and fig. 5.34 shows the same for both ^{33}Ar peaks and the full energy range. In these spectra, the counts in the peak regions are scaled by a factor of 10.

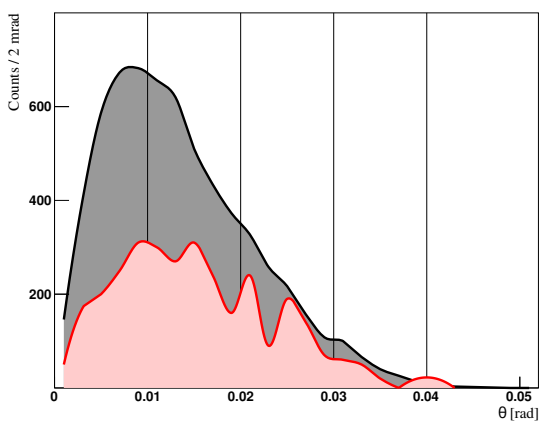


Figure 5.33: Counts per 2 mrad for ^{36}Ar . Black: full energy range and red: 1938-2016 keV (scaled x10).

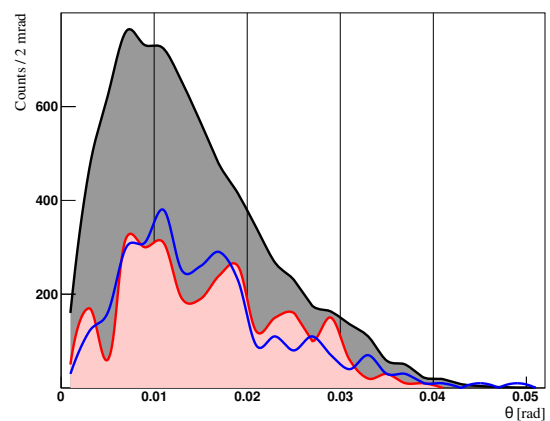
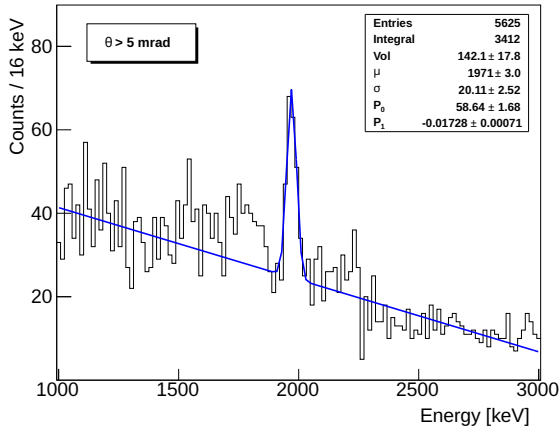
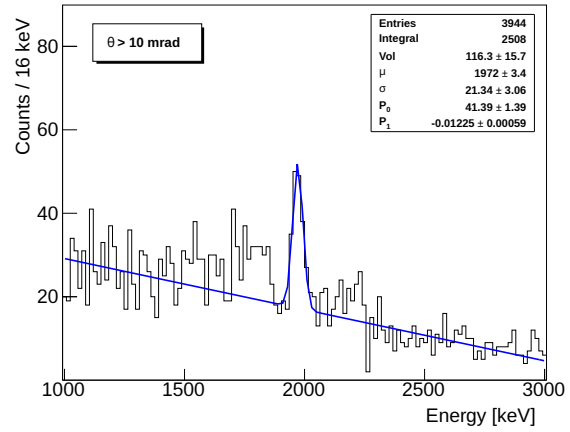


Figure 5.34: Counts per 2 mrad for ^{33}Ar . Black: full energy range, blue: 1328-1392 keV and red: 1760-1840 keV (both scaled x10).

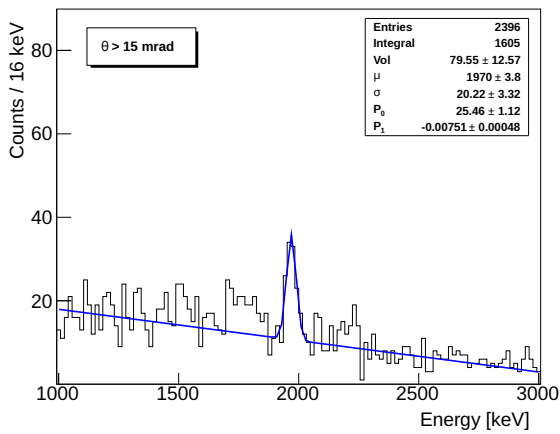
In the small scattering angle range under extreme forward angles ($\theta < 20$ mrad), the discrep-



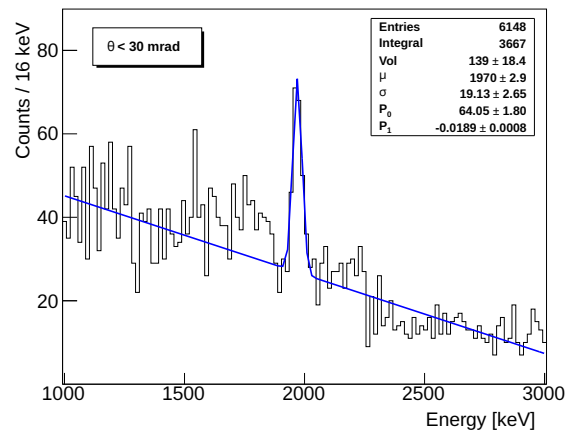
(a) $\theta > 5$ mrad.



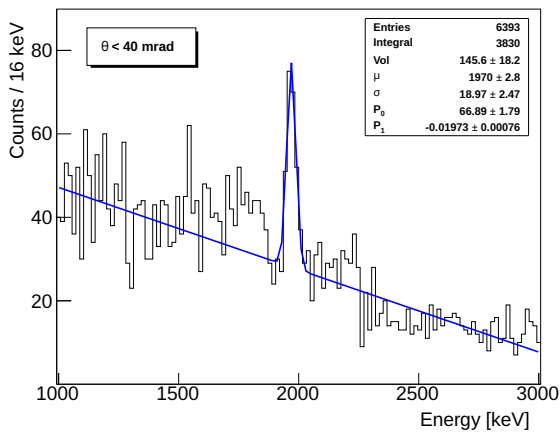
(b) $\theta > 10$ mrad.



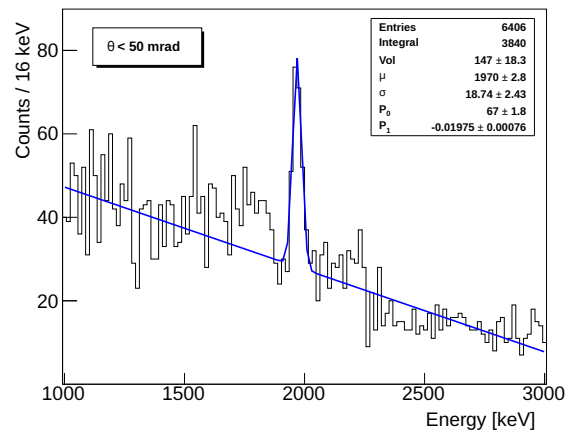
(c) $\theta > 15$ mrad.



(d) $\theta < 30$ mrad.



(e) $\theta < 40$ mrad.



(f) $\theta < 50$ mrad.

Figure 5.35: γ -spectra of ^{36}Ar for different limitations on θ .

ancy between the black and coloured distributions seems to be more pronounced than for larger scattering angles. Fig. 5.35 shows γ -spectra for different lower/upper limits on θ . The results of the fits are summarized in tab. 5.3.

θ condition	Peak volume	Error	Res_{vol} [%]	Fraction of data [%]
none	146.4	18.2	12.4	100
> 5 mrad	142.1	17.8	12.5	88.9
> 10 mrad	116.3	15.7	13.5	65.3
> 15 mrad	79.6	12.6	15.8	27.3
< 30 mrad	139.0	18.4	13.2	95.5
< 40 mrad	145.6	18.2	12.5	99.7
< 50 mrad	147.0	18.3	12.4	99.9

Table 5.3: Results of the fits from fig. 5.35.

Comparing the relative error ratios of the peak volume (Res_{vol}) for the different θ conditions, the result is that all tested θ conditions worsen the final result. A plausible interpretation is that the applied particle conditions suppress most other reaction channels beside Coulomb excitation (cf. section 5.2). Furthermore, events with scattering angles in the range of the grazing angle are rare compared to events with smaller scattering angles (1-3 % of all events). Moreover, the uncertainty of the determination of the scattering angle is $\Delta\theta = 0.4^\circ = 7$ mrad. Thus, the changes caused by upper limits on the scattering angle, appear to be random fluctuations.

As a conclusion, the analysis is continued without any selection on the scattering angle θ .

5.5.7 Background subtraction

The time spectra of the Cluster detectors shown in fig. 5.36 comprises of four different contributions:

1. The prompt γ -ray peak from excited ions at the secondary target.
2. Delayed γ -rays from excited ions when being stopped in the LYCCA CsI scintillators.
3. A peak that is caused by the closing of the TDC time gate.
4. A time-independent, flat background.

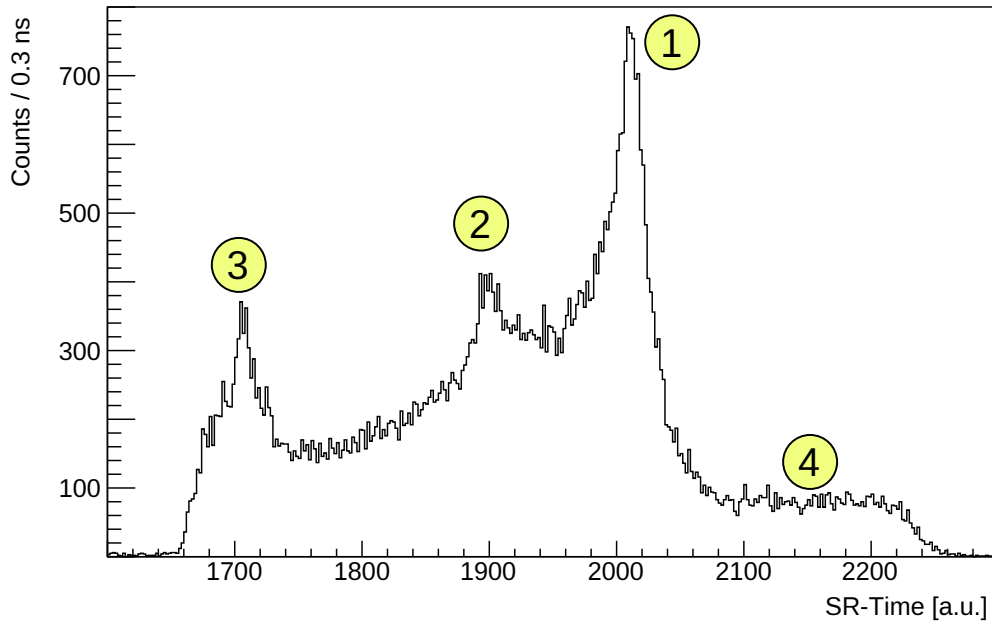


Figure 5.36: *SR* spectrum from the Cluster detectors which has an arbitrary offset where one channel is the equivalent to 0.3 ns. The numbers mark the different time regions that are described in the text.

The determination of the volume of the peaks in $^{36,33}\text{Ar}$ is affected by the background contributions. The background is formed by a superposition of different effects as, for example, ions that hit matter at undetected places close to the HPGe detectors, neutrons coming from the FRS and a continuous component. This background contribution cannot be completely removed by using the time correlations between the γ -ray and the SC41 which was the subject of the optimization procedure for the prompt time gate, because the contributions marked with '2' and '4' affect the prompt γ -peak ('1') within the chosen time gate. Thus, a background subtraction was applied to get the smallest error for the peaks in the γ -spectra. This is done by fitting the sum of a Gaussian function (for the prompt γ -peak) and a background function (4th order polynomial) to the time spectra to reproduce the distribution in the important area between channel 1900 and 2140. The background function (as function of the channel number ξ) that is shown fitted in fig. 5.37 is defined as:

$$b(\xi) = P_0 + P_1 \cdot \xi + P_2 \cdot \xi^2 + P_3 \cdot \xi^3 + P_4 \cdot \xi^4.$$

Background representing regions are defined (cf. fig. 5.37). Time gates on these regions are used to reproduce the background with a specific weight factor. Therefore, integrals of the function over the three marked regions are calculated. The weight factors (W_{1900} and W_{2100}) for both background regions are deduced as follows:

$$\frac{1}{2} \cdot \int_{1700}^{1940} b(\xi) d\xi = W_{1900} \cdot \int_{1900}^{1940} b(\xi) d\xi = W_{2100} \cdot \int_{2100}^{2140} b(\xi) d\xi.$$

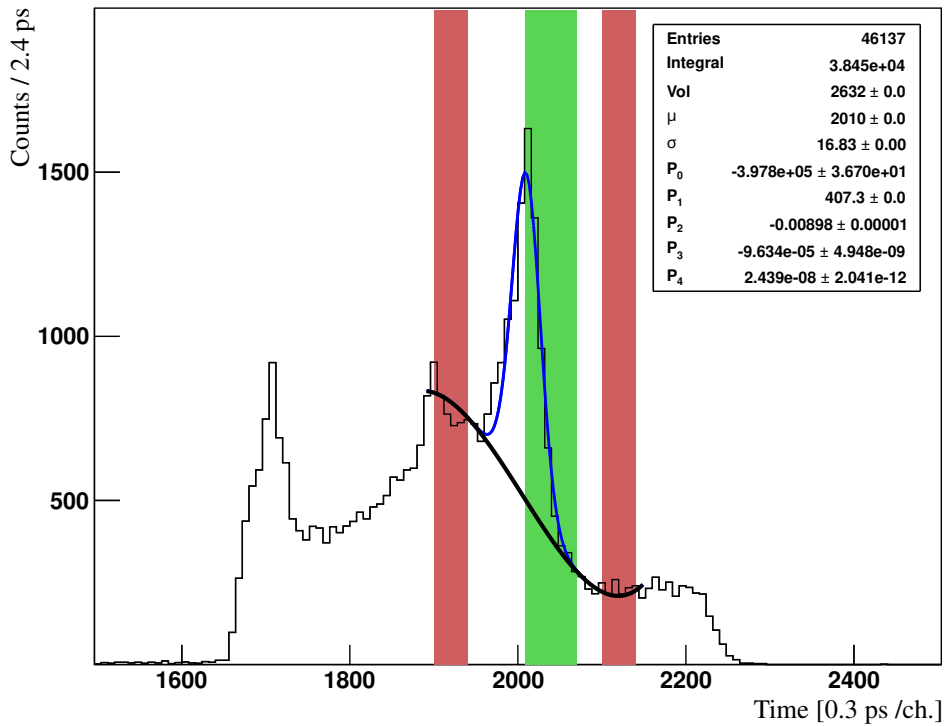
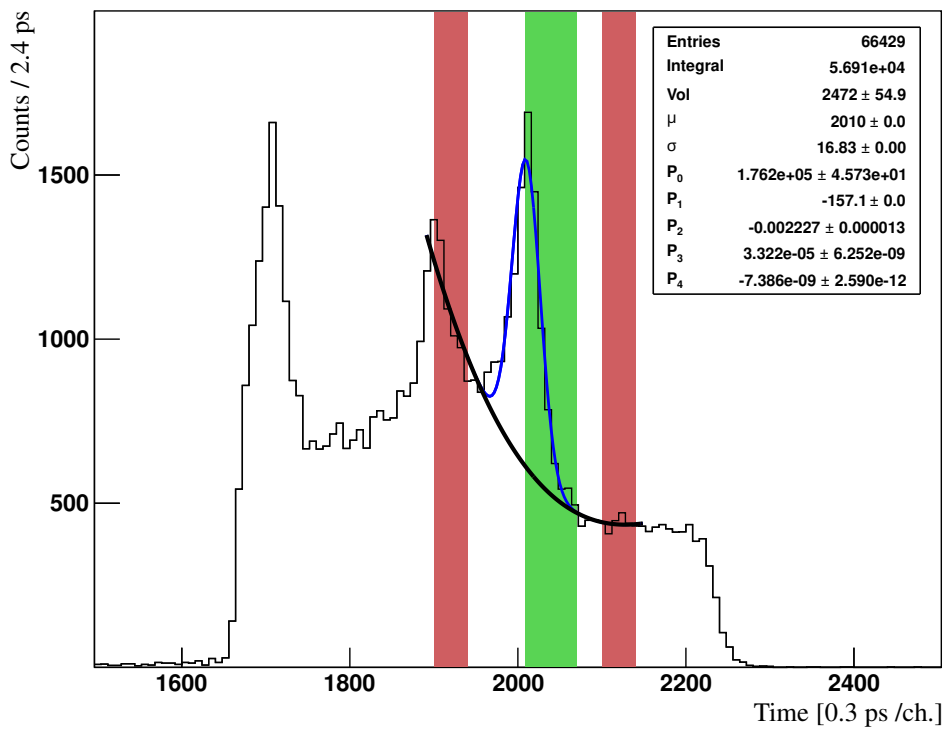
(a) ^{36}Ar .(b) ^{33}Ar .

Figure 5.37: Time difference between SC41 and the Cluster detector TDCs. Green box: time gate defined as in sec. 5.5.3, red boxes: background regions, black line: fitted background polynomial and blue line: fitted prompt (Gaussian shape) signal.

	^{36}Ar	^{33}Ar
P_0	-3.98E+05	1,76E+05
P_1	4.08E+02	-1,57E+02
P_2	-9.28E-03	-2,23E-03
P_3	-9.62E-05	3,32E-05
P_4	2.44E-08	-7,39E-09
\int_{1900}^{1940}	3080	4297
\int_{2009}^{2070}	4074	5584
\int_{2100}^{2140}	1154	2351
W_{1900}	0,377962	0,384746
W_{2100}	1,334844	0,913855

Table 5.4: Parameters and integrals of the background function and the calculated weight factors for the background subtraction.

Projecting the time intervals [1900;1940] and [2100;2140] of the energy versus time spectra (cf. fig. 5.16) with weight factors (given in tab. 5.4) yields the background spectra that are shown in fig. 5.38.

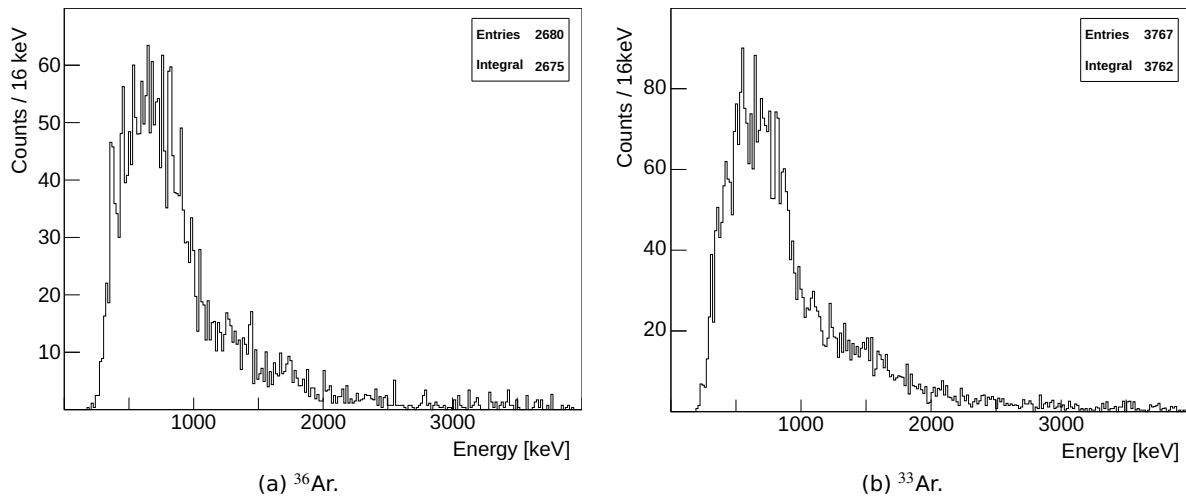


Figure 5.38: Background γ -spectra of the marked regions with the above described weighting factors.

The background spectra are then subtracted from the γ -spectra (fig. 5.30 and 5.31) which have been shown in sec. 5.5.5.

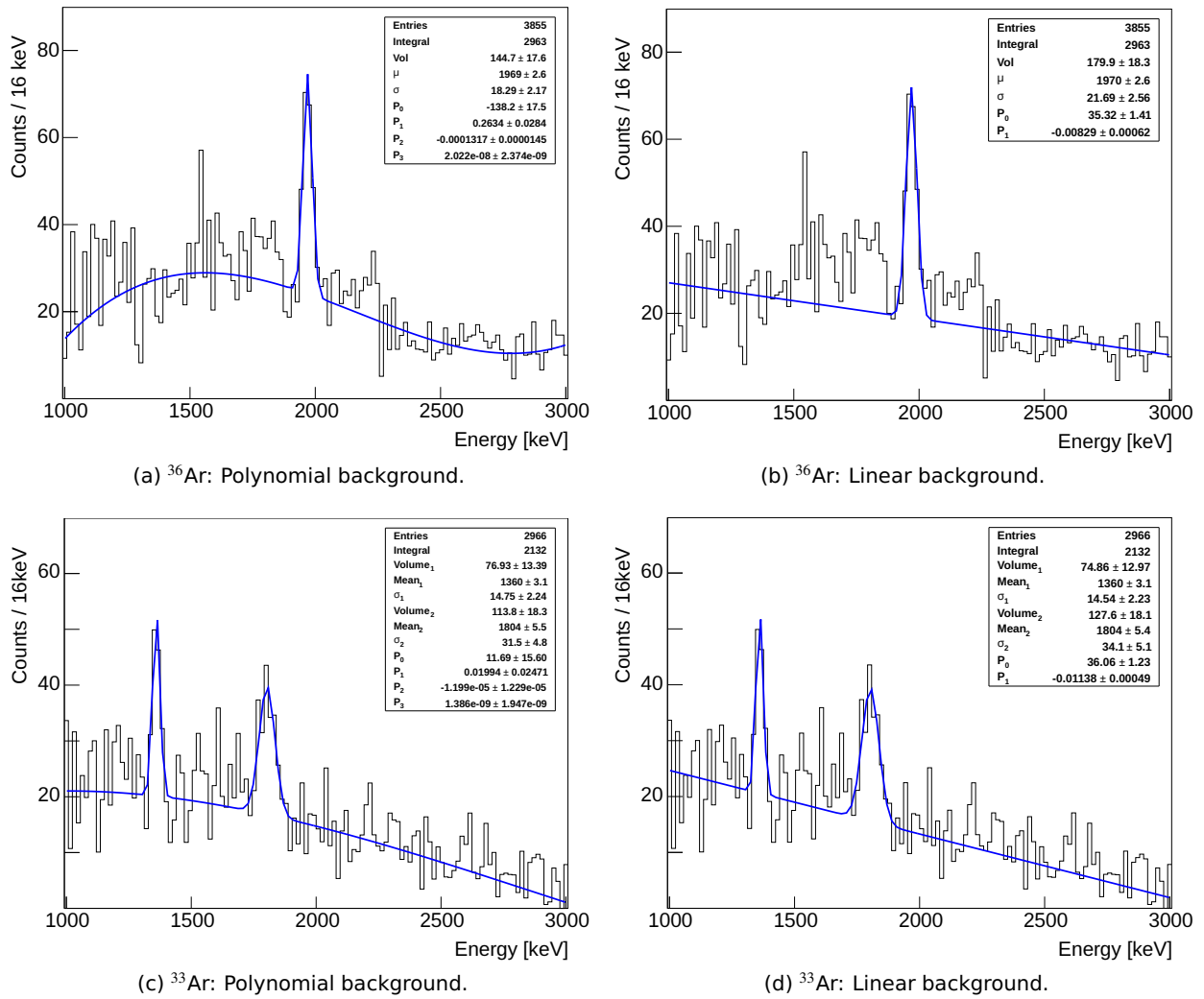


Figure 5.39: γ -spectra after background subtraction.

The result of these fits are shown in tab. 5.5.

Nucleus		^{36}Ar	^{33}Ar	
Energy		1970 keV	1359 keV	1798 keV
Poly. fit	Vol	144.7	76.93	113.8
	ΔVol	17.6	13.39	18.3
	Res_{vol}	12.2	17.4	16.1
Lin. fit	Vol	179.9	74.86	127.6
	ΔVol	18.3	12.97	18.1
	Res_{vol}	10.2	17.3	14.2

Table 5.5: Results of the fits after applying the background subtraction.

The background subtraction gives improved values for Res_{vol} following the fits. A linear fitted background yields better results than fitting a fourth order polynomial to the background.

5.5.8 Disparities in the γ -ray spectra of the different germanium detector rings

In the background subtracted ^{36}Ar spectrum (fig. 5.30, 5.40), the background is reduced by 20 %, compared to earlier phases of the data analysis. However, in the energy interval 1700 - 1900 keV and also around 1600 keV, large background contributions remain. While the latter does not affect the measurement of the ^{33}Ar transitions, the former influences the measurement of the 1798 keV transition.

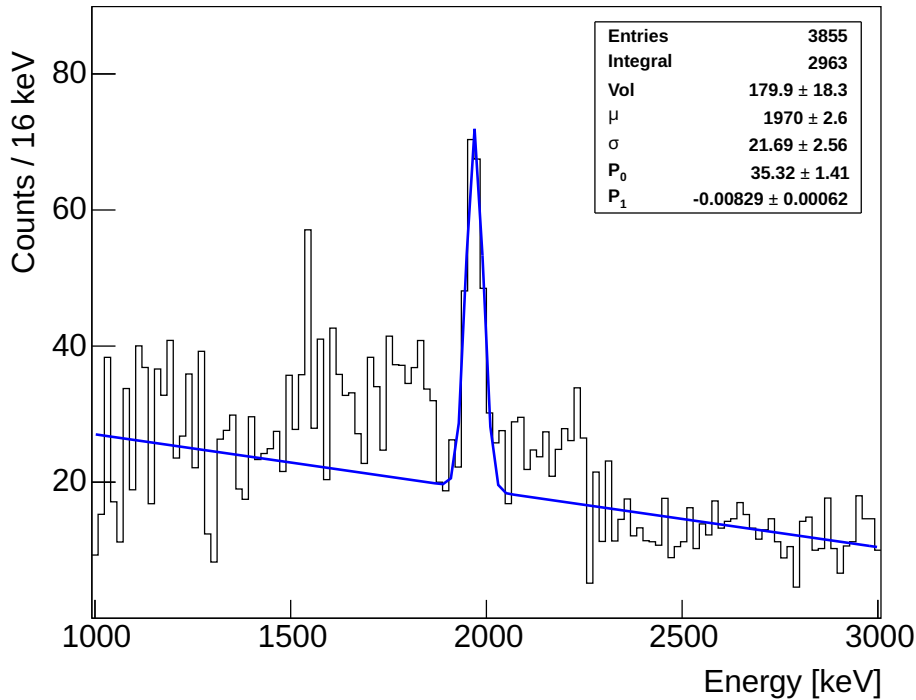


Figure 5.40: Background subtracted ^{36}Ar γ -ray spectrum.

To investigate the origin of the background structure, the γ -spectra of the different Ar isotopes are shown in fig. 5.41 for both germanium detector rings individually.

Fig. 5.41 illustrates that the main contribution to the background in the region 1700 - 1900 keV is caused by the outer ring (cf. fig. 5.41b). This is confirmed by fig. 5.41c and 5.41d, where the inner ring spectrum shows a much narrower 1798 keV peak (FWHM = 49 keV) than the outer ring spectrum (FWHM = 82 keV). Tab. 5.6 summarizes the final numbers of detected γ -rays for both isotopes.

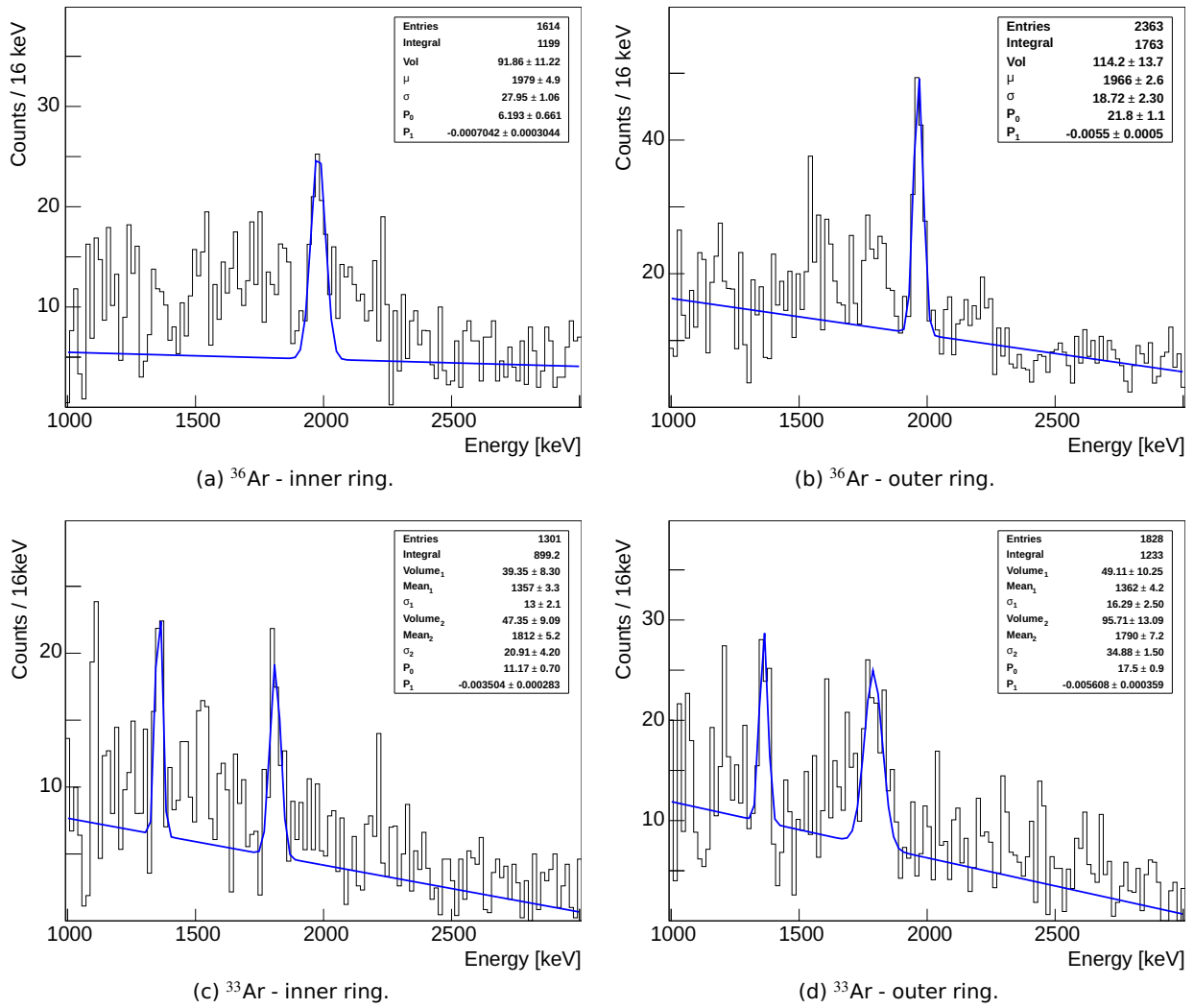


Figure 5.41: Background subtracted γ -spectra of $^{33,36}\text{Ar}$ for both individual germanium rings.

Ion	^{36}Ar		^{33}Ar			
	energy of γ -ray		1359 keV		1798 keV	
	value	error	value	error	value	error
Counts (inner ring)	91.9	11.2	39.4	8.3	47.4	9.1
Counts (outer ring)	114.2	13.7	49.1	10.3	95.7	13.1
$\frac{\text{Counts}(oR)}{\text{Counts}(iR)}$	1.24	0.21	1.25	0.31	2.02	0.48
Total counts	179.9	18.3	74.9	13.0	127.6	18.1

Table 5.6: Detected γ -rays according to section 5.5.7 and 5.5.8.

The count-ratio between the outer and inner germanium detector rings greatly differs between the higher energetic ^{33}Ar peak and the other two peaks. Thus, the calculation of the exact value of this transition strength is done by only taking the data of the inner ring of germanium detectors (cf. sub sec. 6.3.3).

5.6 Summary of data analysis

A detailed analysis of all components was needed to separate the signals from discrete gamma-transitions and to get the best peak-to-background ratio in the spectra. Table 5.7 summarizes the evolution of these improvements depending on the different analysis steps. The values of the Res_{vol} (in %) resolution has direct impact on the error of the final $B(E2)$ value calculated in chapter 6.

Step of analysis	^{36}Ar		^{33}Ar	
	poly. bg.	lin. bg.	poly. bg.	lin. bg.
prelim. time/particle gates	18.8	18.7	22.2	21.3
$M_{tar} = 1$	16.9	16.4	21.5	21.0
optimal particle gate	16.7	15.5	23.5	21.9
optimal time gate	16.3	15.3	22.5	31.1
add back	12.0	12.4	19.8	19.3
background subtraction	12.2	10.2	17.4	15.2

Table 5.7: Values of Res_{vol} (in %) after each step of the analysis. The steps are applied cumulatively, replacing gates of the same type.

The Res_{vol} value drops smoothly for ^{36}Ar . For ^{33}Ar , Res_{vol} shows also steady trend except in the step, where the time gate is changed and a linear background function is used. This is caused by the poor matching of the linear background fit in the special case (e.g. fig. 5.28, right).

Finally, all analysis steps that are shown in this chapter (except scattering angle, cf. sec. 5.5.6) are helpful and are used to extract the needed experimental information.

Loss of the ^{33}Ar beam with respect to the trigger

Fig. 5.42 shows the relative loss of ions in the analysis on their flight path from the FRS downstream to the position of rest in the LYCCA chamber for the two different triggers. The particle trigger is given by the SC41 scintillator, the particle- γ -trigger requires a coincidence between a signal from the EUROBALL Cluster detectors and the SC41.

The quantity of ^{33}Ar ions is normalized to the number of ions that is identified in the FRS as being ^{33}Ar . The following accumulations describe the losses of the ^{33}Ar ions at the different stages of the analysis. The three central columns are related to a valid signal in the target DSSD, a proper tracking by LYCCA and valid time-of-flight signal by the LYCCA plastic scintillators. The four columns on the right hand side represent the influence of the particle gates (as described in sec. 5.2).

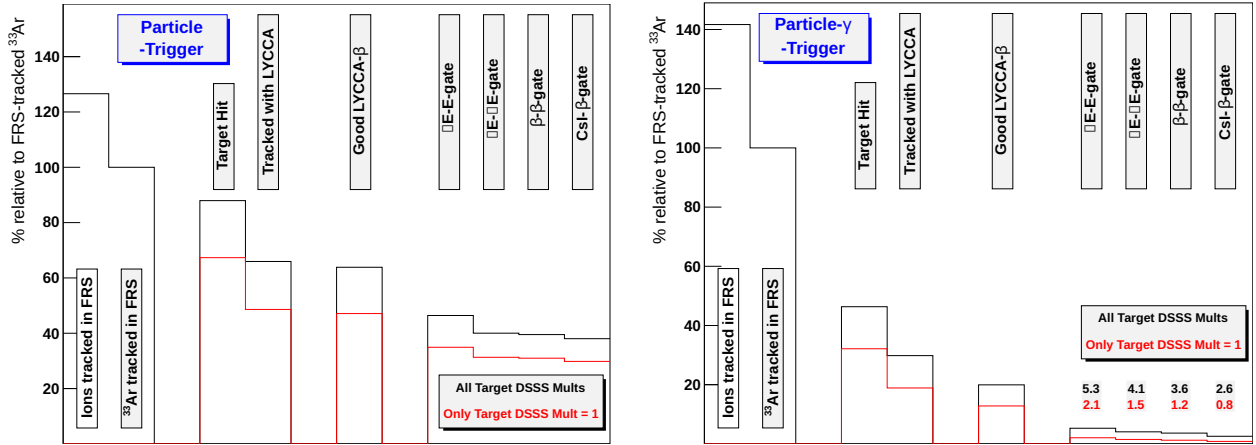


Figure 5.42: Relative ion transmission for the particle trigger (left) and particle- γ -trigger (right).

Discussion of transmission and efficiency of the setup relates to the distribution of the particle-trigger, because most particle- γ -triggers were not caused by reactions at the secondary target but by background effects.

For the given geometry of the setup and typical FRS beams (small angular spread: $\vartheta < 13$ mrad, beam spot in the range of 4 cm FWHM), the bottleneck should be to hit the target. By design, most ions (> 95 %) that hit the target are expected to reach the LYCCA chamber. This assumption cannot be verified by fig. 5.42. A steady loss is visible with approximately 10 % due to not hitting the target, 25 % due to not hitting the chamber and another 20 % due to applying the particle gates (all values with respect to the ^{33}Ar beam identified by the FRS).

	Lise++ simulation	Experimental data from experiment S377
Accumulated ^{36}Ar ions on production target	$2.9 \cdot 10^{14}$	$\approx 5.9 \cdot 10^{14}$
Identified ^{33}Ar ions by the FRS	$1.0 \cdot 10^9$	$1.27 \cdot 10^9$
Detected ^{33}Ar ions by LYCCA	$8.9 \cdot 10^8$	$4.623 \cdot 10^8$
Detected ^{33}Ar ions by LYCCA, $M_{tar} = 1$	$> 8.8 \cdot 10^8$	$3.695 \cdot 10^8$

Table 5.8: Summary of ^{33}Ar production in experiment S377.

In summary, the loss due to target miss can be explained by the large beam spot at the final focal plane of the FRS. Furthermore, the last 20 % loss (caused by the particle gates) is accepted to reject other nuclear reactions other than Coulomb excitation. However, the loss of one fourth of the ions that hit the target DSSD but do not reach the detectors inside of the LYCCA chamber is striking.

The FRS-LYCCA-transmission (FLT) is defined as $FLT_{exp/sim} = \left(\frac{\text{Detected } ^{33}\text{Ar} \text{ ions by LYCCA}}{\text{Identified } ^{33}\text{Ar} \text{ ions by the FRS}} \right)_{exp/sim}$ and deduced from experimental data and simulations (cf. 5.8):

$$FLT_{exp} = 36.4\%$$

$$FLT_{sim} = 89.0\%.$$

This has to be studied further using detailed simulations and in future experiments.

Chapter 6

Experimental results

The aim of the experiment is the investigation of the reduced transition strengths ($B(E2)$ values) of the two lowest energetic excited states in ^{33}Ar (1359 keV and 1798 keV).

Therefore, the absolute γ -efficiency of the the PreSpec setup ε is determined by the measurement of γ -rays from a transition with a known $B(E2)$ value. Although, several measurements with different experimental techniques provide a trustable $B(E2; 2_1^+ \rightarrow g.s.)$ value for ^{36}Ar , a new measurement shows a clear deviation [111]. For this analysis, the adopted value provided by ref. [57] is used, whereas the effect of the new result is discussed in subsection 6.3.4. In this experiment, this was the decay from the first excited state in ^{36}Ar to the ground state (pure $E2$ -transition, $2_1^+ \rightarrow 0^+$, 1970 keV, cf. eq. 6.1). Feeding from the higher lying 3_1^- state is considered. After the application of relative efficiency corrections, the transition strengths of the ^{33}Ar transitions can be deduced from the Coulomb excitation cross sections (cf. eq. 6.2).

$$N^{36\text{Ar}} = \sigma_{tot}^{36\text{Ar}} \cdot n \cdot I \cdot \varepsilon \quad (6.1)$$

$$N^{33\text{Ar}} = \sigma_{tot}^{33\text{Ar}} \cdot n \cdot I \cdot \varepsilon \cdot \varepsilon_{cor}(E_\gamma, \beta^{33\text{Ar}}) \quad (6.2)$$

Here $N^{36,33\text{Ar}}$ is the number of detected γ -rays, n is the number of reaction centers in the secondary target, I is the number of ions impinging on the target, ε is the γ -ray detection efficiency for γ -rays of 1.97 MeV (in the rest frame) that is emitted from a source moving with $\beta = 0.5714$ and $\varepsilon_{cor}(E_\gamma, \beta^{33\text{Ar}})$ is the relative correction to the efficiency for different energies of γ -rays and a change of the velocity of the source. I is measured by the particle detectors and n is the same for the measurement of both isotopes. The absolute efficiency calibration is shown in section 6.1. The efficiency of the germanium detectors depends on the energy of the γ -rays and the velocity of the emitting ion. Both is different for ^{36}Ar and ^{33}Ar . The relative corrections for these effects changing the γ -efficiency are shown in section 6.2. With these corrections, it possible to deduce σ_{tot} for both transitions in ^{33}Ar from the experimental data. Subsection 6.3 describes the calculation of the reduced transition strengths of ^{33}Ar .

6.1 γ -ray detection efficiency

The total Coulomb excitation cross section, σ_{tot} , of ^{36}Ar is related to the known $B(E2)$ value.

$$\begin{aligned}\sigma_{tot} &\propto \frac{1}{2J_i + 1} \cdot B(E2) \\ \Leftrightarrow \sigma_{tot} &= F \cdot B(E2)\end{aligned}$$

The proportionality factor, F , is the ratio between Coulomb excitation cross section and the $B(E2, 0^+ \rightarrow 2^+)$ value; F depends on mass, spins, the energy of the transition and the energy of the projectile, is calculated by 'dweiko'. The computer program 'dweiko' (Distorted Wave EIKOnal Approximation) calculates the elastic and inelastic scattering in intermediate and high energy nuclear collisions. A coupled-channels method is used for Coulomb and nuclear excitations of $E1$, $E2$, $E3$, $M1$ and $M2$ multipolarities, respectively. The program applies to an arbitrary nucleus, specified by the spins and energies of the levels and by reduced matrix elements. For given bombarding conditions, the angular distribution of elastic and inelastic scattered particles and angular distributions of gamma-rays from the excited nucleus are computed [56]. Tab. 6.1 lists the proportionality factors for all observed transitions in $^{36,33}\text{Ar}$ (the values for ^{33}Ar are used in section 6.3).

	transition	F [$mb/e^2 fm^4$]
^{36}Ar	$0^+ \rightarrow 2^+$	0.193(1)
^{33}Ar	$\frac{1}{2}^+ \rightarrow \frac{3}{2}^+$	0.093(1)
	$\frac{1}{2}^+ \rightarrow \frac{5}{2}^+$	0.094(1)

Table 6.1: Proportional factors.

With the known $B(E2)$ value of ^{36}Ar (cf. tab. 6.2, taken from [57]) and the proportionality factor, F , the total Coulomb excitation cross section is calculated:

$$\begin{aligned}\sigma_{tot} &= F \cdot B(E2) \\ &= 0.193 \frac{mb}{e^2 fm^4} \cdot 300(30) e^2 fm^4 \\ &= 57.9(5.8) mb.\end{aligned}\tag{6.3}$$

Only ions with a trajectory that have a smaller angular deviation from the central trajectory of 2.1° (in the following called 'valid trajectory') reach the LYCCA chamber. Thus, the quantity measured experimentally is not σ_{tot} , but $\tilde{\sigma}_{tot}$, which is the Coulomb excitation cross section under the condition that the scattering angle is smaller than 2.1° :

$$\tilde{\sigma}_{tot} = \eta \cdot \sigma_{tot}.\tag{6.4}$$

The factor, η (ratio between total cross section associated with a valid trajectory of the ion and σ_{tot}), has been calculated using 'dweiko'[56] for both ion species.

	Value	Uncertainty
$B(E2, 0^+ \rightarrow 2^+) [e^2 fm^4]$	300	30
$F [mb/e^2 fm^4]$	0.193	0.001
$\sigma_{tot}^{E2} [mb]$	57.9	5.8
η	0.965	0.001
$\tilde{\sigma}_{tot}^{E2} [mb]$	55.87	5.59

Table 6.2: Calculation of the total Coulomb excitation cross section $\tilde{\sigma}_{tot}$ of the $2^+ \rightarrow 0^+$ transition in ^{36}Ar .

In ^{36}Ar , two known transitions that couple to the ground state populate the 2_1^+ state: the mayor $E2$ transition ($0^+ \rightarrow 2_1^+$) and the minor $E3$ transition ($0^+ \rightarrow 3_1^+$). The latter one de-excites with a probability of 93.2 % to the 2_1^+ state. The $B(E3, 0^+ \rightarrow 3^-)$ value of this transition is $1.09(15) \cdot 10^4 e^2 fm^6$ [112]. The total $E3$ cross section is calculated with 'dweiko': $\sigma_{tot}^{E3} = 1.91(19) mb$. Similar to the $E2$ transition the factor $\eta = 0.917(1)$ is calculated, which leads to a $E3$ cross section with valid trajectory of $\tilde{\sigma}_{tot}^{E3} = 1.74(18)$. Thus, the total Coulomb excitation cross section to the 2_1^+ state is given by:

$$\tilde{\sigma}_{tot} = \tilde{\sigma}_{tot}^{E2} + 0.932 \cdot \tilde{\sigma}_{tot}^{E3} = 55.87(5.59) + 0.932 \cdot 1.74(18) mb = 57.49(5.59) mb.$$

Coulomb excitation reaction rates are determined by the equation:

$$\frac{\partial N}{\partial t} = \tilde{\sigma}_{tot} \cdot n \cdot \varepsilon \cdot \frac{\partial I}{\partial t}, \quad (6.5)$$

where $\frac{\partial N}{\partial t}$ is the reaction rate, $\tilde{\sigma}_{tot}$ is the total Coulomb excitation cross section for ions with a valid trajectory, n is the number of reaction centers in the target, ε is the efficiency of the gamma-ray detection (for this specific case) and $\frac{\partial I}{\partial t}$ is the rate of ions on the target. Integrating over the full time of the experiment ($\sigma_{Coulomb}$, n and ε are time-independent) leads to:

$$N = \tilde{\sigma}_{tot} \cdot n \cdot \varepsilon \cdot I \iff \varepsilon = \frac{N}{\tilde{\sigma}_{tot} \cdot n \cdot I}, \quad (6.6)$$

where N is the number of detected γ -rays. I is the number of ^{36}Ar ions passing the secondary target that are associated with $M_{ta} = 1$ events and identified by the FRS and by LYCCA. If all quantities apart from the efficiency are known, the efficiency can be deduced. Tab. 6.3 illustrates the calculation.

	Quantity	Value	Uncertainty
N_{iR}	Number of detected γ -rays in the inner ring	91.9	11.2
N_{oR}	Number of detected γ -rays in the outer ring	114.2	13.7
N	Number of detected γ -rays in both rings	179.9	18.3
I	^{36}Ar ions on target [10^6]	153.8	0.01
n	Scatt. centers at target [mb^{-1}]	$1.18 \cdot 10^{-6}$	$6 \cdot 10^{-8}$
$\tilde{\sigma}_{tot}$	Coulomb exc. cross sec. for ions with valid trajectory [mb]	55.87	5.59
ε_{iR}	Efficiency of the inner ring	0.88	0.14
ε_{oR}	Efficiency of the outer ring	1.10	0.18
$\varepsilon_{iR} + \varepsilon_{oR}$	Sum of efficiencies of both rings (from individual fits)	1.98	0.23
ε	Efficiency of the full array (from fit of the summed spectra)	1.73	0.26

Table 6.3: Calculation of the γ -ray efficiencies of the PreSpec setup and for the germanium detector rings individually.

Within the error bars, the summed efficiency of both detector rings ($\varepsilon_{iR} + \varepsilon_{oR}$) is in agreement with the efficiency of the full array (ε), which is deduced from the summed spectra of all detectors. The values for ε , ε_{iR} and ε_{oR} correspond to the efficiency for the detection of a γ -ray of 1.97 MeV that is emitted by a moving ion at $\beta = 0.5714$. Using the information listed above, the $B(E2)$ values of the ^{33}Ar transitions are calculated in the following subsections.

6.2 Corrections for the γ -ray detection efficiency

The efficiency of the germanium detectors depend on the energy of the γ -rays. Therefore, the fact that the γ -rays originating from ^{33}Ar have lower energies than those from ^{36}Ar (1359 and 1798 keV instead of 1970 keV) has to be taken into account. The energy-dependent change of efficiency of the germanium array is described in sub sec. 6.2.1.

Additionally, the ^{36}Ar and ^{33}Ar ions travel at slightly different mean velocities which also has an effect on the efficiency of the germanium detectors due to a different Lorentz boost. Corrections for these effects are calculated in the following two subsections.

6.2.1 Energy dependence of the efficiency of germanium detectors

The efficiency of germanium detectors and their dependency on the energy of a γ -ray has been studied for a long time and is generally not easy to describe [54]. In this experiment, the γ -ray energies are (due to Doppler shifts at different angles) in the range of 2800 - 3300 keV in the case of ^{36}Ar (1970 keV in the center of mass (c.m.) frame), whereas in the case of ^{33}Ar , the shifted energies are in the ranges 2000 - 2300 keV (1st excited state is 1359 keV in the c.m. frame) and 2600 - 3100 keV (2nd excited state is 1798 in the c.m. frame). To calculate the $B(E2)$ values of these two transitions, the numbers of detected γ -rays have to be compared. Thus, a correction for the energy dependency of the efficiency of the germanium has to be applied.

Fig. 6.1 shows experimentally measured efficiencies of a EUROBALL Cluster detector over a wide energy range, taken from the work of T. Steinhardt [55]. The values correspond to complete absorption of the energy of a γ -ray and are normalized to the efficiency for the detection a γ -ray with an energy of 1 MeV. In this data the add-back technique is included. The curve is fitted with a 5th order polynomial function, to create a correction function for the efficiency which has the form:

$$\varepsilon(E) = a_0 + a_1 \cdot E + a_2 \cdot E^2 + a_3 \cdot E^3 + a_4 \cdot E^4 + a_5 \cdot E^5. \quad (6.7)$$

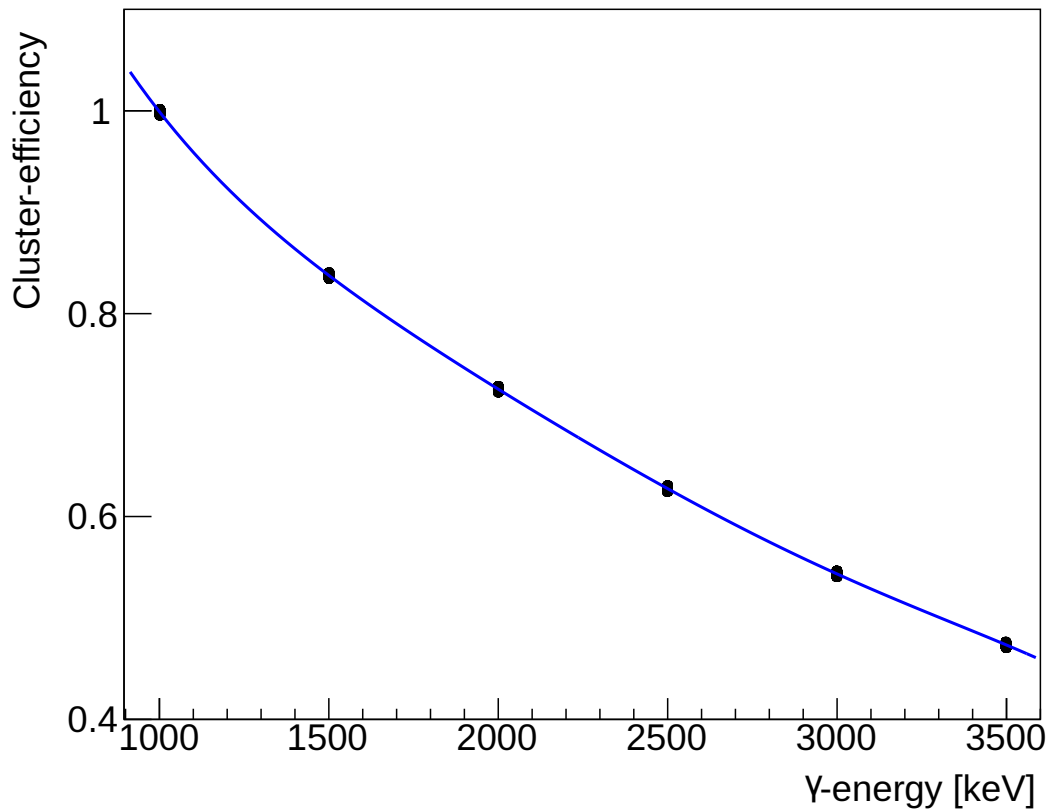


Figure 6.1: Energy-dependent efficiency of an EUROBALL Cluster detector, normalized to the efficiency for detecting a 1 MeV γ -ray, fitted between 1.0 and 3.5 MeV.

a_i	coefficients [(keV) $^{-i}$]	error [(keV) $^{-i}$]
a_0	1.997	1.1E-02
a_1	-1.937E-03	1.1E-05
a_2	1.406E-06	3.9E-09
a_3	-5.744E-10	1.3E-12
a_4	1.172E-13	4.0E-16
a_5	-9.380E-18	9.2E-20

Table 6.4: Parameters of efficiency fit (eq. 6.7).

As the germanium detectors are arranged into two rings with different angles to the beam line, the energy dependent change of the efficiency is calculated for both rings individually. Table

6.5 shows the energies of the observed transitions, the energies detected in the laboratory frame and the energy dependent efficiency correction parameters.

	E [keV]	E_{lab} [keV]	$\frac{\varepsilon(E_{lab})}{\varepsilon(1MeV)}$	$\Delta \left[\frac{\varepsilon(E_{lab})}{\varepsilon(1MeV)} \right]$
inner ring				
^{36}Ar	1970	3232	0.510	0.004
^{33}Ar	1359	2283	0.669	0.001
	1798	3020	0.540	0.003
outer ring				
^{36}Ar	1970	2854	0.566	0.002
^{33}Ar	1359	1997	0.726	0.001
	1798	2642	0.602	0.002

Table 6.5: Calculated efficiencies (and errors) in arbitrary units dependent on the energy of the γ -rays.

The quotient $\zeta_{E_2}^{E_1} = \frac{\varepsilon(E_1)}{\varepsilon(E_2)}$ depends on the different detection efficiency of the germanium detector array at the two γ -ray energy values E_1 and E_2 . Thus, $\zeta_{E_2}^{E_1}$ corrects for the energy-dependence of the germanium detector array, even without knowledge of the absolute efficiency. The correction factors, are calculated for each E_{lab} with respect to the Doppler-shifted energy of the ^{36}Ar 1970 keV transition. The expressions 6.8 to 6.11 give the correction factors for the change in efficiency for detecting Doppler-shifted γ -rays of 1359 keV and 1798 keV (in the c.m. frame) instead of a γ -ray of 1970 keV (in the c.m. frame) for both germanium detector rings.

$$\left(\zeta_{1970keV}^{1359keV} \right)^{iR} = 1.311(8), \quad (6.8)$$

$$\left(\zeta_{1970keV}^{1798keV} \right)^{iR} = 1.059(9) \quad (6.9)$$

$$\left(\zeta_{1970keV}^{1359keV} \right)^{oR} = 1.283(4) \quad (6.10)$$

$$\left(\zeta_{1970keV}^{1798keV} \right)^{oR} = 1.063(5) \quad (6.11)$$

The correction factors are averaged with respect to the efficiencies of both rings as calculated in section 6.1 ($\varepsilon_{iR} = 0.88(14)\%$ and $\varepsilon_{oR} = 1.10(18)\%$).

$$\left(\zeta_{1970keV}^{1359keV} \right) = \frac{\varepsilon_{iR} \cdot \left(\zeta_{1970keV}^{1359keV} \right)^{iR} + \varepsilon_{oR} \cdot \left(\zeta_{1970keV}^{1359keV} \right)^{oR}}{\varepsilon_{iR} + \varepsilon_{oR}} = 1.295(4)$$

$$\left(\zeta_{1970keV}^{1798keV} \right) = \frac{\varepsilon_{iR} \cdot \left(\zeta_{1970keV}^{1798keV} \right)^{iR} + \varepsilon_{oR} \cdot \left(\zeta_{1970keV}^{1798keV} \right)^{oR}}{\varepsilon_{iR} + \varepsilon_{oR}} = 1.061(5)$$

These results are used in sec. 6.3 to determine the B(E2) values of the investigated ^{33}Ar transitions.

6.2.2 Correction for different ion velocities

The ions are the source of the detected γ -rays and move at relativistic velocities. Thus, they are affected by relativistic effects, especially the relativistic length contraction (also Lorentz contraction). Lengths that are parallel to the movement of the ions are shorter in the rest frame of the ions than in the laboratory frame:

$$L = L_0 \sqrt{1 - \beta^2}$$

where L is a length observed in the rest frame of the ions, L_0 is the length in the laboratory frame and β the velocity in units of the speed of light.

This affects the relative angles in particular when changing between the laboratory frame and the center of mass frame of the ion ($\vartheta^{rest} \neq \vartheta^{lab}$). Here, ϑ is the angle between the flight path of the ion and the emitted γ -ray. This has two effects:

- Firstly, the probability to detect a γ -ray at a certain angle is different due to a change of solid angle coverage.
- Secondly, the angular distribution (W) of the emitted γ -rays changes: $W_{rest} \neq W_{lab}$.

Mathematically, the transformation between the different systems of inertia is explained by a Lorentz boost [85]. The angular distribution of an E2 transition in the center-of-mass system of the ion (rest frame) is given by:

$$W_{rest}(\cos \vartheta^{rest}) = \frac{1}{4\pi} (1 + a_2 P_2(\cos \vartheta^{rest}) + a_4 P_4(\cos \vartheta^{rest}) + \dots), \quad (6.12)$$

where P_n are the Legendre polynomials:

$$P_2(x) = \frac{1}{2}(3x^2 - 1) \text{ and } P_4(x) = \frac{1}{8}(35x^4 - 30x^2 + 3).$$

According to references [78, 79], two transformations are needed:

Firstly, the γ -ray emission angle, ϑ , has to be transformed from the rest frame of the ion into the laboratory system:

$$\begin{aligned} \cos \vartheta^{rest} &= \Theta(\cos \vartheta^{lab}) = \frac{\cos \vartheta^{lab} - \beta}{1 - \beta \cos \vartheta^{lab}} \\ \iff \cos \vartheta^{lab} &= \Theta^{-1}(\cos \vartheta^{rest}) = \frac{\beta + \cos \vartheta^{rest}}{\beta \cos \vartheta^{rest} + 1} \end{aligned} \quad (6.13)$$

And secondly, the change of the solid angles of the detectors ($d\Omega$) when switching between the two systems of inertia has to be taken into account:

$$\omega(\cos \vartheta^{lab}) = \frac{d\Omega^{lab}}{d\Omega^{rest}} = \frac{1 - \beta^2}{(1 - \beta \cos \vartheta^{lab})^2} \quad (6.14)$$

To get the angular distribution of an E2 transition that is emitted from a moving ion as observed in the laboratory frame, eq. 6.12, 6.13 and 6.14 have to be combined:

$$\begin{aligned} W_{lab}(\cos \vartheta^{lab}) &= W_{rest}(\cos \vartheta^{rest}) \cdot \omega(\cos \vartheta^{lab}) \\ &= W_{rest}(\Theta(\cos \vartheta^{lab})) \cdot \omega(\cos \vartheta^{lab}). \end{aligned} \quad (6.15)$$

Fig. 6.2 shows

- $W_{rest}(\cos \vartheta^{rest})$, the angular distribution of an E2 transition as seen in the source's rest frame
- $W_{rest}(\cos \vartheta^{lab})$, Lorentz transformed distribution
- $W_{lab}(\cos \vartheta^{lab})$, the observed distribution in the system of inertia of the laboratory

for an ion traveling at $\beta = 0.5714$ (speed of ^{36}Ar).

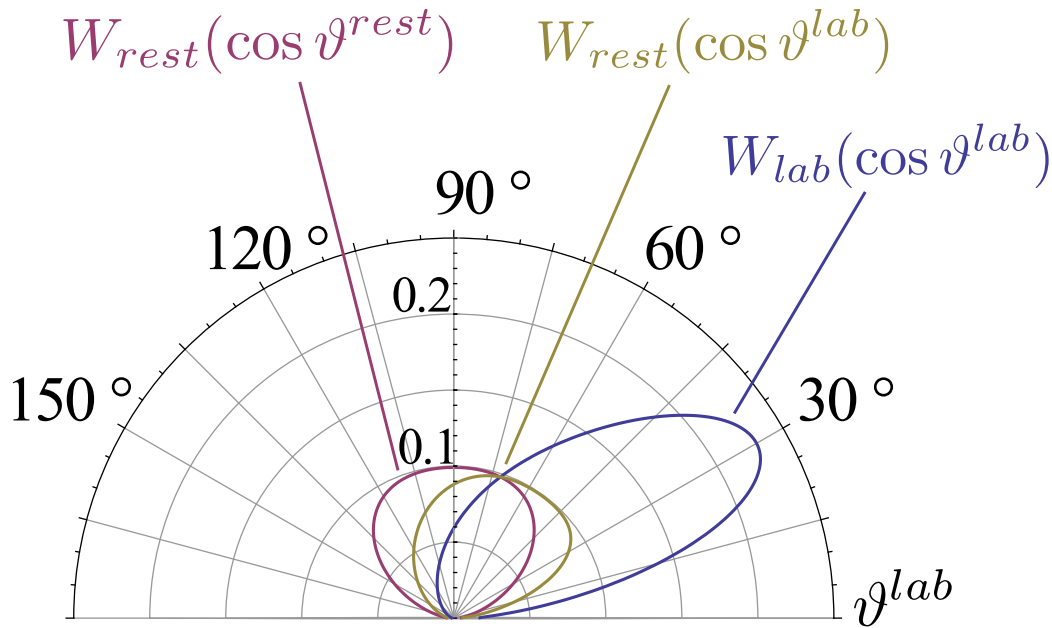


Figure 6.2: Angular distribution of emitted γ -rays of ^{36}Ar in the different systems of inertia (details see above).

$W_{lab}(\cos \vartheta^{lab})$ has additionally been calculated for ^{33}Ar ions that travel at a mean velocity of $\beta = 0.5803$. Both distributions are shown in fig. 6.3.

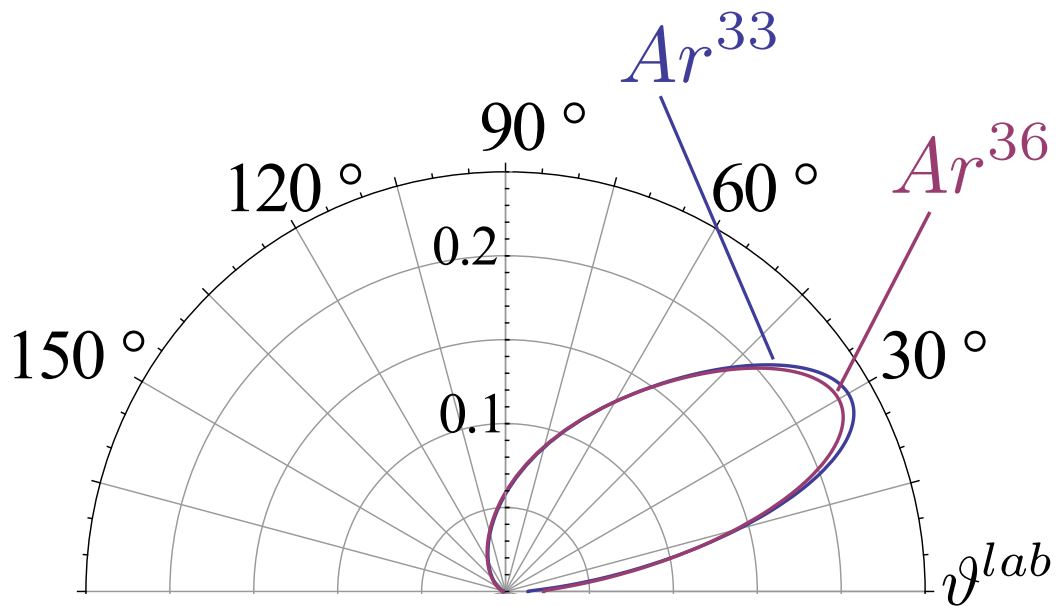


Figure 6.3: Comparison of the angular distributions of γ -ray emission for $^{33,36}\text{Ar}$ in the laboratory frame ($W_{lab}(\cos \vartheta^{lab})$).

The difference between the final distributions is very small for a very slight difference in velocities. Fig. 6.4 shows the ratio of $W_{lab}(\cos \vartheta^{lab})$ for both ion species. The red-marked regions (around $\vartheta^{lab} = 16^\circ$ and $\vartheta^{lab} = 33^\circ$) are the angles that are covered by the two rings of the germanium detectors.

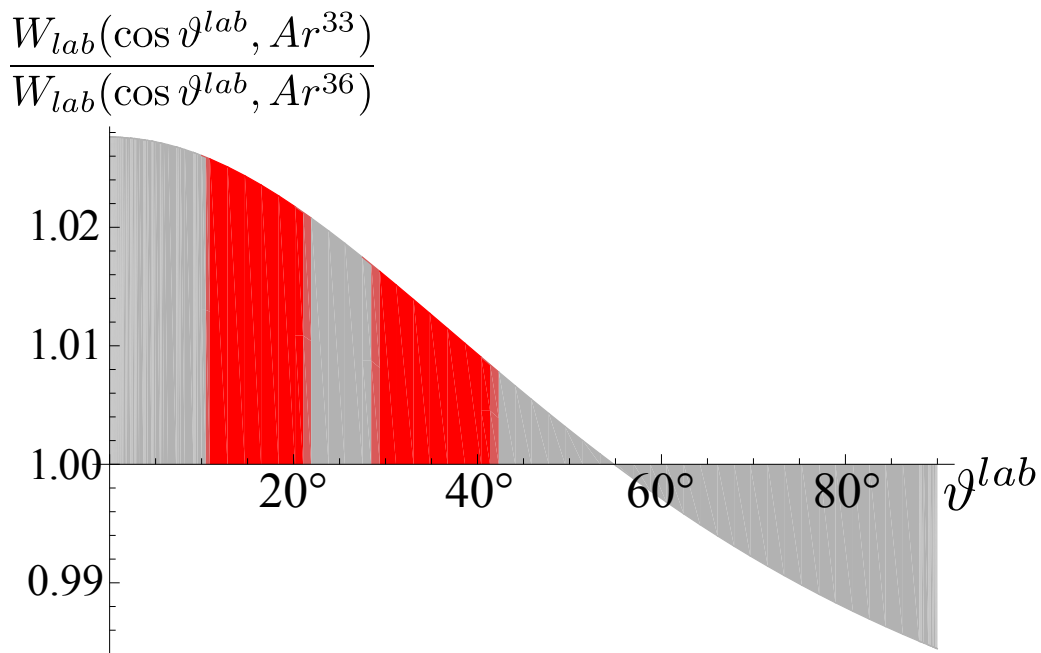


Figure 6.4: Ratio between angular distribution of both isotopes as a function of ϑ^{lab} .

With this ratio, the Lorentz boost correction factors, Λ^{iR} and Λ^{oR} , are defined. This is done for the inner ring (iR) and the outer ring (oR) of the germanium detectors separately.

$$\begin{aligned}\Lambda^{iR} &= \frac{W_{lab}(\cos \vartheta^{iR}, {}^{33}\text{Ar})}{W_{lab}(\cos \vartheta^{iR}, {}^{36}\text{Ar})} \\ \Lambda^{oR} &= \frac{W_{lab}(\cos \vartheta^{oR}, {}^{33}\text{Ar})}{W_{lab}(\cos \vartheta^{oR}, {}^{36}\text{Ar})} \\ \Lambda^{av} &= \frac{\varepsilon_{iR} \cdot \Lambda^{iR} + \varepsilon_{oR} \cdot \Lambda^{oR}}{\varepsilon_{iR} + \varepsilon_{oR}}\end{aligned}$$

The calculation of the correction factors that is performed with the average ϑ values of the detector rings is illustrated in table 6.6.

	ϑ^{av} [deg.]	Λ^x	$\Delta\Lambda^x$
iR	15.9	1.024	0.001
oR	34.5	1.013	0.001
average		1.018	0.001

Table 6.6: Calculated efficiencies dependent on the arrangement of Cluster detectors in arbitrary units.

The correction factors are used in sec. 6.3 to correct the count rate for the change of efficiency due to the Lorentz effect.

6.3 Reduced transition strengths in ${}^{33}\text{Ar}$

The relation between excitation and de-excitation transition strengths is given by:

$$B(E2, f \rightarrow i) = \frac{2J_i + 1}{2J_f + 1} \cdot B(E2, i \rightarrow f), \quad (6.16)$$

where J_i is the spin of the initial level and J_f the spin of the final level.

Ion	Quantity	Value	Uncertainty
${}^{36}\text{Ar}$	Ions on target [10^6]	153.8	0.01
	Avg. velocity [c]	0.5714	0.002
	Mid-target energy [MeV/u]	138	4
${}^{33}\text{Ar}$	Ions on target [10^6]	369.5	0.01
	Avg. velocity [c]	0.5803	0.002
	Mid-target energy [MeV/u]	145	5

Table 6.7: Experimental details.

The calculation is affected by the splitting between the different de-exciting transitions, δ :

$$\delta = \frac{B(E2, \frac{5}{2}^+ \rightarrow \frac{3}{2}^+)}{B(E2, \frac{5}{2}^+ \rightarrow \frac{1}{2}^+)}.$$

The literature value of the branching ratio is $B = 0.024$ [57]. This value is used for all following calculations of $B(E2)$ values. In subsection 6.3.1, the effects of the branching ratio are discussed in more detail.

6.3.1 Effects of the branching ratio

The calculation of the $B\left(E2; \left(\frac{5}{2}\right)_1^+ \rightarrow \left(\frac{1}{2}\right)_1^+\right)$ and $B\left(E2; \left(\frac{3}{2}\right)_1^+ \rightarrow \left(\frac{1}{2}\right)_1^+\right)$ followed the assumption that

$$B(E2, f \rightarrow i) = \frac{2J_i + 1}{2J_f + 1} \cdot B(E2, i \rightarrow f).$$

If this assumption is valid, the de-excitation transition strengths can be deduced from the excitation cross section as done in this experiment. This relation may not be completely valid anymore, if an excited state does not decay entirely in the ground state, but in an excited state as shown in fig. 6.5.

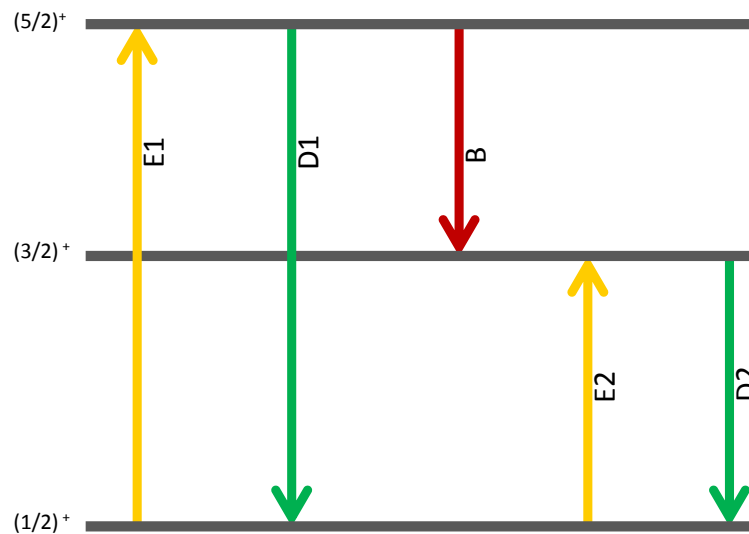


Figure 6.5: Illustration of the transitions in a system with three levels. Excitations are marked yellow, major de-excitations green and minor de-excitations red.

Thus, in this 3-level system $E1 \neq D1$ and $E2 \neq D2$. The ratio $\delta = \frac{B}{E1} = \frac{B}{D1+B}$ is called 'branching ratio'. Neglecting the spin-dependent factors, the relations between excitation strengths ($E1$ and $E2$) and de-excitation strengths ($D1$ and $D2$) are given by:

$$B\left(E2; \left(\frac{5}{2}\right)_1^+ \rightarrow \left(\frac{1}{2}\right)_1^+\right) \propto E1 = D1 + B = (1 + \delta) \cdot D1$$

$$B\left(E2; \left(\frac{3}{2}\right)_1^+ \rightarrow \left(\frac{1}{2}\right)_1^+\right) \propto E2 = D2 - B = D2 - \delta \cdot E1.$$

The branching ratio, δ , was measured directly in an in-beam γ -spectroscopy experiment: $\delta = 2.34(40)\%$ [36]. This value is used in this work to deduce the reduced transition strengths. The effects of different branching ratios on the $B(E2)$ values is illustrated in fig. 6.6. The branching ratio that is predicted by the shell model calculations is much larger than the experimental value.

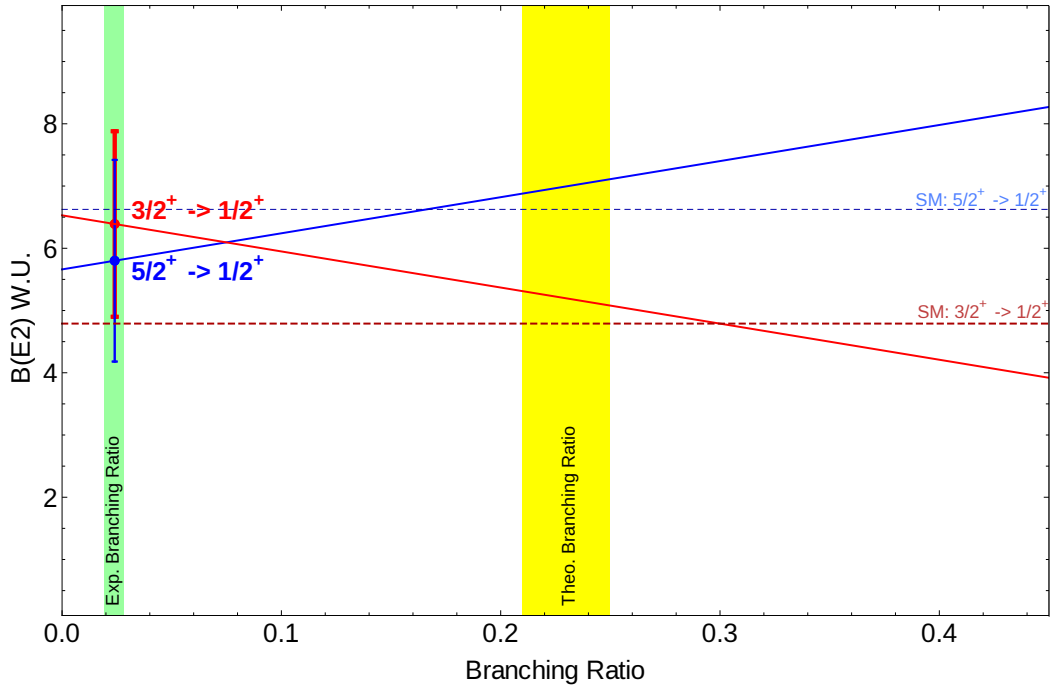


Figure 6.6: Illustration of the effect of the branching ratio on deduced transition strengths.

The effect of branching has a non-negligible effect on transition strengths that are deduced from Coulomb excitation cross sections. Thus, a precise knowledge of the branching ratio δ (as in this case) is a crucial precondition for reliable transition strength measurements.

6.3.2 Calculation of the $B(E2)$ value of the first excited state (1359 keV)

The calculation of the $B(E2)$ value for the first excited state in ^{33}Ar is summarized in tab. 6.8. For this transition, the $B(E2)$ calculation is not disturbed by uncertainties from incomprehensible background effects as seen in sec. 5.5.8.

	Value	Uncertainty	Remark
Counts in peak	74.9	13.0	Tab. 5.6
Identified ^{33}Ar ions [10^6]	387	0.02	Tab. 6.3
Efficiency of setup ε [%]	1.73	0.26	Tab. 6.2
Efficiency factor $\zeta_{51970\text{keV}}^{1359\text{keV}}$	1.295	0.004	Eq. 6.8
Lorentz boost factor Λ^{av}	1.018	0.001	sub sec. 6.2.2
$\tilde{\sigma}_{tot}$ [mb]	7.21	1.69	Eq. 6.6
η	0.944	0.002	[56]
σ_{tot} [mb]	7.64	1.79	Eq. 6.4
F [mb/e ² fm ⁴]	0.0930	0.0001	Tab. 6.1
W.U. [e ² fm ⁴]	6.28740	10^{-5}	[43]
$B(E2, \frac{1}{2}^+ \rightarrow \frac{3}{2}^+)$ [e ² fm ⁴] for $B = 0$	82,17	19.26	Eq. 6.3
$B(E2, \frac{3}{2}^+ \rightarrow \frac{1}{2}^+)$ [W.U.] for $B = 0$	6.53	1.53	Eq. 6.16
$B(E2, \frac{1}{2}^+ \rightarrow \frac{3}{2}^+)$ [e ² fm ⁴] for $B = 0.024$	80,37	18.79	Eq. 6.3
$B(E2, \frac{3}{2}^+ \rightarrow \frac{1}{2}^+)$ [W.U.] for $B = 0.024$	6.39	1.49	Eq. 6.16

Table 6.8: Calculation of the reduced transition strength of the first excited state in ^{33}Ar .

The final value of the de-excitation strength is discussed in chapter 7.

6.3.3 Calculation of the $B(E2)$ value of the second excited state (1798 keV)

As described in sec. 5.5.8, the total number of γ -rays in the outer germanium detector ring for the 1798 keV transition can only be treated as an upper limit, due to uncertainties from incomprehensible background effects. Thus, getting access to the $B(E2)$ value of this transition is split into two parts: firstly, taking all germanium information to calculate an upper limit for the $B(E2)$ value and secondly, using only data from inner germanium detectors to get the exact value. In the second case, the statistics are reduced by more than 60% and as a result the uncertainty will be larger, although this is the only option in order to gain access to the $B(E2)$ value of this transition. Tab. 6.9 summarizes the calculation of an upper limit for the $B(E2)$ value, tab. 6.10 shows the results from the calculation of the $B(E2)$ value using the data from the inner ring of germanium detectors.

	Value	Uncertainty
Upper limit to detected γ -rays	127.6	18.1
ε [%]	1.87	0.27
$\varepsilon_{1798keV}^{1970keV}$	1.061	0.005
Λ^{av}	1.018	0.001
$\tilde{\sigma}_{tot}$ [mb]	< 15.00	3.17
η	0.944	0.002
σ_{tot} [mb]	< 15.89	3.36
F [mb/e ² fm ⁴]	0.0943	0.0001
$B(E2, \frac{1}{2}^+ \rightarrow \frac{5}{2}^+)$ [e ² fm ⁴] for $B = 0$	< 168.51	35.64
$B(E2, \frac{5}{2}^+ \rightarrow \frac{1}{2}^+)$ [W.U.] for $B = 0$	< 8.93	1.90
$B(E2, \frac{1}{2}^+ \rightarrow \frac{5}{2}^+)$ [e ² fm ⁴] for $B = 0.024$	< 172,55	36.50
$B(E2, \frac{5}{2}^+ \rightarrow \frac{1}{2}^+)$ [W.U.] for $B = 0.024$	< 9.14	1.94

Table 6.9: Calculation of an upper limit for $B(E2, \frac{5}{2}^+ \rightarrow \frac{1}{2}^+)$.

	Value	Uncertainty
Counts in peak	39.4	8.3
ε_{iR} [%]	0.91	0.15
$\varepsilon_{1798keV}^{1970keV}$	1.059	0.009
Λ^{iR}	1.024	0.001
$\tilde{\sigma}_{tot}$ [mb]	9.50	2.67
η	0.944	0.002
σ_{tot} [mb]	10.07	2.82
F [mb/e ² fm ⁴]	0.0943	0.0001
$B(E2, \frac{1}{2}^+ \rightarrow \frac{5}{2}^+)$ [e ² fm ⁴] for $B = 0$	106.77	29.94
$B(E2, \frac{5}{2}^+ \rightarrow \frac{1}{2}^+)$ [W.U.] for $B = 0$	5.66	1.58
$B(E2, \frac{1}{2}^+ \rightarrow \frac{5}{2}^+)$ [e ² fm ⁴] for $B = 0.024$	109.33	30.66
$B(E2, \frac{5}{2}^+ \rightarrow \frac{1}{2}^+)$ [W.U.] for $B = 0.024$	5.80	1.62

Table 6.10: Calculation of $B(E2, \frac{5}{2}^+ \rightarrow \frac{1}{2}^+)$ from the data of the inner germanium detector ring.

Both values are in agreement. The interpretation of both $B(E2)$ values and the comparison with shell model calculations are discussed in the following chapter.

6.3.4 Experimental data for the $B(E2; 2_1^+ \rightarrow g.s.)$ value of ^{36}Ar

The $B(E2)$ value of the first excited state is used as reference for the determination of the transition strengths of the excited states in ^{36}Ar in this work. Thus, the precise knowledge is of high importance. This value has been measured over several decades by various experimental techniques. Table 6.11 summarizes the publications about transition strengths in ^{36}Ar , whereas figure 6.7 shows the experimental values with respect to the year of the publication.

Year	Experimental technique	Reaction	Ref.
1969	DSAM	$^{32}\text{S}(\alpha, \gamma)^{36}\text{Ar}$	[103]
1970	Particle spectroscopy	$^{35}\text{Cl}(^3\text{He}, d)^{36}\text{Ar}$	[104]
1971	Coulex	$^{208}\text{Pb}(^{36}\text{Ar}, ^{36}\text{Ar}^*)$	[105]
1972	DSAM	$^{35}\text{Cl}(p, \gamma)^{36}\text{Ar}$	[106]
1974	DSAM	$^{35}\text{Cl}(p, \gamma)^{36}\text{Ar}$	[107]
1977	Inelastic electron scattering	$e^- + ^{36}\text{Ar}$	[108]
1999	Fragment beam Coulex	$^9\text{Be}(^{40}\text{Ar}, ^{36}\text{Ar})$	[109]
1999	Fragment beam Coulex	$^9\text{Be}(^{40}\text{Ca}, ^{36}\text{Ar})$	[110]
2006	Transient field DSAM	$^{12}\text{C}(^{32}\text{S}, ^8\text{Be})^{36}\text{Ar}$	[111]

Table 6.11: Published measurements of the $B(E2)$ value of the first excited state in ^{36}Ar .

The measurements of all experiments are in good agreement with the adopted value, except for the newest publication. This experiment employed the transient field Doppler-shift-attenuation method and the result ($B(E2; 2_1^+ \rightarrow g.s.) = 5.98(17)$) deviates by approximately 30 % from the adopted value (3 times the adopted error).

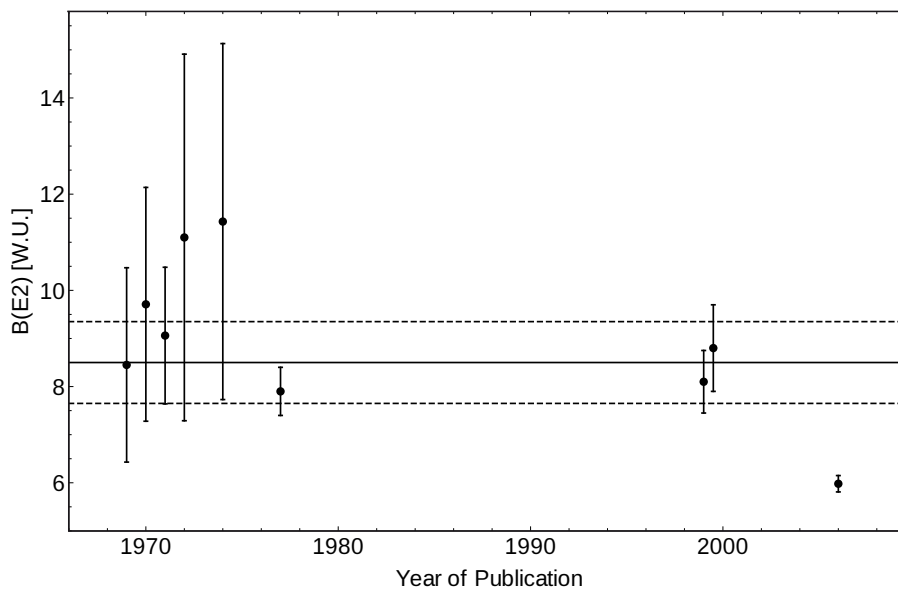


Figure 6.7: Published $B(E2)$ values of ^{36}Ar with respect to the year of the publication.

In experiments as described in this work, the crucial relation is that the investigated transition strengths are proportional to a 'known' transition strength of the reference (cf. eq. 6.1 and 6.2):

$$B\left(E2; {}^{33}\text{Ar}; \left(\frac{3}{2}, \frac{5}{2}\right)^+ \rightarrow \left(\frac{1}{2}\right)^+\right) \propto B\left(E2; {}^{36}\text{Ar}; 2^+ \rightarrow 0^+\right).$$

The influence on the determination of the transition strengths in ${}^{33}\text{Ar}$ of this changed value is summarized in table 6.12.

Origin of ref. value	Ref. value [W.U.]	$B\left(E2; \left(\frac{3}{2}\right)^+ \rightarrow \left(\frac{1}{2}\right)^+\right)$	$B\left(E2; \left(\frac{5}{2}\right)^+ \rightarrow \left(\frac{1}{2}\right)^+\right)$
Adopted value	8.50(85)	6.39(1.49)	5.80(1.62)
Transient field DSAM measurement	5.98(17)	4.50(1.01)	4.08(1.09)

Table 6.12: Deduced transition strengths, dependent on reference value.

A large uncertainty for the transition strength of the reference transition strongly affects the deduced new transition strengths. Although, most of the data shows a consistent picture of the reference transition strength, a dedicated, modern experiment is suggested to validate the adopted value. For this analysis the adopted value is used, because it was confirmed in several experiments, employing various techniques.

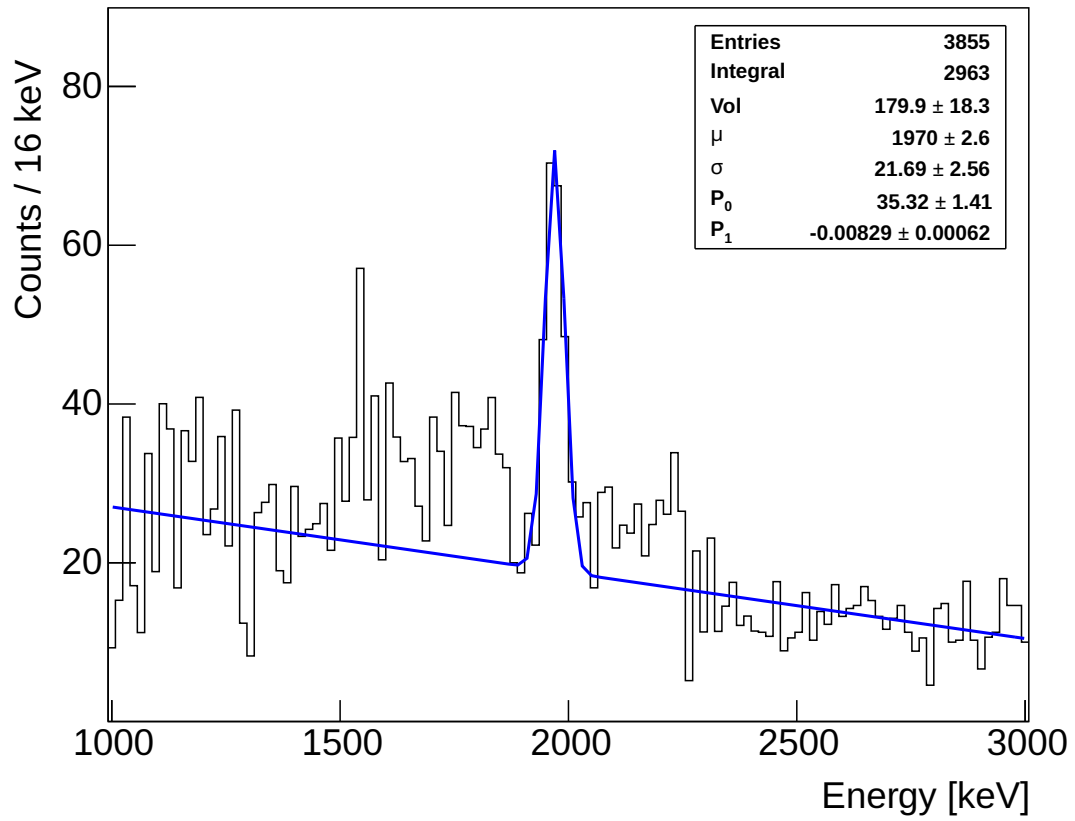
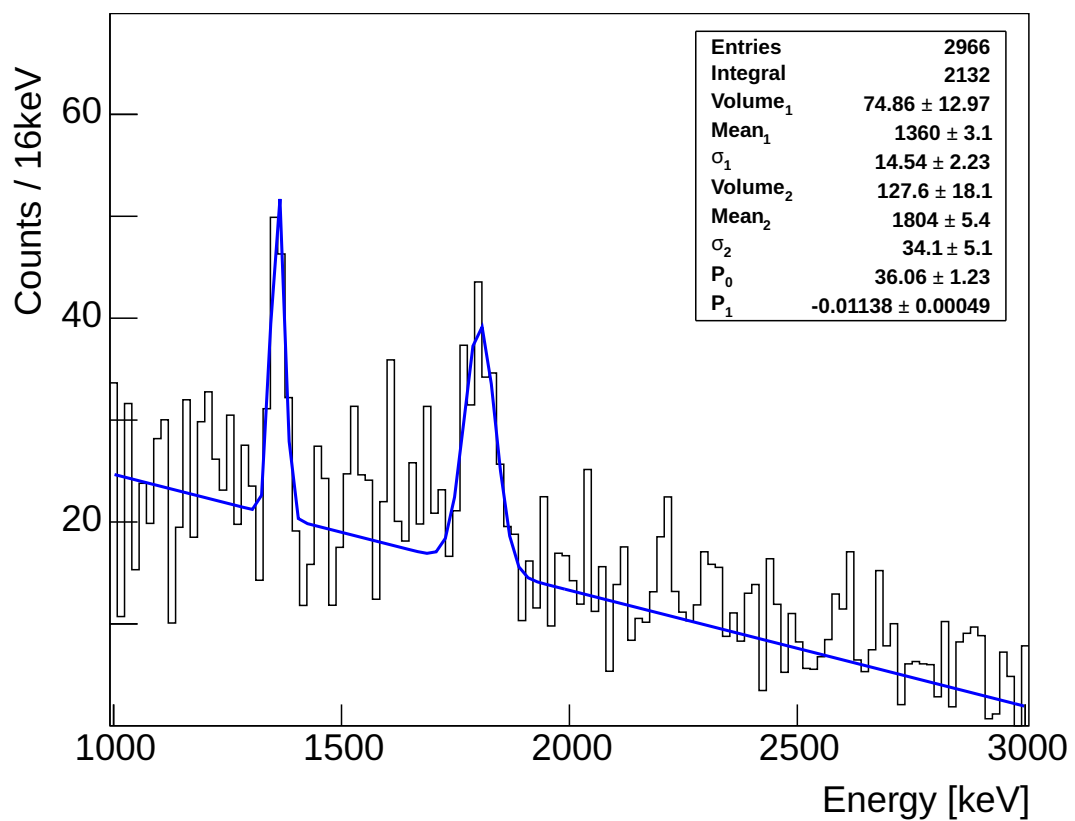
6.4 Summary

The aim of the experiment was to determine the unknown transition strengths of the first two excited states of ${}^{33}\text{Ar}$. For calibration, it was also necessary to detect γ -rays from de-excitations of the 2_1^+ -state of ${}^{36}\text{Ar}$. Fig. 6.8 shows the ultimate γ -ray spectra of the experiment according to the analysis described in chap. 5. The measured excitation energies of these states were in agreement with the values given in the literature [57] (cf. tab. 6.13).

With the data, the unknown transition strengths of the two excited states of ${}^{33}\text{Ar}$ were calculated (cf. sec. 6.3). Table 6.13 summarizes the final values.

	${}^{36}\text{Ar}$		${}^{33}\text{Ar}$			
	$2^+ \rightarrow 0^+$		$\frac{3}{2}^+ \rightarrow \frac{1}{2}^+$		$\frac{5}{2}^+ \rightarrow \frac{1}{2}^+$	
	Lit.	Exp.	Lit.	Exp.	Lit.	Exp.
Energy [keV]	1970.38(5)	1970(3)	1359(2)	1360(3)	1798(2)	1804(6)
B(E2) [W.U.]	8.5(8)	–	–	6.39(1.49)	–	5.80(1.62)

Table 6.13: Summary of the experimental results and literature values taken from ref. [57].

(a) ^{36}Ar .(b) ^{33}Ar .Figure 6.8: Final γ -ray spectra of the experiment.

Chapter 7

Comparison with shell model calculations

7.1 Effective interactions for shell model calculations

Modern shell-model calculations (basics concepts of the nuclear shell model are described in chapter A) incorporate many of the multi-nucleon configurations that arise under the assumption that the valence protons and neutrons of the nucleus simultaneously occupy several different single-particle quantum states. Calculations of these types are a natural extension of the original nuclear shell-model of Mayer and Jensen [113], which assumed a single configuration for each nuclear level, corresponding to a single nucleon in one single-particle orbit. The actual research is aiming for a thorough theoretical understanding, including a detailed reproduction of the complete spectroscopic characterization of nuclear levels provided by experiments. Such a complete characterization includes a variety of observables, like the ground-state binding energies, quantum numbers of excited states as spin, isospin and parity as well as excitation energies and transition strengths between different states.

A major fraction of the shell-model research is increase of the configuration space with the relevant configurations and couplings. Also the effective single-particle potential for, and the effective two-body interaction between, the considered nucleons is subject of ongoing theoretical effort. With these two ingredients, the Hamiltonian matrices for the chosen energy operator in the selected model space can be found and diagonalized to obtain eigenvalues, eigenfunctions and be used to calculate the overlaps of the wave functions.

In the *sd* model space ($1s_{\frac{1}{2}}, 0d_{\frac{3}{2}}, 0d_{\frac{5}{2}}$ single-particle orbits) are only 24 active *m* states (specified by the quantum numbers $n = 0, 1, l = 0, 2, j = \frac{1}{2}, \frac{3}{2}, \frac{5}{2}, j_z = \pm\frac{1}{2}, \pm\frac{3}{2}, \pm\frac{5}{2}$ and $t_z = \pm\frac{1}{2}$). Nonetheless, the full-basis dimensions for many-particle states can become quite large. For example the basis of the 12-particle state with $J_z = \sum j_z = 0$ and $T_z = \sum j_t = 0$ (ground state of ^{28}Si) has the dimension of approximately 100,000 in the *m* scheme [86]. Calculations of this complexity could be solved even with the limited computing power of the early 1980s within a reasonable time. Modern shell model codes (in combination with the available computing power) can solve calculations with a basis dimension of several billions.

Model-independent approach: the USD interaction

The primary problem of shell-model calculations is finding an appropriate nucleon-nucleon interaction, which defines the effective Hamiltonian operator. This can be directly extracted from experimental nucleon-nucleon scattering data and fundamental theoretical concepts. Another concept is based on effective interactions, where parameters are deduced from experimental measurements. The parametrizations can be made in many different ways, ranging from those that depend strongly on a model for the interaction (for example in the form of a δ -function) to those that are essentially independent of any additional assumptions (for example the use of two-body matrix elements without further limitations). Within the 'model-independent' approach the two-body matrix elements (TBME) and single-particle energies (SPE) are treated as parameters in a fit to the experimentally known binding energies and excitation energies. This procedure has been applied to the *sd* shell, fitting 66 parameters (3 SPEs and 63 TBMEs) for all experimental known data (447 binding and excitation energies) [86]. A subsequent modification for this interaction was the application of a mass dependence of the TBME. The matrix elements depend of the mass of the nucleus: $\langle V^{TBME} \rangle(A) = \langle V^{TBME} \rangle(A = 18) \cdot \left(\frac{A}{18}\right)^{-0.3}$. The TBME for $A = 18$ are given in ref. [114]. This fully isospin symmetric interaction is called the 'Universal *sd* shell interaction' (USD). For a recent review see the publication of Brown and Wildenthal [86].

Isospin symmetry breaking modification of the USD interaction

The SPE are crucial parameters for the USD shell model calculation. They can be obtained in principle by three different ways:

1. Deduced from an empirical adjusted central potential (for example of Woods-Saxon or folded Yukawa type).
2. Fitted as free parameter in the shell model calculation (as done for the USD interaction).
3. Extracted from experimentally determined differences in binding energies (BE) of nuclei close to a doubly-magic (DM) nucleus: $SPE_j = BE(\text{DM} \pm 1; I = j) - BE(\text{DM}; g.s.)$ [3], where $j = (n, l, j, t_z)$ labels the single particle state in the nucleus that is close-by the DM nucleus.

The first empirical approach to break the isospin symmetry in this model was to employ experimentally determined SPEs from the $A = 17$ neighbours of ^{16}O (^{17}O and ^{17}F) and to replace the isospin symmetric SPEs (cf. tab. 7.2) by the measured SPEs. The resulting isospin symmetry breaking interaction is called USD^m. Comparison of the corresponding proton separation energy in ^{17}F ($S_p = 600$ keV) and the neutron separation energy in ^{17}O ($S_n = 4143$ keV) shows a large difference.

This USD^m interaction works well in reproducing excitation energies over the full *sd* shell, but is not able to reproduce certain particle separation energies. A major example is the two-neutron separation energy, S_{2n} , of ^{26}O . This nucleus is unstable against two-neutron decay, thus the two-neutron separation energy $S_{2n} < 0$ [115], which was not reproduced by shell model calculations employing the USD^m interaction. This information motivated Y. Utsuno et al. to modify the monopole part of the TBME [88]. The total monopole modifications relative to the USD interaction are according to ref. [16]:

$$\begin{aligned}
\delta V_{d_{\frac{5}{2}},d_{\frac{3}{2}}}^{T=1} &= +0.2 \text{ MeV} \\
\delta V_{d_{\frac{5}{2}},s_{\frac{3}{2}}}^{T=0} &= -0.6 \text{ MeV} \\
\delta V_{d_{\frac{5}{2}},s_{\frac{1}{2}}}^{T=1} &= -0.1 \text{ MeV} \\
\delta V_{d_{\frac{5}{2}},s_{\frac{1}{2}}}^{T=0} &= +0.1 \text{ MeV}
\end{aligned}$$

This modified interaction (referred as USD_1^m) keeps the isospin symmetry in the TBME (while the SPEs are isospin dependent, as they originate from the experimental values of ^{17}O and ^{17}F). This interaction was employed to reproduce all MEDs of $T = 1, 2$ sd shell mirror pairs (cf. fig. 7.1) [17]. While the most mirror energy differences of the nuclei are well reproduced, the MEDs of $A = 30, 32$ as well as those of $A = 18, 24$ are not in good agreement with the USD_1^m interaction. Thus, for an additional improvement of the description of the data, two new empirical interactions are used, one for lower and one for the higher mass triangle in the sd shell [16]. The following modifications are done:

- USD_2^m for $A \leq 28$: The $\pi 0d_{\frac{5}{2}}$ SPE is increased by 200 keV and the $\pi(0d_{\frac{5}{2}}, 0d_{\frac{5}{2}})$ TBME are quenched by the factor 0.95 to improve the USD_1^m agreement for ^{18}Ne .
- USD_3^m for $A > 28$: The $\pi 0d_{\frac{5}{2}}$ SPE is reduced by 300 keV and $\nu 0d_{\frac{5}{2}}$ SPE is increased by 900 keV.

The mirror energy differences provided by the described interactions are shown in figure 7.1. The black square at $A = 20$ shows an experimental value that was published after the publication of these interactions [18], indicating some predictive power of the modified interactions. The SPE values for all compared interactions are summarized in table 7.2.

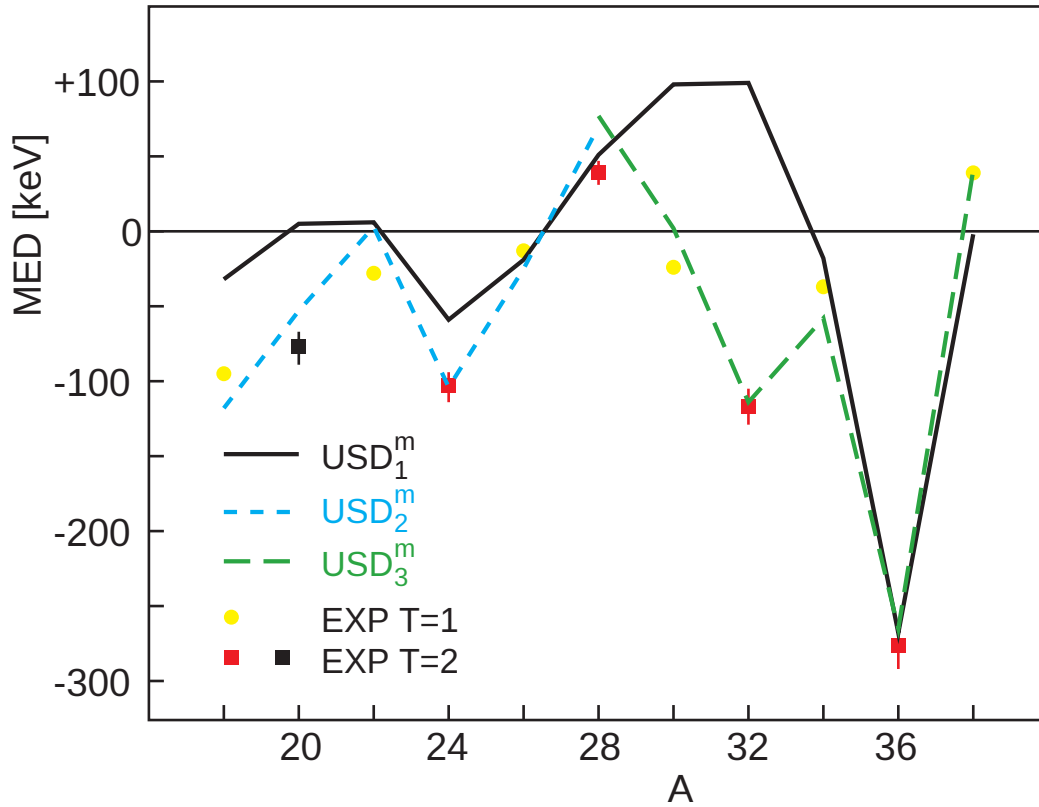


Figure 7.1: Experimental MEDs of the 2_1^+ states of the $T = 1, 2$ sd shell mirror pairs and shell model calculations employing different interactions. For details see text. (Fig. modified from ref. [17]). Data has been taken from refs. [20], [97], [21] and [16]. Details see text.

	Orbit	USD	USD ^m / USD ₁ ^m	USD ₂ ^m	USD ₃ ^m
protons	$\pi 0d_{5/2}$	-3948	- 600	- 400	- 900
	$\pi 0s_{1/2}$	-3164	- 105	- 105	- 105
	$\pi 0d_{3/2}$	+1647	+ 4400	+ 4400	+ 4400
neutrons	$\nu 0d_{5/2}$	-3948	- 4143	- 4143	- 3243
	$\nu 0s_{1/2}$	-3164	- 3272	- 3272	- 3272
	$\nu 0d_{3/2}$	+1647	+ 942	+ 942	+ 942

Figure 7.2: Single particle energies used for the different effective interactions, given in keV. See text for details. (Values taken from [17]).

The mirror pair ^{33}Ar - ^{33}P is used for a detailed study of the interactions. USD, USD₁^m and USD₃^m are employed to reproduce the known level schemes of ^{33}Ar and ^{33}P (cf. fig. 7.4) as well as their mirror energy differences (cf. fig. 7.5).

7.2 The $T_z = \pm\frac{3}{2}$ mirror pair ^{33}Ar - ^{33}P

The excitation energies in the $A = 33$, $T_z = \pm\frac{3}{2}$ mirror pair are shown and compared to values obtained by shell model calculations employing different interactions. The energies of excited states in ^{33}Ar are established up to 3.819 MeV from two experiments. The first experiment populated excited states in ^{33}Ar by the $^{36}\text{Ar}(^3\text{He}, ^6\text{He})^{33}\text{Ar}$ transfer reaction, employing a 70 MeV ^3He beam from the Michigan State University (MSU) cyclotron. The energies of the two lowest-energetic excited states were deduced from a measurement of the mass excess and published in 1974 [35]. The second experiment was using a 150 MeV/u ^{36}Ar beam, which was provided by the MSU coupled cyclotron facility to generate a fragment beam of ^{34}Ar . The secondary beam was selected using a fragment separator and shot on a polypropylene target. Neutron removal reactions populated excited states in ^{33}Ar , which de-excited by emission of γ -rays that were detected by a germanium detector array. The results of this experiment were published in 2004 [36].

^{33}P is very close to the valley of stability and has been studied extensively over several decades (1952-2009) by various experimental techniques:

- β spectroscopy: ^{33}P produced via the $^{33}\text{S}(n,p)^{33}\text{P}$ reaction [24, 25].
- Transfer reactions employing magnetic spectrometers: $^{30}\text{Si}(\alpha, p)^{33}\text{P}$ [28], $^{31}\text{P}(t, p)^{33}\text{P}$ [31] and $^{34}\text{S}(d, ^3\text{He})^{33}\text{P}$ [33].
- Transfer reactions using Ge(Li) γ -ray detectors: $^{31}\text{P}(t, p\gamma)^{33}\text{P}$ [29, 30, 32].
- γ -spectroscopy following the β -decay of ^{33}Si [26].
- γ -spectroscopy in combination with the Doppler-shift attenuation method using the $^{31}\text{P}(t, p\gamma)^{33}\text{P}$ reaction [83, 84].
- Transfer reaction with a polarized deuteron beam employing particle detectors: $^{34}\text{S}(\vec{d}, ^3\text{He})^{33}\text{P}$ [34].
- A fusion-evaporation reaction in combination with in-beam γ -spectroscopy employing high purity Ge detectors: $^{18}\text{O}(^{18}\text{O}, p2n\gamma)^{33}\text{P}$ [27].

Fig. 7.3 shows the level scheme of ^{33}Ar (all known states) and a partial level scheme of ^{33}P (up to 4 MeV excitation energy). The adopted experimental data on levels and transitions of both nuclei is listed in table 7.1.

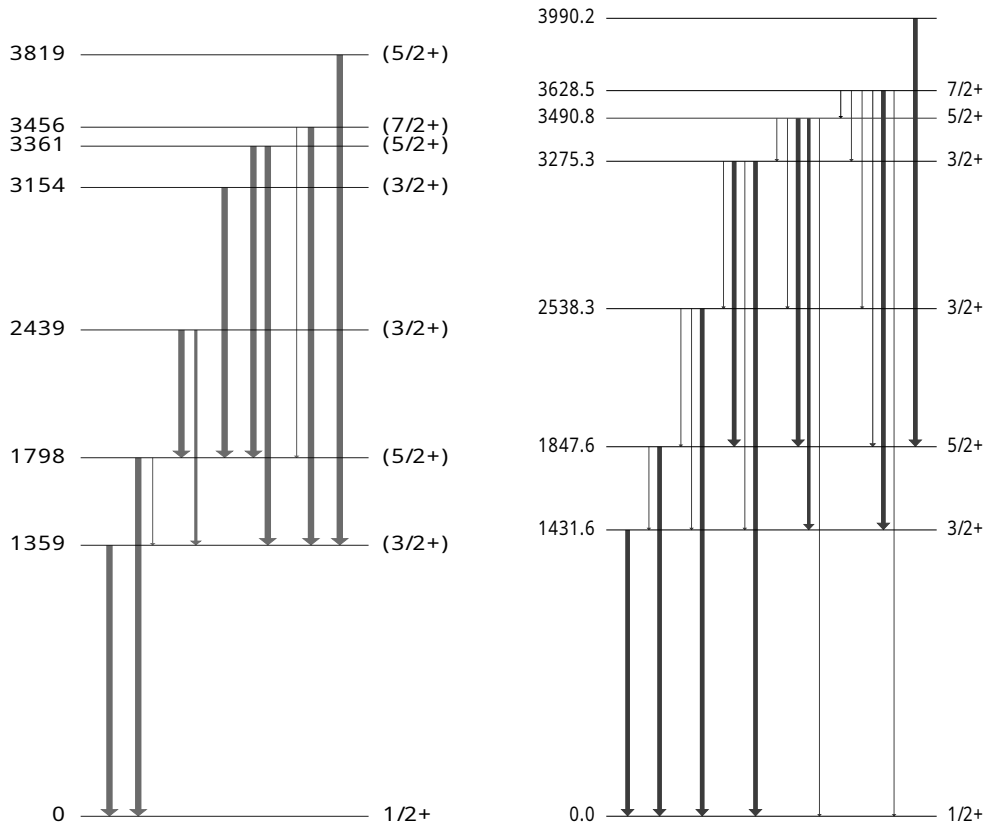


Figure 7.3: Level schemes of ^{33}Ar (left) and ^{33}P (partial, right).

For ^{33}Ar the agreement increases from USD to USD_1^m and to USD_3^m . For ^{33}P this improvement is not that evident.

The so-called 'Mean Level Deviation' (MLD) is used to quantify the level of agreement between theory and experiment:

$$\text{MLD} = \sqrt{\frac{1}{n} \sum_i^n [E_i(\text{exp}) - E_i(\text{SM})]^2}.$$

The MLDs for the three used interactions is calculated with states up to the 3456 keV in ^{33}Ar and 3629 keV in ^{33}P and is shown in table 7.2. The deviation is largest for the three highest energetic states in all cases, thus the MLDs are also given only accounting for the three lower lying excited states.

All states	USD	USD_1^m	USD_3^m	Three lowest exc. states	USD	USD_1^m	USD_3^m
^{33}Ar	352	348	229	^{33}Ar	193	204	29
^{33}P	240	248	315	^{33}P	120	97	168
Average	296	298	272	Average	156	150	98

Table 7.2: Mean level deviations of the different interactions applied on the ^{33}Ar - ^{33}P mirror pair.

The USD_3^m values reproduce the level schemes in the best way. This is true for all levels as well as for the lowest three excited states in both nuclei.

^{33}Ar						^{33}P						
E_{level}	J^π	E_γ	I_γ	E_{final}		E_{level}	J^π	$T_{1/2}$	E_γ	I_γ	Multipole.	E_{final}
0	(1/2 ⁺)					0	1/2 ⁺	25.35(11) d				
1359(2)	(3/2 ⁺)	1359(2)	100	0		1431.6(2)	3/2 ⁺	0.43(7) ps	1431.7(2)	100	M1+E2	0
1798(2)	(5/2 ⁺)	437(3) 1798(2)	2.4(4) 100(15)	1359 0		1847.6(2)	5/2 ⁺	0.77(11) ps	416.2(3) 1847.7(2)	6.8(6) 100(1)	M1+(E2) E2+(M3)	1431 0
2439(3)	(3/2 ⁺)	639(2) 1084(4)	100(29) 100(57)	1798 1359		2538.3(10)	3/2 ⁺	35 fs	691.0(4) 1106.8(3) 2538.5(5)	8.2(12) 9.4(12) 100(35)	(M1) (M1) (M1+E2)	1847 1431 0
3154(9)	(3/2 ⁺)	1356(8)	100	1798		3275.3(10)	3/2 ⁺	0.14(3) ps	737.7 1428.6(4) 1843.9 3275(1)	< 6 100(6) < 10 92(6)		2538 1847 1431 0
3361(5)	(5/2 ⁺)	1556(8) 2005(5)	100(14) 60(40)	1798 1359		3490.8(7)	5/2 ⁺	58(12) fs	215.1 952.8 1642.7 2058.9(4) 3491.1(10)	< 6 < 6 100(6) 78(6) 7.4(37)		3275 2538 1847 1431 0
3456(6)	(7/2 ⁺)	1651(6) 2097(5)	30(20) 100(50)	1798 1359		3628.5(9)	7/2 ⁺	0.14(3) ps	137.9 353 1090.7 1779.8(8) 2196.3(10) 3628.3	< 5.8 < 8.6 < 7 43(4) 100(4) < 1		3490 3275 2538 1847 1431 0
3819(3)	(5/2 ⁺)	2460(2)	100	1359		3990.2(10)	5/2 ⁺		2141.6(10)	100		1847

Table 7.1: Energies (in keV), spins, parities, branching ratios and multipolarities of all known levels and transitions in ^{33}Ar and the corresponding levels and transitions in the mirror nucleus ^{33}P .

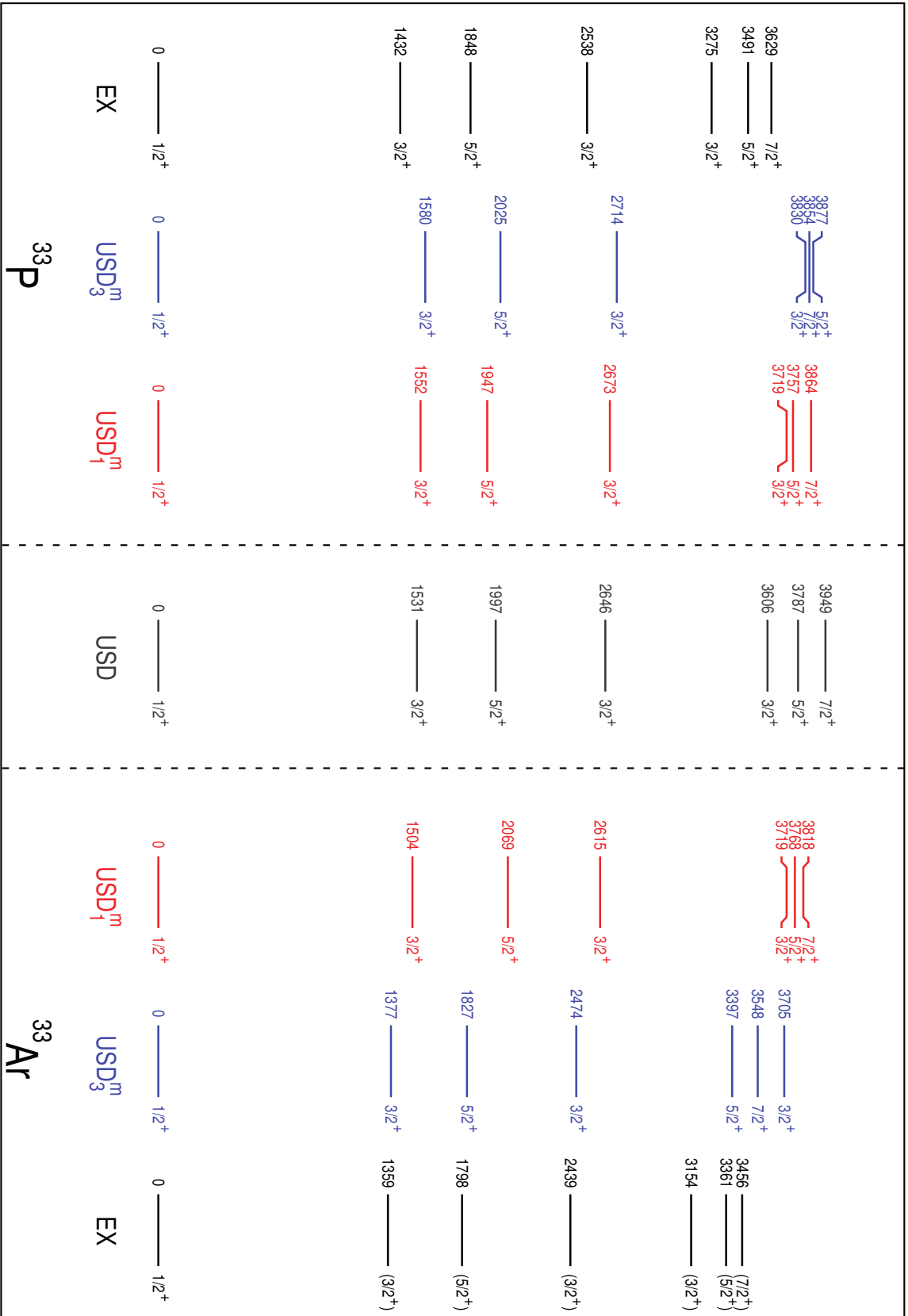


Figure 7.4: Shell model calculations employing the USD, USD₁^m and USD₃^m interactions for the mirror pair $^{33}\text{Ar}/^{33}\text{P}$.

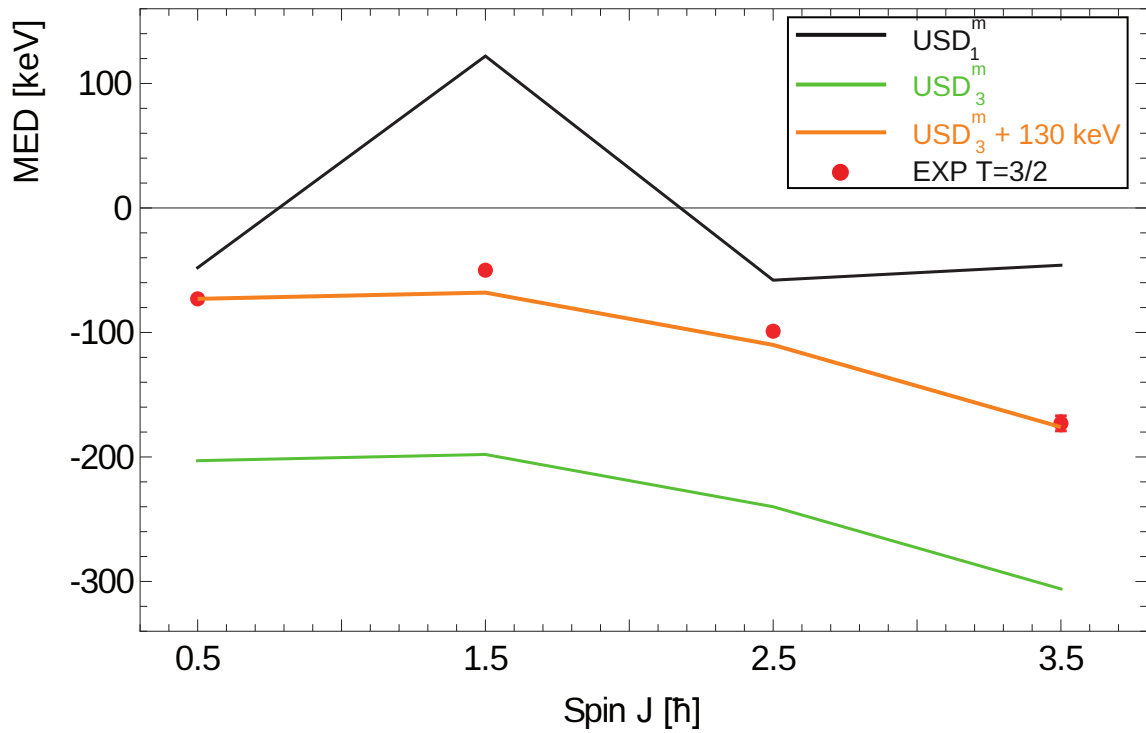


Figure 7.5: MED of $^{33}\text{Ar}-^{33}\text{P}$ vs spins of the excited states. Details see text.

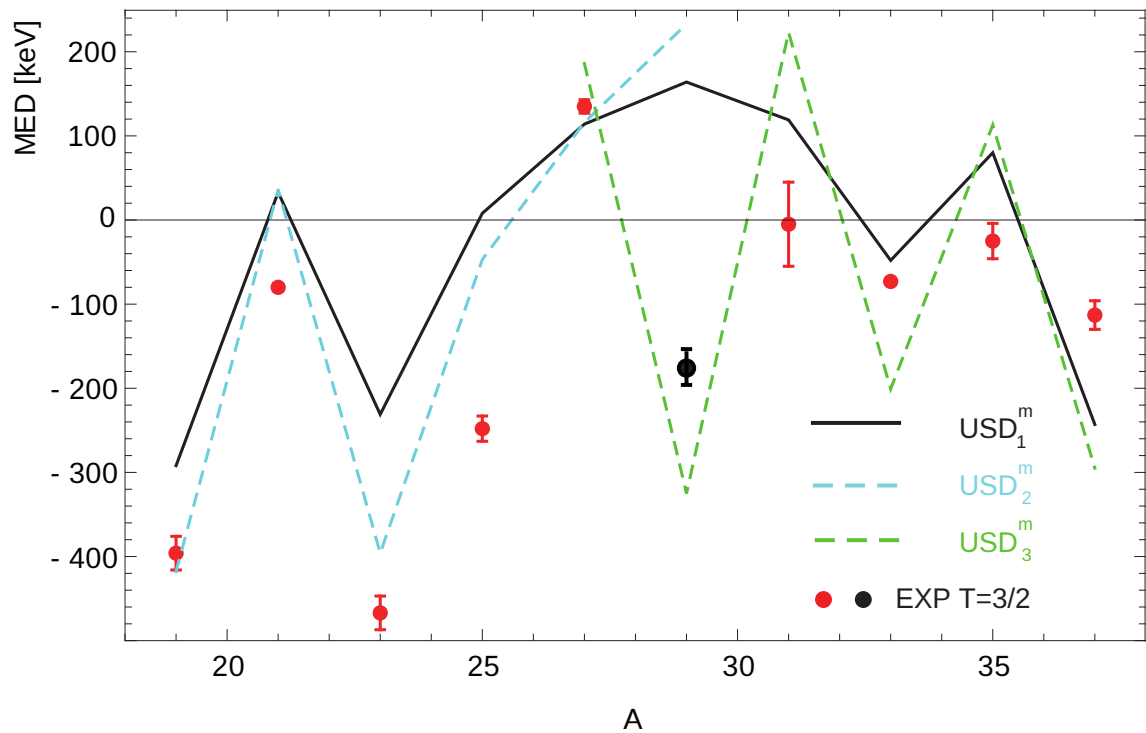


Figure 7.6: Experimental MEDs of the first excited states of the $T = \frac{3}{2}$ sd shell mirror pairs and shell model calculations [52]. The black circle indicates a measurement [15] that was published after the creation of these interactions. The experimental data is taken from [57].

The *sd* shell nuclei are shown in figure 7.7. Diagonals with the same T_z value are indicated. Nuclei with the same mass number are called 'isobaric nuclei'. If two isobaric nuclei have the same T_z value but opposite sign, they are called 'mirror nuclei'. This chapter gives an overview about the available experimental information on transition strengths in *sd* shell mirror nuclei as well as predictions of recent shell model calculations. All known $B(E2)$ values of $T = \pm 1, \pm 2$ *sd* shell nuclei are shown in figure 7.8. Only 'even-even' nuclei are regarded, because the first excited states are always 2^+ states. Due to the identical underlying structure, the transition strengths of these states to the ground state can be directly compared. In addition the results of shell model calculations are displayed. In all plots of this type the solid cyan / orange lines represent the original USD interaction, the solid blue / red lines the USD_1^m interaction and the dashed blue / red lines the $USD_{2,3}^m$ (USD_2^m for $A \leq 28$, USD_3^m for $A > 28$) interactions. The experimental data is marked by the blue (proton-rich) and red (neutron-rich) dots.

For the $T_z = \pm 1$ *sd* shell nuclei the transition strengths are known (^{22}Mg only with a large uncertainty, $B(E2; 2_1^+ \rightarrow 0_1^+) = 24(10)$ W.U.). The calculated $B(E2)$ values are in good agreement with the experimental data. Only in the case of ^{26}Si larger discrepancies between the different interactions occur. USD_2^m provides the best results. For all $T_z = \pm 2$ *sd* shell nuclei the transition strengths are known, except the proton rich ^{28}S and ^{36}Ca . The calculated transition strengths of all interactions are very similar for all neutron rich nuclei as well as for ^{20}Mg and ^{32}Ar and are in good agreement with the experimental data. Only the transition strength of ^{24}Si is not well reproduced by any interaction. The transition strengths that are determined in this work for ^{33}Ar and all other experimentally known transition strengths of $T_z = \pm \frac{3}{2}$ nuclei are compared with results of shell model calculations.

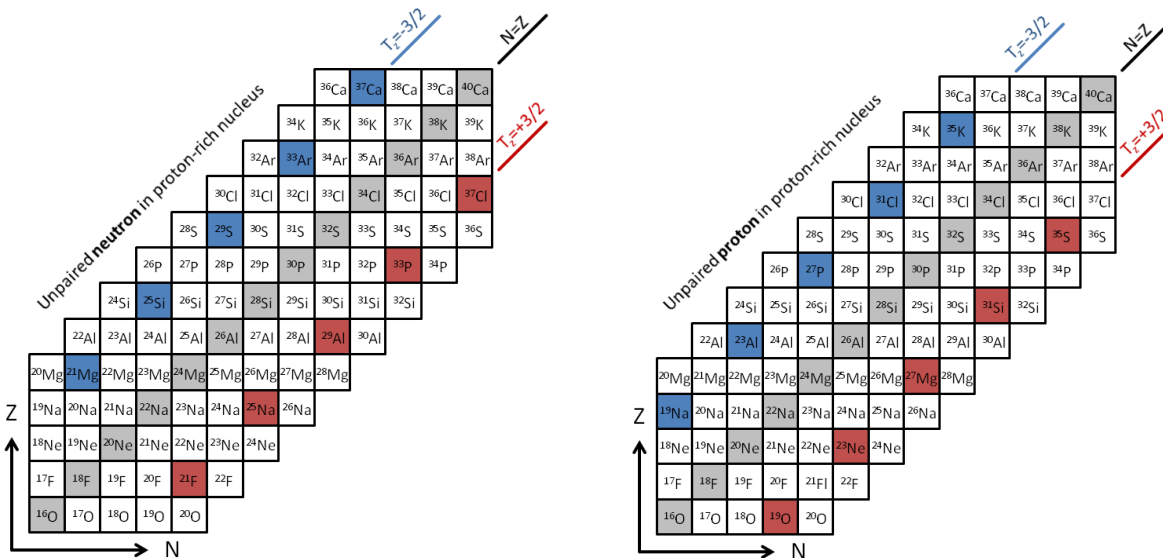
Nucl.	$J_i \rightarrow J_f$	Multipole	USD	USD_1^m	USD_3^m	Exp.	Ref.	Exp.	Ref.
^{33}Ar	$\frac{3}{2} \rightarrow \frac{1}{2}$	(E2+(M1))	5.115	5.013	4.790	6.39(1.49)	this work		
	$\frac{5}{2} \rightarrow \frac{1}{2}$	(E2)	6.705	6.684	6.225	5.80(1.62)			
	$\frac{5}{2} \rightarrow \frac{3}{2}$	E2	1.533	1.550	1.410	–			
		M1	0.0174	0.0167	0.00017	–			
^{33}P	$\frac{3}{2} \rightarrow \frac{1}{2}$	E2+M1	5.830	5.916	5.827	10.0(4.0)	[83]	8.1(2.4)	
	$\frac{5}{2} \rightarrow \frac{1}{2}$	E2(+M3)	4.558	4.932	4.658	5.1(0.8)		4.8(0.6)	[84]
	$\frac{5}{2} \rightarrow \frac{3}{2}$	E2	0.676	0.809	0.797	< 24		< 37	
		M1	0.0202	0.0154	0.0304	0.025(5)		0.031(9)	

Table 7.3: $B(E2)$ and $B(M1)$ values from experiments and shell model calculations [52], given in Weisskopf units.

The available information on transition strengths in the $A = 33$, $T_z = \pm \frac{3}{2}$ mirror pair is summarized in table 7.3. Furthermore, the results of the new shell model calculations are shown. The values for ^{33}P are deduced from a lifetime measurement employing the ‘Doppler-Shift-Attenuation Method’, published by P. Wagner et al. [83] and by A. R. Poletti et al. [84]. The $T_z = \pm \frac{3}{2}$ mirror pairs separate in two groups: one with an unpaired neutron (‘UN’) in the proton rich partner and another one with an unpaired proton (‘UP’). Nuclei of these groups differ largely in their proton separation energies (S_p), the unpaired proton is much weakly bound than a paired proton. This difference causes that the ‘UP’ nuclei do not provide excited states below the S_p . Thus, no excited states can be compared with neutron rich nuclei in this group. The S_p for the proton rich $T_z = -\frac{3}{2}$ sd shell nuclei are summarized in table 7.4. The $T_z = \pm \frac{3}{2}$ mirror pairs are illustrated in figure 7.10 and the experimentally known transition strengths and values from shell model calculations are shown in figure 7.9.

Unpaired proton		Unpaired neutron	
Nucleus	S_p [MeV]	Nucleus	S_p [MeV]
^{19}Na	-0.32(1)	^{21}Mg	3.23(2)
^{23}Al	0.13(3)	^{25}Si	3.41(1)
^{27}P	0.86(3)	^{29}S	3.30(5)
^{31}Cl	0.29(5)	^{33}Ar	3.34(1)
^{35}K	0.09(1)	^{37}Ca	3.01(1)

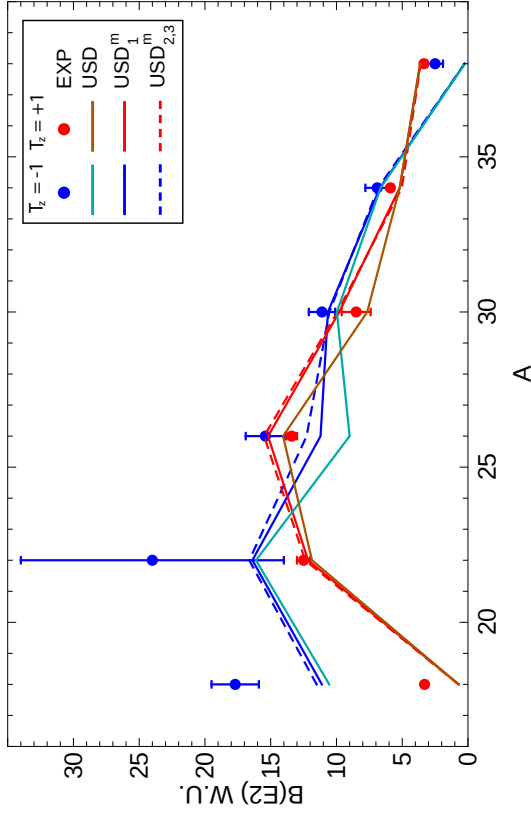
Table 7.4: Proton separation energies of $T_z = -\frac{3}{2}$ sd shell nuclei.



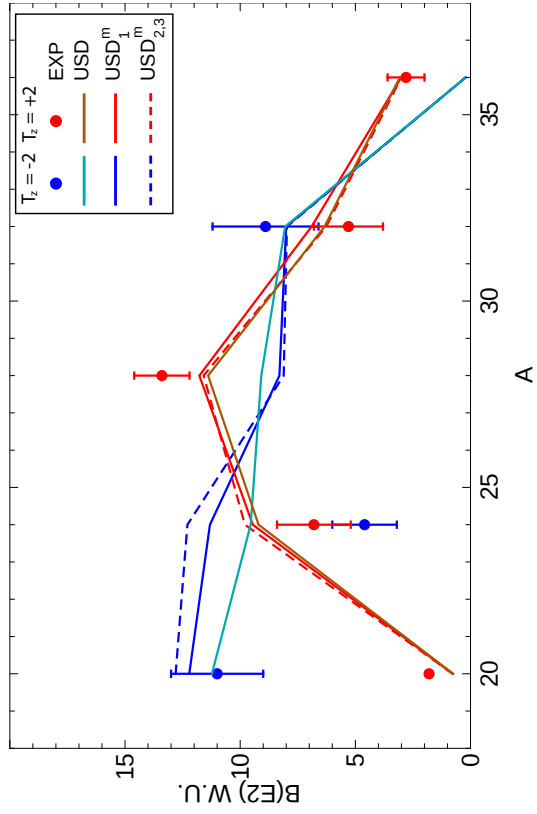
(a) Nuclei with unpaired neutron in the proton rich partner (‘UN’).

(b) Nuclei with unpaired proton in the proton rich partner (‘UP’).

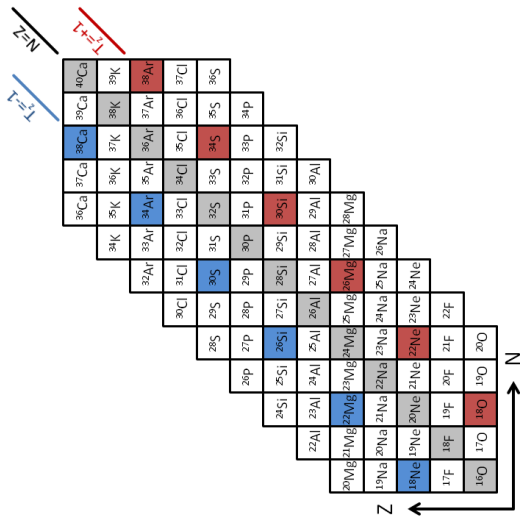
Figure 7.10: Illustration of $T_z = \pm \frac{3}{2}$ sd shell nuclei. The proton rich nuclei are marked blue, the neutron rich are marked red.



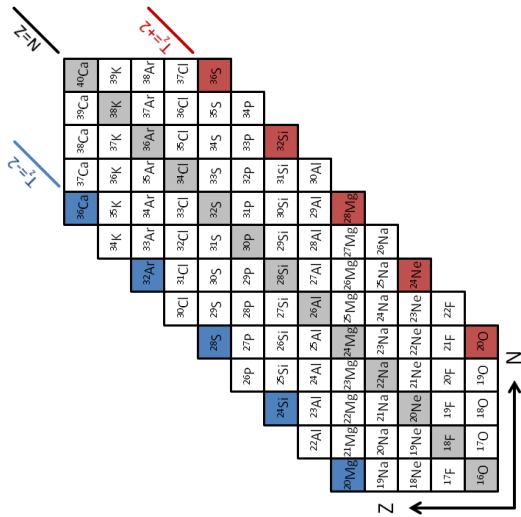
(a) $T_z = \pm 1$ nuclei. Data is taken from ref. [57].



(b) $T_z = \pm 2$ nuclei. Data is taken from ref. [99, 98, 21] and ref. [57].



(a) Illustration of the $T_z = \pm 1$ *sd* shell nuclei.



(b) Illustration of the $T_z = \pm 2$ *sd* shell nuclei.

Figure 7.8: Experimental $B(E2, 2_1^+ \rightarrow 0_1^+)$ values and shell model calculations of $T_z = \pm 1, 2$ *sd* shell nuclei. The proton rich nuclei are marked blue, the neutron rich are marked red. The shell model calculations are taken from ref. [52].

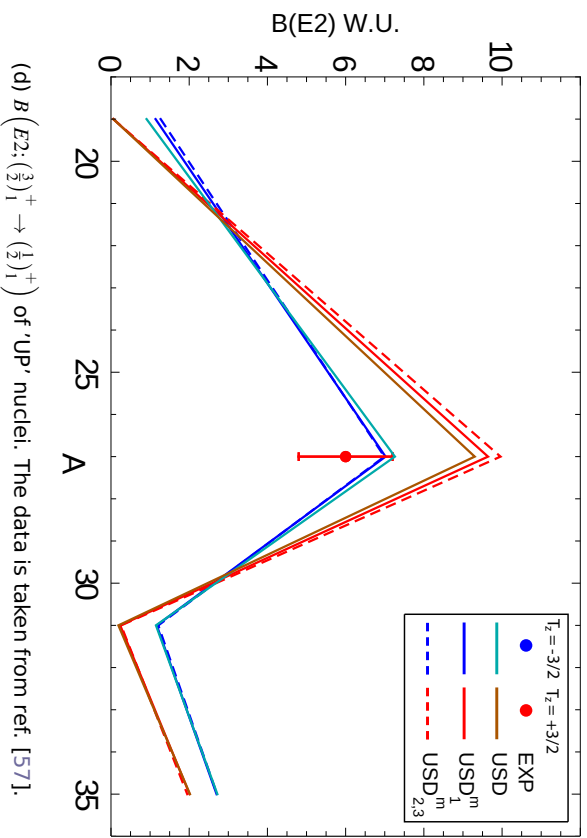
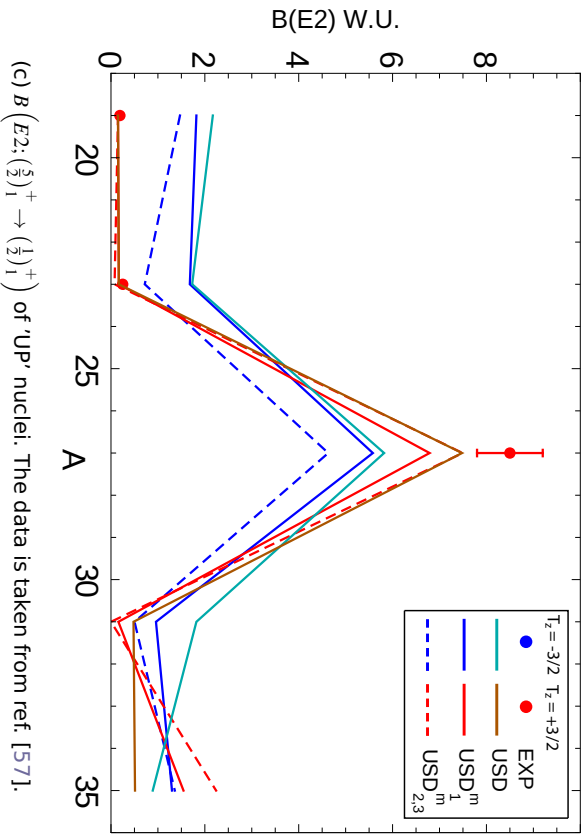
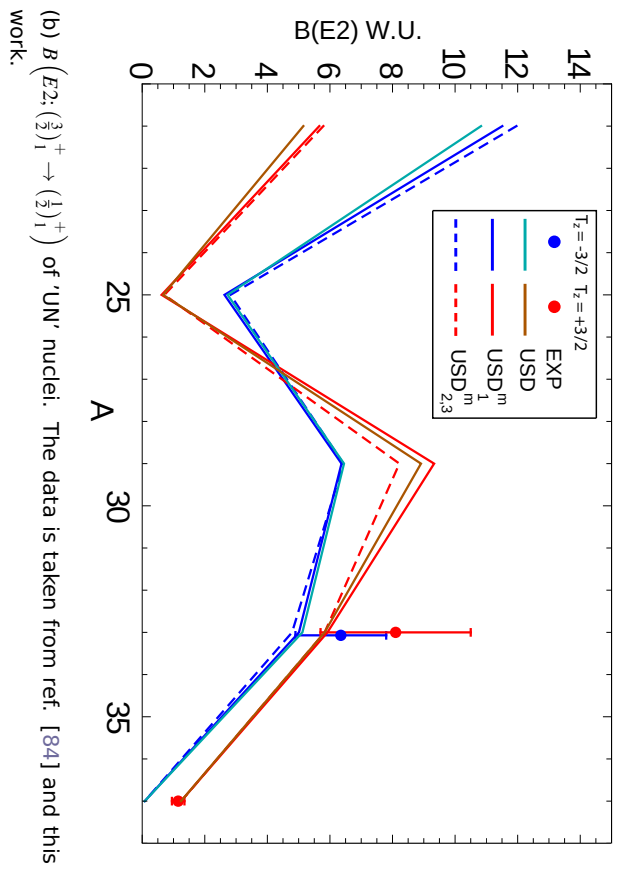
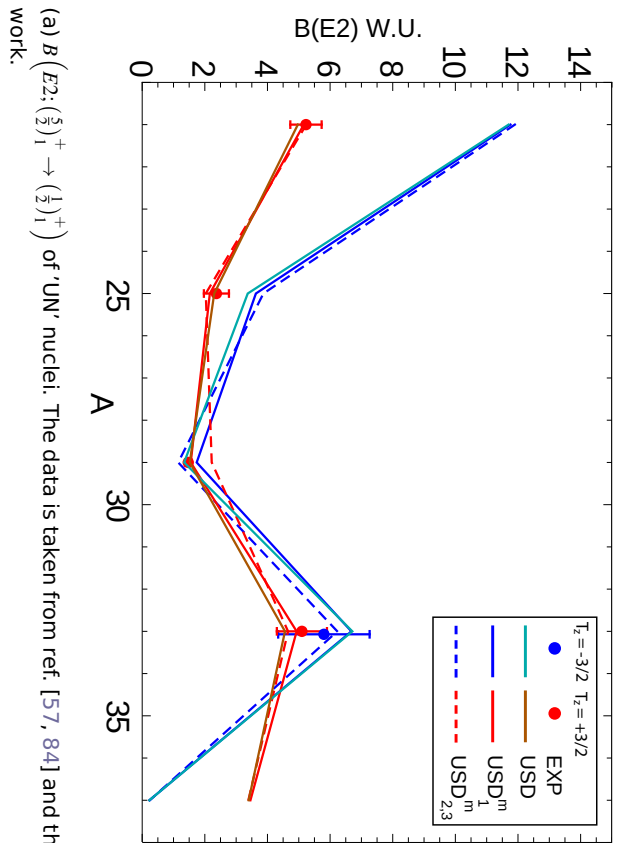


Figure 7.9: Experimental $B(E2)$ values and shell model calculations of $T_z = \pm \frac{3}{2}$ sd shell nuclei as shown in fig. 7.10. The nuclei are separated in 'UN' and 'UP' nuclei (details see text). The shell model calculations are taken from ref. [57].

For the 'UN' nuclei the largest amount of data is available. For the $(\frac{5}{2})_1^+ \rightarrow (\frac{1}{2})_1^+$ transition four $B(E2)$ values for the neutron rich and only one $B(E2)$ value of a proton rich nuclei (deduced in this work) is available. All experimental data is in excellent agreement with the shell model calculations. For confirmation of the trend more experimental data, especially from the lighter proton rich nuclei is needed. The experimental information for the $(\frac{3}{2})_1^+ \rightarrow (\frac{1}{2})_1^+$ transition is even more limited. Only the data for the $A = 33$ mirror pair exists. It is remarkable that for the first discussed transitions, the $B(E2)$ values are in general larger for the proton rich nuclei, whereas for the $(\frac{3}{2})_1^+ \rightarrow (\frac{1}{2})_1^+$ transition this is true for only $A < 27$. This characteristic is seen in the experimental data as well as in the calculated values. For the 'UP' nuclei experimental data is only available for the neutron rich partners. The protons are that bound in the proton rich nucleus, that excited states are most likely to de-excite via proton emission. Nonetheless, the calculations are in good agreement with the data. Experimental measurements of ^{31}Si and ^{35}S are of highest interest to confirm the predicted drop of the $B(E2)$ values for $A > 27$ in 'UP' nuclei. Furthermore, the study of the $(\frac{3}{2})_1^+ \rightarrow (\frac{1}{2})_1^+$ transitions in the (close to stable) $T_z = +\frac{3}{2}$ *sd* shell nuclei would be able to evaluate the predictive power of the effective interactions. All experimentally known $B(E2)$ values and the results of shell model calculations employing the described interactions are summarized in tables 7.5 and 7.6. The nuclei that are labeled 'unbound', provide only excited state that are unbound with respect to proton emission.

Summary

This chapter shows experimental excitation energies and $B(E2)$ values of transitions in *sd* shell nuclei and a comparison with modern shell model calculations. In particular, the first experimental data on $T_z = -\frac{3}{2}$ $B(E2)$ values is given. The presented effective interactions ($\text{USD}_{2,3}^m$) are capable to reproduce the mirror energy differences as well as the transition strengths in $T_z = \pm 1, \pm 2, +\frac{3}{2}$ nuclei.

The first experimental $B(E2)$ values for a $T_z = -\frac{3}{2}$ nucleus was deduced in the current work. The measurement of transition strengths in exotic nuclei is a challenging task. The presented experiment yields a finding, which provides comparable accuracy as the former measurements of less exotic nuclei. For further tests of this theory more experimental data on transition strengths of proton rich *sd* shell nuclei is needed.

Nucleus	Transition	Exp.	USD	USD ₁ ^m	USD ₂ ^m	USD ₃ ^m
¹⁹ Na	$(\frac{1}{2})^+ \rightarrow (\frac{5}{2})^+$	(unbound)	6.541	5.458	4.412	6.378
	$(\frac{1}{2})^+ \rightarrow (\frac{3}{2})^+$		1.824	2.284	2.550	2.017
	$(\frac{3}{2})^+ \rightarrow (\frac{5}{2})^+$		26.311	26.763	27.122	26.328
¹⁹ O	$(\frac{1}{2})^+ \rightarrow (\frac{5}{2})^+$	0.58(12)	0.440	0.444	0.444	0.227
	$(\frac{1}{2})^+ \rightarrow (\frac{3}{2})^+$		0.123	0.127	0.127	0.178
	$(\frac{3}{2})^+ \rightarrow (\frac{5}{2})^+$		1.769	1.769	1.769	1.853
²¹ Mg	$(\frac{1}{2})^+ \rightarrow (\frac{5}{2})^+$		35.096	35.270	35.706	35.851
	$(\frac{3}{2})^+ \rightarrow (\frac{5}{2})^+$		8.295	8.809	8.806	8.193
	$(\frac{9}{2})^+ \rightarrow (\frac{5}{2})^+$		15.398	15.851	16.116	15.671
	$(\frac{3}{2})^+ \rightarrow (\frac{1}{2})^+$		10.832	11.508	11.955	12.359
²¹ F	$(\frac{1}{2})^+ \rightarrow (\frac{5}{2})^+$	15.7(1.6)	14.983	15.485	15.712	15.584
	$(\frac{3}{2})^+ \rightarrow (\frac{5}{2})^+$	4.1(5)	0.675	1.050	1.157	1.017
	$(\frac{9}{2})^+ \rightarrow (\frac{5}{2})^+$		3.701	3.832	3.896	3.852
	$(\frac{3}{2})^+ \rightarrow (\frac{1}{2})^+$		5.145	5.657	5.790	5.485
²³ Al	$(\frac{1}{2})^+ \rightarrow (\frac{5}{2})^+$	(unbound)	5.178	5.033	2.156	4.418
	$(\frac{3}{2})^+ \rightarrow (\frac{5}{2})^+$		3.958	5.021	5.414	4.864
	$(\frac{3}{2})'^+ \rightarrow (\frac{5}{2})^+$		1.899	1.331	0.841	2.358
²³ Ne	$(\frac{1}{2})^+ \rightarrow (\frac{5}{2})^+$	0.75(5)	0.625	0.798	0.414	0.312
	$(\frac{3}{2})^+ \rightarrow (\frac{5}{2})^+$		0.947	0.943	0.896	1.230
	$(\frac{3}{2})'^+ \rightarrow (\frac{5}{2})^+$		0.518	0.440	0.230	2.071
²⁵ Si	$(\frac{1}{2})^+ \rightarrow (\frac{5}{2})^+$		10.111	10.877	11.619	8.913
	$(\frac{3}{2})'^+ \rightarrow (\frac{5}{2})^+$		2.729	2.697	2.819	2.810
	$(\frac{3}{2})^+ \rightarrow (\frac{5}{2})^+$		16.338	18.878	20.216	16.563
	$(\frac{1}{2})^+ \rightarrow (\frac{3}{2})^+$		5.465	5.258	5.647	5.030
²⁵ Na	$(\frac{1}{2})^+ \rightarrow (\frac{5}{2})^+$	7.1(1.1)	6.916	6.488	6.078	7.206
	$(\frac{3}{2})'^+ \rightarrow (\frac{5}{2})^+$		0.293	0.308	0.405	0.170
	$(\frac{3}{2})^+ \rightarrow (\frac{5}{2})^+$		26.854	27.867	28.052	28.558
	$(\frac{1}{2})^+ \rightarrow (\frac{3}{2})^+$		1.375	1.233	1.426	1.102
²⁷ P	$(\frac{3}{2})^+ \rightarrow (\frac{1}{2})^+$	(unbound)	7.259	7.016	6.995	7.970
	$(\frac{5}{2})^+ \rightarrow (\frac{1}{2})^+$		5.817	5.582	4.634	7.122
	$(\frac{5}{2})'^+ \rightarrow (\frac{1}{2})^+$		1.258	2.043	3.290	0.700
	$(\frac{5}{2})^+ \rightarrow (\frac{3}{2})^+$		0.447	0.105	0.007	0.416
²⁷ Mg	$(\frac{3}{2})^+ \rightarrow (\frac{1}{2})^+$	6.0(1.2)	9.302	9.643	9.961	8.712
	$(\frac{5}{2})^+ \rightarrow (\frac{1}{2})^+$	8.5(7)	7.483	6.789	7.492	2.402
	$(\frac{5}{2})'^+ \rightarrow (\frac{1}{2})^+$	1.8(4)	4.628	6.176	5.769	10.441
	$(\frac{5}{2})^+ \rightarrow (\frac{3}{2})^+$		1.258	0.983	1.112	0.164

Table 7.5: Experimental $B(E2)$ values and shell model calculations for $T_z = \pm \frac{3}{2}$, sd shell nuclei with $A \leq 27$.

Nucleus	Transition	Exp.	USD	USD _{1^m}	USD _{2^m}	USD _{3^m}
²⁹ S	$(\frac{1}{2})^+ \rightarrow (\frac{5}{2})^+$		4.034	5.226	5.987	3.346
	$(\frac{7}{2})^+ \rightarrow (\frac{5}{2})^+$		12.798	11.961	12.057	12.112
	$(\frac{3}{2})'^+ \rightarrow (\frac{5}{2})^+$		2.218	2.558	2.244	3.563
	$(\frac{3}{2})'^+ \rightarrow (\frac{1}{2})^+$		1.4458	0.565	0.722	0.204
	$(\frac{3}{2})^+ \rightarrow (\frac{5}{2})^+$		3.331	33.57	3.933	2.324
	$(\frac{3}{2})^+ \rightarrow (\frac{1}{2})^+$		6.448	6.374	6.501	6.425
²⁹ Al	$(\frac{1}{2})^+ \rightarrow (\frac{5}{2})^+$	4.4(3)	4.561	4.644	4.253	6.667
	$(\frac{7}{2})^+ \rightarrow (\frac{5}{2})^+$		11.009	12.135	12.951	11.351
	$(\frac{3}{2})'^+ \rightarrow (\frac{5}{2})^+$		1.374	2.122	2.382	0.806
	$(\frac{3}{2})'^+ \rightarrow (\frac{1}{2})^+$		1.324	0.725	0.699	1.702
	$(\frac{3}{2})^+ \rightarrow (\frac{5}{2})^+$		4.376	4.415	4.610	5.216
	$(\frac{3}{2})^+ \rightarrow (\frac{1}{2})^+$		8.914	9.329	9.424	8.215
³¹ Cl	$(\frac{5}{2})^+ \rightarrow (\frac{3}{2})^+$	(unbound)	12.978	12.895	13.070	12.837
	$(\frac{1}{2})^+ \rightarrow (\frac{3}{2})^+$		1.876	2.306	2.351	2.420
	$(\frac{5}{2})^+ \rightarrow (\frac{1}{2})^+$		1.822	0.959	0.670	0.502
³¹ Si	$(\frac{5}{2})^+ \rightarrow (\frac{3}{2})^+$	11.5(2.3)	11.718	13.708	14.856	13.080
	$(\frac{1}{2})^+ \rightarrow (\frac{3}{2})^+$		0.382	0.473	0.495	0.518
	$(\frac{5}{2})^+ \rightarrow (\frac{1}{2})^+$		0.483	0.158	0.087	0.002
³³ Ar	$(\frac{3}{2})^+ \rightarrow (\frac{1}{2})^+$	6.39(1.49)	5.115	5.013	5.126	4.790
	$(\frac{5}{2})^+ \rightarrow (\frac{1}{2})^+$	5.80(1.62)	6.705	6.684	6.732	6.225
	$(\frac{5}{2})^+ \rightarrow (\frac{3}{2})^+$		1.533	1.550	1.597	1.410
	<i>M1</i>		0.0174	0.0167	0.0178	0.0002
³³ P	$(\frac{3}{2})^+ \rightarrow (\frac{1}{2})^+$	9.0(3.2)	5.830	5.916	6.000	5.827
	$(\frac{5}{2})^+ \rightarrow (\frac{1}{2})^+$	5.0(0.7)	4.558	4.932	5.291	4.658
	$(\frac{5}{2})^+ \rightarrow (\frac{3}{2})^+$	< 31	0.676	0.809	0.859	0.797
	<i>M1</i>	0.028(7)	0.0202	0.0154	0.0061	0.0304
³⁵ K	$(\frac{1}{2})^+ \rightarrow (\frac{3}{2})^+$	(unbound)	5.436	5.390	5.390	5.423
	$(\frac{5}{2})^+ \rightarrow (\frac{3}{2})^+$		0.551	0.715	0.789	0.711
	$(\frac{5}{2})^+ \rightarrow (\frac{1}{2})^+$		0.890	1.299	1.578	1.361
³⁵ S	$(\frac{1}{2})^+ \rightarrow (\frac{3}{2})^+$	(3.8(7))	4.044	4.014	4.148	3.898
	$(\frac{5}{2})^+ \rightarrow (\frac{3}{2})^+$		3.658	2.757	2.605	1.894
	$(\frac{5}{2})^+ \rightarrow (\frac{1}{2})^+$		0.512	1.545	1.745	2.238
³⁷ Ca	$(\frac{1}{2})^+ \rightarrow (\frac{3}{2})^+$		0.166	0.166	0.166	0.162
	$(\frac{5}{2})^+ \rightarrow (\frac{3}{2})^+$		0.325	0.330	0.330	0.324
	$(\frac{5}{2})^+ \rightarrow (\frac{1}{2})^+$		0.288	0.277	0.277	0.242
³⁷ Cl	$(\frac{1}{2})^+ \rightarrow (\frac{3}{2})^+$	2.3(5)	2.475	2.481	2.460	2.497
	$(\frac{5}{2})^+ \rightarrow (\frac{3}{2})^+$	3.6(9)	4.840	4.750	4.711	4.773
	$(\frac{5}{2})^+ \rightarrow (\frac{1}{2})^+$		3.394	3.456	3.543	3.390

Table 7.6: Experimental $B(E2)$ values and shell model calculations for $T_z = \pm\frac{3}{2}$, *sd* shell nuclei with $A \geq 29$.

Chapter 8

Outlook

In October / November 2012 the PreSpec-AGATA campaign is taking place. For this, the AGATA demonstrator replaces the EUROBALL Cluster detectors. This increases the γ -ray detection efficiency by a factor of 2-2.5 for detecting a ^{36}Ar γ -ray, under similar conditions as in the presented experiment. Photographs of the AGATA demonstrator array at the Legnaro National Lab (fig. 8.1) and at the PreSpec setup (fig. 8.2) are shown.

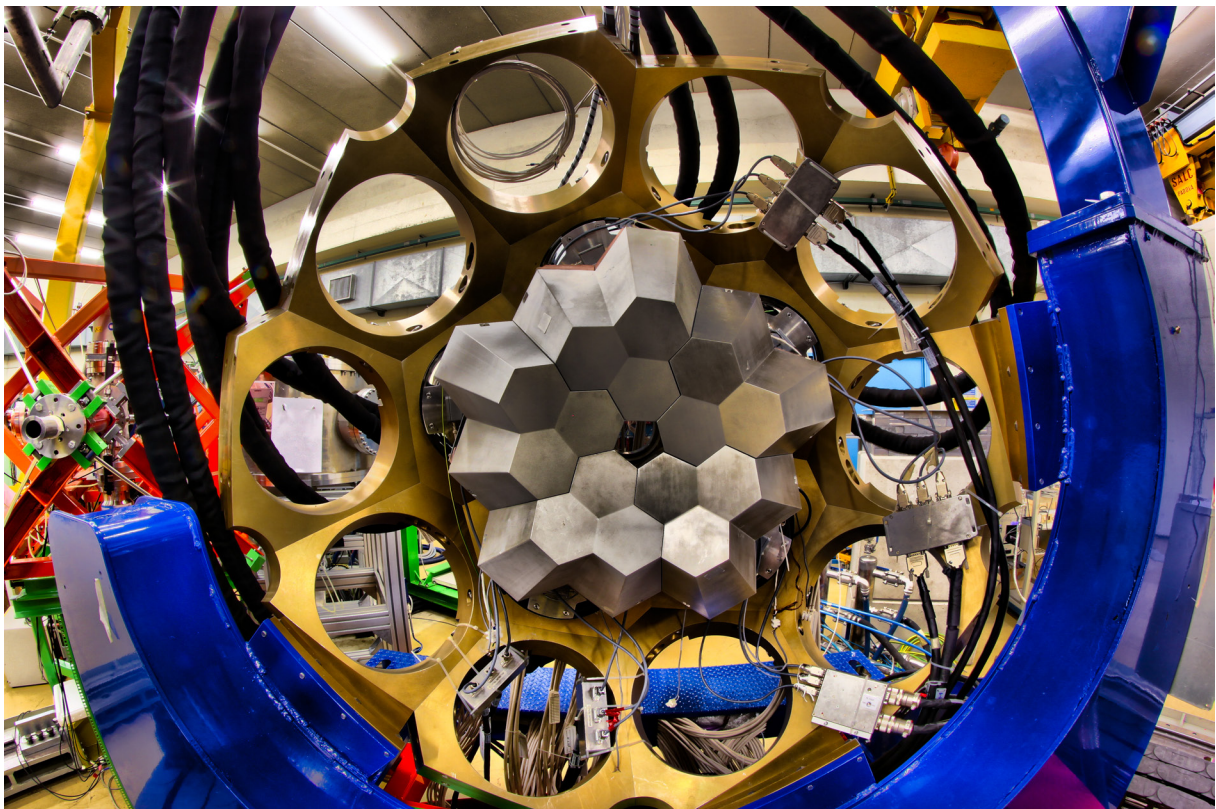


Figure 8.1: The AGATA demonstrator array, installed at the Legnaro National Lab.

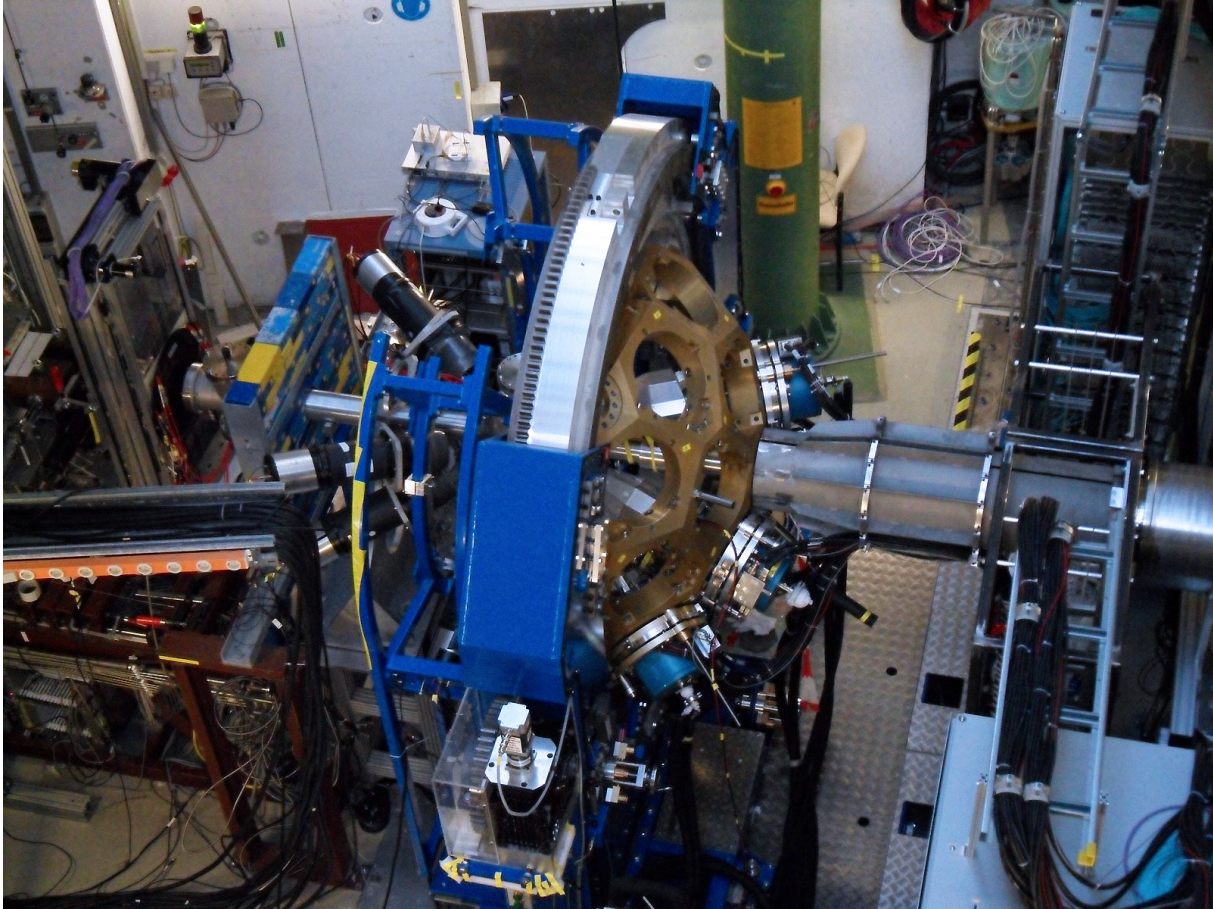


Figure 8.2: The AGATA demonstrator array, installed at the FRS-S4 experimental area.

Furthermore, LYCCA is extended by four more detector modules. While LYCCA-0 employed twelve $\Delta E - E$ modules the intermediate LYCCA-1 houses 16 detector modules, which are still read-out by the conventional electronics. First hit patterns of the LYCCA-1 detectors, taken during the PreSpec-AGATA commissioning in September 2012 and a photograph of the installed detector modules are shown in 8.3. The calorimeter will be upgraded for the future HiSpec campaign (starting in 2017), then LYCCA will employ the full amount of 26 detector modules, which will be coupled to modern digital electronics.

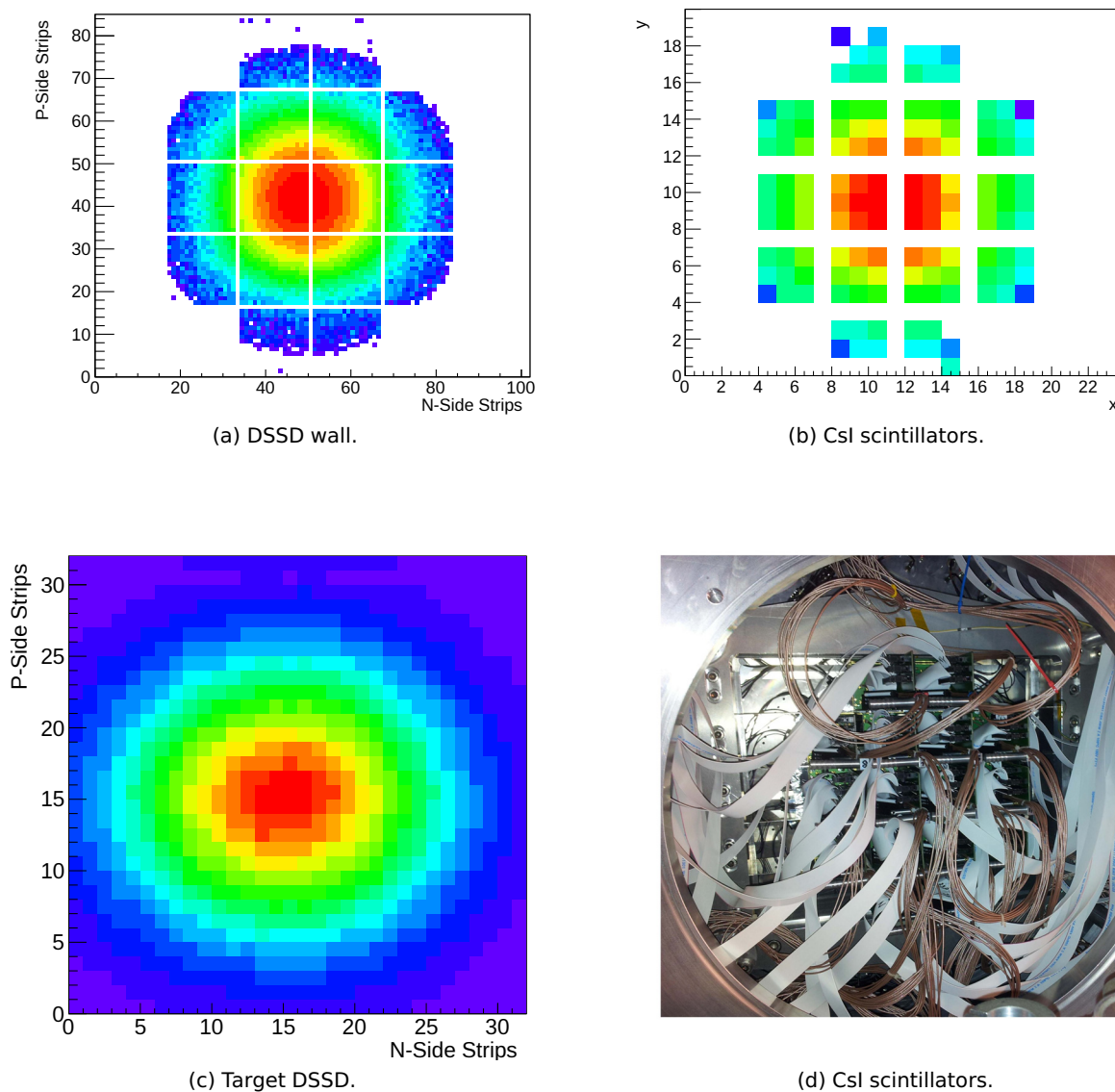


Figure 8.3: Hit pattern and photograph of the LYCCA-1 detectors.

The investigations on transition strengths for the proton rich sd shell nuclei is still a comprehensive testing ground for shell model interactions. Thus, further experiments are needed to verify the conclusion that transition strengths can be reproduced by modern shell model calculations. Therefore, a Coulomb excitation experiment of ^{25}Si and ^{29}S , to determine the $B(E2)$ values, is of highest interest. This experiment could not be realized yet, due to technical problems.

Appendix A

The nuclear shell model

The nuclear shell model was founded on the very successful atomic shell model. When it was published [4, 5], experimental data of the ground states (mass, spin, parity and magnetic moments) were available.

The fundamental assumption in the nuclear shell model is that each nucleon moves independently in an average field (created by the nucleons forming the nucleus). Together with the effect of the spin-orbit coupling, the shell model was able to predict the magic numbers up to the heaviest existing nuclei.

In contrast to the atomic shell model no elementary description of the constitutive interaction is available. This means, that the information about the interaction has to be extracted from experimental data.

The natural starting point for any theoretical description of nuclei is the Schrödinger equation

$$H\Psi = E\Psi.$$

Ψ can be written as a product of single particle wave functions. For a nucleus consisting of A nucleons, the nuclear Hamiltonian H can be written as a sum of kinetic energy and potential energy of the nucleons in the nuclear mean field (U_i) [3]:

$$\begin{aligned} H &= T + V \\ &= \sum_{i=1}^A \frac{p_i^2}{2m_i} + \frac{1}{2} \sum_{i \neq j}^A V_{i,j}(|\vec{r}_i - \vec{r}_j|) \\ &= \sum_{i=1}^A \left[\frac{p_i^2}{2m_i} + U_i(\vec{r}) \right] + \frac{1}{2} \sum_{i \neq j}^A V_{i,j}(|\vec{r}_i - \vec{r}_j|) - \sum_{i=1}^A U_i(\vec{r}) \\ &= H_0 + H_{res} \end{aligned}$$

The solutions of the Schrödinger equation

$$H_0\Psi = E\Psi$$

are the nucleon single particle energies (SPE) in the central potential of the nucleus. In experiments they can be studied in nuclei that have single valence nucleons or holes outside of a closed shell (e.g. ^{17}O / ^{17}F or ^{39}Ca / ^{39}K , cf. fig. A.1). If a second valence nucleon is provided, the nucleon-nucleon interaction becomes important. It is described as two-body matrix elements (TBME) of the residual interaction H_{res} .

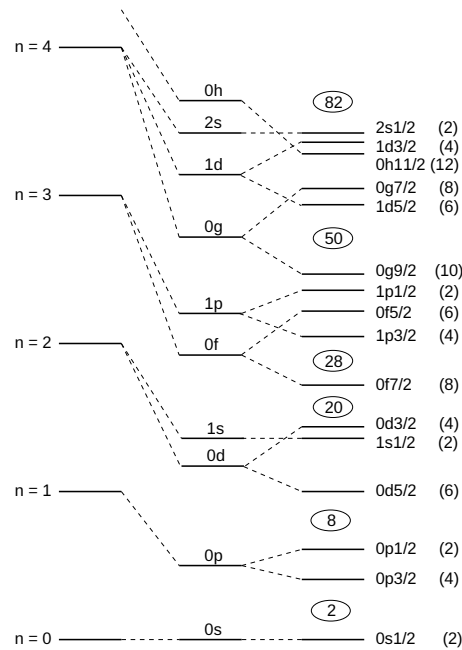


Figure A.1: Illustration of single-particle orbits in the shell model. Left: harmonic oscillator, Wood-Saxon potential without (middle) and with (right) spin-orbit splitting. On right-hand side the maximum number of nucleons in this orbit is given. Summing them leads to the magic numbers at the energy gaps (in circles). (Fig. based on ref. [5], modified from ref. [37]).

Within the last years several successful (empirical) interactions have been published (e.g. [87, 86, 88, 16] for the *sd* shell). The shell model is the major tool to interpret experimental data. Different interactions are used to find a good description of the energies and transition strengths of excited states.

Appendix B

Transition probabilities

This experiment focuses determination the reduced transition strengths of the first two excited states of ^{33}Ar . These observables are directly linked to important characteristics of the levels as the quadrupole moment and the lifetime.

The lifetime of any excited state, that de-excites via the emission of γ -rays depends on the transition energy E_γ , its electromagnetic character σ (electric or magnetic), the multipolarity L and the transition operator $O(LM)$. According to [43, p. 136] the reduced transition probability is given by

$$B(\sigma L; J_i \rightarrow J_f) = \sum_{M_i, M_f} |\langle \alpha_f; J_f M_f | O(\sigma LM) | \alpha_i; J_i M_i \rangle|^2.$$

Here, $J_{i/f}$ are the spin, $M_{i/f}$ the magnetic quantum number and $\alpha_{i/f}$ a set of quantum numbers, that describe the initial / final state. Applying the Wigner-Eckhart theorem leads to

$$B(\sigma L; J_i \rightarrow J_f) = \frac{1}{2J_i + 1} |\langle \alpha_f J_f || O(\sigma L) || \alpha_i J_i \rangle|^2,$$

if no initial orientation or polarization is assumed.

If initial and final states are interchanged reduced transition strengths convert in the following way [44, p. 63]:

$$B(\sigma L; J_f \rightarrow J_i) = \frac{2 \cdot J_i + 1}{2 \cdot J_f + 1} \cdot B(\sigma L; J_i \rightarrow J_f).$$

The lifetime τ of a state depends on the reduced transition strength of the decay. According to [43], for electric transitions ($\sigma = E$) this is given by:

$$\frac{\hbar}{\tau} = \frac{8\pi(L+1)}{L[(2L+1)!!]^2} \cdot \left[\frac{E}{\hbar c} \right]^{2L+1} \cdot B(\sigma L; J_i \rightarrow J_f).$$

The transitions that are under investigation in this experiment are electric-quadrupole radiation ($E2$). The transition strength ($B(E2)$) is related to the quadrupole moment Q_0 as follows:

$$B(E2; J_{g.s.} \rightarrow J_{g.s.} + 2) = \frac{5}{16} e^2 Q_0^2,$$

if the transition belongs to pure a rotational band. Thus, the quadrupole moment is linked to the deformation of the nucleus. The $B(E2)$ value is expected to be small close to shell closures and large in mid-shell regions (cf. fig. B.1, b).

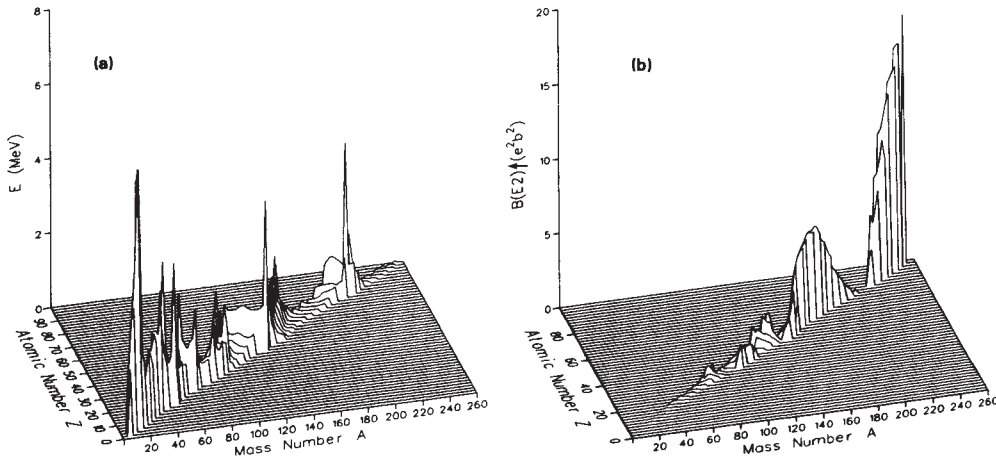


Figure B.1: Experimental $E(2_1^+)$ energies and $B(E2)$ values. (Fig. taken from [45]).

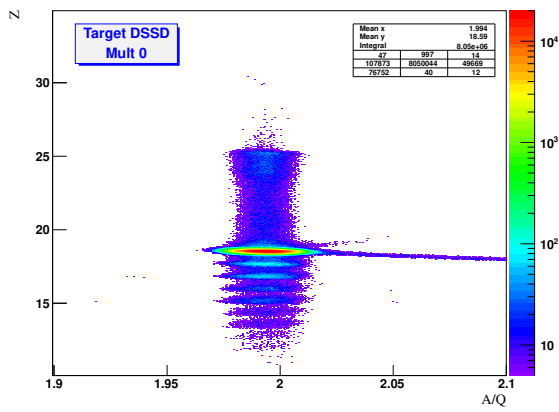
Weisskopf units The common unit to describe the strength of a transition is the Weisskopf unit (W.U.). Its value depends on the type of transition, for an EL transition it is [3]

$$B(EL)[W.U.] = \frac{1}{4\pi} \left(\frac{3}{l+3} \right)^2 (1.2 \cdot A^{-1/3})^{2L} e^2 [e^2 fm^{2l}]. \quad (B.1)$$

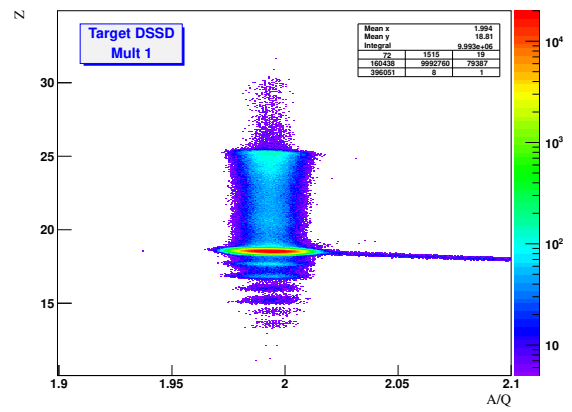
The transition strength in W.U. can roughly be identified with the number of nucleons, that are involved in the transition. Thus, the $B(E2)$ value gives a good insight into the collectivity of a transition.

Appendix C

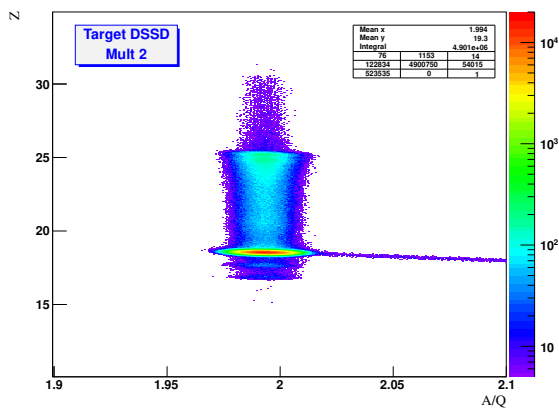
Graphs and pictures



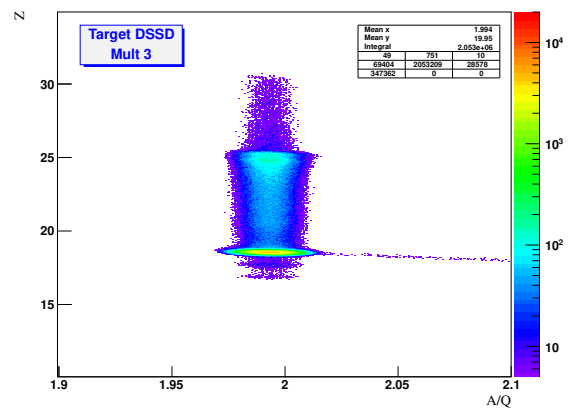
(a) $M_{tar} = 0$



(b) $M_{tar} = 1$

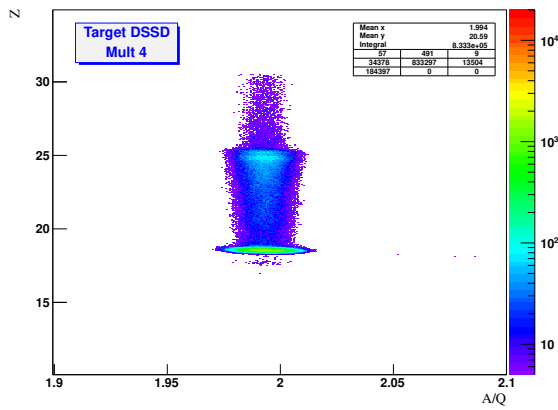


(c) $M_{tar} = 2$

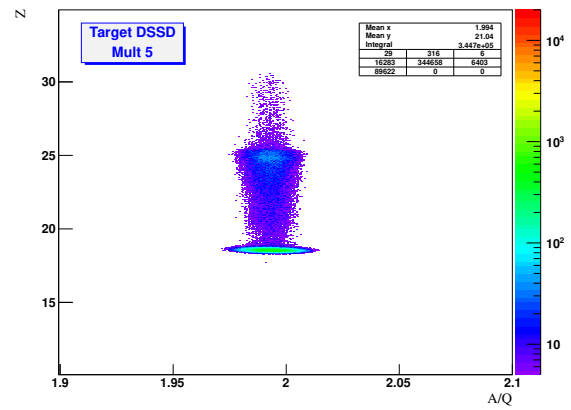


(d) $M_{tar} = 3$

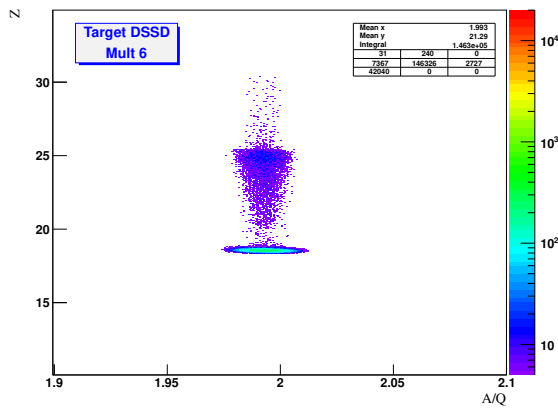
Figure C.1: A/Q vs. Z for target DSSD multiplicities 0 to 3.



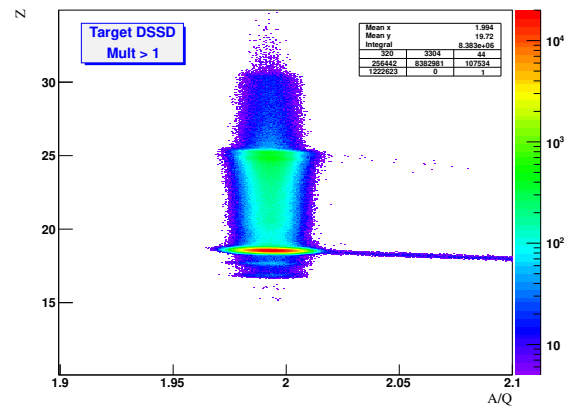
(a) $M_{tar} = 4$



(b) $M_{tar} = 5$

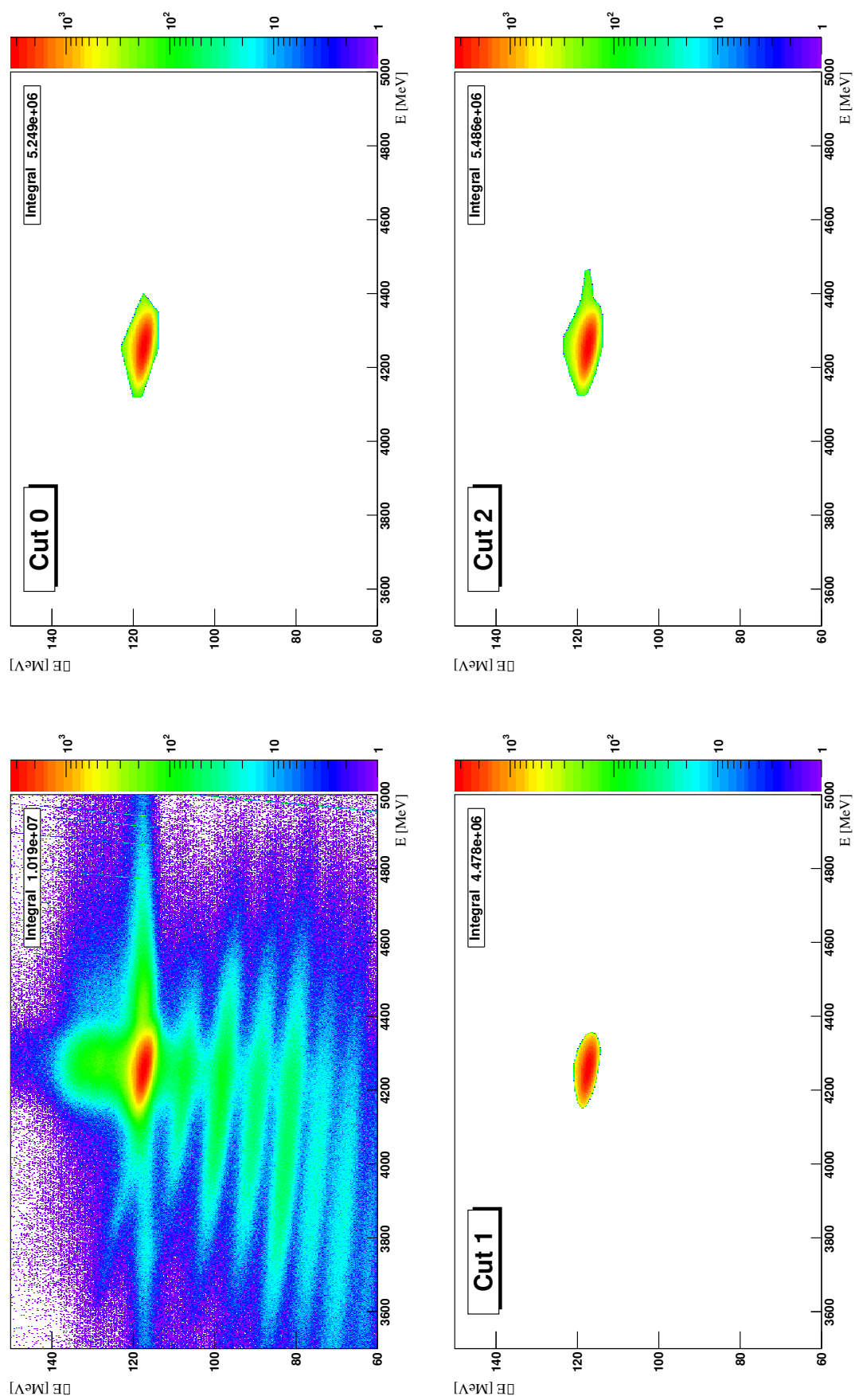


(c) $M_{tar} = 6$



(d) $M_{tar} > 1$

Figure C.2: A/Q vs. Z for target DSSD multiplicities 4 to 6 and $M_{tar} > 1$.

Figure C.3: $\Delta E - E$ gates.

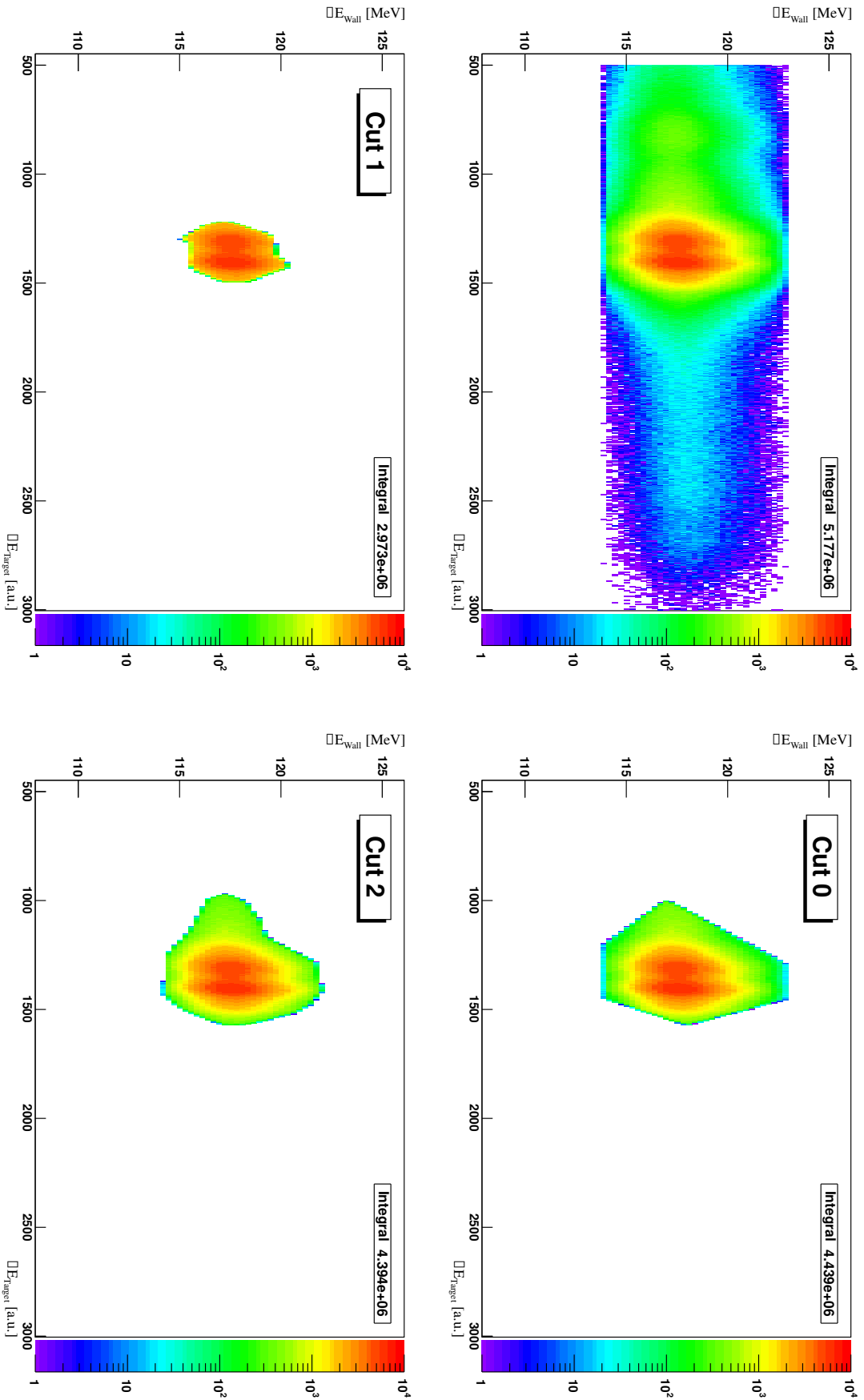


Figure C.4: $\Delta E - \Delta E$ gates.

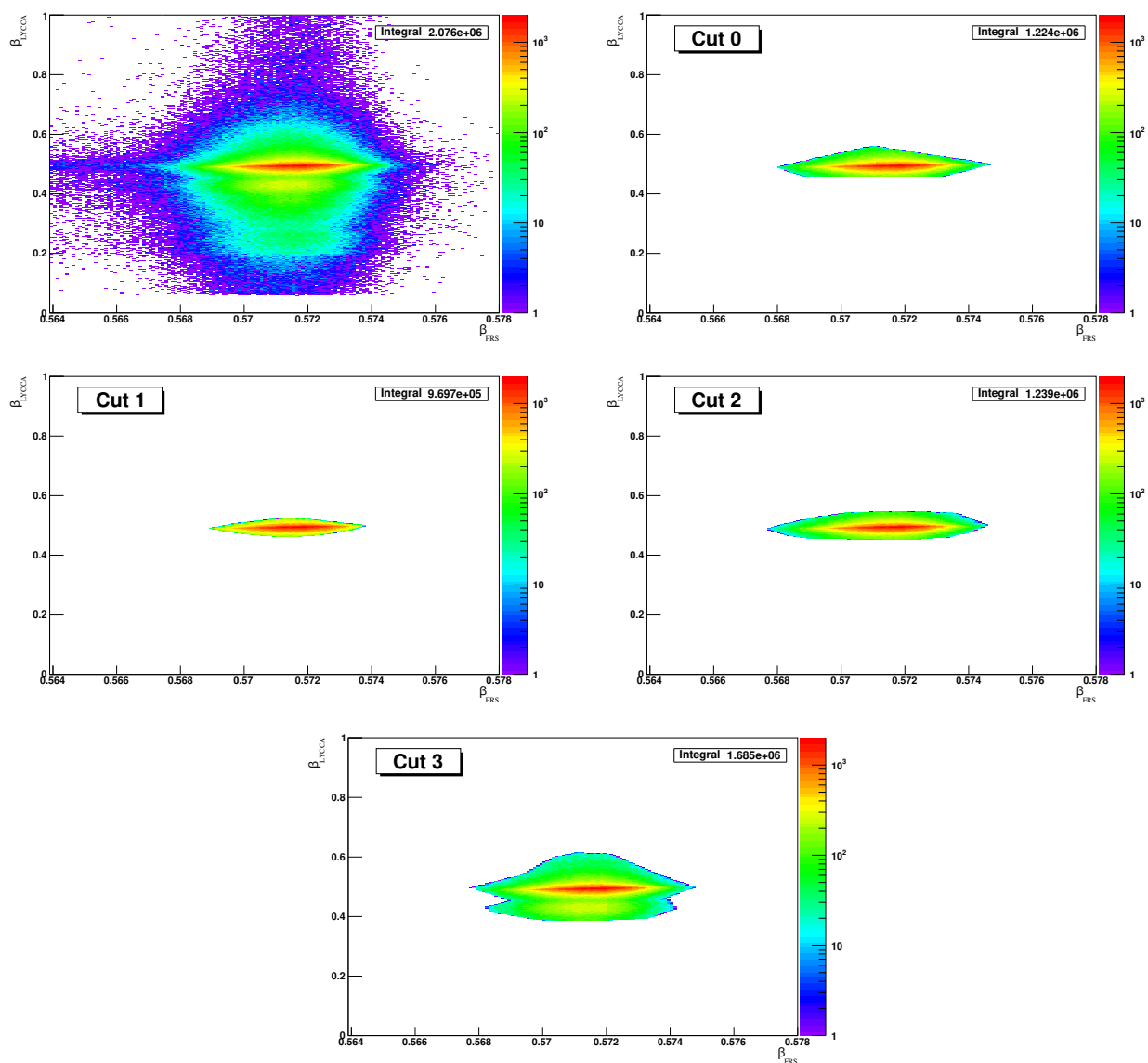


Figure C.5: $\beta_{FRS} - \beta_{LYCCA}$ gates.

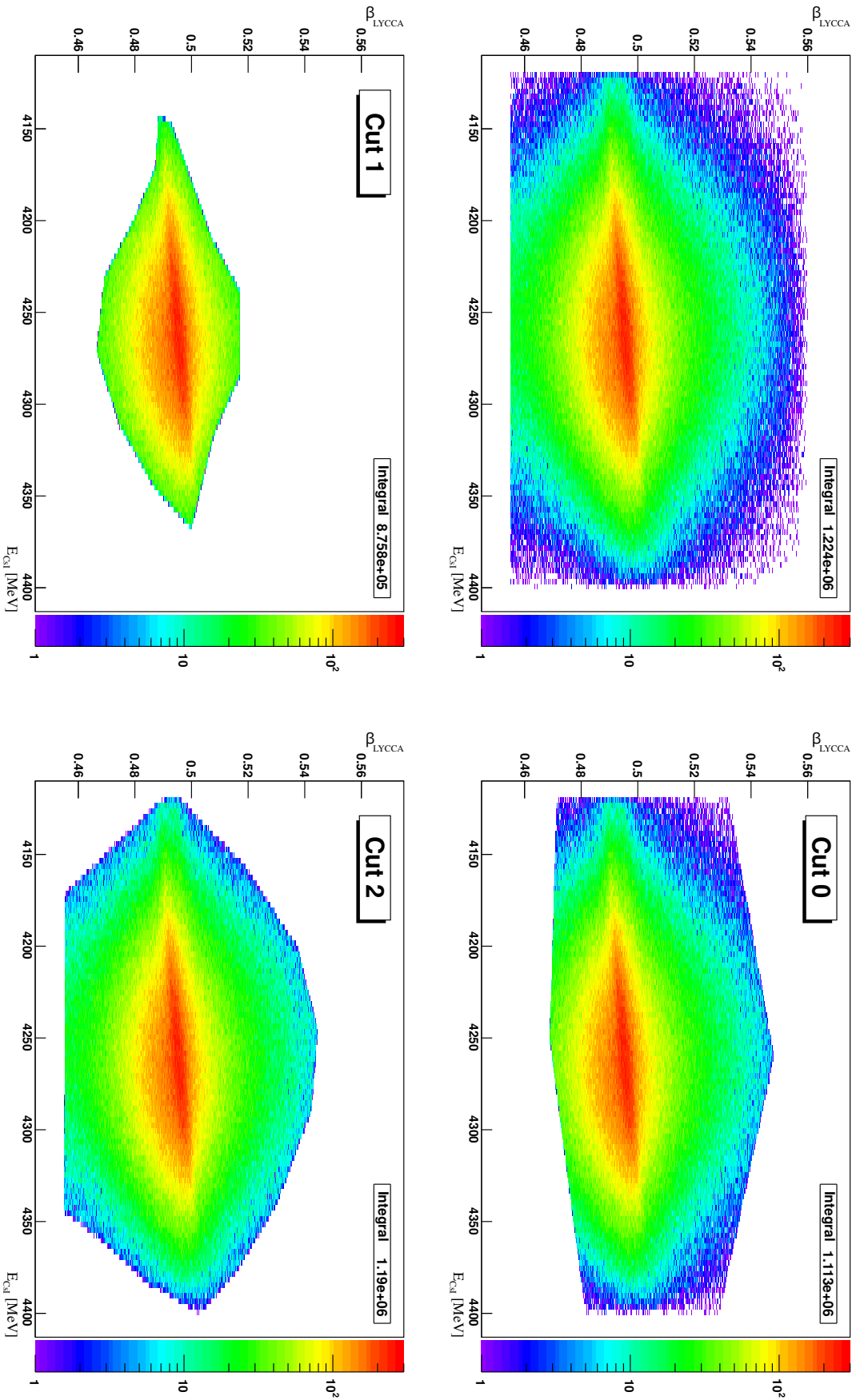
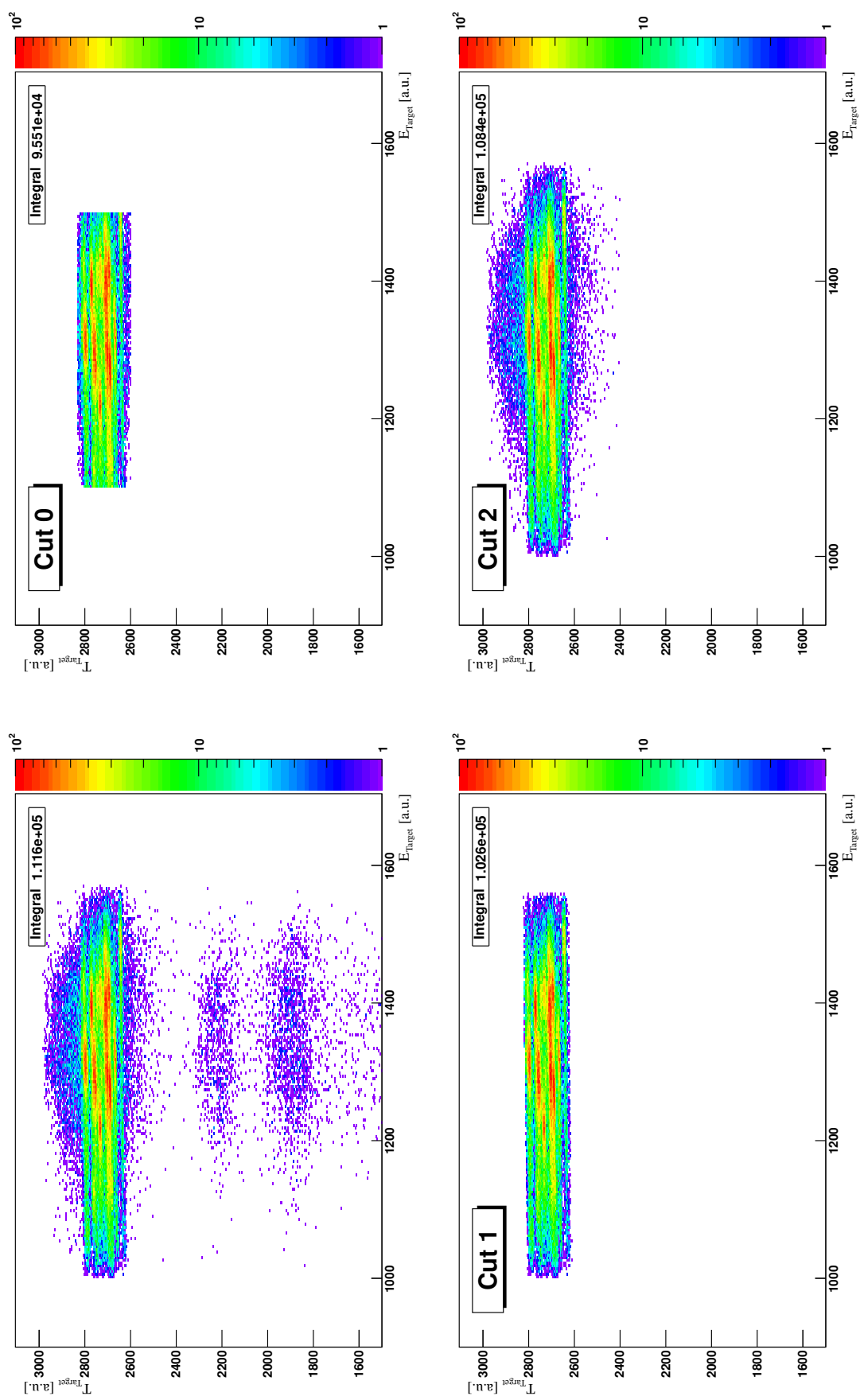


Figure C.6: $\beta_{LYC} - E_{CsI}$ gates.

Figure C.7: Target DSSD $E - T$ gates.

Appendix D

Technical drawings

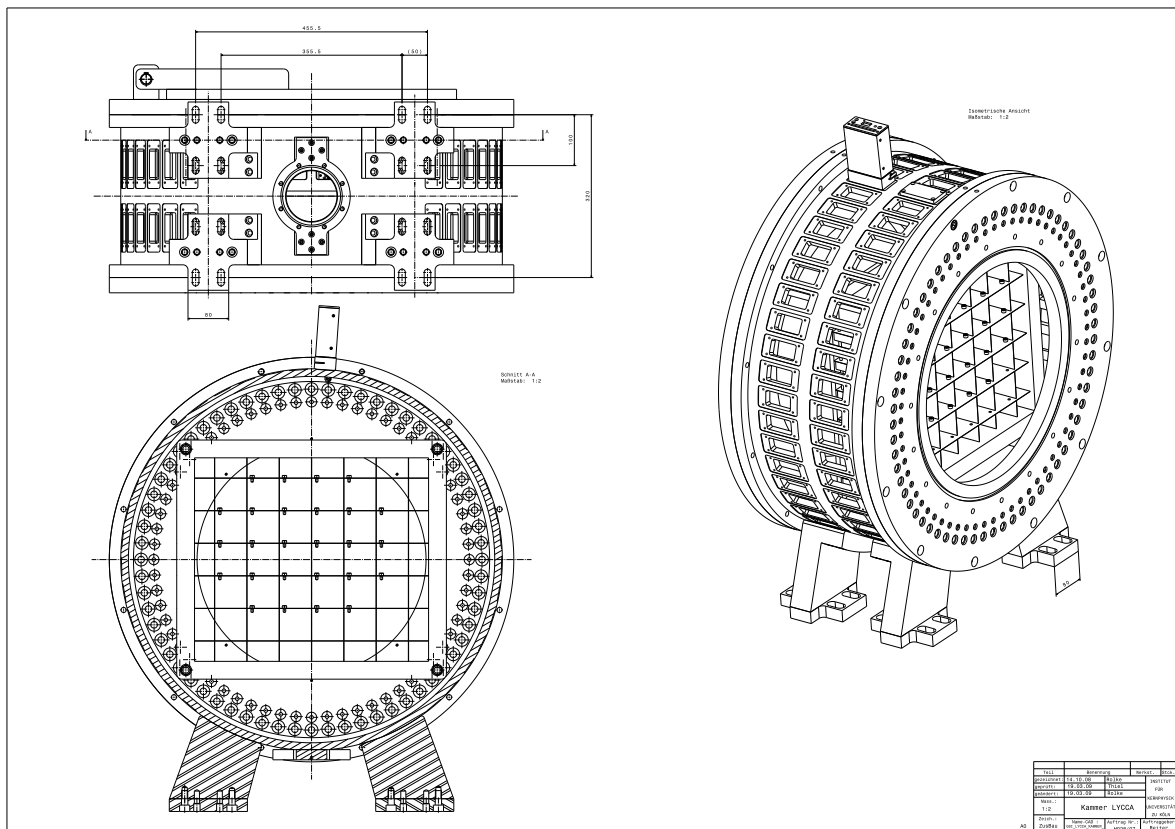
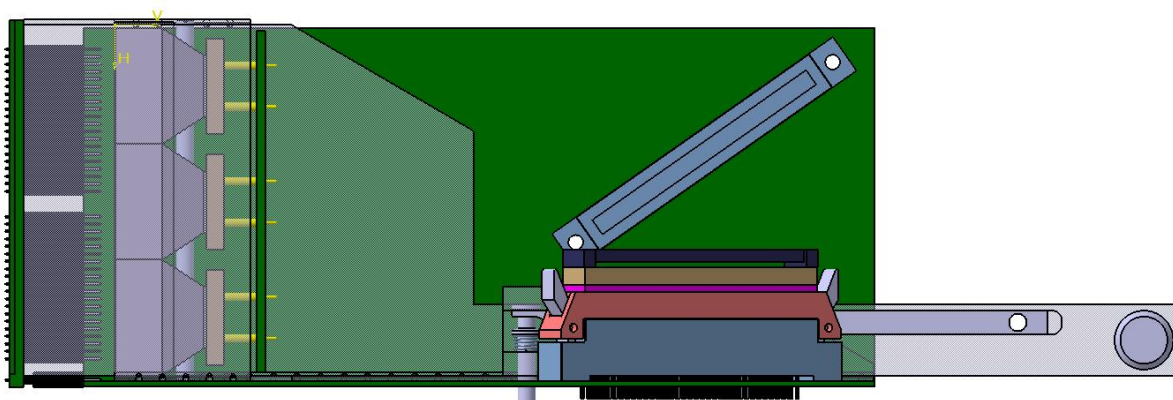
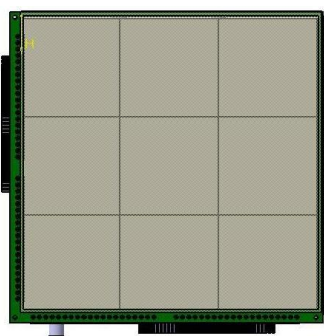


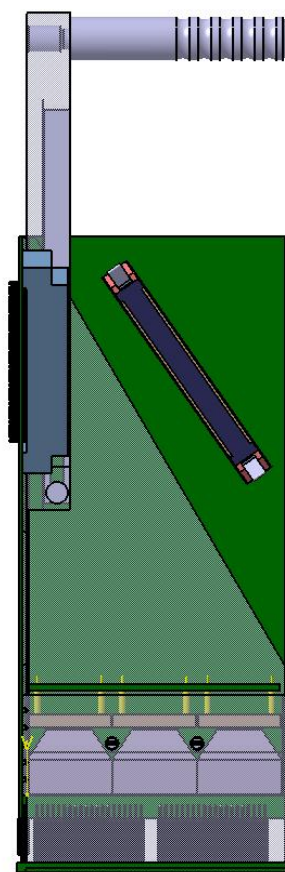
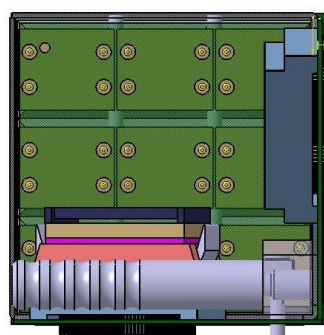
Figure D.1: Technical drawings of the LYCCA chamber.



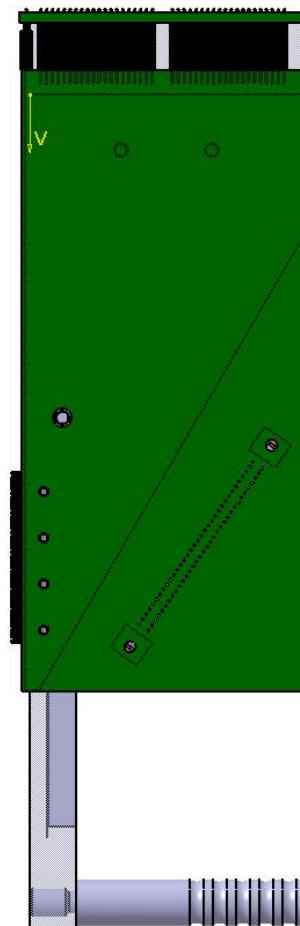
(a) View from side.



(b) Front / rear view.



(c) Top view.



(d) Bottom view.

Figure D.3: Technical drawings of detector module.

List of Figures

2.1	Possible couplings of a pair of nucleons	8
2.2	Ground states and IASs of the $A = 21, T = \frac{3}{2}$ quadruplet	10
2.3	MEDs of the $A = 51, T_z = \pm\frac{1}{2}$ doublet	12
2.4	Illustration of level configurations for ^{51}Fe	13
2.5	MEDs of the $T_z = \pm 1$ pair $^{48}\text{Mn} - ^{48}\text{V}$	15
2.6	MEDs of the $T_z = \pm 1$ pair $^{54}\text{Ni} - ^{54}\text{Fe}$	16
2.7	Increase and decrease of neighbouring orbits	17
2.8	Level schemes of the $A = 35, T = \pm\frac{1}{2}$ mirror pair	18
2.9	Experimental MEDs for the $A = 35, 39, T = \pm\frac{1}{2}$ mirror pairs	19
2.10	SM calculations of the MEDs of the 2_1^+ states in $T = 1, 2$ sd shell mirror pairs	20
2.11	SM calculations of the MEDs of $T = \frac{1}{2}$ sd shell mirror pairs	22
2.12	SM calculations of the MEDs of $T = \frac{3}{2}$ sd shell mirror pairs	22
2.13	Level schemes of ^{33}Ar and ^{33}P	23
3.1	Illustration of the fragmentation mechanism	27
3.2	Scheme of the GSI accelerator complex	28
3.3	Scheme of the FRS	29
3.4	Illustration of the Finger detector	31
3.5	Picture of a MUSIC detector	31
3.6	Pictures of a TPC	32
3.7	Monte Carlo simulation of fragmentation reaction.	38
3.8	FRS identification plot for the ^{33}Ar setting	38
3.9	Schematic layout of the FRS/PreSpec setup	40
3.10	Photo of the PreSpec setup	41
3.11	Photo of EUROBALL Cluster detectors and HECTOR	41
3.12	Structure of the Multi Branch System	43

3.13	Photo of the trigger logic modules	44
4.1	Schematic view of the LYCCA array	46
4.2	Photographs of a DSSD	47
4.3	Images of a DSSD	48
4.4	Illustration of the different types of CsI scintillators	49
4.5	Photograph CsI crystals	49
4.6	CsI scintillator of the long type	49
4.7	Technical drawings of $\Delta E - E$ modules	50
4.8	Final version of the $\Delta E - E$ module's frame	51
4.9	Images of a plastic scintillator	53
4.10	Technical drawing of the LYCCA chamber	54
4.11	Technical drawing of the holding structure	54
4.12	Technical drawings of the LYCCA chamber 1	55
4.13	Photo of a single bank of the holding structure	56
4.14	Alignment of LYCCA detector modules.	56
4.15	LYCCA chamber with four installed detector modules	56
4.16	Charge sensitive preamplifier prototype	57
4.17	Final version of the charge sensitive preamplifier	57
4.18	LYCCA test chamber for off-beam-tests.	58
4.19	Energy spectrum of a DSSD strip	58
4.20	Decomposition of an α -transition	58
4.21	Position plot with mask	59
4.22	Mask for signal allocation check	59
4.23	$\Delta E - E$ module during the first in-beam test	60
4.24	LYCCA's first $\Delta E - E$ plot	61
4.25	2d distribution of hit DSSD pixels	61
4.26	Partial projection on the x-axis	61
4.27	LYCCA chamber with four installed detector modules	62
4.28	Energy spectra of detector module 6	63
4.29	Energy resolutions of LYCCA module 6 in S377 experiment	64
4.30	Plots for LYCCA DSSD calibration	65
4.31	Calibration functions	66
4.32	Identification plots from S369 the experiment (^{84}Kr fission beam)	67

4.33	β -corrected Z-identification plots	67
4.34	Mass identification plots	68
4.35	Mass identification plots	69
4.36	Tracking along the path of an ion	70
4.37	Hit pattern of the LYCCA DSSDs	70
4.38	Distribution of the change in scattering angle	71
5.1	γ -ray spectra of a ^{152}Eu source	75
5.2	$A/Q - Z$ plots	76
5.3	LYCCA $\Delta E - E$ plot	77
5.4	LYCCA $\Delta E - \Delta E$ plot	78
5.5	Velocity correlation plot	78
5.6	LYCCA $\beta - \text{CsI}$ plot	79
5.7	LYCCA target DSSD $T - \Delta E$ plot	80
5.8	Multiplicity of the target DSSD for different triggers	80
5.9	Energy and time correlations of $M_{tar} = 2$ events	81
5.10	Correlations of hits in neighbouring strips	82
5.11	Definition of energy- and time-regions	82
5.12	$E - E$ correlation for different time and space conditions	83
5.13	$T - T$ correlation for different energy and space conditions	84
5.14	SR spectrum from the Cluster detectors	86
5.15	Energy spectra of Cluster detectors	87
5.16	Doppler corrected $SR - E$ plot from the Cluster detectors	87
5.17	Fit of the peak	88
5.18	Crystal multiplicity	89
5.19	Multiplicity of the target DSSD	90
5.20	Doppler corrected energy spectra of Cluster detectors	91
5.21	Cluster spectra without Doppler correction	92
5.22	Doppler corrected γ -spectra, without and with cutout	92
5.23	Different $\Delta E - E$ gates	93
5.24	Plot of $(Res_{vol})^{-1}$ for different combinations of gates	94
5.25	γ -spectra for the optimal particle gate combination	95
5.26	Plot of $(Res_{vol}^{poly})^{-1}$ in dependency of different time gates	96
5.27	^{36}Ar γ -spectra for both new time gates	97

5.28	^{33}Ar γ -spectra for both new time gates	98
5.29	Add back γ -spectrum	100
5.30	^{36}Ar γ -spectra with optimal gates, singles + add-back	100
5.31	^{33}Ar γ -spectra with optimal gates, singles + add-back	100
5.32	Illustration of determination of the scattering angle	101
5.33	^{36}Ar , counts per 2 mrad	101
5.34	^{33}Ar , counts per 2 mrad	101
5.35	γ -spectra of ^{36}Ar for different limitations on θ	102
5.36	<i>SR</i> spectrum from the Cluster detectors	104
5.37	Time difference SC41 - Cluster detector TDCs	105
5.38	Background γ -spectra of the marked regions	106
5.39	γ -spectra after background subtraction.	107
5.40	Background subtracted ^{36}Ar γ -ray spectrum	108
5.41	γ -spectra of $^{33,36}\text{Ar}$, for germanium rings individually	109
5.42	Relative ion transmission for different triggers	111
6.1	Relative ion transmission for different triggers	117
6.2	Angular distribution of emitted γ -rays of ^{36}Ar in the different systems of inertia	120
6.3	Comparison of angular distributions of γ -ray emission for $^{33,36}\text{Ar}$	121
6.4	Ratio between angular distribution of both isotopes	121
6.5	Illustration of the transitions in a system with three levels	123
6.6	Illustration of the effect of the branching ratio	124
6.7	Published $B(E2)$ values of ^{36}Ar	127
6.8	Final γ -ray spectra of this experiment	129
7.1	Experimental MEDs of the $T = 1, 2$ <i>sd</i> shell mirror pairs	134
7.2	SPEs used in the $\text{USD}_{1,3}^m$ interactions	134
7.3	Level schemes of ^{33}Ar and ^{33}P	136
7.4	Shell model calculations employing the USD, USD_1^m and USD_3^m interactions	138
7.5	MED of ^{33}Ar - ^{33}P vs spins	139
7.6	SM calculations of the MEDs of $T = \frac{3}{2}$ <i>sd</i> shell mirror pairs	139
7.7	Illustration of the nuclei in the <i>sd</i> shell	140
7.10	Illustration of $T_z = \pm\frac{3}{2}$ <i>sd</i> shell nuclei	142
7.8	Experimental $B(E2, 2_1^+ \rightarrow 0_{g.s.}^+)$ values of $T_z = \pm 1, 2$ <i>sd</i> shell nuclei	143

7.9	Experimental $B(E2)$ values of $T_z = \pm \frac{3}{2}$ sd shell nuclei	144
8.1	Photograph of the AGATA demonstrator, Legnaro	149
8.2	Photograph of the AGATA demonstrator, GSI	150
8.3	Hit pattern of LYCCA-1 detectors	151
A.1	Illustration of single-particle orbits in the shell model	154
B.1	Experimental $E(2_1^+)$ energies and $B(E2)$ values	156
C.1	A/Q vs. Z for target DSSD multiplicities 0 to 3	157
C.2	A/Q vs. Z for target DSSD multiplicities 4 to 6 and $M_{tar} > 1$	158
C.3	$\Delta E - E$ gates	159
C.4	$\Delta E - \Delta E$ gates	160
C.5	$\beta_{FRS} - \beta_{LYCCA}$ gates	161
C.6	$\beta_{LYC} - CsI$ gates	162
C.7	Target DSSD $E - T$ gates	163
D.1	Technical drawings of the LYCCA chamber 2	165
D.2	Technical drawings of the LYCCA chamber 3	166
D.3	Technical drawings of detector module	167

List of Tables

2.1	SPEs used in the USD _{1,2,3} ^m interactions	20
3.1	FRS settings for commissioning experiment	35
3.2	FRS settings for ³³ Ar experiment	36
3.3	Mocadi calculation of beam contaminations	37
3.4	Plan and realization of the S377 experiment.	37
3.5	Composition of the secondary fragmentation beam	39
3.6	Used triggers in the described S377 experiment	43
4.1	Overview of DSSD characteristics	47
4.2	Covered scattering angles	52
4.3	Specifications of LYCCA preamplifiers	57
4.4	Resolutions of the first LYCCA DSSD	59
4.5	Energy resolutions of central DSSDs	63
4.6	Energy resolutions of CsI scintillators	64
4.7	Energy deposition at LYCCA detectors	65
5.1	Mean Z values from FRS identification	85
5.2	Values of Res_{vol} after each step of the analysis	99
5.3	Results of the fits	103
5.4	Parameters and integrals of background function	106
5.5	Results of the fits after applying the background subtraction	107
5.6	Detected γ -rays	109
5.7	Values of Res_{vol} after each step of the analysis	110
5.8	Summary of ³³ Ar production	111
6.1	Proportional factors	114
6.2	Calculation of the setup efficiency	115

6.3	Experimental details	116
6.4	Parameters of efficiency fit	117
6.5	Calculated energy-dependence of efficiency	118
6.6	Calculated angular-dependence of efficiency	122
6.7	Experimental details	122
6.8	Calculation of the $B(E2, \frac{3}{2}^+ \rightarrow \frac{1}{2}^+)$	125
6.9	Calculation of an upper limit for $B(E2, \frac{5}{2}^+ \rightarrow \frac{1}{2}^+)$	126
6.10	Calculation of $B(E2, \frac{5}{2}^+ \rightarrow \frac{1}{2}^+)$	126
6.11	Published measurements of the $B(E2)$ value of ^{36}Ar	127
6.12	Deduced transition strengths, dependent on reference value	128
6.13	Summary of experimental results	128
7.2	Mean level deviations of the different interactions	136
7.1	Characteristics of ^{33}Ar and ^{33}P states	137
7.3	Reduced transition strengths from experiments and shell model calculations	141
7.4	Proton separation energies of $T_z = -\frac{3}{2}$ <i>sd</i> shell nuclei	142
7.5	$B(E2)$ values and SM calculations for $T_z = \pm\frac{3}{2}$ with $A \leq 27$	146
7.6	$B(E2)$ values and SM calculations for $T_z = \pm\frac{3}{2}$ with $A \geq 29$	147

Bibliography

- [1] D. D. Warner, M. A. Bentley and P. Van Isacker, *The role of isospin symmetry in collective nuclear structure*, Nature Phys. 2, 311 (2006). [2.1](#), [2.2](#), [2.2](#), [2.3.2](#)
- [2] J. Chadwick, *The possible existence of the Neutron*, Nature 192, 312 (1932). [2.1](#)
- [3] H. Grawe, *Shell Model from a Practitioner's Point of View*, Lect. Notes Phys. 651, 33 (2004). [3](#), [A](#), [B](#)
- [4] O. Haxel, J. H. D. Jensen and H. E. Suess, *On the 'Magic Numbers' in Nuclear Structure*, Phys. Rev. 75, 1766 (1949). [A](#)
- [5] M. Göppert-Mayer, *On Closed Shells in Nuclei II*, Phys. Rev. 75, 1969 (1949). [A](#), [A.1](#)
- [6] C. F. von Weizsäcker, *Zur Theorie der Kernmassen*, Zeitschrift für Physik 96, 431 (1935). [2.3.1](#)
- [7] S. M. Lenzi and M. A. Bentley, *Test of Isospin Symmetry Along the $N = Z$ Line*, Lect. Notes Phys. 764, 57 (2009). [2.3.1](#), [2.3.2](#), [2.3](#), [2.3.2](#), [2.5](#), [2.6](#)
- [8] M. A. Bentley, C. Chandler, M. J. Taylor, J. R. Brown, M. P. Carpenter, C. Davids, J. Ekman, S. J. Freeman, P. E. Garrett, G. Hammond, R. V. F. Janssens, S. M. Lenzi, C. J. Lister, R. du Rietz and D. Seweryniak, *Isospin Symmetry of Odd-Odd Mirror Nuclei: Identification of Excited States in $N=Z-2$ ^{48}Mn* , Phys. Rev. Lett. 97, 132501 (2006). [2.5](#)
- [9] S. M. Lenzi, N. Marginean, D. R. Napoli, C. A. Ur, A. P. Zuker, G. de Angelis, A. Algora, M. Axiotis, D. Bazzacco, N. Belcari, M. A. Bentley, P. G. Bizzeti, A. Bizzeti-Sona, F. Brandolini, P. von Brentano, D. Bucurescu, J. A. Cameron, C. Chandler, M. De Poli, A. Dewald, H. Eberth, E. Farnea, A. Gadea, J. Garces-Narro, W. Gelletly, H. Grawe, R. Isocrate, D.T. Joss, C. A. Kalfas, T. Klug, T. Lampman, S. Lunardi, T. Martínez, G. Martínez-Pinedo, R. Menegazzo, J. Nyberg, Zs. Podolyak, A. Poves, R.V. Ribas, C. Rossi Alvarez, B. Rubio, J. Sánchez-Solano, P. Spolaore, T. Steinhardt, O. Thelen, D. Tonev, A. Vitturi, W. von Oertzen and M. Weiszflog, *Coulomb Energy Differences in $T = 1$ Mirror Rotational Bands in ^{50}Fe and ^{50}Cr* , Phys. Rev. Lett. 87, 122501 (2001). [2.3.2](#)
- [10] E.P. Wigner, Proceedings of the Robert A Welch Conference on Chemical Research (1957). [2.3.1](#)
- [11] P. E. Garrett, W. E. Ormand, D. Appelbe, R. W. Bauer, J. A. Becker, L. A. Bernstein, J. A. Cameron, M. P. Carpenter, R. V. F. Janssens, C. J. Lister, D. Seweryniak, E. Tavukcu and D. D. Warner, *Observation of ^{46}Cr and Testing the Isobaric Multiplet Mass Equation at High Spin*, Phys. Rev. Lett. 87, 132502 (2001). [2.3.1](#)

- [12] J. A. Nolen and J. P. Schiffer, *Coulomb energies - an anomaly in nuclear matter radii*, Ann. Rev. Nucl. Sci 19, 471, 64 (1969). [2.3.1](#), [2.3.2](#)
- [13] M. H. Shahnas, *Nolen-Schiffer anomaly of mirror nuclei and charge symmetry breaking in nuclear interactions*, Phys. Rev. C 50, 2346 (1994). [2.3.1](#)
- [14] J. Duflo and A. P. Zuker, *Mirror displacement energies and neutron skins*, Phys. Rev. C 66, 051304 (2002). [2.3.1](#), [2.3.2](#)
- [15] R. R. Reynolds, P. D. Cottle, A. Gade, D. Bazin, C. M. Campbell, J. M. Cook, T. Glasmacher, P. G. Hansen, T. Hoagland, K. W. Kemper, W. F. Mueller, B. T. Roeder, J. R. Terry and J. A. Tostevin, *^{25}Si and ^{29}S studied via single neutron knockout reactions*, Phys. Rev. C 81, 067303 (2010). [2.3.2](#), [2.3.4.2](#), [2.12](#), [7.6](#)
- [16] P. Doornenbal, P. Reiter, H. Grawe, T. Otsuka, A. Al-Khatib, A. Banu, T. Beck, F. Becker, P. Bednarczyk, G. Benzoni, A. Bracco, A. Burger, L. Caceres, F. Camera, S. Chmel, F. C. L. Crespi, H. Geissel, J. Gerl, M. Gorska, J. Grebosz, H. Hubel, M. Kavatsyuk, O. Kavatsyuk, M. Kmiecik, I. Kojouharov, N. Kurz, R. Lozeva, A. Maj, S. Mandal, W. Meczynski, B. Million, Zs. Podolyak, A. Richard, N. Saito, T. Saito, H. Schaffner, M. Seidlitz, T. Stiepling, Y. Utsuno, J. Walker, N. Warr, H. Weick, O. Wieland, M. Winkler, H. J. Wollersheim, *The $T = 2$ mirrors ^{36}Ca and ^{36}S : A test for isospin symmetry of shell gaps at the driplines*, Phys. Lett. B 647, 237 (2007). [2.3.2](#), [2.3.4](#), [2.3.4.1](#), [2.10](#), [7.1](#), [7.1](#), [A](#)
- [17] P. Doornenbal, *In-beam γ -ray spectroscopy of two-step fragmentation reactions at relativistic energies — The case of ^{36}Ca* , PhD thesis, University of Cologne (2007). [2.3.4.1](#), [2.1](#), [2.10](#), [7.1](#), [7.1](#), [7.2](#)
- [18] A. Gade, P. Adrich, D. Bazin, M. D. Bowen, B. A. Brown, C. M. Campbell, J. M. Cook, T. Glasmacher, K. Hosier, S. McDaniel, D. McGlinchery, A. Obertelli, L. A. Riley, K. Siwek and D. Weisshaar, *Spectroscopy of ^{20}Mg : The isobaric mass multiplet equation for the 2^+ states of the $A = 20$, $T = 2$ quintet and distant mirror nuclei*, Phys. Rev. C 76, 024317 (2007). [2.3.4.1](#), [2.10](#), [7.1](#)
- [19] A. Gade, D. Bazin, B. A. Brown, C. M. Campbell, J. A. Church, D. C. Dinca, J. Enders, T. Glasmacher, P. G. Hansen, Z. Hu, K. W. Kemper, W. F. Mueller, H. Olliver, B. C. Perry, L. A. Riley, B. T. Roeder, B. M. Sherrill, J. R. Terry, J. A. Tostevin and K. L. Yurkewicz, *Reduced Occupancy of the Deeply Bound $0d_{5/2}$ Neutron State in ^{32}Ar* , Phys. Rev. Lett. 93, 042501 (2004). [2.3.4.1](#)
- [20] H. Schatz, J. Görres, H. Herndl, N. I. Kaloskamis, E. Stech, P. Tischhauser, M. Wiescher, A. Bacher, G. P. A. Berg, T. C. Black, S. Choi, C. C. Foster, K. Jiang and E. J. Stephenson, *First Measurement of Excited States in the Very Proton Rich Nucleus ^{24}Si and the Consequences for ^{22}Na Nucleosynthesis in Novae*, Phys. Rev. Lett. 79, 203845 (1997) [2.3.4.1](#), [2.10](#), [7.1](#)
- [21] P. D. Cottle, Z. Hu, B. V. Pritychenko, J. A. Church, M. Fauerbach, T. Glasmacher, R. W. Ibbotson, K. W. Kemper, L. A. Riley, H. Scheit, M. Steiner, *$0_{gs}^+ \rightarrow 2_1^+$ Excitations in the Mirror Nuclei ^{32}Ar and ^{32}Si* , Phys. Rev. Lett. 88, 172502 (2002). [2.3.2](#), [7.1](#), [7.8d](#)
- [22] A. P. Zuker, S. M. Lenzi, G. Martinez-Pinedo and A. Poves, *Isobaric Multiplet Yrast Energies and Isospin Nonconserving Forces*, Phys. Rev. Lett. 89, 142502 (2002). [2.3.2](#), [2.3.3](#)

- [23] Th. Andersson, D. Rudolph, C. Baktash, J. Eberth, C. Fahlander, D. Haslip, D. R. LaFosse, S. D. Paul, D. G. Sarantites, C. E. Svensson, H. G. Thomas, J. C. Waddington, W. Weintraub, J. N. Wilson, B. A. Brown, *High-spin states in the $A = 39$ mirror nuclei ^{39}Ca and ^{39}K* , Eur. Phys. J. A 6, 5 (1999). [2.3.4](#)
- [24] E. N. Jensen, R. T. Nichols, J. Clement and A. Pohm, *The Beta-Spectra of ^{32}P and ^{33}P* , Phys. Rev. 85, 112 (1952). [2.4](#), [7.2](#)
- [25] R. T. Nichols and E. N. Jensen, *Radioisotope ^{33}P* , Phys. Rev. 94, 369 (1954). [2.4](#), [7.2](#)
- [26] D. R. Goosman, C. N. Davids and D. E. Alburger, *Accurate Masses and β -Decay Schemes for ^{34}P and ^{33}Si* , Phys. Rev. C 8, 1324 (1973). [2.4](#), [7.2](#)
- [27] R. Chakrabarti, S. Mukhopadhyay, Krishichayan, A. Chakraborty, A. Ghosh, S. Ray, S. S. Ghugre, A. K. Sinha, L. Chaturvedi, A. Y. Deo, I. Mazumdar, P. K. Joshi, R. Palit, Z. Naik, S. Kumar, N. Madhavan, R. P. Singh, S. Muralithar, B. K. Yogi and U. Garg, *Experimental study of nuclei in the vicinity of the "island of inversion" through the fusion-evaporation reaction*, Phys. Rev. C 80, 034326 (2009). [2.4](#), [7.2](#)
- [28] R. C. Barse, D. H. Youngblood and J. L. Yntema, *Proton Hole States in ^{29}Al , ^{31}P , and ^{33}P* , Phys. Rev. 167, 1043 (1968). [2.4](#), [7.2](#)
- [29] E. H. Berkowitz, A. A. Rollefson, E. D. Berners and C. P. Browne, *Excitation energies in ^{33}P* , Nuclear Physics A 140, 173(1970). [2.4](#), [7.2](#)
- [30] C. E. Moss, R. V. Poore, N. R. Roberson and D. R. Tilley, *Spins of Levels in ^{33}P* , Phys. Rev. 174, 420 (1968). [2.4](#), [7.2](#)
- [31] W. G. Davies, J. C. Hardy and W. Darcey, *The $^{31}\text{P}(t, p)^{33}\text{P}$ reaction and the usefulness of double-stripping in distinguishing among shell-model calculations*, Nucl. Phys. A 128, 2 465 (1969). [2.4](#), [7.2](#)
- [32] W. R. Harris, K. Nagatani and J. W. Olness, *Levels in ^{33}P of $E_{ex} < 4.3$ MeV*, Phys. Rev. C, 1412 (1970). [2.4](#), [7.2](#)
- [33] C. E. Thorn, J. W. Olness, E. K. Warburton and S. Raman, *$^{36}\text{S}(d, p)^{37}\text{S}$ and $^{34,36}\text{S}(d, ^3\text{He})^{33,35}\text{P}$ reactions*, Phys. Rev. C 30, 1442 (1984). [2.4](#), [7.2](#)
- [34] S. Khan, G. Mairle, K. T. Knöpfle, Th. Kihm, Pao Liu-KenP. Grabmayr, G.J. Wagner and L. Friedrich, *Hole-strength distributions from the $^{34}\text{S}(\vec{d}, ^3\text{He})^{33}\text{P}$ and $^{34}\text{S}(\vec{d}, t)^{33}\text{S}$ reactions*, Nucl. Phys. A 481, 2 253 (1988). [2.4](#), [7.2](#)
- [35] H. Nann, W. Benenson, E. Kashy and P. Turek, *Isobaric mass quartets in $A=33$ nuclei*, Phys. Rev. C 9, 1848 (1974). [2.4](#), [7.2](#)
- [36] R. R. C. Clement, D. Bazin, W. Benenson, B. A. Brown, A. L. Cole, M. W. Cooper, P. A. DeYoung, A. Estrade, M. A. Famiano, N. H. Frank, A. Gade, T. Glasmacher, P.T. Hosmer, W. G. Lynch, F. Montes, W. F. Mueller, G. F. Peaslee, P. Santi, H. Schatz, B.M. Sherrill, M.-J. van Goethem and M. S. Wallace, *New Approach for Measuring Properties of rp -Process Nuclei*, Phys. Rev. Lett. 92, 172502 (2004). [2.4](#), [6.3.1](#), [7.2](#)
- [37] M. Seidlitz, *Private communication: Shell structure of nuclei* (2012). [A.1](#)

- [38] J. Ekman, D. Rudolph, C. Fahlander, A. P. Zuker, M. A. Bentley, S. M. Lenzi, C. Andreoiu, M. Axiotis, G. de Angelis, E. Farnea, A. Gadea, T. Kröll, N. Marginean, T. Martinez, M. N. Mineva, C. Rossi-Alvarez and C. A. Ur, *Unusual Isospin-Breaking and Isospin-Mixing Effects in the $A = 35$ Mirror Nuclei*, Phys. Rev. Lett. 92 132502 (2004). 2.3.2, 2.3.4, 2.3.4, 2.8, 2.9
- [39] N. S. Pattabiraman, D. G. Jenkins, M. A. Bentley, R. Wadsworth, C. J. Lister, M. P. Carpenter, R. V. F. Janssens, T. L. Khoo, T. Lauritsen, D. Seweryniak, S. Zhu, G. Lotay and P. J. Woods, *Analog $E1$ transitions and isospin mixing*, Phys. Rev. C 78, 024301 (2008). 2.3.4
- [40] F. D. Vedova, *Isospin Symmetry in the sd shell: The $A=31$ and $A=35$ Mirror Nuclei*, PhD thesis (2004). 2.3.4, 2.7
- [41] A. Poves, J. Sánchez-Solano, E. Caurier and F. Nowacki, *Shell model study of the isobaric chains $A = 50$, $A = 51$ and $A = 52$* , Nuclear Physics A 694, 157 (2001). 2.3.3
- [42] E. Caurier, K. Langanke, G. Martínez-Pinedo, F. Nowacki and P. Vogel, *Shell model description of isotope shifts in calcium*, Physics Letters B 522, 240 (2001). 2.3.4
- [43] K. L. G. Heyde, *The Nuclear Shell Model*, Springer (1990). ??, B
- [44] B. A. Brown, *Lecture Notes in Nuclear Structure Physics*, <http://www.scribd.com/doc/58152887/17/Reduced-transition-probabilities-for-gamma-decay> (2005). B
- [45] S. Raman, C. W. Nestor and K. H. Bhatt, *Systematics of $B(E2; 0_1^+ \rightarrow 2_1^+)$ values for even-even nuclei*, Physical Review C 37, 805 (1988). B.1
- [46] Kogut, J.B.: *Introduction to Relativity*, Hartcourt/Academic Press, Massachusetts (2001). 4.3.4.2
- [47] K. Bethge, G. Walter and B. Wiedemann: *Kernphysik*, Springer (2008). 3.3.2.3, 4.3.4.1
- [48] R. Hoischen, S. Pietri, D. Rudolph, W. Prokopowicz, H. Schaffner, S. Emde, P. Golubev, A. Wendt, N. Kurz, H. J. Wollersheim, J. Gerl: *Fast timing with plastic scintillators for in-beam heavy-ion spectroscopy*, Nuclear Instr. and Meth. A 654, 1 354 (2011). 4.9, 4.2.4
- [49] R. Hoischen, *Isotope-selective spectroscopy: fast timing R&D and pf shell mirror isomers*, PhD thesis, Lund University (2011). 4.2.4
- [50] J. Taprogge, *First in-beam measurements with the $\Delta E - E$ -TOF LYCCA-Array at relativistic energies*, Master thesis, University of Cologne (2011). 4, 4.3.4.1, 4.3.4.2, 4.38
- [51] Electronics workshop, Institut für Kernphysik University of Cologne, *Private communication: Technical drawings* (2012). 4.2.6
- [52] H. Grawe, *Private communication: Shell model calculations for sd shell nuclei* (2012). 2.11, 2.12, 7.6, 7.3, 7.8, 7.9
- [53] D. Rudolph, C. Fahlander, P. Golubev, R. Hoischen, V. Avdeichikov, M. A. Bentley, S. P. Fox, J. Gerl, Ch. Görge, M. Gorska, G. Pascovici, P. Reiter, H. Schaffner, M. J. Taylor, S. Thiel and H. J. Wollersheim, *LYCCA - the Lund-York-Cologne CALorimeter*, <http://www.nuclear.lu.se/fileadmin/nuclear/Grundlaeggande/lycca-TDR.pdf> (2011). 4.3.3, 4.4

- [54] Z. Kis, B. Fazekas, J. Östör, Zs. Révay, T. Belgya, G.L. Molnár, L. Koltay: *Comparison of efficiency functions for Ge gamma-ray detectors in a wide energy range*, Nuclear Instr. and Meth. A 418, 374 (1998). 6.2.1
- [55] T. Steinhardt, *Die Hochspineigenschaften der neutronenarmen Kerne ^{73,74,75,76}Kr*, PhD thesis, University of Cologne (2005). 6.2.1
- [56] C.A. Bertulani, C.M. Campbell, T. Glasmacher, *A computer program for nuclear scattering at intermediate and high energies*, Computer Physics Communications 152, 317 (2003). 6.1, 6.1, ??
- [57] National Nuclear Data Center, <http://www.nndc.bnl.gov> (2012). 2.11, 2.12, 2.13, 6, 6.1, 6.3, 6.4, 6.13, 7.6, 7.8b, 7.8d, 7.9a, 7.9c, 7.9d
- [58] J. Simpson, *The Euroball Spectrometer*, Z. Phys. A 358, 139–143 (1997) 3.5
- [59] A. Maj, J.J. Gaardhøje, A. Ataç, S. Mitarai, J. Nyberg, A. Virtanen, A. Bracco, F. Camera, B. Million, M. Pignanelli, *Angular distribution of photons from the delay of the GDR in hot and rotating light Yb nuclei from exclusive experiments*, Nucl. Phys. A 571, 1 185 (1994). 3.5
- [60] The AGATA collaboration, *AGATA - Advanced GAMMATrackingArray*, Nucl. Instr. and Meth. A 668, 26 (2012). 3.5
- [61] W. A. Friedman, *Heavy ion projectile fragmentation: A reexamination*, Phys. Rev. C 27, 2 (1983) 3.2
- [62] J. J. Gaimard and K. H. Schmidt, *A reexamination of the abrasion-ablation model for the description of the nuclear fragmentation reaction*, Nucl. Phys. A 531 (1991) 709. 3.2
- [63] GSI LINAC Department, <http://www-inj.gsi.de> (2012). 3.3.1
- [64] GSI Schwerionensynchrotron SIS 18, <http://www.gsi.de/beschleuniger/sis18/sis.html> (2012). 3.3.1
- [65] D. Bazin, O. Tarasov, M. Lewitowicz, O. Sorlin, *LISE: Simulation of Fragment Separators*, <http://lise.nscl.msu.edu/lise.html>, NIM A 482, 307 (2002). 3.1, 3.2
- [66] <http://www-linux.gsi.de/~wolle/TELEKOLLEG/KERN/LECTURE/Wollersheim/2012/2-Beschleuniger.ppt> (2012). 3.2
- [67] G. Münzenberg, *Separation techniques for secondary beams*, Nucl. Instrum. Meth. B 70, 265 (1992) 3.3.2
- [68] H. Geissel and G. Münzenberg, *Secondary Exotic Nuclear Beams*, Annu. Rev. Nucl. Part. Sci. 163 (1995) 3.3.2
- [69] H. Geissel, P. Armbruster, K. H. Behr, A. Brünle, K. Burkard, M. Chen, H. Folger, B. Franczak, H. Keller, O. Klepper, B. Langenbeck, F. Nickel, E. Pfeng, M. Pfützner, E. Roeckl, K. Rykaczewski, I. Schall, D. Schardt, C. Scheidenberger, K.-H. Schmidt, A. Schröter, T. Schwab, K. Sümmerer, M. Weber and G. Münzenberg, *The GSI Projectile Fragment Separator (FRS) : a versatile magnetic system for relativistic heavy ions*, Nucl. Instrum. Meth. B70 (1992) 286 3.3.2

- [70] *Relativistic Beams of Exotic Nuclei - A Powerful Tool for Nuclear Structure Physics*, GSI-Nachrichten 3/1997, <http://www-wnt.gsi.de/frs/intro.asp> (1997). 3.3
- [71] R. Schneider and A. Stolz, *Technical Manual Ionisation Chamber MUSIC80, 2000*, http://www-wnt.gsi.de/frs/technical/FRSsetup/detectors/music80/music80_manual.pdf (2012). 3.3.2.1, 3.5
- [72] P. Reiter, F. Becker, M. A. Bentley, A. Bracco, G. de Angelis, C. Fahlander, J. Gerl, M. Gorska, H. Grawe, H. Hübel, J. Jolie, A. Maj, P. Mayet, T. Saito, K.-H. Speidel and H. J. Wollersheim, *Future RISING Experiments at relativistic energies*, Acta Phys. Pol. B 36, 4 (2005). 3
- [73] High-Resolution In-flight Spectroscopy / Decay Spectroscopy, https://www.gsi.de/forschung/fair_experiments/NUSTAR/hispec_e.html (2012). 3
- [74] Nuclear Structure, Astrophysics and Reactions, <http://www.fair-center.com/index.php?id=334> (2012). 3
- [75] Facility for Antiproton and Ion Research, <http://www.fair-center.com> (2012). 3
- [76] Gesellschaft für Schwerionenforschung mbH, <http://www.gsi.de> (2012). 3
- [77] A. Prochazka, *Time Projection Chambers as part of the FRS*, Private Communication, May 2012. 3.6
- [78] H.J. Wollersheim, D.E. Appelbe, A. Banu, R. Bassini, T. Beck, F. Becker, P. Bednarczyk, K.-H. Behr, M.A. Bentley, G. Benzoni, C. Boiano, U. Bonnes, A. Bracco, S. Brambilla, A. Brünle, A. Bürger, K. Burkard, P.A. Butler, F. Camera, D. Curien, J. Devin, P. Doornenbal, C. Fahlander, K. Fayz, H. Geissel, J. Gerl, M. Gorska, H. Grawe, J. Grebosz, R. Griffiths, G. Hammond, M. Hellström, J. Hoffmann, H. Hübel, J. Jolie, J.V. Kalben, M. Kmiecik, I. Kojouharov, R. Kulesa, N. Kurz, I. Lazarus, J. Li, J. Leske, R. Lozeva, A. Maj, S. Mandal, W. Meczynski, B. Million, G. Münzenberg, S. Muralithar, M. Mutterer, P.J. Nolan, G. Neyens, J. Nyberg, W. Prokopowicz, V.F.E. Pucknell, P. Reiter, D. Rudolph, N. Saito, T.R. Saito, D. Seddon, H. Schaffner, J. Simpson, K.-H. Speidel, J. Styczen, K. Sümmerer, N. Warr, H. Weick, C. Wheldon, O. Wieland, M. Winkler and M. Zieblinski, *Rare ISotopes INvestigation at GSI (RISING) using gamma-ray spectroscopy at relativistic energies*, Nucl. Instr. Meth. A 537 (2005) 637. 3, 6.2.2
- [79] M. Hackstein, *Lorentz Boost for different velocities*, Private Communication, May 2012. 6.2.2
- [80] P. van Duppen, *Isotope Separation On Line and Post Acceleration*, Lect. Notes Phys. 700, 37 (2006). 3.2
- [81] <http://www.mesytec.com> (2012). 4.2.6
- [82] <http://www.caen.it> (2012). 4.2.6
- [83] P. Wagner, J. P. Coffin, M. A. Ali, D. E. Alburger and A. Gallmann, *Lifetime Measurements of Low-Lying States of ^{33}P* , Phys. Rev. C 7, 2418 (1973) 2.4, 7.2, ??, 7.3
- [84] A. R. Poletti, T. T. Bardin, J. G. Pronko and R. E. McDonald, *Lifetimes in P by the Doppler-Shift-Attenuation Method*, Phys. Rev. C 7, 1433 (1973) 2.4, 7.2, ??, 7.3, 7.9a, 7.9b

- [85] A. Einstein, *On the Electrodynamics of Moving Bodies*, Annalen der Physik 322, 10, 891, (1905) [5.4](#), [6.2.2](#)
- [86] B. A. Brown and B. H. Wildenthal, *Status of the nuclear shell model*, Ann. Rev. Nucl. Part. Sci., 38, 29 (1988) [2.3.4.1](#), [7.1](#), [7.1](#), [A](#)
- [87] B. H. Wildenthal, E. C. Halbert, J. B. McGrory and T. T. S. Kuo, Calculations with a $1s, 0d$ Shell Model for $A = 34 - 38$ Nuclei, Phys. Rev. C 4, 1266 (1971). [2.3.4.1](#), [A](#)
- [88] Y. Utsuno, T. Otsuka, T. Mizusaki and M. Honma, *Varying shell gap and deformation in $N \sim 20$ unstable nuclei studied by the Monte Carlo shell model*, Phys. Rev. C 60, 054315 (1999). [2.3.4.1](#), [7.1](#), [A](#)
- [89] A. Wendt, P. Reiter, A. Algora, F. Ameil, M. A. Bentley, A. Blazhev, D. Bloor, N. Bondili, P. Boutachkov, M. Bowry, A. Bracco, N. Braun, F. Camera, J. Cederkall, F. Crespi, A. de la Salle, D. Dijulio, P. Doornenbal, K. Geibel, J. Gellanki, J. Gerl, P. Golubev, H. Grawe, J. Grebosz, G. Guastalla, T. Habermann, M. Hackstein, R. Hoischen, J. Jolie, A. Jungclaus, I. Kojouharov, N. Kurz, S. Lenzi, E. Merchan, B. Million, A. Morales, K. Moschner, S. Pietri, Z. Podolyak, D. Ralet, F. Recchia, D. Rudolph, H. Schaffner, L. Scruton, B. Siebeck, J. Taprogge, O. Wieland and H.-J. Wollersheim, *Coulomb Excitation of ^{33}Ar – a test of isospin symmetry in the sd shell*, GSI scientific report 2011 PHN-NUSTAR-FRS-10, 152 (2011). [3.1.4](#)
- [90] K. Moschner, A. Blazhev, N. Braun, M. Hackstein, J. Jolie, F. Naqvi, P. Reiter, M. Rudigier, J. Taprogge, T. Thomas, N. Warr, A. Wendt, F. Ameil, P. Boutachkov, J. Gerl, M. Górska, T. Habermann, I. Kojouharov, N. Kurz, E. Merchán, C. Nociforo, S. Pietri, A. Prochazka, H. Schaffner, H. Weick, H.-J. Wollersheim, M. Bentley, B. S. Nara Singh, L. Scruton, A. Algora, S. Brambilla, F. Camera, A. Corsi, A. Giaz, O. Wieland, J. Cederkäll, D. Dijulio, C. Fahlander, P. Golubev, R. Hoischen, D. Rudolph, M. Danchev, J. Grebosz, Z. Podolyak, T. Möller, M. Reese, N. Marginean and T. Sava, *Relativistic Coulomb excitation of ^{88}Kr* , GSI scientific report 2011 PHN-NUSTAR-FRS-11, 153 (2011). [3.1.2](#), [4](#)
- [91] N. Pietralla, P. von Brentano and A. F. Lisetskiy, *Experiments on multiphonon states with proton–neutron mixed symmetry in vibrational nuclei*, Prog.Part.Nucl.Phys. 60, 225 (2008). [3.1.2](#)
- [92] J. Cederkall, D. Dijulio, A. Ekström, C. Fahlander, J. Gellanki, P. Golubev, R. Hoischen, D. Rudolph, M. Gorska, J. Gerl, H.-J. Wollersheim, H. Schaffner, I. Kojouharov, N. Kurz, G. Tveten, J. Nyberg, P. A. Söderström, T. Bäck, B. Cederwall, J. Jolie, P. Reiter, M. Bentley, R. Wadsworth, T. Engeland, M. Hjorth-Jensen, Z. Janas, M. Karny, A. Korgul, S. Mianowski, M. Pfuetzner, Z. Dombradi, A. Algora, Z. Elekes, D. Sohler, A. Atac, *Relativistic Coulomb Excitation of Neutron Deficient Isotopes in the ^{100}Sn region*, GSI Proposal (2009). [3.1.3](#)
- [93] D. Ralet, *Trigger logic development for the PreSpec collaboration*, Internship report for an engineer degree, GSI, Darmstadt (2011). [3.6](#), [3.13](#), [3.6](#)
- [94] H.G. Essel and N. Kurz, *GSI Multi-Branch System - Reference Manual. GSI, version: 5.1 edition* (2010). [3.6](#)
- [95] J. Hoffmann, N. Kurz and M. Richter. *TRIVA, VME Trigger Module*, GSI (2003). [3.6](#)

- [96] H. Schaffner, *Private communication: PreSpec DAQ* (2012). [3.12](#)
- [97] K. Yoneda, A. Obertelli, A. Gade, D. Bazin, B. A. Brown, C. M. Campbell, J. M. Cook, P. D. Cottle, A. D. Davies, D.-C. Dinca, T. Glasmacher, P. G. Hansen, T. Hoagland, K. W. Kemper, J.-L. Lecouey, W. F. Mueller, R. R. Reynolds, B. T. Roeder, J. R. Terry, J. A. Tostevin, and H. Zwahlen, *Two-neutron knockout from neutron-deficient ^{34}Ar , ^{30}S and ^{26}Si* , Phys. Rev. C 74, 021303 (2006). [2.3.4.1](#), [2.10](#), [7.1](#)
- [98] S.Kanno, T.Gomi, T.Motobayashi, K.Yoneda, N.Aoi, Y.Ando, H.Baba, K.Demichi, Z.Fulop, U.Futakami, H.Hasegawa, Y.Higurashi, K.Ieki, N.Imai, N.Iwasa, H.Iwasaki, T.Kubo, S.Kubono, M.Kunibu, Y.U.Matsuyama, S.Michimasa, T.Minemura, H.Murakami, T.Nakamura, A.Saito, H.Sakurai, M.Serata, S.Shimoura, T.Sugimoto, E.Takeshita, S.Takeuchi, K.Ue, K.Yamada, Y.Yanagisawa, A.Yoshida, M.Ishihara, *Coulomb Excitation of ^{24}Si* , Prog.Theor.Phys.(Kyoto), Suppl. 146, 575 (2002). [7.8d](#)
- [99] N.Iwasa, S.Bishop, Z.Elekes, J.Gibelin, M.Hosoi, K.Ieki, K.Ishikawa, H.Iwasaki, S.Kawai, S.Kubono, K.Kurita, M.Kurokawa, N.Matsui, T.Minemura, H.Morikawa, T.Nakamura, M.Niikura, M.Notani, S.Ota, A.Saito, H.Sakurai, S.Shimoura, K.Sugawara, T.Sugimoto, H.Suzuki, T.Suzuki, I.Tanihata, E.Takeshita, S.Takeuchi, T.Teranishi, Y.Togano, K.Yamada, K.Yamada, K.Yamaguchi, Y.Yanagisawa, T.Motobayashi, *Coulomb Excitation of ^{20}Mg* , RIKEN Accelerator Progress Report 2005, p.59 (2006). [7.8d](#)
- [100] P.Reiter, A. Blazhev, B. Bruyneel, A. Dewald, K. Geibel, J. Jolie, M. Seidlitz, B. Siebeck, N. Warr, A. Wendt, H. Grawe, J. Gerl, M. Gorska, I. Kojouharov, N. Kurz, S.Pietri, H. Schaffner, H.J. Wollersheim, M. A.Bentley, R. Wadsworth, T. Brock, I. Paterson, B. S. Nara Singh, S. P. Fox, M. J.Taylor, C. Fahlander, P.Golubev, R.Hoischen, D.Rudolph, N. Pietralla, J. Leske, O. Möller, N. V. Zamfir, S. M. Lenzi, F. Recchia, D. R. Napoli, *Neutron-deficient sd-shell nuclei and mirror symmetry at the proton drip line – a PreSPEC Proposal*, unpublished.
- [101] F. Ameil, *Finger detector*, Private communication, May 2011. [3.4](#)
- [102] N. Iwasa, H. Geissel, G. Münzenberg, C. Scheidenberger, Th. Schwab, H. Wollnik, *MO-CADI, a universal Monte Carlo code for the transport of heavy ions through matter within ion-optical systems*, Nucl. Instr. and Meth. B 126, 284 (1997). [3.4.1](#), [3.3](#)
- [103] H. Grawe and K. P. Lieb, *E2 Transitions in Doubly Even sd shell nuclei*, Nuclear Physics A 127, 13 (1969). [??](#)
- [104] M. A. Moinester and W. Parker Alford, *The structure of ^{36}Ar And ^{38}Ar via the ($^3\text{He},D$) reaction on ^{35}Cl and ^{37}Cl* , Nuclear Physics A 145, 143 (1970). [??](#)
- [105] K. Nakai, F.S. Stephens and R. M. Diamond, *Quadrupole moment of the first excited state in ^{36}Ar* , Physics Letters, 34b, 5 (1971) [??](#)
- [106] G. A. Hokken, J. A. J. G. Hendricx and J. De Kogel, *Investigation of ^{36}Ar with the $^{35}\text{Cl}(p,\gamma)^{36}\text{Ar}$ reaction. Branching ratios, excitation energies and lifetimes of ^{36}Ar levels*, Nuclear Physics A194, 481 (1972). [??](#)
- [107] P. M. Johnson, M. A. Meyer and D. Reitmann, *A study of the $^{35}\text{Cl}(p,\gamma)^{36}\text{Ar}$ reaction and the energy levels of ^{36}Ar* , Nuclear Physics A 218, 333 (1974). [??](#)

- [108] J. M. Finn, H. Crannell, P. L. Hollowell And J. T. O'brien, *Inelastic electron scattering from low-lying states in the nuclei ^{36}Ar and ^{40}Ar* , Nuclear Physics A 290, 99 (1977). ??
- [109] B. V. Pritychenko, T. Glasmacher, P. D. Cottle, M. Fauerbach, R. W. Ibbotson, K. W. Kemper, V. Maddalena, A. Navin, R. Ronningen, A. Sakharuk, H. Scheit and V. G. Zelevinsky, *Role of intruder configurations in $^{26,28}\text{Ne}$ and $^{30,32}\text{Mg}$* , Physics Letters B 461, 322 (1999). ??
- [110] P. D. Cottle, M. Fauerbach, T. Glasmacher, R. W. Ibbotson, K. W. Kemper, B. Pritychenko H. Scheit and M. Steiner, *The $0_{g.s.}^+ \rightarrow 2_1^+$ transition in ^{38}Ca and isospin symmetry in $A = 38$ nuclei*, Phys. Rev. C 60, 031301 (1999). ??
- [111] K.-H. Speidel, S. Schielke, J. Leske, J. Gerber, P. Maier-Komor, S.J.Q. Robinson, Y.Y. Sharon And L. Zamick, *Experimental g factors and $B(E2)$ values in Ar isotopes: Crossing the $N = 20$ semi-magic divide*, Physics Letters B 632, 207 (2006). 6, ??
- [112] T. Kibedi and R. H. Spear, *Reduced electric-octupole transition probabilities, $B(E3; 0_1^+ \rightarrow 3_1^-)$ - An update*, Atomic Data and Nuclear Data Tables 80, 35 (2002). 6.1
- [113] M. G. Mayer, J. H. D. Jensen, *Elementary Theory of Nuclear Structure*, Wiley (1955). 7.1
- [114] B. A. Brown, W. A. Richter, R. E. Julies and B. H. Wildenthal, *Semi-empirical Effective Interactions for the $1s - 0d$ Shell*, Ann. Phys. 182, 191 (1988). 7.1
- [115] D. Guillemaud-Mueller, J. C. Jacrnat, E. Kashy, A. Latimier, A. C. Mueller, F. Pougheon, A. Richard, Yu. E. Penionzhkevich, A. G. Artuhk, A. V. Belozyorov, S. M. Lukyanov, R. Anne, P. Bricault, C. Detraz, M. Lewitowicz, Y. Zhang, Yu. S. Lyutostansky, M. V. Zverev, D. Bazin and W. D. Schmidt-Ott, *Particle stability of the isotopes ^{26}O and ^{32}Ne in the reaction $44 \text{ MeV / nucleon } ^{48}\text{Ca} + \text{Ta}$* , Phys. Rev. C 41, 41937 (1990). 7.1

Danksagung / Acknowledgment

Zuallererst möchte ich Prof. Dr. Peter Reiter für die intensive Betreuung dieser Arbeit danken. Er hatte stets ein offenes Ohr und brachte mir großes Vertrauen entgegen. Dies ermöglichte mir eigenständiges, selbstorganisiertes Arbeiten. Außerdem danke ich Prof. Dr. Jan Jolie für die Übernahme des Koreferats. Darüber hinaus danke ich den weiteren Mitgliedern der Prüfungskommission, Prof. Dr. Achim Rosch und Dr. Karl-Oskar Zell, für die investierte Zeit.

Jan Taprogge danke ich für seine hervorragende Mitarbeit bei den Tests der LYCCA Detektoren und der Teilchenidentifikation, Matthias Hackstein und Dr. Wolfram Rother für die fachkundige Unterstützung meiner Arbeit über viele Jahre. Ihr Engagement und Wissen trug maßgeblich zum Gelingen dieser Arbeit bei.

I owe special thanks to the complete LYCCA collaboration; in particular to Prof. Dr. Dirk Rudolph and Dr. Pavel Golubev, for the great cooperation in developing the LYCCA $\Delta E - E$ detectors. Furthermore I would like to thank all collaborators of the S377 experiment.

Ich danke der Elektronikwerkstatt unter Leitung von Christoph Goergen und der Feinmechanikwerkstatt unter Leitung von Stefan Thiel, sowie Dr. Gheorghe Pascovici für die gute Zusammenarbeit bei Konstruktion und Entwicklung der gesamten LYCCA Hardware und Elektronik.

I thank the whole γ -spectroscopy group of GSI for the support of the S377 experiment; in particular Dr. Stephane Pietri, who worked with great commitment on the preparation of the experiment. Also I thank Dr. Edana Merchan and Norbert Braun for providing the required software to operate LYCCA within experiments. I am also grateful to Prof. Dr. Andrea Jungclaus and Prof. Dr. Mike A. Bentley for the kind support during the GSI experiments.

I would like to thank Dr. Kerstin Geibel, Lianne Scruton, Dan Bloor and Douglas DiJulio for their attentive revision of my thesis. Natürlich gilt mein Dank auch allen weiteren aktuellen und ehemaligen Mitgliedern der Arbeitsgruppe, die einen großen Teil zur angenehmen Arbeitsatmosphäre im IKP beigetragen haben.

Besonderer Dank gebührt meiner Frau Michèle, die mich die letzten vier Jahre konstant unterstützt und motiviert hat. Darüber hinaus danke ich Christine Stotz, Silja Woltmann und Ilka Westerhoff für angenehme Zerstreuung während der Mittagspausen. Natürlich danke ich auch meiner Familie: meinen Eltern sowie Emma, Charly, Pauline und Lotta die mich fortwährend ermutigt haben. Schlussendlich gebührt aller Dank Gott, der alles ermöglicht hat.

Erklärung

Ich versichere, dass ich die von mir vorgelegte Dissertation selbständig angefertigt, die benutzten Quellen und Hilfsmittel vollständig angegeben und die Stellen der Arbeit – einschließlich Tabellen, Karten und Abbildungen –, die anderen Werken im Wortlaut oder dem Sinn nach entnommen sind, in jedem Einzelfall als Entlehnung kenntlich gemacht habe; dass diese Dissertation keiner anderen Fakultät oder Universität zur Prüfung vorgelegen hat; dass sie – abgesehen von unten angegebenen Teilpublikationen – noch nicht veröffentlicht ist, sowie dass ich eine solche Veröffentlichung vor Abschluss des Promotionsverfahrens nicht vornehmen werde. Die Bestimmungen der Promotionsordnung sind mir bekannt. Die von mir vorgelegte Dissertation ist von Prof. Dr. Peter Reiter betreut worden.

Teilveröffentlichungen: keine

Lebenslauf

Name		Andreas Wendt
Email-Adresse		a.wendt@ikp.uni-koeln.de
Geburtsdatum		05.11.1981
Geburtsort		Göttingen
Familienstand		verheiratet
Nationalität		deutsch
Schulische Ausbildung	1988-1990	Grundschule Sigmaringen
	1990-1992	Grundschule Hermeskeil
	1992-1994	Gymnasium Hermeskeil
	1994-2001	Gymnasium Erftstadt-Lechenich
	2001	Abitur
Wehrdienst	2001-2002	Allg. Wehrdienst, PzBtl. 203, Hemer
Universitäre Ausbildung	2002-2005	Physikstudium in Bonn
	16.03.2005	Vordiplom in Physik
	2005-2008	Physikstudium in Köln
	Seit Nov. 2006	SHK/WHK/WMA im Institut für Kernphysik
	02.09.2008	Diplom in Physik
	Seit Okt. 2008	Promotion im Institut für Kernphysik